LINEAR LIBRARY
C01 0068 3867

50
Ps

Coincident Proton Decay of the Continuum Induced by 200 MeV Protons on ^{12}C

University of Cape Town

J. V. Pilcher

A thesis submitted in partial fulfilment of the requirements
for the degree of Doctor of Philosophy
in the Department of Physics
University of Cape Town

March 1989

The University of Cape Town has been given the right to reproduce this thesis in whole or in part. Copyright is held by the author.

The copyright of this thesis vests in the author. No quotation from it or information derived from it is to be published without full acknowledgement of the source. The thesis is to be used for private study or non-commercial research purposes only.

Published by the University of Cape Town (UCT) in terms of the non-exclusive license granted to UCT by the author.

University of Cape Town

DST 530 PILC
90/2870

Coincident Proton Decay of the Continuum Induced by 200 MeV Protons on ^{12}C

John Victor Pilcher

National Accelerator Centre, P.O.Box 72, Faure, 7131, South Africa

March 1989

Abstract

Coincident protons from the reaction ^{12}C(p,2p) at an incident proton energy of 200 MeV, have been measured using conventional particle telescopes. Data were acquired at nine pairs of angles (θ_2=20°, 45°, 70°, 95°, 120° and 145° for θ_1=-20°, and θ_2=35°, 85° and 135° for θ_1=-45°).

An improved model, based on previous theoretical and experimental work, has been proposed to describe the reaction mechanism leading to the observed coincident proton yield from the nuclear continuum. This model considers an initial quasifree nucleon-nucleon interaction — described by a distorted wave impulse approximation (DWIA) treatment — between the incident proton and a single target nucleon, followed by the rescattering of the struck nucleon, which behaves as an intranuclear projectile, from the spectator part of the target nucleus.

The validity of the DWIA treatment used in the continuum study, has been tested by analysing the kinematic regions of the coincident proton energy spectra corresponding to the knockout of protons from the outer $1p_{3/2}$ orbital of ^{12}C which do not undergo further interactions with the residual nucleus. Good agreement in shape has been found between the calculated and measured cross sections in the kinematic region of interest to the continuum study. An average spectroscopic factor of 1.1±0.3 was extracted. Except in the -20°,20° case, the DWIA treatment was found to be insensitive to the choice of the initial or final energy prescriptions for the two-body scattering approximation. Nonlocality effects were found to be small, changing the absolute value of spectroscopic factors by a maximum of 20%.

Coincident continuum cross sections were extracted from the experimental data corresponding to the detection of protons at the θ_1 angles with energies of 70±5 MeV, 100±5 MeV and 130±5 MeV. Comparisons were made with calculations which modelled the proposed reaction mechanism in terms of a convolution integral over the DWIA cross sections describing the initial quasifree knockout process and experimental inelastic scattering probabilities describing the further multiple scattering interactions undergone by the knocked out nucleons. Good agreement has been found between the normalized calculated and measured continuum cross sections (spectroscopic factors varying from 0.8 to 2.3 between sets of data, depending on the kinematic region sampled and the prescription used for the two-body scattering approximation).

It has been shown that contributions from nucleons that are knocked out both in- and out-of-plane in the initial quasifree process should be considered, and that the contribution from neutron knockout in the initial interaction is significant, ranging from 0.13 to 0.62 that of the proton knockout contribution.

Acknowledgements

I wish to express my thanks to all those who have assisted in bringing this thesis to completion. I am particularly indebted to

- my supervisor, Dr A. A. Cowley of the National Accelerator Centre, for his guidance and enthusiasm during the execution of this project;
- my university supervisor, Professor F. D. Brooks of the University of Cape Town, for his encouragement and support throughout the many years of my association with his department;
- my colleagues at the National Accelerator Centre, Dr J. J. Lawrie, D. M. Whittal and S. V. Förtsch, for their assistance during the running of the experiments, and many helpful discussions of the work;
- the technical staff of the National Accelerator Centre, V. C. Wikner, K. A. Springhorn, D. A. Raavé and C. J. Stevens, for the efficient fabrication of electronic and mechanical requirements;
- Dr A. H. Botha and his accelerator operations staff, for the high quality proton beams, particularly that at 200 MeV after only three weeks of regular accelerator operation;
- Professors P. G. Roos and N. S. Chant of the University of Maryland for providing us with the computer code *THREEDEE* which enabled us to perform the theoretical DWIA calculations; and
- most importantly, my wife Heather, for bearing with patience and understanding the long hours of overtime spent away in conducting this project, when I should have been at home mending the plumbing.

Contents

1 Introduction **1**

1.1 Continuum States in Nuclei 2

  1.1.1 Inclusive spectra 2

  1.1.2 Coincidence spectra 8

1.2 Theoretical Background 10

  1.2.1 Impulse approximation 10

  1.2.2 Coincident continuum decay 18

1.3 Present Study 21

2 The Experiment **27**

2.1 Overview 28

2.2 Proton Beam 29

2.3 Scattering Chamber 34

2.4 Targets 36

2.5 Detector Telescopes 37

2.6 Electronics 43

  2.6.1 Earthing and power 43

  2.6.2 Preamplifiers 43

  2.6.3 Linear signals 44

  2.6.4 Current integrator 46

2.6.5 Pulsers 47
2.6.6 Timing signals 47
2.6.7 Event trigger 51
2.6.8 Computer busy 52
2.6.9 Pattern register 53
2.6.10 Scalers 54
2.6.11 Computer interface 55
2.7 Data Handling 56
2.7.1 Hardware configuration 56
2.7.2 Software 58
2.8 Experimental Procedure 65
2.8.1 Coincidence experiment 65
2.8.2 Singles experiments 72

3 Data Analysis **75**
3.1 Overview 76
3.2 Replay 77
3.2.1 Data recovery 77
3.2.2 Software 78
3.3 Particle Identification 80
3.4 Energy Calibrations 82
3.4.1 Si detectors 82
3.4.2 NaI(Tl) detectors 84
3.5 Energy Spectra 91
3.6 Coincidence Time Distributions 94
3.7 Pattern Register 97
3.8 Event Tape Sorting 97
3.8.1 Coincidence experiment 97
3.8.2 Singles experiments 98

3.9 Corrections 99

3.9.1 NaI(Tl) crystal reactions 99

3.9.2 Electronic dead time 101

3.9.3 Computer dead time 102

3.9.4 Target thickness 102

3.10 Error Analysis 103

3.10.1 Statistical errors 103

3.10.2 Systematic errors 104

3.11 Experimental Cross Sections 106

3.11.1 Inclusive ^{12}C(p,p′) cross sections 106

3.11.2 ^{12}C(p,2p) knockout cross sections 107

3.11.3 Continuum cross sections 109

3.12 DWIA Calculations 112

3.13 Continuum Decay Model Calculations 116

4 Results and Discussion **121**

4.1 Overview 122

4.2 Inclusive ^{12}C(p,p′) Cross Sections 122

4.3 ^{12}C(p,2p) Discrete-State Knockout 126

4.4 Continuum Decay 136

5 Summary and Conclusion **179**

A Cross Section Tables **187**

References **211**

List of Figures

1.1 Schematic representation of the reaction mechanism 19

2.1 Layout of the NAC cyclotron facility. 30
2.2 Telescope assemblies 38
2.3 Detector and target geometry 41
2.4 Linear electronics for Telescopes 1 and 2. 45
2.5 Simplified timing electronics for Telescopes 1 and 2. 49
2.6 Block diagram of data acquisition system 57
2.7 Simplified flow diagram of the event analysis program. . . . 64

3.1 Sample particle identification histograms 81
3.2 1 mm Si detector calibration 83
3.3 30 μm Si detector calibration 85
3.4 NaI(Tl) detector calibration 89
3.5 120 MeV experiment NaI(Tl) detector calibration 90
3.6 Summed reaction product energy versus E_1 92
3.7 Proton energy spectrum 93
3.8 Sample coincidence time distributions. 95
3.9 Gated coincidence proton energy distributions 110
3.10 100 MeV projection gate on (-20°,20°) data 111

4.1 Differential $^{12}C(p,p')$ cross sections at 90 MeV 124

4.2 Differential ^{12}C(p,p′) cross sections at 120 MeV 125
4.3 ^{12}C(p,2p) knockout cross sections (i) 127
4.4 ^{12}C(p,2p) knockout cross sections (ii) 128
4.5 ^{12}C(p,2p) knockout cross sections (iii) 129
4.6 ^{12}C(p,2p) knockout cross sections (iv) 134
4.7 Continuum decay cross sections for E_1=100 MeV compared with inelastic (p,p′) measurements at 90 MeV 138
4.8 Continuum decay cross sections for E_1=70 and 130 MeV compared with (p,p′) measurements at 120 and 62 MeV . . 139
4.9 In-plane ^{12}C(p,2p) DWIA cross sections for 70 MeV protons observed at the primary angle 142
4.10 In-plane ^{12}C(p,pn) DWIA cross sections for 70 MeV protons observed at the primary angle 143
4.11 In-plane ^{12}C(p,2p) DWIA cross sections for 100 MeV protons observed at the primary angle 144
4.12 In-plane ^{12}C(p,pn) DWIA cross sections for 100 MeV protons observed at the primary angle 145
4.13 In-plane ^{12}C(p,2p) DWIA cross sections for 130 MeV protons observed at the primary angle 146
4.14 In-plane ^{12}C(p,pn) DWIA cross sections for 130 MeV protons observed at the primary angle 147
4.15 Continuum decay cross sections for E_1=100 MeV compared with in-plane FEP continuum decay model calculations . . 152
4.16 Continuum decay cross sections for E_1=70 and 130 MeV compared with in-plane FEP continuum decay model calculations 153
4.17 Continuum decay cross sections for E_1=100 MeV compared with in-plane IEP continuum decay model calculations . . . 154

4.18 Continuum decay cross sections for E_1=70 and 130 MeV compared with in-plane IEP continuum decay model calculations 155
4.19 In- and out-of-plane (p,2p) DWIA cross sections for 70 MeV protons observed at $\theta_1 = -20°$ 158
4.20 In- and out-of-plane (p,2p) DWIA cross sections for 70 MeV protons observed at $\theta_1 = -45°$ 159
4.21 In- and out-of-plane (p,pn) DWIA cross sections for 70 MeV protons observed at $\theta_1 = -20°$ 160
4.22 In- and out-of-plane (p,pn) DWIA cross sections for 70 MeV protons observed at $\theta_1 = -45°$ 161
4.23 In- and out-of-plane (p,2p) DWIA cross sections for 100 MeV protons observed at $\theta_1 = -20°$ 162
4.24 In- and out-of-plane (p,2p) DWIA cross sections for 100 MeV protons observed at $\theta_1 = -45°$ 163
4.25 In- and out-of-plane (p,pn) DWIA cross sections for 100 MeV protons observed at $\theta_1 = -20°$ 164
4.26 In- and out-of-plane (p,pn) DWIA cross sections for 100 MeV protons observed at $\theta_1 = -45°$ 165
4.27 In- and out-of-plane (p,2p) DWIA cross sections for 130 MeV protons observed at $\theta_1 = -20°$ 166
4.28 In- and out-of-plane (p,2p) DWIA cross sections for 130 MeV protons observed at $\theta_1 = -45°$ 167
4.29 In- and out-of-plane (p,pn) DWIA cross sections for 130 MeV protons observed at $\theta_1 = -20°$ 168
4.30 In- and out-of-plane (p,pn) DWIA cross sections for 130 MeV protons observed at $\theta_1 = -45°$ 169

4.31 Continuum decay cross sections for E_1=100 MeV compared with in- and out-of-plane FEP continuum decay model calculations 171
4.32 Continuum decay cross sections for E_1=70 and 130 MeV compared with in- and out-of-plane FEP continuum decay model calculations 172
4.33 Continuum decay cross sections for E_1=100 MeV compared with in- and out-of-plane IEP continuum decay model calculations 173
4.34 Continuum decay cross sections for E_1=70 and 130 MeV compared with in-and out-of-plane IEP continuum decay model calculations 174

List of Tables

2.1 Detector and target geometry parameters 42
2.2 Pattern register input definitions 53
2.3 Scaler input definitions 54

3.1 Si detector energy calibration parameters 86
3.2 Energy-dependent optical parameters 113
3.3 Average energy optical parameters 114

4.1 ^{12}C(p,p′) normalization factors 140
4.2 Average intranuclear "beam" direction, θ_2'' 148
4.3 Continuum decay spectroscopic factors 175

A.1 Continuum cross sections at E_1=70±5 MeV, θ_1=-20° 188
A.2 Continuum cross sections at E_1=70±5 MeV, θ_1=-20° 189
A.3 Continuum cross sections at E_1=70±5 MeV, θ_1=-20° 190
A.4 Continuum cross sections at E_1=70±5 MeV, θ_1=-20° 191
A.5 Continuum cross sections at E_1=70±5 MeV, θ_1=-45° 192
A.6 Continuum cross sections at E_1=70±5 MeV, θ_1=-45° 193
A.7 Continuum cross sections at E_1=100±5 MeV, θ_1=-20° . . . 194
A.8 Continuum cross sections at E_1=100±5 MeV, θ_1=-20° . . . 195
A.9 Continuum cross sections at E_1=100±5 MeV, θ_1=-20° . . . 196
A.10 Continuum cross sections at E_1=100±5 MeV, θ_1=-20° . . . 197

A.11 Continuum cross sections at E_1=100±5 MeV, θ_1=-45° . . . 198
A.12 Continuum cross sections at E_1=100±5 MeV, θ_1=-45° . . . 199
A.13 Continuum cross sections at E_1=130±5 MeV, θ_1=-20° . . . 200
A.14 Continuum cross sections at E_1=130±5 MeV, θ_1=-20° . . . 201
A.15 Continuum cross sections at E_1=130±5 MeV, θ_1=-45° . . . 202
A.16 Knockout cross sections at θ_1=-20°,θ_2=20° 203
A.17 Knockout cross sections at θ_1=-20°,θ_2=45° 204
A.18 Knockout cross sections at θ_1=-20°,θ_2=70° 205
A.19 Knockout cross sections at θ_1=-20°,θ_2=95° 206
A.20 Knockout cross sections at θ_1=-20°,θ_2=120° and θ_1=-20°,θ_2=145° 207
A.21 Knockout cross sections at θ_1=-45°,θ_2=35° 208
A.22 Knockout cross sections at θ_1=-45°,θ_2=85° 209

Chapter 1

Introduction

1.1 Continuum States in Nuclei

The study of the excitation of nuclei into continuum states is now in its third decade of ongoing endeavour in the dual fields of experimental and theoretical nuclear physics. Both hadronic and non-hadronic probes have found their place in the search for a fuller understanding of the reaction mechanisms giving rise to the observed deexcitation of these states, a major component of which occurs through particle emission. The more recent availability of accelerated charged-particle beams of superior quality has enabled experiments to be performed with a much greater precision than was previously obtainable, and has resulted in continued interest in this challenging area.

1.1.1 Inclusive spectra

The energy spectra of charged particle reaction products, resulting from the interaction of incident protons in the energy range of many tens to many hundreds of MeV with targets covering the whole mass region of the periodic table, are characterized by a set of peaks at the higher energies due to elastic and inelastic scattering to discrete states of the target nucleus, while at the low energy end of each spectrum a somewhat broader peak occurs due to the emission of particles from a fully equilibrated nucleus — that is, the energy of the incident particle is dissipated amongst most of the nucleons, followed by statistical evaporation of particles from the excited nucleus. Between these two regions, the broad continuum or "pre-equilibrium" portion of the spectrum occurs, containing a significant fraction of the charged particle reaction strength.

In addition to the fundamental need to understand the reaction mechanisms which give rise to this region in the spectra, direct excitations with a high degree of collectivity, such as the Gamow-Teller states and the so-called "giant resonances" of various multipolarities, are superimposed on the continuum, and a knowledge of the exact shape of this continuum is required to reliably subtract its contribution from the total yield in the energy region of the state of interest.

Studies of the inelastic scattering of protons to the continuum have historically led the way in providing information which has formed the foundation of an understanding of the reaction mechanisms. The pioneering inclusive (p,p′) measurements of Roos and Wall [Roo65][Wal66] suggested that an initial quasifree nucleon-nucleon (N-N) interaction plays an important, if not dominant, role in the formation of the continuum yields. Using a proton beam of 160 MeV, they measured the outgoing proton spectra from 40 to 160 MeV between the angles of 10° to 80° for a range of target masses from ^{9}Be to ^{209}Bi. They found a broad peak in each of the spectra whose energy varied with the scattering angle (out to at least 60°) in a manner similar to that expected in the scattering of the proton from a free nucleon. The large width of the peak was attributed to the momentum of the initially-struck nucleon within the target nucleus. From the yield observed on the low energy side of the peak, Wall and Roos postulated that the effect of multiple scattering is small (or results in sufficent energy loss to place the outgoing proton below the approximately 40 MeV threshold of their detection system). The interpretation of the observations in terms of "quasifree" or "quasielastic" scattering evoked a great deal of further interest due to this analogy with free N-N scattering, as it offered the prospect of studying how the N-N interaction is modified in the nuclear medium.

Since this work, a considerable number of inclusive (p,p′) measurements, in the energy range from approximately 100 to 200 MeV, have been performed by many workers at different laboratories using a variety of techniques for measuring the proton spectra (for example, [Pee68] [Wu79] [Cow80a] [Che81] [Seg82] [Mac84] [Lis84] [Seg85] [För88]). There have been discrepencies in the published data, particularly with regard to the appearance of the broad peak in the spectra ascribed to quasifree N-N scattering, and this has led to debate on the relative importance of an initial quasifree N-N interaction in the production of the observed continuum yields. A consensus seems to have emerged in recent years that, in this energy range, there is strong evidence for such a peak in the forward-angle data (up to approximately 30°), and that the magnitude of this peak exhibits both an incident energy and a target mass dependence.

At energies much below 100 MeV the effects of Pauli blocking and the relatively long de Broglie wave length of the incident proton inhibit its interaction with single nucleons in the target nucleus. As the energy of the incident proton is increased these effects become less important, while simultaneously the N-N cross sections are decreasing, with the result that the mean free path of the nucleon in the nuclear medium increases. If the mean free path is considerably less than the nuclear radius, multiple scattering of the nucleon within the nucleus should tend to wash out any quasifree N-N peak in the observed spectra. This argument is supported by the forward angle observations at increasing incident proton energies up to 200 MeV (cited above), and at still higher energies (for example, [Wac72] at 450 MeV, and [Chr80] and [Tan81] at 800 MeV). As the energy of the incident proton is increased, the broad peaked structure in the continuum, exhibiting a kinematic shift which tracks single-step quasifree N-N scattering, becomes more prominent.

N-N elastic cross sections may be parametrized in the simple form [Boa85]

$$\frac{d\sigma}{dt} = Ae^{bt}$$

where t is related to the centre-of-mass momentum, p_{cm}, in the N-N interaction by

$$t = -2p_{cm}^2(1 - cos\theta)$$

where θ is the scattering angle. For scattering angles close to zero, t becomes small, while at large angles t takes on large negative values. Boal plots the parameter b as a function of energy, and shows that in this simplified view, the quasielastic peak should decrease rapidly at larger angles and lower energies.

A dependence on target mass is also expected, since the probability of the initially-scattered proton undergoing further interactions should increase as the number of nucleons in the target increases, thus contributing to the washing out of the quasifree peak. Such a dependence is supported by the more recent observations.

Despite the many experiments that have been performed to measure inclusive proton spectra in the energy range of 100 to 200 MeV, there is still some dispute as to the dominance of the quasifree reaction mechanism in the production of these yields, and the Research Group at the National Accelerator Centre has an active experimental programme in this area. Initial indications from this work suggest that, for some targets, the peak attributed to quasifree scattering, which is seen close to 100 MeV, becomes less prominent near 150 MeV, and once again increases in magnitude relative to the broad uniform continuum at energies close to 200 MeV.

A number of different routes have been taken in gaining a theoretical understanding of the mechanisms giving rise to the formation of continuum yields in inclusive (p,p′) reactions. These models may be divided into two main groups. Firstly, those that view the process as an intranuclear cascade consisting of a series of two-body particle-hole excitations which develops with a certain statistical probability for particle emission from the excited configuration at each step in the series. Prominent among this group are the "exciton" model proposed by Griffin [Gri66], the "hybrid" model of Blann [Bla71], and the multistep direct theory of Feshbach *et al.* [Fes80]. These models have been extended and applied with a good deal of success (for example, [Aga75] [Tam77] [Ern87]) in predicting both the angular and energy dependence of the (p,p′) experimental data, including the dominance of the first step in the reaction leading to the observed peak at forward angles. However, the calculations based on many of these models become extremely complicated as they are extended to include larger and larger numbers of multistep possibilities. The resulting simplifying assumptions, made to enable less arduous computation, contribute to the considerable differences in the predictions obtained from different versions of the same basic model [Mac87].

The quasifree model [Wol52] forms the basis of the second class of theoretical descriptions of the processes giving rise to the observed (p,p′) continuum yields. This views the scattering of the incident particle from a single nucleon, bound in the target with some form of momentum distribution, in a manner in which the remaining nuclear constituents simply act as spectators to the interaction. Despite their conceptual simplicity, these models have had some success in fitting the observed continuum yields. The impulse approximation was introduced by Chew [Che50] to describe the scattering of an energetic particle by a complex nucleus. Both plane-wave (PWIA) and distorted wave (DWIA) calculations have been performed in subsequent refinements of these models in a bid to accommodate a more quantitative description of other processes, such as multiple scattering, which can contribute significantly to the continuum yield (for example, [Wal66] [Kro70] [Jac71] [Cow80a]).

Two final points should be made concerning inclusive spectra. The first is that, if an initial quasifree N-N interaction plays a dominant role in the production of the continuum yield, then the spectra of neutrons from the (p,n) reaction should be directly related to the inclusive (p,p′) spectra, and the ratio of these two yields should take the approximate form

$$\frac{Y(p,p')}{Y(p,n)} = \frac{Z\sigma_{pp} + N\sigma_{pn}}{N\sigma_{pn}}$$

where Z and N are the numbers of target protons and neutrons, and σ_{pp} and σ_{pn} are the p-p and p-n scattering cross sections averaged over the energy and angular region determined by the initial N-N interaction. Measurements (for example, [Wac72] [Bon78] [And81] [Kal83]) show reasonable agreement with this rough approximation, giving a value close to 2, while a value much closer to 1 is expected from a model in which a large number of multiple scattering interactions occur before the observed particles emerge [Boa85]. In addition, calculations based on an exciton model in which the characteristics of the first step in the cascade are preserved [Mac79] and an impulse approximation model [Wu80] both predict the observed relative (p,p′) and (p,n) yields and give reasonable angular and energy dependent fits to the forward angle data.

The second point which should be mentioned is the results from analysing power measurements with polarized protons. Once again, if the initial N-N interaction plays the major role, the analysing power measured in ($\vec{p}$,p′) reactions should be related to the polarization measured in free p-p and p-n scattering. Some experimental evidence [Hol82] indicates that the analysing powers at the higher energies of the observed protons tracks free N-N polarization, while at lower energies, as expected from multiple scattering considerations, the analyzing powers are washed out. However, because of the inherent difficulties presented in calculating these analysing powers [Boa85], much uncertainty exists in attempting to extract reliable information on the reaction mechanisms from such measurements.

1.1.2 Coincidence spectra

Although studies of inclusive (p,p′) spectra have provided invaluable information on the dominant reaction mechanisms leading to the observed continuum proton yields, further important insights into these mechanisms are provided by the experimentally far more difficult (p,2p) coincidence measurements. In these experiments a larger region of phase space is sampled than that usually of interest in (p,2p) knockout studies (for example, [Jam69] [Hou71] [Bho76] [Dev79] [Fra81] [Gre83]). At intermediate energies these latter studies typically select specific detector geometries to probe a restricted region of the momentum distribution of the knocked out proton so that conditions are similar to that for free N-N scattering. These lend support to the validity of the distorted wave impulse approximation description in predicting a quasifree scattering mechanism for the knockout process. This field has been recently reviewed by Kitching *et al.* [Kit85].

Very few detailed experimental studies of the coincident proton decay of the continuum in the energy region of interest between 100 and 200 MeV have been performed up to the present time [Cow80b] [Cia83] [Cia84a].

In the first of these experiments [Cow80b], in which 100 MeV protons were incident on a ^{58}Ni target, a detector at a small forward angle (-15°) measured protons in coincidence with protons observed in a second detector placed at various angles ranging from 18° to 145° with respect to the incident beam direction. The resultant two-dimensional energy spectra showed distinct regions due to quasifree proton knockout and evaporation of low energy protons from an equilibrated system, and an area bounded by these regions due to "preequilibrium" proton emission from the continuum.

In order to gain some insight into the mechanism giving rise to this continuum, rectangular cuts were made in the two-dimensional energy spectra for each coincident angle pair, corresponding to the observation of a proton with an energy between 30 and 50 MeV in the -15° detector. The data falling within each of these cuts were projected onto the energy axis of the proton observed in the second detector. The resulting coincident proton energy spectra were interpreted in terms of an inelastic scattering in which the 100 MeV incident proton transfers on average 60 MeV to a nucleon in the target nucleus before being emitted at an angle of -15° relative to the incident beam direction. The struck nucleon then interacts with the remainder of the nucleus in a manner similar to an incident 60 MeV proton. These spectra were compared with arbitrarily normalized (p,p′) data for 62 MeV protons incident on ^{54}Fe, and a remarkable similarity in the shape of the two sets of spectra was found, and led the authors to conclude that this strongly suggested the dominance of an initial N-N interaction giving rise to the observed coincident continuum decay yields.

In a similar experiment at an incident proton energy of 200 MeV on a ^{58}Ni target, Ciangaru *et al.* [Cia83] [Cia84a] measured two sets of coincident proton energy spectra at forward angles of -12° and -30° relative to the incident proton beam. The coincident protons were measured at six secondary angles ranging from 20° to 155°. In the analysis two 40 MeV wide rectangular cuts were made in the coincident energy data centered at 100 and 130 MeV along the primary (forward angle) energy axis. As in the previous study described above, the data falling in these cuts were projected onto the secondary proton energy axis. The resulting spectra were compared with experimental inelastic cross section data for protons of 62 MeV incident on ^{54}Fe and protons of 90 MeV incident on ^{58}Ni respectively. As before, remarkable agreement in the shape of the different data sets was obtained, adding further support to the importance of an initial quasifree (p,2p) interaction between the incident proton and a valence nucleon as a doorway to more complicated processes leading to the observed continuum yield.

Ciangaru *et al.* took the analysis of their data a step further by developing a theoretical model [Cia84a] [Cia84b] in which the coincidence continuum cross section is expressed as the convolution of the initial quasifree doorway step with the experimental inelastic scattering cross sections of the quasifree particles scattered off the residual nucleus. This formalism is described in more detail in the following section. Calculations based on this model were performed and compared with the ^{58}Ni(p,2p) continuum data taken at 200 MeV incident proton energy. The results showed good agreement with the data, with renormalization factors for the calculated cross sections close to unity, giving further encouragement to this interpretation of the basic physics involved.

1.2 Theoretical Background

1.2.1 Impulse approximation

When an incident high energy (>100 MeV) proton knocks a nucleon (or cluster of nucleons) out of a target nucleus with a sufficiently large transfer of the momentum to the knocked out particle, the impulse approximation assumes that the interaction occurs solely between the incoming and knocked out particles, while the remaining nucleons in the nucleus act merely as spectators to the interaction, and their influence on the knockout process can be neglected. In this approximation, therefore, the residual "spectator" nucleus recoils with the same momentum that it had before the interaction. The major difference between such a quasifree (or quasielastic) process and free scattering is that the knocked out particle itself is not at rest in the nucleus, but has some momentum distribution and separation energy.

The plane wave impulse approximation (PWIA) was introduced by Chew [Che50], and further generalized by Chew and co-workers [Che52a] [Che52b]. This approximation does not take the interaction of the incoming and outgoing particles with the residual nucleus into account, and, in the case of (p,2p) knockout,

$$\frac{d^3\sigma}{d\Omega_1 d\Omega_2 dE_1} \propto \frac{d\sigma}{d\Omega_{pp}} \times |\phi(\vec{q})|^2$$

where $\frac{d^3\sigma}{d\Omega_1 d\Omega_2 dE_1}$ is the three-body breakup cross section, $\frac{d\sigma}{d\Omega_{pp}}$ is the half off-shell p-p scattering cross section, and $\phi(\vec{q})$ is the distribution of the momentum $\vec{q}$ of the struck proton in the target nucleus. Although applied with success over the years, the PWIA suffers from its failure to take into account the interaction of the incident and emitted particles with the residual nucleus. This has led to the introduction of drastic and often arbitrary procedures to simulate such interactions, which places some doubt on the resulting nuclear structure information obtained from the calculations based on such models.

In an attempt to account for some of these problems, a distorted wave impulse approximation (DWIA) was first proposed by Maris *et al.* [Mar58] [Mar59], and subsequently refined by numerous other workers (for example, [Ber62] [Lim64] [Lim66] [Jac65] [Jai67] [Jai70] [Jai73] [Cha77] [Cha82]). In this approximation the effects of multiple scattering on the incoming and outgoing particles are included by considering the corresponding plane waves describing these particles to be distorted by complex optical potentials.

Despite the fact that this is a rather extreme simplification to simulate the multiple scattering process, the DWIA has been very effective in the quantitative description of cross sections in a wide range of knockout studies, particularly where the experimental conditions have been chosen so as to minimize the errors introduced by these rather crude assumptions [Kit85]. It has had a great deal of success in reducing the knockout cross sections, predicted by PWIA models, to more realistic values [Kro70]. The theory does not, however, have anything to say about where in the continuum region of the energy spectra, the particles removed from the quasifree knockout locus end up.

The DWIA treatment of Chant and Roos [Cha77] is used in the present study for determining the cross sections for the initial quasifree interaction which, it is proposed, gives rise to the observed continuum yields, and is summarized below.

This treatment considers the knockout reaction $A(a,a'b)B$ where $A = B + b$, b is the emitted nucleon or cluster, and the $'$ indicates the particle a in the exit channel. The differential cross section for this reaction is written

$$\sigma_{BA} = \frac{2\pi}{\hbar v}|T_{BA}|^2\omega_B \tag{1.1}$$

where v is the relative velocity of a and A in the entrance channel, T_{BA} is the "reduced transition amplitude", and ω_B is the energy density of final states. A t operator is defined by the relation

$$T_{BA} = \langle\Phi^{(-)}(\widetilde{B,a'},b)|t_{BA}|\Phi^{(+)}(\widetilde{A,a})\rangle \tag{1.2}$$

where $\Phi^{(-)}(\widetilde{B,a'},b)$ is the eigenfunction of the total Hamiltonian when the interaction between particles a' and b in the exit channel is neglected, and $\Phi^{(+)}(\widetilde{A,a})$ is the similar function in the entrance channel. The $\tilde{}$ indicates that both wave functions are antisymmetric with respect to the interchange of any two nucleons.

The wave functions in equation 1.2 are then expressed in terms of separately antisymmetrized wave functions, and a simplification is made by neglecting exchange effects between the projectile a and the residual nucleus B. The impulse approximation is applied by replacing t_{BA} with the two-body operator, $t_f^{\dagger}$, for the $a+b$ scattering process. A factorized form for T_{BA} is obtained by making the additional assumption that the resultant two-body t matrix varies sufficiently slowly with momenta that its arguments may be replaced by their asymptotic values, giving

$$\begin{aligned} T_{BA} &= C \sum_{\alpha L J \sigma_b \Lambda M} {S_{\alpha LJ}}^{1/2} (J M J_B M_B | J_A M_A)(L \Lambda s_b \sigma_b | J M)(2L+1)^{1/2} \times \\ & \qquad T_{BA}^{\alpha L \Lambda} \langle \vec{k}_f, \sigma'_a, \sigma'_b | t_f^{(+)} | \vec{k}_i, \sigma_a, \sigma_b \rangle \end{aligned} \tag{1.3}$$

where the angular momentum quantum numbers for the target nucleus ($i = A$) and residual nucleus ($i = B$) are J_i (projection M_i), the corresponding quantities for the incident and emitted particles are s_i (projection σ_i), the relative angular momentum of b and B is L (projection Λ), and any other quantum numbers needed to specify the motion are in α; $\vec{k}_i$ and $\vec{k}_f$ are the initial and final relative momenta of particles a and b, and C is the isospin coupling (Clebsch-Gordan) coefficient. Substituting equation 1.3 into equation 1.1, averaging over initial spin projections and summing over final spin projections, and making the further assumption that the two-body t matrix is independent of σ_b, gives

$$\sigma_{BA} = \frac{2\pi}{\hbar v} \omega_B C^2 |\overline{\langle t \rangle}|^2 S_{LJ} \sum_{\Lambda} |T_{BA}^{\alpha L \Lambda}|^2 \tag{1.4}$$

where

$$|\overline{\langle t \rangle}|^2 = \frac{1}{(2s_a+1)(2s_b+1)} \sum_{\sigma_a \sigma_b \sigma'_a \sigma'_b} |\langle \vec{k}_f, \sigma'_a, \sigma'_b | t_f^{(+)} | \vec{k}_i, \sigma_a, \sigma_b \rangle|^2 \tag{1.5}$$

is the square of the two-body matrix averaged over initial, and summed over final, spin projections. Also, assumimg $T_{BA}^{\alpha L \Lambda}$ is independent of α, the spectroscopic factor S_{LJ} is defined as

$$S_{LJ} = \left| \sum_{\alpha} {S_{\alpha LJ}}^{1/2} \right|^2 . \tag{1.6}$$

$T_{BA}^{\alpha L\Lambda}$ needs to be evaluated, and this amplitude may be written

$$T_{BA}^{\alpha L\Lambda} = (2L+1)^{-1/2}\langle\eta_{Bab}^{(-)}|\delta(\vec{r}_a - \vec{r}_b)|\eta_{Aa}^{(+)}\phi_{L\Lambda}^{\alpha}(\vec{r}_{bB})\rangle \tag{1.7}$$

where $\phi_{L\Lambda}^{\alpha}(\vec{r}_{bB})$ describes the motion of the centre of mass of b with respect to the centre of mass of B and is normalized to unity, and $\eta_{Aa}^{(+)}$ and $\eta_{Bab}^{(-)}$ are the wave functions describing the relative motion of the mass centres of the particles in the entrance and exit channel respectively. It is assumed that $V_{aA} - V_{ab} = V_{aB}$ where V_{aB} is the optical potential for $a + B$ scattering averaged over the target nucleus A, and the potential is expected to differ little from the optical potential for $a + A$ scattering. $\eta_{Aa}^{(+)}$ satisfies the wave equation

$$(T_{aA} + V_{aB} - \epsilon_{aA})\eta_{Aa}^{(+)} = 0 \tag{1.8}$$

where

$$T_{aA} = \frac{-\hbar^2 \nabla_{aA}{}^2}{2\mu_{aA}} .$$

μ_{aA} is the reduced mass of a and A, and ϵ_{aA} is the relative kinetic energy defined by

$$\epsilon_{aA} = \frac{P_{aA}{}^2}{2\mu_{aA}}$$

where

$$\vec{P}_{aA} = \frac{A}{A+a}\vec{P}_a$$

and $\vec{P}_a$ is the laboratory momentum of the incident particle.

In the exit channel scattering solution, the Hamiltonian, expressed in terms of the momentum operators conjugate to $\vec{r}_{aB}$ and $\vec{r}_{bB}$, contains a kinetic energy coupling term. Provided $m_B \ll \mu_{aB}$ and/or $m_B \ll \mu_{bB}$, this term should have little effect and is neglected — the so-called "kinetic energy approximation" [Jac65] — and the exit channel wave function factorizes

$$\eta_{Bab}^{(-)} = \chi_{aB}^{(-)}(\vec{k}_{aB}, \vec{r}_{aB})\chi_{bB}^{(-)}(\vec{k}_{bB}, \vec{r}_{bB}) \tag{1.9}$$

where the χs are solutions of the wave equations

$$(T_{aB} + V_{aB} - \epsilon_{aB})\chi^{(-)}_{aB}(\vec{k}_{aB}, \vec{r}_{aB}) = 0 \tag{1.10}$$

and

$$(T_{bB} + V_{bB} - \epsilon_{bB})\chi^{(-)}_{bB}(\vec{k}_{bB}, \vec{r}_{bB}) = 0 \ . \tag{1.11}$$

The bound state wave function $\phi^{\alpha}_{L\Lambda}(\vec{r}_{bB})$ is the projection of the many-body wave function of the target nucleus A on to the residual nucleus B and the emitted particle b. To generate this function, Chant and Roos introduce a phenomenological Woods-Saxon potential V_{WS} which is adjusted to reproduce the empirical $A \rightarrow B + b$ separation energy S_{Bb}

$$(T_{bB} + V_{WS} - S_{Bb})\phi^{\alpha}_{L\Lambda}(\vec{r}_{bB}) = 0 \ . \tag{1.12}$$

Substituting for $\eta^{(+)}_{Aa}$ and $\eta^{(-)}_{Bab}$ in equation 1.7, and integrating over $\vec{r}_{ab}$ gives

$$T^{\alpha L\Lambda}_{BA} = \frac{1}{(2L+1)^{1/2}} \int \chi^{(-)*}_{aB}(\vec{k}_{aB}, \vec{r})\chi^{(-)*}_{bB}(\vec{k}_{bB}, \vec{r})\chi^{(+)}_{aA}(\vec{k}_{aA}, \gamma\vec{r})\phi^{\alpha}_{L\Lambda}(\vec{r})d\vec{r} \tag{1.13}$$

where $\vec{r}_{aB} = \vec{r}_{ab} + \vec{r}_{bB}$, $\vec{r}_{aA} = \vec{r}_{ab} + \gamma\vec{r}_{bB}$ and $\gamma = \frac{B}{(B+b)}$.

The χs are expressed as partial wave expansions. For $\chi^{(+)}_{aA}$ this expansion takes the form

$$\chi^{(+)}_{aA}(\vec{k}_{aA}, \gamma\vec{r}) = \frac{4\pi}{\gamma k_{aA} r} \sum_{l_a\lambda_a} u_{l_a}(k_{aA}, \gamma r) i^{l_a} Y_{l_a\lambda_a}(\hat{r}) Y^{*}_{l_a\lambda_a}(\hat{k}_{aA}) \ . \tag{1.14}$$

The "bound state" cluster wave function is written

$$\phi^{\alpha}_{L\Lambda}(\vec{r}) = R_{\alpha L}(r) i^{L} Y_{L\Lambda}(\vec{r}) \ . \tag{1.15}$$

Choosing the $\vec{z}$ axis along $\vec{k}_{aA}$ and the $\vec{y}$ axis along $\vec{k}_{aA} \times \vec{k}_{aB}$, and defining the centre of mass angles at which the emitted particles are detected to be

$(\theta_a, 0)$ and (θ_b, ϕ_b), a final expression for $T_{BA}^{\alpha L\Lambda}$ is obtained

$$\begin{aligned} T_{BA}^{\alpha L\Lambda} &= \frac{\sqrt{4\pi}}{\gamma k_{aA} k_{aB} k_{bB}} \sum_{l_a l_{a'} l_b \lambda_b k q} i^{l_a + L - l_{a'} - l_b} \frac{(2l_a+1)(2l_{a'}+1)(2l_b+1)}{(2k+1)} \times \\ & \qquad (l_b \lambda_b L \Lambda | kq)(l_b 0 L 0 | k0)(l_a 0 l_{a'} q | kq)(l_a 0 l_{a'} | k0) \times \\ & \qquad I^L_{l_a l_{a'} l_b} d^{l_{a'}}_{q0}(\theta_a) d^{l_b}_{\lambda_b 0}(\theta_b) e^{-i\lambda_b \phi_b} \qquad (1.16) \end{aligned}$$

where $d^l_{mn}(\theta)$ is a reduced rotation matrix, and the radial integral

$$I^L_{l_a l_{a'} l_b} = \int_0^\infty u_{l_a}(k_{aA}, \gamma_r) u_{l_{a'}}(k_{aB}, r) u_{l_b}(k_{bB}, r) R_{\alpha L}(r) dr/r \ .$$

The energy density of final states in the laboratory system may be written

$$w_B = \frac{d^3 P_{a'}}{(2\pi\hbar)^3} \frac{d^3 P_b}{(2\pi\hbar)^3} \frac{1}{dE} \ . \qquad (1.17)$$

Substituting $E_{a'} dE_{a'} = c^2 P_{a'} dP_{a'}$ and $d^3 P_i = P_i^2 dP_i d\Omega_i$

$$w_B = \frac{P_{a'} E_{a'} dE_{a'} d\Omega_{a'} P_b^2 dP_b d\Omega_b}{(2\pi\hbar)^6 c^2 dE} \ . \qquad (1.18)$$

Writing the total energy as

$$E = \sqrt{p_{a'}{}^2 c^2 + m_{a'}{}^2 c^4} + \sqrt{p_b{}^2 c^2 + m_b{}^2 c^4} + \sqrt{(\vec{p}_a - \vec{p}_{a'} - \vec{p}_b)^2 c^2 + m_B{}^2 c^4},$$

fixing $E_{a'}$, and taking the differential of E,

$$dE = \frac{c^2 P_b dP_b}{E_b} + \frac{c^2 (P_b - P_a \cos\theta_{ab} + P_{a'} \cos\theta_{a'b}) dP_b}{E_b} . \qquad (1.19)$$

Substituting into equation 1.1, the final expression for the differential cross section for specific values of L and J becomes

$$\begin{aligned} \frac{d^3 \sigma^{LJ}}{d\Omega_{a'} d\Omega_b dE_{a'}} &= C^2 |\overline{\langle t \rangle}|^2 S_{LJ} \left\{ \frac{E_a E_{a'} E_b}{(2\pi)^5 (\hbar c)^7} \frac{P_{a'} P_b c}{P_a} \times \right. \\ & \qquad \left. \frac{1}{1 + (E_b/E_B)[1 - (P_a/P_b)\cos\theta_{ab} + (P_{a'}/P_b)\cos\theta_{a'b}]} \right\} \times \\ & \qquad \sum_\Lambda |T_{BA}^{\alpha L\Lambda}|^2 \ . \qquad (1.20) \end{aligned}$$

The two-body t matrix can be shown to be

$$|\overline{\langle t \rangle}|^2 = (2\pi\hbar^2c^2)^2 \frac{P_i^{cm}}{P_f^{cm}} \frac{{E_{cm}}^2}{E_a E_{b'} E_{a'} E_b} \frac{d\sigma(E_{cm}, \theta_{cm})}{d\Omega} \tag{1.21}$$

where P_i^{cm}, P_f^{cm}, E_{cm} and θ_{cm} are the initial momentum, final momentum, total energy and scattering angle in the $a' + b$ centre of mass system. E_k is the laboratory energy of particle k, while $E_{b'}$ is the laboratory energy for the virtual particle b' where

$$E_{b'} = m_A c^2 - E_B .$$

Finally, to evaluate the "half off the mass shell" two-body cross section $\frac{d\sigma(E,\theta)}{d\Omega}$ Chant and Roos use an on-shell amplitude, interpolated from available differential cross sections for free $a + b$ scattering. This is determined using two different prescriptions for E. In the final energy prescription (FEP) approximation, E is taken to be the relative centre of mass energy of the emitted particles in the exit channel, while in the initial energy prescription approximation (IEP), E is the relative centre of mass energy of the incident and struck particles in the entrance channel. These two prescriptions represent the extreme cases, and a more correct half off-shell prescription should fall between these limits.

In this treatment spin-orbit effects were ignored by omitting the spin-orbit terms in the optical potentials used to generate the incident and emitted particle scattering wave functions. It has been suggested [Jac76] that such effects could, in principle, be profound. Chant and Roos have extended the above treatment [Cha83] by including such spin-orbit terms in the distorting potentials, and replacing the explicit calculation of angular momentum coupling coefficients by a numerical integration technique. Applying their results to (p,2p) reaction data close to 150 MeV, they found major differences for some polarization analysing powers involving a range of residual nucleus recoil momenta, but no major qualitative changes were found in the predicted differential cross sections compared with calculations in which the spin-orbit effects were neglected.

1.2.2 Coincident continuum decay

A model has been developed by Ciangaru [Cia84b] to account for the observed continuum spectra in (a,a′b) reactions, in which the particles emitted from an initial quasifree three-body knockout interaction undergo a series of subsequent collisions with the residual nucleus. These collisions degrade the energies of the particles which, by the time they are finally scattered into the exit channel, have been removed from the quasifree kinematic locus and appear in the the continuum region of the energy spectrum.

Ciangaru extended the statistical two-body theory of Feshbach *et al.* [Fes80] for the (a,b) inclusive reaction continuum to also describe the exclusive (a,a′b) continuum process. Assuming that, following the doorway quasifree interaction, the emitted particles do not interact simultaneously with the residual nucleus and do not interact with each other, a computable expression for the direct (a,a′b) continuum cross section was derived in terms of a convolution integral over a three-body quasifree knockout doorway cross section, and a rescattering chain describing the multiple scattering probabilities of the quasifree particles.

This model was applied [Cia84a] to the analysis of the ^{58}Ni(p,2p) continuum experiment data at an incident proton energy of 200 MeV, described in subsection 1.1.2. A number of simplifications were made to enable a straightforward computation of the continuum cross sections to be performed. Figure 1.1 shows schematically the mechanism proposed in this treatment for the formation of the continuum spectrum. The incident proton p_0 with energy E_0 undergoes an initial quasifree interaction with a

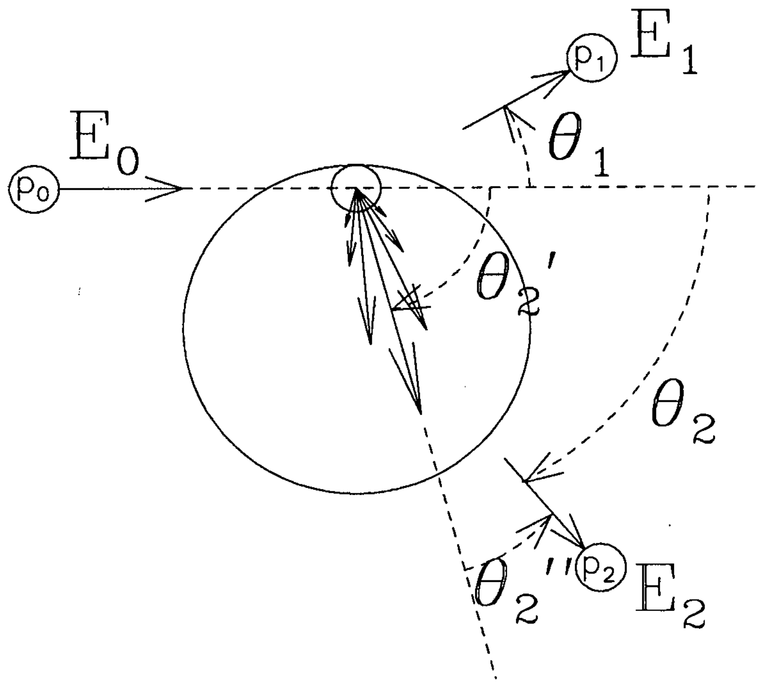

Figure 1.1: *Schematic representation of the steps in the proposed reaction mechanism leading to the formation of the observed continuum coincidence energy spectrum.*

nucleon in the target nucleus, and is observed (p_1) at an angle θ_1 with energy E_1. The struck nucleon, quasifree scattered at an angle θ_2', and with an energy E_2', interacts with the residual nucleus, and a resulting proton is emitted to be detected at an angle θ_2 and with energy E_2.

The first simplifying assumption made in the model is that the incident (p_0) proton undergoes an initial quasifree scattering and is emitted (p_1) without undergoing any further interactions. This is expected to be a reasonable approximation provided that the proton is detected at relatively small angles with respect to the incident beam direction, and that its energy after the initial quasifree interaction is sufficiently large, to make it unlikely that it would suffer further collisions before being emitted.

The second simplifying assumption is that the rescattering chain for the knocked out quasifree particle, with energy E_2' at angle θ_2', may be replaced with the probability for the inelastic scattering of this particle, through angle $\theta_2'' = \theta_2 - \theta_2'$, and the final detection of p_2 with energy E_2 at angle θ_2. It is assumed that this inelastic scattering probability is related to the cross section for inelastic scattering off the residual nucleus by the expression

$$\frac{d^2\sigma^{inel}(\theta_2'' E_2 E_2')}{d(\Omega_2 - \Omega_2')dE_2} \times \frac{1}{2\pi\sigma_{tot}^{inel}(E_2')}$$

where $\sigma_{tot}^{inel}(E_2')$ is the differential inelastic cross section integrated over the scattering angle θ_2''.

It should be noted that the Ciangaru treatment does not explicitly consider contributions to the continuum from events in which the initial quasifree interaction gives rise to a knocked out particle out of plane, with the subsequent rescattering resulting in the detection of an in-plane proton. In addition, Ciangaru *et al.* only included knockout protons in the analysis of the ^{58}Ni data. Other initial quasifree knockout processes may be expected to contribute to the yield of p_2 protons observed in the exit channel. In particular, the initial knockout of a neutron from the target nucleus followed by an (n,p) interaction of this neutron with the residual nucleus could lead to significant increase in the measured p_2 proton yield.

The cross section for the (a,a′b) continuum in the Ciangaru treatment is then written

$$\begin{aligned}\frac{d^4\sigma(\theta_1 E_1 \theta_2 E_2)}{d\Omega_1 dE_1 d\Omega_2 dE_2} &= \int d\theta_2' \sin\theta_2' \sum_{\lambda} \frac{d^3\sigma_{\lambda\alpha}^{QF}(\theta_1 E_1 \theta_2' E_2')}{d\Omega_1 dE_1 d\Omega_2'} \times \\ &\qquad \frac{1}{2\pi\sigma_{tot}^{inel}(E_2')} \frac{d^2\sigma^{inel}(\theta_2'' E_2 E_2')}{d(\Omega_2 - \Omega_2')dE_2} \qquad (1.22)\end{aligned}$$

where the cross section for the initial quasifree interaction, $\frac{d^3\sigma^{QF}_{\lambda\alpha}(\theta_1 E_1 \theta'_2 E'_2)}{d\Omega_1 dE_1 d\Omega'_2}$, assumes distorted waves for the p_0 and p_1 protons, and plane waves for the p_2 protons. Although the contribution to the continuum at positive detection angles of the p_1 protons initially scattered at negative angles, is neglected, the reduction in the total flux of these protons due to target absorption is taken into account by the distorted wave representation. Since the interaction of the p_2 proton with the residual nucleus is described by the inelastic scattering cross section, $\frac{d^2\sigma^{inel}(\theta''_2 E_2 E'_2)}{d(\Omega_2-\Omega'_2)dE_2}$, a plane wave representation for this particle is appropriate. The summation is over the orbits λ in the target nucleus from which the quasifree particles are knocked out, leaving the residual nucleus B in quantum state α. The energies E_1 and E'_2 are related through the conservation of energy equation, which determines the appropriate quasifree locus,

$$E_1 + E'_2 = E_0 + E_\lambda - \epsilon_\alpha - E_B$$

where E_λ is the binding energy of the particle knocked out of the target orbital λ, ϵ_α is the excitation energy of the residual nucleus in the quantum state α, and E_B is the recoil energy of the residual nucleus.

As described in subsection 1.1.2, this treatment yielded encouraging overall agreement, in both magnitude and shape, with the measured continuum cross sections in the single reaction studied, giving support to the basic physics underlying this description of the generation of coincidence continuum yields.

1.3 Present Study

The present study was undertaken to measure the coincident proton decay of the continuum induced by protons with an incident energy of 200 MeV on a ^{12}C target, and to determine whether the observed proton spectra may, following a procedure similar to that introduced by Ciangaru, be interpreted in terms of a relatively simple model in which an initial quasifree process is succeeded by the interaction of the knocked out particle with the residual nucleus.

As described in subsection 1.1.2, detailed experimental studies of the coincident proton decay of the continuum in the energy region between 100 MeV and 200 MeV have been limited to measurements using ^{58}Ni targets. Apart from the obvious requirement to determine whether the proposed reaction mechanism is capable of explaining the observed continuum energy spectra from targets spanning the mass range, the ^{12}C nucleus offers a number of advantages compared with the heavier ^{58}Ni.

An assumption used in the reaction model is that the incident proton is scattered in an initial quasifree interaction, and is emitted without undergoing any further interactions. It is assumed that this particle is observed in a detector placed at relatively small (20° and 45°) forward angles so that, at an incident energy of 200 MeV, the probability of it having undergone a further scattering is small. In addition, the validity of this assumption is expected to be enhanced for lighter mass (that is, fewer nucleon) targets, and this expectation is supported by inclusive measurements. For example, Machner *et al.* [Mac84] measured the inclusive proton spectra from ^{27}Al and ^{197}Au at an incident proton energy of 200 MeV, and found that the peak in the spectra attributed to quasifree scattering was prominent for the ^{27}Al target out to at least 30°, whereas for the ^{197}Au target the peak was discernable only at 14°. It was assumed that in the latter case the peak had been washed out at the larger angles by further interactions of the particles with the residual target nucleus. Strong evidence for the presence of such a quasifree peak in the inclusive proton energy spectra from ^{12}C targets has been found at incident proton energies of 150 MeV [Seg85] and 200 MeV [För88].

In the analysis of the ^{58}Ni data, contributions from the knockout of particles from the outermost ($f_{7/2}$ and $s_{1/2}$) orbitals were included in the calculations, while that from the $d_{3/2}$ shell was excluded due to uncertainties in its nucleon occupancy [Cia84a]. ^{12}C, on the other hand, is a nucleus which has been studied extensively, the properties of its simple shell structure ($p_{3/2}$ and $s_{1/2}$) are reasonably well understood, and shell model calculations (for example, [Coh65]) accurately predict its low-lying states. Furthermore, the knockout mechanism, which in the present study is assumed to play a major role in the formation of the continuum yield, has received a deal of attention (for example, [Bho76] [Dev79]).

In analysing the measured coincident continuum spectra, it was proposed to extend the model introduced by Ciangaru, which was described in the previous section, by including the contribution to the continuum yield of those particles which are scattered out of plane in the initial quasifree knockout process, and, after the subsequent interaction of the knocked out particle with the residual nucleus, a proton is observed in an in-plane detector.

In addition, it was proposed to include the contributions of both protons and neutrons which are knocked out in the initial quasifree process, and whose further interaction with the residual nucleus (namely, (p,p′) and (n,p) respectively), give rise to the observed continuum proton yield.

For comparison with the measured continuum cross sections, the procedure requires suitable inelastic scattering data to be convoluted with the quasifree cross sections (calculated in a DWIA treatment). As these inelastic (p,p′) scattering data describe the interaction of the knocked out particle with the residual nucleus, these data should strictly be for the ^{11}B nucleus.

However, it is expected that any slight differences in the inelastic data over the energy range of interest (that is, below the discrete states) between mass-11 and mass-12 systems are not significant. Inclusive ^{12}C(p,p$'$) data were therefore required at three energies (60 MeV, 90 MeV and 120 MeV) to enable the necessary calculations to be performed. Data at the first energy were already available [Ber73], while it was proposed to measure the inclusive cross sections at the other two energies.

Before convoluting the quasifree cross sections with the inelastic scattering data, it is necessary to determine whether the DWIA treatment, which is employed to calculate the yield of knocked out protons and neutrons in the initial quasifree interaction, is appropriate for the ^{12}C nucleus at an incident proton energy of 200 MeV. In order to test this, it was proposed to compare DWIA calculations with the measured (coincident) data for the "clean" quasifree knockout of protons from the outer ($p_{3/2}$) shell of ^{12}C (that is, the knockout protons that are emitted without undergoing further interactions before detection). Events due to the knockout of protons from the inner ($s_{1/2}$) shell are not clearly identifiable in the coincident energy spectra, and, in addition, these events are superimposed on the continuum resulting from the further interaction of some of the knocked out $p_{3/2}$ protons before emission.

The primary aim was to determine whether the proposed model represents a reasonable interpretation of the basic physics underlying the interactions giving rise to the observed continuum yield, namely, that the reaction mechanism may be viewed as an initial quasifree nucleon-nucleon interaction followed by the rescattering of the knocked out particles with the residual nucleus. To achieve this it was proposed to extract continuum decay cross sections from the measured coincident proton energy spectra at each angle pair by making rectangular cuts in these spectra centred at energies of 70 MeV, 100 MeV and 130 MeV for the proton observed in the "primary" forward angle detector, and to project the data in these cuts onto the axis corresponding to the energy of the proton detected in the "secondary" detector. The resulting continuum cross sections could then be compared directly with the calculations based on the model.

The following chapter describes the exclusive (coincident) ^{12}C(p,2p) and inclusive ^{12}C(p,p$'$) measurements which were performed to gather the required data for this study. This is succeeded by a chapter describing the procedures employed in the analysis of the measured data, and the calculations which were performed for comparison with the data, and a chapter presenting the results and their interpretation. Finally, the conclusions of the present study are summarized.

Chapter 2

The Experiment

2.1 Overview

The primary object of the experiment was to investigate the decay of the continuum induced by 200 MeV protons in the reaction ^{12}C(p,2p), and, in particular, to determine whether the continuum yield can be understood in terms of a reaction mechanism in which an initial quasifree nucleon-nucleon knockout process is followed by the interaction of the quasifree particles with the spectator part of the target nucleus. "Exclusive" (coincidence) proton measurements were performed, and two "inclusive" (singles) sets of measurements were performed to gather data required for interpretation of the coincident data in terms of the proposed reaction mechanism.

In the coincidence measurements both outgoing particles resulting from the initial proton-nucleon quasi-free scattering are subject to possible further interactions with the spectator part of the nucleus. To reduce the possibility of the scattered incident particle undergoing such further interactions, one of the detectors used to observe the outgoing particles was situated at relatively small angles with respect to the incident proton beam (namely, 20° and 45°). This we called the "primary" angle, and it was assumed that the incident particle was scattered into the detector positioned at this angle. The second, coincident, particle was observed in a detector at various angles (ranging from 20° to 135°) on the opposite side of the incident beam to the primary angle. This was called the "secondary" angle.

In the singles experiments, protons from the reaction ^{12}C(p,p′x), where x is a possible unobserved reaction product, were measured in two independent detectors at a series of angles ranging from 10° to 160° relative to the proton beam. The proton energies of the incoming beam for the two sets of measurements, required for the interpretation of the coincidence measurements at 200 MeV, were 90 and 120 MeV.

In the measurements, energy and angular resolutions were not of primary concern, energy resolutions of the order of 4% and relatively large detector solid angles of the order of 2 msr being quite acceptable. The contribution of "random coincidences" in the coincidence measurements had an important role in limiting the acceptable count rate and thus, the magnitude of the beam current on the target. These are described in detail in the following sections.

2.2 Proton Beam

The cyclotron facility of the National Accelerator Centre [Bot84] is a multidisciplinary institute providing particle beams for nuclear physics, isotope production and radiotherapeutic treatment of cancer patients. A layout of the facility is shown in Figure 2.1. A solid-pole light-ion injector cyclotron (SPC1) accelerates protons to a maximum energy of 8 MeV for injection into the first orbit of the separated-sector cyclotron (SSC) in which the protons are accelerated to a maximum energy of 200 MeV. The charged particles extracted from the SSC are transported via the optics of the high-energy beam lines (X, P and R) through two 90 degree bending magnets before being directed by a switching magnet into one of the lines which enter the three shielded experimental physics vaults. In the current measurements this was line A, on which the 1.5 m scattering chamber is mounted. Two quadrupole focussing and two steering magnets are situated between the switching magnet and the entrance to the scattering chamber. The charged particle beam is focussed onto the target situated at the centre of the chamber, then exits from the chamber and after travelling a further 3 metres down an evacuated beam pipe enters the 3 m beam dump, buried in an iron and concrete shield.

The beam is stopped in a block of aluminium which is divided into four

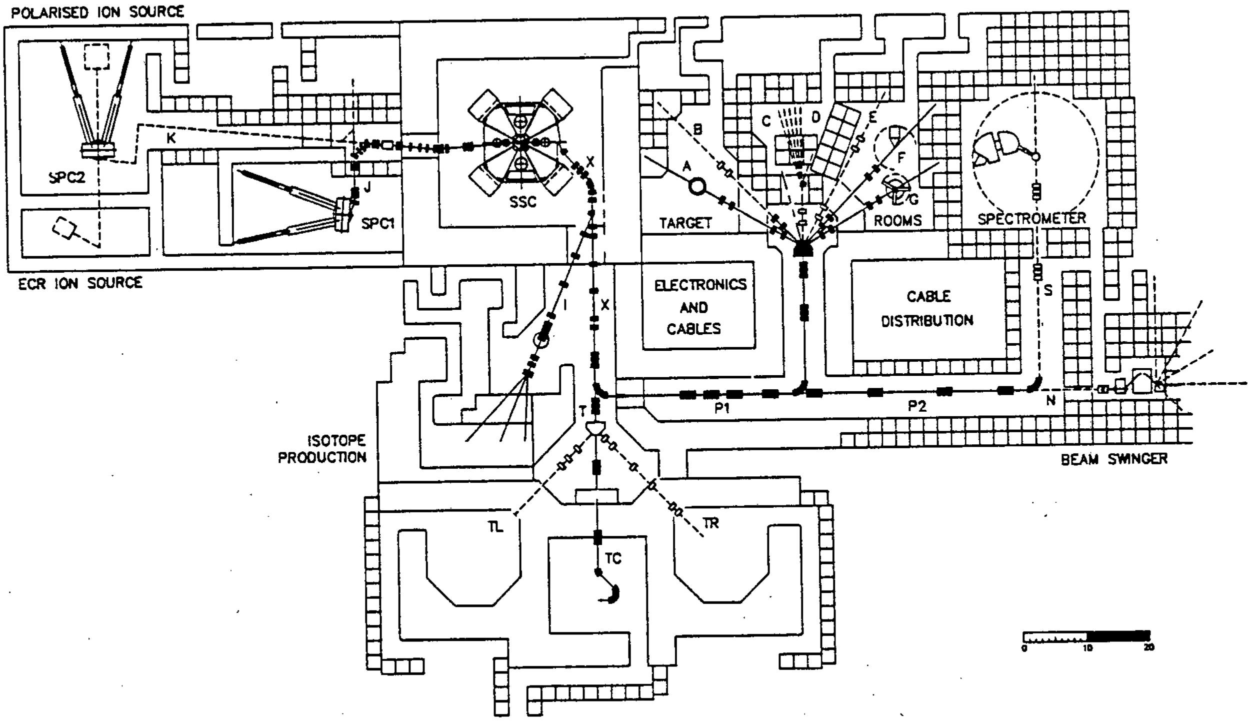

Figure 2.1: *Layout of the NAC cyclotron facility.*

electrically-isolated quadrants. Three 160 mm diameter×800 mm long aluminium cylinders, through which the charged particle beam passes before striking the beam stop, are mounted upstream of these quadrants inside the beam dump pipe. Each of these cylinders is also electrically isolated, and, together with the individual quadrants, is connected to a current integration system which digitizes and displays the charge intercepted by these components.

The experiment required the quality of the incident proton beam to be as high as practically obtainable, and for the singles measurements in particular, the beam had to be free of halo or other effects due to slit scattering or beam scanning devices in the beam transport system upstream of the target.

During measurements, the operations personnel maintained a focussed beam spot of less than 2 mm×2 mm within 0.2 mm of the centre of the target (when viewed on the scribed BeO target with the aid of a closed-circuit television (cctv) camera). Beam halo was monitored on a regular basis during the measurements (at more frequent intervals for the singles than the coincidence measurements) by comparing the count rates, produced by a ^{12}C target and an empty target frame, in a detector positioned at a particular angle. The energy of the beam was determined by the centering of the beam within the SSC and the setting of the sector magnetic fields. For the coincidence measurements this was 200.0±1.0 MeV, and for the singles measurements 90.0±0.5 MeV and 120.0±0.5 MeV.

The beam from the cyclotron consists of bunches of protons, the repetition period and bunch width being dependent on the characteristics of the radio-frequency voltage and phase interval involved in the acceleration process. This pulsed nature of the cyclotron beam complicates coincidence measurements, since it increases the effective resolving time of the counting instrumentation, and therefore results in a detrimental increase in the rate of accidental (or "random") coincidences compared with measurements made with a non-pulsed source of protons [Hry67]. This imposes a limitation on the acceptable count rates in the individual detectors, and thus on the magnitude of the beam current falling on the target.

The average random coincidence rate may be expresssed in the form

$$\bar{N}_R = \bar{N}_1 \cdot \bar{N}_2 \cdot \tau_{eff}$$

where $\bar{N}_1$ and $\bar{N}_2$ are the average singles counting rates in the two detectors, and τ_{eff} is defined as the "effective" resolving time. If τ_1 and τ_2 are the width of the fast timing pulses from the detectors, τ_{eff} is in general larger than $\tau_1 + \tau_2$, the effective resolving time when a continuous source of protons is used. $\bar{N}_1$ and $\bar{N}_2$ are related to the counting rates, N_1 and N_2, in the detectors during the beam bunch by

$$\bar{N}_1 = N_1 b/T \qquad \bar{N}_2 = N_2 b/T$$

where T is the period of the beam bunches, and b is the bunch width. Hrynkiewicz *et al* [Hry67] derive an equation for τ_{eff} of the form

$$\tau_{eff} = (T/b^2) \int_0^b g(t)dt$$

where the function $g(t)$ depends on the position of the time t with respect to the edge of the cyclotron beam bunch and the width of the pulses τ_1 and τ_2. In the case where $b \leq \tau_2 \leq \tau_1$ and $\tau_1 \leq T - b$ (that is, an instrumental resolving time short compared to the bunch repetition period, but of the order of the bunch width — the case most commonly found in practice), the integral evaluates to

$$\int_0^b g(t)dt = b^2$$

and thus

$$\tau_{eff} = T.$$

In this case, the average random coincidence rate becomes

$$\bar{N}_R = \bar{N}_1 \cdot \bar{N}_2 \cdot T.$$

While both the "true" coincidence rate and the average singles rates in the detectors are proportional to the beam current, it is apparent from the above equation that the "random" coincidence rate is proportional to the product of the average singles rates and the relatively large effective resolving time, and it is this fact which limits the acceptable magnitude of the beam current incident on the target.

For the coincidence measurements, a total of 32 shifts of useable beam on target at 200 MeV was achieved during March and May 1987. Much to the delight of the experimenters, the cyclotron operations personnel were able to extract a high quality beam of the required energy from the SSC and transport it to the target after only three weeks of scheduled operation. This was the first occasion on which a 200 MeV beam had been delivered to a target in the experimental physics vaults. Apart from relatively minor rf resonator and ion source problems, beam was delivered reliably over a ten-day period for a total of 29 8-hour shifts. This period of data collection was interrupted by a period of scheduled beam delivery to the neutron radiotherapy vault. This interruption entailed a change in the proton beam energy to 66 MeV. Following this interruption a power outage damaged some of the cyclotron control electronics, and the operations personnel experienced great difficulty in restoring and maintaining the high quality 200 MeV beam for the second period of coincidence data collection. During these two periods data were collected for the first setting of the primary detector angle (-20°) with six secondary angle settings, and the second primary angle (-45°) with three secondary angle settings.

Beam time (with protons of 90 MeV) was allocated to the first set of singles measurements during May 1987. Because of the stringent beam quality requirements of the singles experiments, much time was spent eliminating halo, and all the data were collected during a 2-shift period. The second set of singles measurements at a proton energy of 120 MeV was made during June 1988 when the ^{12}C(p,p′x) data were acquired along with that from a number of other targets during a 6-shift period — by this time the operations personnel had a good deal more experience in tuning the acccelerator and beam-transport system, and were able to reduce halo to an acceptable limit much more efficiently than previously.

2.3 Scattering Chamber

The measurements were made in the National Accelerator Centre's 1.5 metre diameter scattering chamber [Rav87], which was originally acquired from the University of Maryland. This chamber is electrically isolated from the beam line, vacuum pumps, etc., and for safety reasons, is connected to a local "mother earth" when not in use. During measurements the chamber is attached to a 25 mm^2 "clean earth" cable which is connected to the earthing bar in the data room.

To obtain the operational vacuum in the scattering chamber within a reasonable time after closing the lid, a 60 m^3·h^{-1} double stage rotary pump is used as the roughing pump and a 1000 litre·h^{-1} turbo molecular pump is used as the second stage pump. In addition, a cryogenic pump, which is also an effective pump for water vapour, is used for the final stage evacuation of the chamber. As a considerable amount of equipment in addition to the detectors (consisting mostly of preamplifiers, and signal and high voltage cabling) was to be installed within the chamber for these measurements, some concern was expressed about the attainment of an operational vacuum in a reasonable pumping time. In practice it was found that, after the initial pump down, if vacuum was always broken with dry nitrogen, then an operational vacuum below 10^{-4} mbar was obtainable in less than 2 hours (compared with an initial pump down of 24 hours duration to achieve 10^{-4} mbar after all the equipment had been assembled inside the chamber). During measurements a vacuum close to 10^{-5} mbar was maintained.

The target ladder mounted at the centre of the chamber may be driven vertically to enable selection of one of five targets, and rotated about its vertical axis. The vertical positioning of the target can be made to an accuracy of 0.01 in. (this movement is not metricated – the ladder's target holder mounts are at a 1.5 in. pitch for historical reasons), and the angular positioning of the ladder made to an accuracy of 0.1 deg.

There are two independently movable arms in the scattering chamber to which the detectors, collimators, etc. required for the experiments are attached. These arms are driven by stepping motors, and the positions of the arms are read out by means of shaft encoders with an angular resolution of 0.01 deg.

All these movable components in the chamber may be controlled locally, or remotely at a console in the data room. The remote console also displays the position readouts of the shaft encoders (converted to convenient units).

For the coincidence measurements, a plate was constructed and mounted on one of the chamber arms to allow three independent detector assemblies to be mounted on the arm at angles of 50 deg between one another. A single detector assembly was mounted on the other arm. For the singles measurements, a single detector assembly was mounted on each of the arms.

Before measurements were begun the alignment of the arms of the scattering chamber was carried out by the laboratory's surveyor, and the readouts were set to correspond to the measured angles of the arms. The target ladder angle and the vertical positions of the centres of the five target frames were calibrated in a similar way.

One of the ports in the lid of the chamber is made of transparent perspex enabling a cctv camera to view the target positioned in the particle beam. This is used primarily for tuning the beam onto the target centre with the aid of a scribed scintillator in the target position. This required that the vault be kept in darkness during operation to minimize the light entering the chamber and affecting the detectors.

2.4 Targets

The target ladder at the centre of the scattering chamber has the facility for mounting five target holder frames. The 3 mm thick aluminium frames are 47.5 mm wide × 38 mm high, with a 25 mm hole drilled through the centre. During the proton-proton coincidence measurements four target frames were mounted on the ladder. These held a Beryllium Oxide (BeO) scintillator with a cross-hair drawn on the surface which was used for tuning a finely focussed beam spot at the central position, a polythene plastic foil (CH_2) used for calibration purposes, an empty frame for background minimisation purposes and a ^{12}C foil (with a nominal thickness of 5 mg·cm^{-2}). During the singles measurements the same targets were used, and in addition, a second natural carbon foil was mounted on a fifth frame on the ladder.

The ^{12}C (more accurately, natural carbon, which is 98.8% ^{12}C, the remainder being mostly ^{13}C) targets were prepared from a concentrated dispersion of pure ultra-fine graphite particles in propanol-(2) [Cow87]. A clean glass slide, having been weighed on a chemical balance, was clamped in a motorised assembly which enabled the slide to be immersed in the suspension and then withdrawn at a constant speed. After allowing the suspending fluid to evaporate, the slide and its film of carbon were weighed to determine the thickness of the carbon film. The film was then floated off the slide in a water bath and mounted on a rectangular aluminium target frame with a 25 mm hole.

The carbon target thickness was confirmed by measuring the energy lost by alpha particles from a ^{228}Th source as they passed through the target [Law87]. The carbon target was placed 23 mm from the ^{228}Th source and a silicon semiconductor detector was placed 24 mm from the target on the opposite side to the source, all within an evacuated chamber. A collimator with a hole 4 mm in diameter was placed between the target and the detector, some 15 mm away from the target. The measuring system was calibrated by removing the target and recording the pulse heights of the amplified detector output pulses produced by alphas of five distinct energies from the source. The target was replaced and the pulse height produced by the same alphas was recorded. From the measured energy lost in the carbon target by the alphas, the thickness was calculated [Jip84], based on known parameters for the stopping of ions in matter [And77]. The thickness measurement was repeated for both carbon targets at a number of positions up to approximately 10 mm from the centre.

An average thickness of 4.8 ± 0.4 mg·cm^{-2} was measured for the first carbon target and 5.1 ± 0.4 mg·cm^{-2} for the second. The uniformity in the target thicknesses close to the centres, however, was found to be better than 1 percent·mm^{-1}.

During the 90 MeV singles experiment a cross calibration of the two carbon targets was performed. The energy spectra of protons scattered from the two targets into a detector telescope positioned at 35 ° were measured. The number of counts in the elastic peak and two intense inelastic peaks in each of these spectra were determined. The ratio of these totals from the two spectra gave a target thickness ratio of 1.03±0.05.

2.5 Detector Telescopes

The detector assemblies used in all measurements were conventional 2- or 3-element charged particle telescopes each consisting of a sodium iodide (NaI(Tl)) stopping (E) detector and one or two silicon (Si) charged particle (ΔE) detectors. These assemblies are illustrated in figure 2.2.

The telescope (labelled T1), positioned at the primary angle, consisted

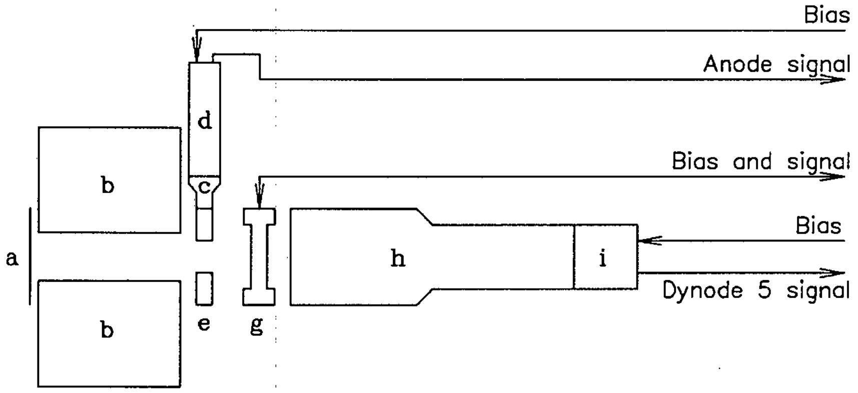

Telescope 1

a = 8μm Kapton foil
b = 48mm thick brass collimator
c = Perspex light pipe
d = EMI 9826B phototube and base
e = 6mm thick NE102A plastic scintillator
f = 30μm thick Si detector
g = 1mm thick Si detector
h = 127mm thick NaI(Tl) crystal with 6μm Havar entrance foil, coupled to an SRC B75B01 phototube
i = EMI TRB/B75B01 transistorised phototube base

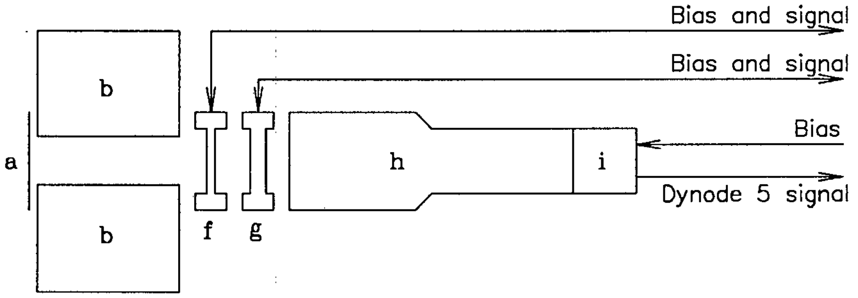

Telescopes 2, 3 and 4

Figure 2.2: *Particle telescope detector assemblies. The two-element telescope with active collimation, positioned at the primary angle is shown above, and one of the three similar three-element telescopes, positioned at the secondary angles, is illustrated below.*

of a 1 mm Ortec Si detector, followed by a 76 mm diameter × 127 mm thick Bicron NaI(Tl) crystal coupled to a 76 mm diameter SRC B75B01 photomultiplier tube. The photomultiplier tube was connected to an EMI TRB/B75B01 transistorised base assembly. The NaI(Tl) detector has a thin 6 μm Havar entrance window, and a light-emitting diode (LED) embedded in the crystal, close to the outer edge for efficient illumination of the photo-cathode of the tube to which it is coupled. The LED is wired to a connector on the phototube can, and may be driven by a suitable pulser for gain stabilization purposes — such a pulser was not available at the laboratory for the coincidence and 90 MeV singles experiments, but was used during the 120 MeV singles experiment. The three telescopes (T2, T3 and T4) positioned at the secondary angles each consisted of a 30 μm Ortec Si detector, followed by a 1 mm Ortec Si detector and a 76 mm×127 mm NaI(Tl) detector, similar to the elements of the primary angle telescope. In each of these three-element telescopes, the two Si detectors were mounted so that their entrance (front) surfaces faced one another. This was done to minimize the dead layer between the two Si detectors, and thus improve the particle identification resolution of low energy charged particles which were stopped in the second detector. (The 30 μm detector of a telescope was called "⟨A⟩", the 1 mm detector "⟨B⟩", and the NaI(Tl) detector "⟨C⟩").

Each of the Bicron NaI(Tl) detectors had a resolution of less than 7% for γ-rays from a ^{137}Cs source. The four Ortec 1 mm Si detectors had resolutions of between 15 and 18 keV FWHM for 5.486 MeV alpha particles. The resolution of Ortec 30 μ Si detectors are not specified. During measurements, the leakage currents of all the Si detectors were monitored on a regular basis, and, if necessary, the bias voltages were adjusted to ensure full depletion of the detectors' active volumes.

A 6 mm NE 102A plastic scintillator with a central 14 mm circular hole was mounted immediately in front of the Si detector of T1. This scintillator was painted with NE 560 reflector paint, except for the top edge surface which was coupled with optical grease to a cylindrical perspex light pipe which had been similarly painted. The light pipe in turn, was coupled to the face of a 19 mm diameter EMI 9826B photomultiplier tube which was mounted vertically. This detector was operated as an active collimator for the telescope at the primary angle.

Solid brass collimators 48 mm thick (thick enough to stop 200 MeV protons) were mounted immediately in front of the first detector of each telescope. Brass inserts in these collimators had circular holes drilled through which defined the solid angles subtended by the front detectors. The insert in the T1 collimator had a hole of 19 mm diameter. This collimator reduced the flux striking the scintillator of the active collimator, while the 14 mm hole in the active collimator defined the solid angle subtended by the telescope. The brass inserts in the other three collimators had holes of 14 mm diameter, and these defined the solid angles subtended by the respective telescopes.

Kapton foils with a thickness of 8 μm were placed over the front hole of the brass collimators to decrease the flux of low energy electrons, emitted from the target, reaching the front detectors of the telescopes.

The detector assemblies were mounted in the same horizontal reaction plane on stands bolted to the rotating arms of the scattering chamber. The arrangement of the detectors in the scattering chamber for the coincident measurements is shown in figure 2.3.

After alignment of the chamber arms, target ladder and telescopes, measurements of the required geometrical parameters were made. The angle between T2 and T3 was 50.03 deg, and that between T3 and T4 was 50.02 deg. The remaining parameters are summarized in table 2.1.

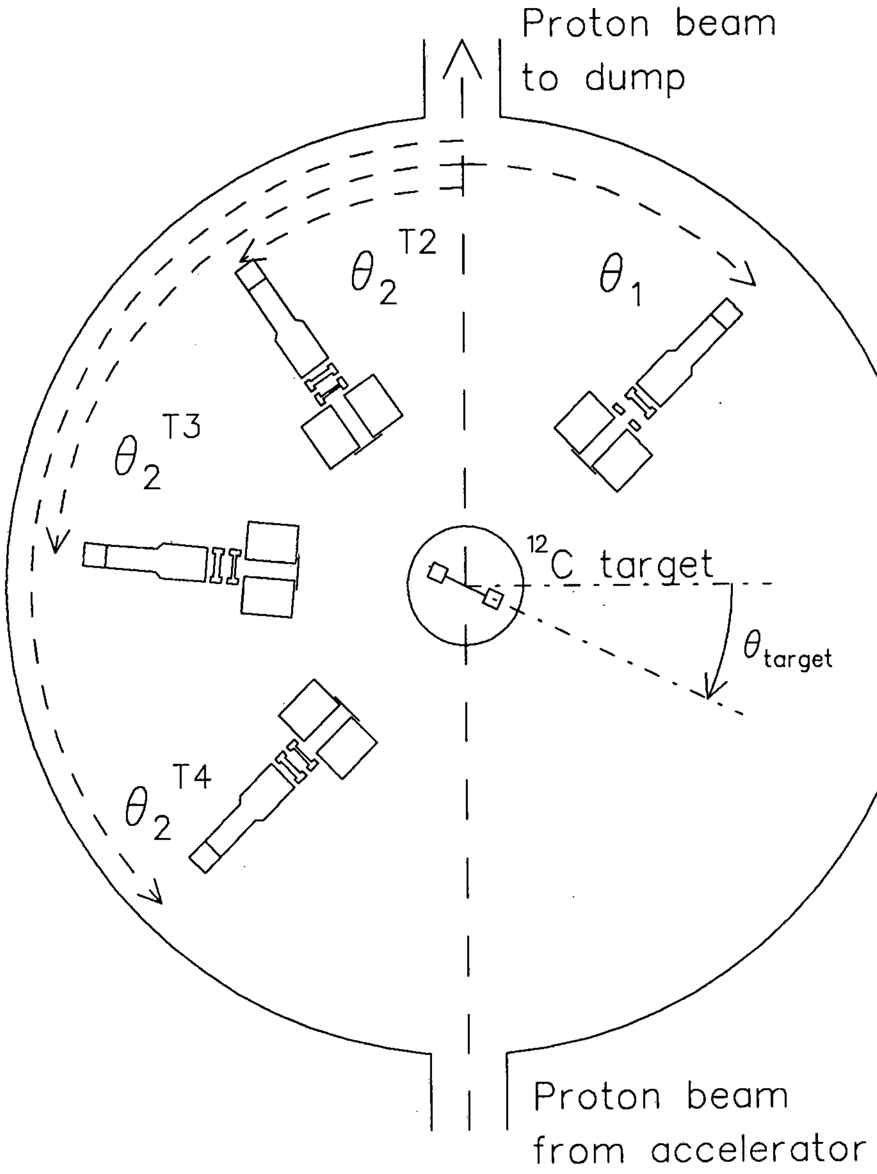

Figure 2.3: *Detector and target geometry inside the 1.5 metre diameter scattering chamber.*

	Distance from target centre to exit hole in collimator (mm)	Diameter of hole in collimator (mm)	Solid angle (msr)
Coincidence measurements			
T1	288.84±0.16	13.835±0.013	1.802±0.003
T2	286.76±0.07	13.944±0.024	1.857±0.005
T3	287.80±0.05	13.950±0.006	1.845±0.001
T4	287.97±0.15	13.955±0.010	1.844±0.002
Singles measurements at 90 MeV			
T1	353.29±0.05	13.800±0.016	1.198±0.002
T3	287.80±0.05	13.950±0.006	1.845±0.001
Singles measurements at 120 MeV			
T1	414.40±0.10	13.835±0.013	0.875±0.002
T3	414.80±0.10	14.000±0.010	0.895±0.002

Table 2.1: *Detector and target geometry parameters*

The two telescopes used in the singles measurements were similar to the telescopes T1 and T3 of the coincidence measurements. For the first of the singles measurements (at 90 MeV proton beam energy), the solid brass collimators were replaced by collimators 13 mm thick, capable of stopping 90 MeV protons. Collimators with a thickness similar to those of the coincidence measurements were used in the singles measurements at 120 MeV proton beam energy, as these measurements formed part of a set, performed up to a beam energy of 200 MeV. Other details of the telescopes and the set-up procedures were similar to those of the coincidence measurements. The geometrical parameters are also listed in table 2.1.

2.6 Electronics

2.6.1 Earthing and power

In an attempt to reduce ground loops and other earthing and noise pick-up problems a "clean earth" is installed in the experimental physics area. This consists of a 25 mm^2 insulated copper cable which is connected to the power distribution box in the data room (the data room is where all the data acquisition electronic modules and computers are situated). The power to this box is sourced from one of the main site transformers reserved for computer power (no heavy motors, power supplies, etc. receive their power from this transformer). The clean earth cable passes around the data room under the false flooring with connectors spaced along its length at regular intervals. The electronics racks, computers, etc. are earthed to this cable.

A patch panel in the data room allows similar cables which travel to the experimental vaults to be connected to the clean earth. This enables equipment in these vaults to be properly earthed — in the present measurements, this included the scattering chamber, the detectors and preamplifiers.

In a similar manner the mains ac power and preamplifier power are supplied to the experimental vaults from a patch panel in the data room.

The signal and high voltage cables from the data room patch panel to the experimental area distribution panels are isolated from any local earth.

2.6.2 Preamplifiers

The distances between the detectors and preamplifiers were kept as short as possible to reduce noise pick-up. All the preamplifiers, therefore, were placed inside the scattering chamber, strapped to the rotating arms on which the detectors were mounted.

The five photomultiplier tube outputs (from dynode 5 of the four telescope tubes and the anode of the active collimator tube) were connected to scintillation preamplifiers (Ortec model 113) with an input capacitance of approximately 150 pF (100 pF selectable and ~50 pF fixed). The electrically-floating phototube cans were attached to an earthing pin on the phototube bases to reduce noise pick-up on the outputs. The single output from each scintillation preamplifier was carried to the data room via 93 Ω cable.

The outputs of the Si detectors were connected to charge sensitive preamplifiers (Ortec model 142). These preamplifiers each have two outputs — the "E" output used for energy measurements was carried to the data room via 93 Ω cable, while the "T" output used for timing measurements was carried via 50 Ω cable.

The outputs of the pulsers (see subsection 2.6.5) in the data room were fed into the test inputs of the preamplifiers via 93 Ω cable. The high voltage detector bias supply outputs were fed into the phototube bases and the charge-sensitive preamplifier "BIAS" inputs.

The signal and bias cables, together with a multi-core cable supplying preamplifier power, were connected to vacuum-tight feed-throughs in ports of the scattering chamber. A distribution box inside the chamber divided the power between the individual preamplifiers.

2.6.3 Linear signals

The linear signals from the preamplifiers, containing information on the amount of energy deposited in the respective detectors, were carried via 93 Ω RG 62 coaxial cables. A block diagram of the linear electronics for the 2-element telescope T1 and the 3-element T2 is shown in figure 2.4 (T3 and T4 were similar to T2).

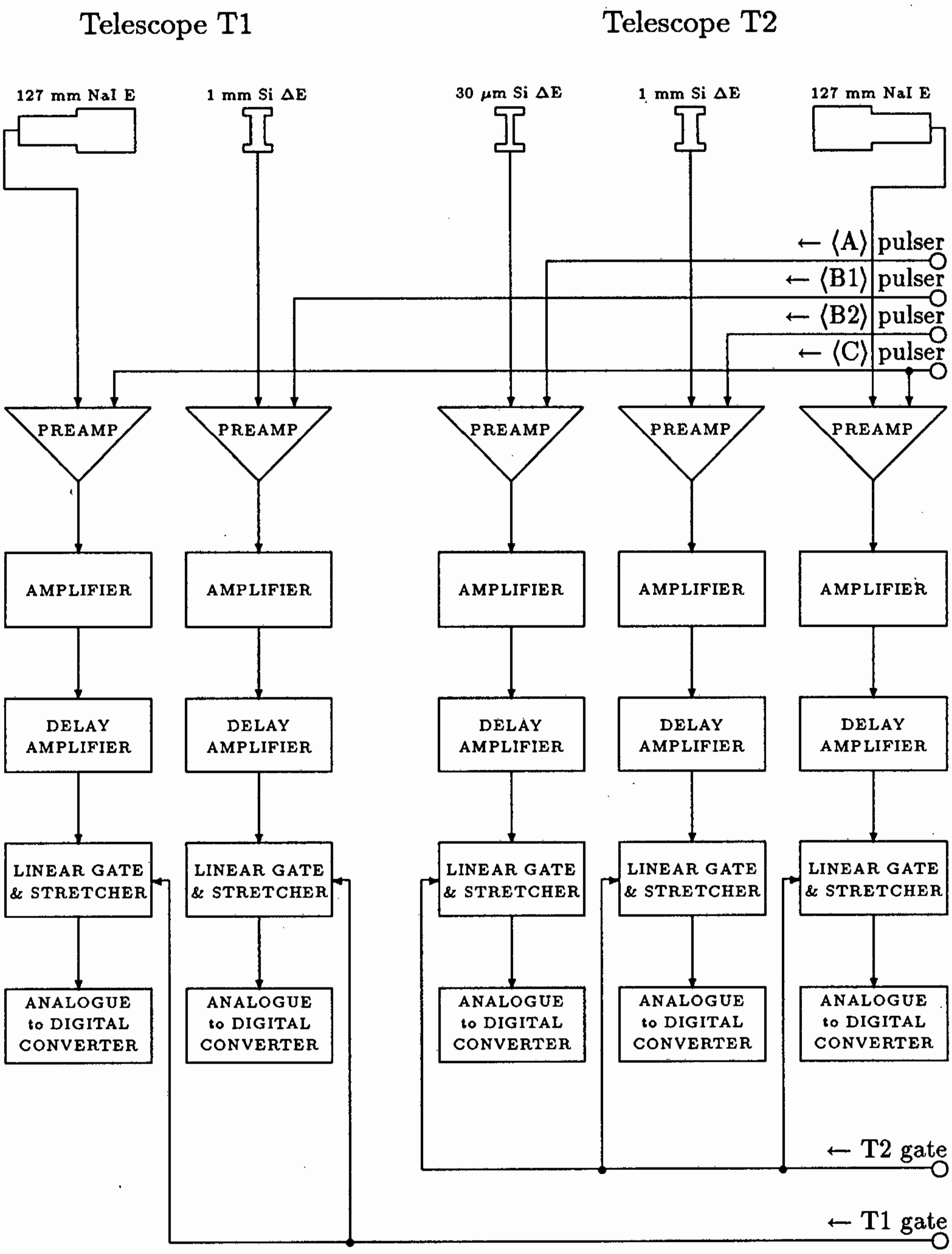

T1 gate ≡ (T1∩T2) ∪ (T1∩T3) ∪ (T1∩T4) ∪ (T1 prescaled singles)
T2 gate ≡ (T1∩T2) ∪ (T2 prescaled singles)

Figure 2.4: *Linear electronics for Telescopes 1 and 2.*

For each telescope element, the signal passed through a linear amplifier (Ortec model 572 for the NaI and 1 mm Si detectors, and Canberra model 2020 for the 30 μm Si detectors), a delay amplifier (Ortec model 427A) and a linear gate and stretcher (Ortec model 542 LGS) to the input of a peak-sensing analogue-to-digital converter (Canberra model 8077 ADC — this uses the Wilkinson method of digitization with a 450 MHz clock rate). The signal was terminated with a 93 Ω resistor at the input to the ADC.

The gate to the LGS modules of a particular telescope was generated by the timing electronics (see subsection 2.6.6), and indicated that the corresponding linear pulses originated from an event of interest (either a coincidence between telescope 1 and one of the other telescopes, a pre-scaled singles event in the telescope, or a pulser event (see subsection 2.6.5)). The gate signals were inhibited by the computer busy signal (see subsection 2.6.8) to ensure that only events that were capable of being processed by the data acquisition hardware were passed to the ADCs for digitization.

2.6.4 Current integrator

The proton beam current intercepted by the beam dump components was fed via Bedea low-noise "measuring cable" to a Brookhaven Instruments current integrator (BIC model 1000C). This module outputs digital pulses with a width of 5 μs whose number is proportional to the accumulated charge. A range selection rotary switch determines the number of pulses output per unit of accumulated charge.

The various parameter settings of the current integrator may be read electronically, and the NAC electronics staff have developed a current integration control and display system which amongst other capabilities, presents the position of the range selection switch to a CAMAC module, which may in turn be read by the computer running the data acquisition program.

2.6.5 Pulsers

The digital output of the current integrator was fed to the input of a prescaler (a continuously-running Ortec model 719 timer with the STOP output connected to the START input). The STOP ouput of the prescaler was also used to drive the external trigger inputs of six tail pulse generators (BNC model BH-1). A pulser event therefore occurred after a fixed number of protons were stopped in the beam dump.

As these were the only available pulsers in the laboratory at the time, the output of one pulser was fed (see figure 2.4) to the TEST inputs of the four preamplifiers connected to the NaI detectors ($\langle C \rangle$ elements), another to the TEST inputs of the three preamplifiers on the 30 μm Si detectors ($\langle A \rangle$ elements), and the outputs from the remaining four individually to the TEST inputs of the preamplifiers on the 1 mm Si detectors ($\langle B \rangle$) elements). 93 Ω RG 62 cable was used for all the pulser signals.

The need to share a single pulser amongst different detector signal channels resulted in complications when the coincidence timing circuitry was tuned, since changing any of the settings of the pulser, including the amplitude, resulted in large changes in the timing of the derived logic pulses from the preamplifier outputs. This led to many frustrations during experiment set-up.

2.6.6 Timing signals

The timing signals were obtained from the preamplifiers — the charge-sensitive preamplifiers provide a timing output, separate from the linear output, while the scintillation preamplifiers provide a single output. In the latter case the signal was teed at the timing filter amplifier input, the one leg going to this amplifier and the other to the linear amplifier. All timing signals were carried on 50 Ω cable — between the experimental vault and the data room this was low loss RG 213 cable, while between modules RG 58 or RG 174 cable was used (depending on whether the particular modules had BNC or LEMO connectors). A simplified block diagram of the coincidence measurements' timing electronics for telescopes 1 and 2, which excludes various signal delay and buffering components as well as the computer busy vetoing, is shown in figure 2.5. The electronics for telescopes 3 and 4 was similar to that of telescope 2.

All the timing signals from the preamplifiers were passed through timing filter amplifiers (Ortec model 474 TFA) followed by constant fraction discriminators (Ortec model 934 CFD).

The first requirement for the detection of an acceptable event in a particular telescope was that a signal must have been produced in element ⟨B⟩ and in at least one of the other elements.

For T1, with only two elements, a logic AND function was performed between the signals from elements ⟨B⟩ and ⟨C⟩. The output of the CFD associated with the active collimator of T1 was used to veto this function, that is, events originating from particles which passed through the T1 active collimator before producing signals in elements ⟨B⟩ and ⟨C⟩ were discarded. The ANDing and vetoing functions were performed simultaneously by a 4-fold logic unit (LeCroy model 365AL).

For T2, T3 and T4, each with 3 elements and no active collimator, a logic OR function was first performed between the signals from elements ⟨A⟩ and ⟨C⟩ (in a LeCroy logic fan in/out model 429A), followed by a logic AND of the resulting signal from the fan-in and the signal from element ⟨B⟩ (in a LeCroy 4-fold logic unit). Thus acceptable T2, T3 and T4 events must

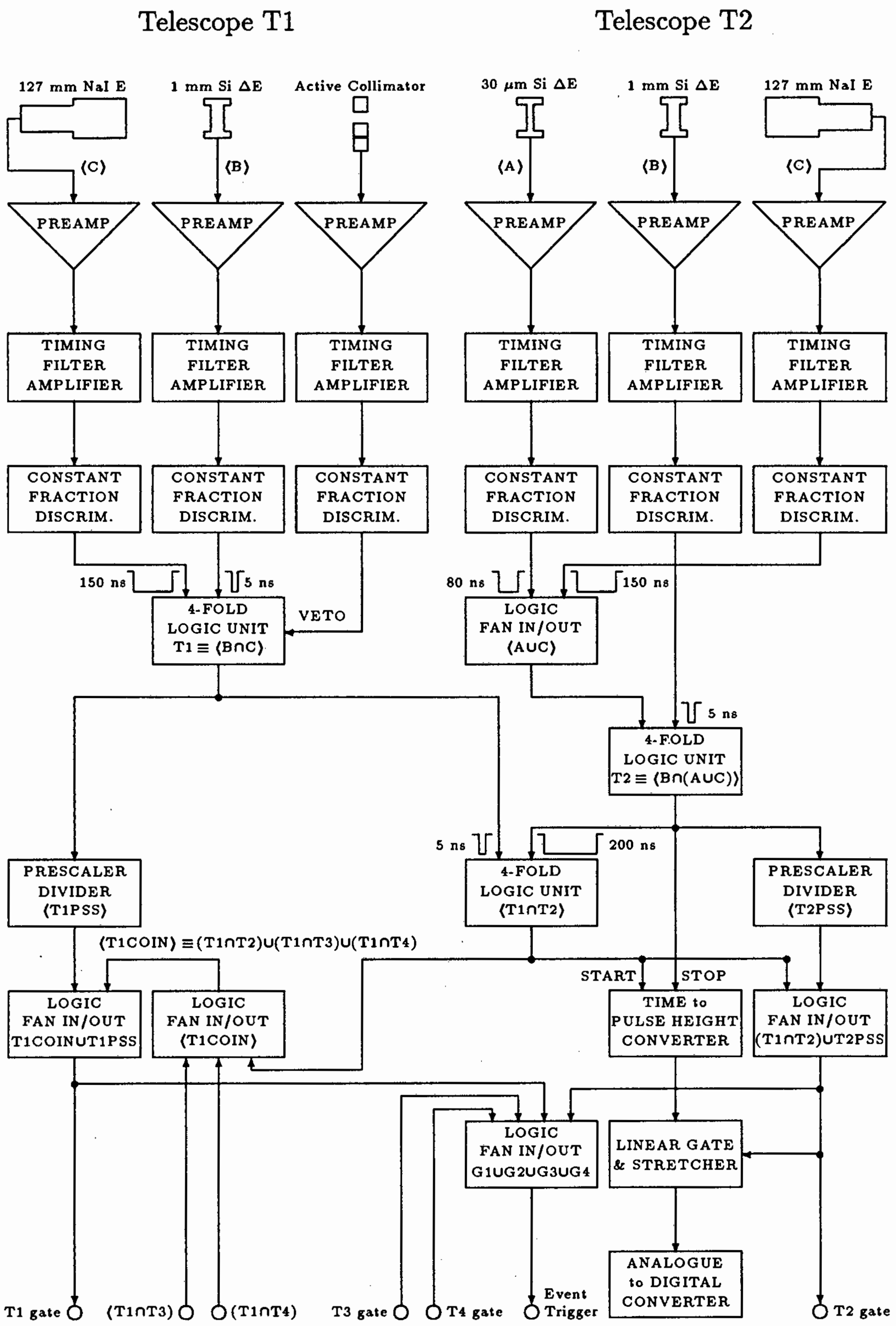

Figure 2.5: *Simplified timing electronics for Telescopes 1 and 2. Signal buffering, delay components and computer busy vetoing have been omitted. Signal processing for telescopes 3 and 4 is similar to telescope 2.*

have produced a signal in ⟨B⟩ and a signal in at least one of the other two elements.

The timing reference for each telescope was determined by the signal from element ⟨B⟩. This is illustrated in figure 2.5. The width of the signal from the CFD of element ⟨B⟩ was set to approximately 5 ns, while that from element ⟨A⟩ was set to 80 ns and that from element ⟨C⟩ to 150ns.

One of the outputs from each of these 4-fold logic units, which determined an acceptable telescope event, was fed to a prescaler divider (consisting of an Ortec 416A gate and delay generator, a continuously running Ortec 719 timer and a LeCroy 688 level adapter). The output of this prescaler enabled a sample of telescope singles events to be collected by the data acquisition program.

Coincidences between T1 and T2 were determined by the logic ANDing of the outputs from the four-fold logic units of these two telescopes in another four-fold logic unit. The time reference of each coincidence was determined by the width of the output signal of the T1 logic unit, which was set to approximately 5 ns, while the output width of the T2 signal was set to approximately 200 ns. This latter width was chosen to allow coincidences between events in five accelerator beam packets to be acquired (proton packets are separated by 38.5 ns at 200 MeV). The collection of "random" coincidences, originating in events from different beam packets adjacent to the "true" coincidence packet is essential for accurate random background subtraction during data analysis (this is described in more detail in subsection 2.7.2). The signal delays were adjusted so that the "true" coincidences (that is, detection of particles in different telescopes originating from the same event in the target) occurred near the middle of this 200 ns coincidence window. Similar logic was employed to detect T1-T3 and T1-T4 coincidences.

The time distribution of telescope coincidences was measured by time-to-pulse-height converters (Ortec TPHC model 467). In the case of T1-T2 coincidences an output of the T1$\cap$T2 logic unit provides the start pulse for the TPHC while the output of the T2 logic unit provides the stop pulse. The analogue outputs from the three TPHCs passed through Ortec 442 linear gate and stretchers (LGSs), and thence to Canberra 8077 ADCs.

Fourteen analogue signals required digitization by the ADCs. Telescope 1 had two (energy information) signals, and the other three telescopes four (three energy and one coincidence time information) signals each, which were passed to the ADCs by the LGSs. The four separate gates (one for each telescope's set of LGS modules) were driven by logic pulses derived from the timing electronics (see figure 2.5). The T1 gate indicated a T1-T2, T1-T3 or T1-T4 coincidence or a T1 prescaled singles event. T2 gate indicated a T1-T2 coincidence or a T2 prescaled singles event. T3 and T4 gates were similar to T2.

For the singles measurements where only two independent telescopes were used, a rather simpler arrangement was required. The telescope-telescope coincidence condition was removed from the timing logic and the singles events prescaling was set to 1 — all acquired events were, by definition, singles events. The number of analogue signals requiring digitization by the ADCs was reduced to five (namely, the energy information signals from the two telescopes, there being no coincidence time information).

2.6.7 Event trigger

The event trigger, that is, the logic signal which told the data acquisition program that an event of interest had occurred and initiated the data read-out cycle, was generated from the telescope timing signals logic. In the coincidence measurements it was in essence a suitably delayed logic OR of the four telescope gate signals performed by a LeCroy 429A logic fan in module (see figure 2.5). In the singles measurements it was a delayed logic OR of the two individual telescope event signals.

This trigger signal was fed to the input of an event trigger module — a CAMAC module designed and constructed by the NAC electronics staff. On receipt of the trigger, the module sets a busy flag, waits a preset time, and then interrupts the front-end processor by raising a CAMAC LAM (look-at-me) signal to initiate the event read-out cycle.

The preset delay between receipt of the trigger and raising the LAM is adjustable, and ensures that all the analogue signals are digitized and the logic levels are latched before the data are read by the computer. In this experiment all the ADCs were set to a maximum of 1024-channel conversion gain, and thus the digitized data were available to be read in something less than 5 μs, in the worst case, after the pulse peak was detected. The delay was adjusted, conservatively, to a value of 10 μs after the arrival of the peak of the most delayed analogue pulse at its ADC.

2.6.8 Computer busy

The busy output from the event trigger module is set by the hardware on receipt of the event trigger signal. This output was used to inhibit the generation of further event triggers, and also to inhibit the generation of the pulses which drove the telescope LGS gates. (To avoid clutter this is not shown in figure 2.5).

The busy output was also fed to the inhibit input of one of the scaler modules (see subsection 2.6.10), which prevented these scalers from updating while a read-out cycle was in progress.

The data aquisition program cleared the event trigger module on completion of an event read-out cycle, and this reset the busy output, allowing further events to be digitized, triggers to be acted upon, and the scalers to be updated.

2.6.9 Pattern register

A 12-input Bi-Ra 2351 pattern register was supplied with levels from the timing electronics. The latched data in the pattern register indicated the nature of the event which caused the trigger, and was read during the event read-out cycle. A list of the functions of the eight inputs used in the experiment is given in table 2.2. These were generated from the timing electronics, but to avoid clutter, are not shown in figure 2.5.

Bit	Active Status
1	$T1\langle B \cap C\rangle$
2	$T2\langle (A \cup C) \cap B\rangle$
3	$T3\langle (A \cup C) \cap B\rangle$
4	$T4\langle (A \cup C) \cap B\rangle$
5	$T2\langle A \cap B \cap \overline{C}\rangle$
6	$T3\langle A \cap B \cap \overline{C}\rangle$
7	$T4\langle A \cap B \cap \overline{C}\rangle$
8	Prescaled singles event

Table 2.2: *Pattern register input definitions*

From the table it can be seen that the first four bits of the pattern register defined which of the four telescopes fired in the event. The following three bits specified whether a "low energy" event was detected in each of the three corresponding 3-element telescopes, that is, that the two Si detectors (elements ⟨A⟩ and ⟨B⟩) of a telescope fired while nothing was detected in the relevant NaI crystal (element ⟨C⟩). The eighth bit defined the event to be a prescaled singles event (all events in the singles measurements).

The logic signals input to the pattern register were stretched by fast logic buffering modules (LeCroy model 821 quad discriminators) to ~1μs width to ensure that all the inputs were settled before the strobe signal arrived to latch the data to the pattern register output. The strobe signal itself was essentially a delayed version of the event trigger described above.

2.6.10 Scalers

Various significant pulses derived from the fast electronics were counted in two LeCroy model 2551 12-fold scalers. One of these modules was inhibited by the computer busy signal (see subsection 2.6.8). The scaler inputs are listed in table 2.3.

Bit	Uninhibited Scalers	Inhibited Scalers
1	10Hz clock	10Hz clock
2	Current integrator	Current integrator
3	$T1 \cap T2$	$T1 \cap T2$
4	$T1 \cap T3$	$T1 \cap T3$
5	$T1 \cap T4$	$T1 \cap T4$
6	$T1$	Pulser trigger in
7	$T2$	Pulser trigger out
8	$T2$"low energy"	
9	$T3$	
10	$T3$"low energy"	
11	$T4$	
12	$T4$"low energy"	

Table 2.3: *Scaler input definitions*

The first two scalers in both sets count the digital outputs of a 10 Hz clock and the current integrator (see subsection 2.6.4). The following three scalers in both sets count the number of coincidence events detected for the three telescope pairs. The last seven scalers of the uninhibited set count the total number of events detected in each of the four telescopes and the number of "low energy" events in the three 3-element telescopes (that is, where elements ⟨A⟩ and ⟨B⟩ fired while element ⟨C⟩ did not). Finally, the sixth and seventh scalers of the inhibited set count the number of pulser triggers input to the first pulser and the number of trigger outputs from the last (sixth) pulser (the six pulsers were daisy chained, the trigger output from each feeding the trigger input of the next,and the last trigger output pulse was counted to ensure that all the pulsers were firing consistently).

2.6.11 Computer interface

The electronic signal processing equipment is interfaced to the data acquisition computer by means of CAMAC.

In the current coincidence experiment, each event consisted of the digital coincidence pattern word and fourteen analogue signals which were digitized by the Canberra 8077 ADCs (the eleven energy-information signals from the detectors — described in subsection 2.6.3 — and the three time-information signals from the time to pulse height converters — described in subsection 2.6.6). The digital data output of each of these ADCs was connected to a CAMAC interface module which was designed and constructed by the NAC electronics staff. This module allows the ADC connected to it to be controlled (enabled, disabled and cleared), and the digitized data to be read over the CAMAC dataway as a 16-bit word. The fourteen ADC interface modules were plugged into slots 1 to 14 of a CAMAC crate, and the Bi-Ra 2351 CAMAC input register containing the event pattern information — described in subsection 2.6.9 — was plugged into the same crate.

The crate also contained the two LeCroy 2551 CAMAC 12-fold scalers, the CAMAC event trigger module and the current integrator status readout module.

2.7 Data Handling

2.7.1 Hardware configuration

The data handling hardware at the National Accelerator Centre is based on Digital VAX computers, integrated in an Ethernet-based local area network. A simplified block diagram of the data acquisition computer system used in the research programmes conducted around the cyclotron is shown in figure 2.6. Other components of the data handling system connected to the network are not shown.

A VAX-11/750 computer is used for programme development, data replay and analysis tasks, while the VAX-11/730 computer, shown in figure 2.6, is usually dedicated to on-line data acquisition from experiments based on the cyclotron. Both computers have a standard set of peripherals to support the applications, namely, fixed and removable mass-storage disks, magnetic tape drives handling 800, 1600 and 6250 bpi (bytes per inch) density formats, Ethernet network interface, and interactive terminals, some of which support graphics applications. Terminal servers are also connected to the Ethernet local area network, and in addition to providing terminal connections, the servers also support plotters and printers, thus enabling these output devices to be shared by all the computers on the network.

The VAX-11/730 has a (Digital standard) UNIBUS input/output bus. The interface between this bus and the CAMAC components of the data acquisition hardware is a Bi-Ra microprogrammed branch driver (MBD-11)

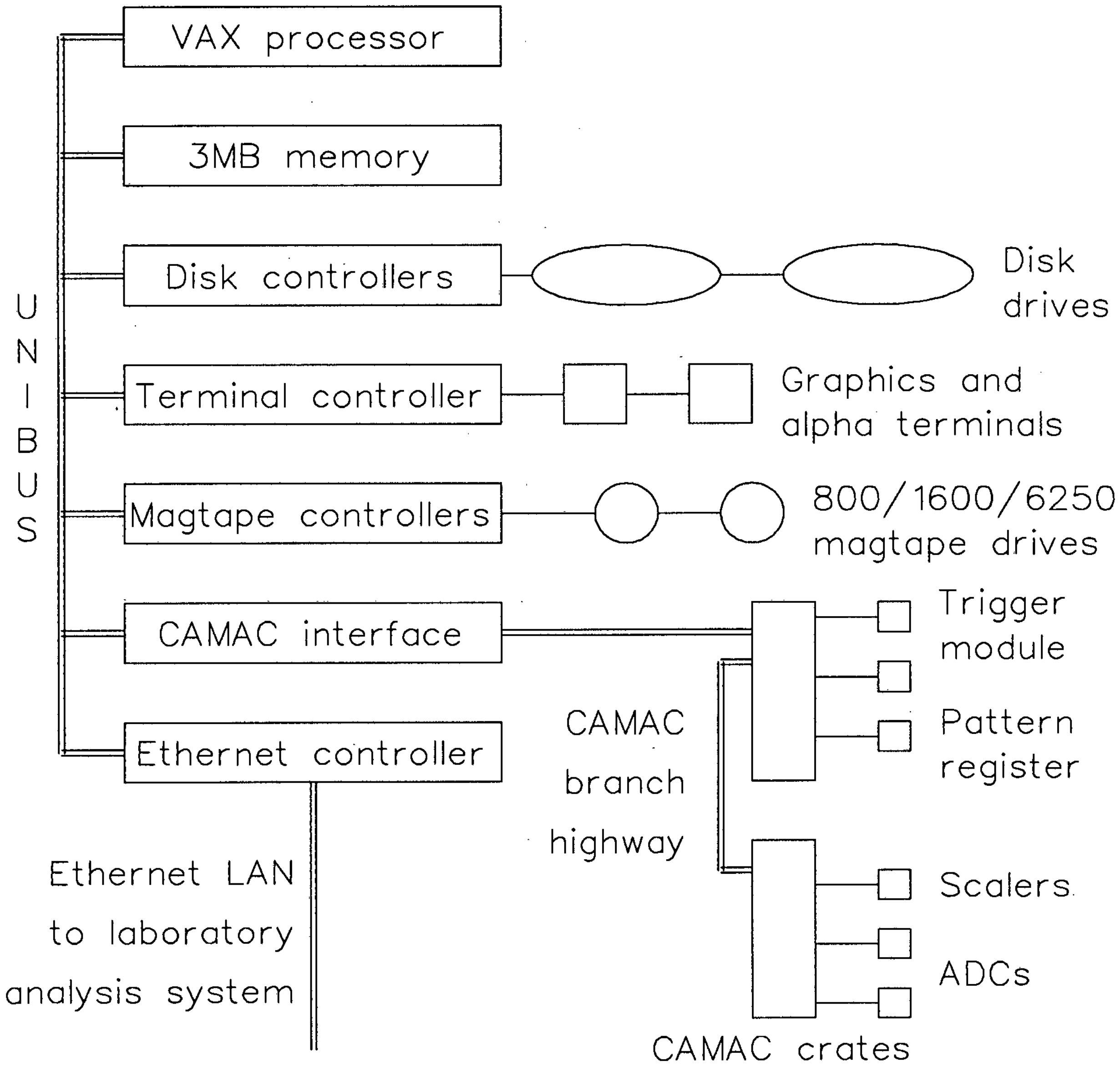

Figure 2.6: *Block diagram of data acquisition system*

[Kin81]. This device is a 16-bit microprocessor with a limited instruction set having an execution time of 450 ns. It has 4 kilowords of memory (with a 35 ns access time), and multiplexes eight DMA (direct memory access) channels controlling the flow of commands and data between the CAMAC branch and the computer's UNIBUS. MBD-11 operations are controlled by programs in its memory, the programs being down-loaded over the UNIBUS by the VAX computer.

The basic mode of operation of the MBD-11 is to obtain a CAMAC command from a list in either the VAX or MBD-11 memory, issue the command to the CAMAC branch, wait for the return of data, and then transfer the data to VAX memory via a DMA operation. Each of the eight DMA channels operates on a separate command list, and the channels are interleaved depending on channel priority and the source of the request which initiates activity on a particular channel. The MBD-11 is able to generate 25 unique interrupt vectors to the computer.

2.7.2 Software

The principle software package used for data acquisition and replay is called XSYS. This software had its origins as an integrated package at TUNL (Tri-Universities Nuclear Laboratory) [Gou81][Gou83]. It drew components from various sources including Stanford Linear Accelerator Centre and the Niels Bohr Institute [Hol79]. XSYS forms the basis of the data acquisition software at a number of laboratories [Smi83][IUC83], and the version in use at the NAC follows closely that developed at the Indiana University Cyclotron Facility [IUC84]. The NAC version was modified by the current author to suit the particular requirements of this laboratory.

XSYS runs under the VAX/VMS operating system. It creates common areas (called global sections) of virtual memory in which all common data such as histogram definitions, histogram data, run stati, control information, etc. are stored. On initialization, the software defines a set of XSYS commands which are executable from the DCL (Digital Command Language) command line, that is, to the user they look like regular VAX/VMS commands. Commands are available for defining and deleting histograms, storage of data on disk and tape, setting sorting gates, manipulation and display of histogram data, etc.

XSYS includes the code for the MBD-11 CAMAC branch driver. This code is downloaded when the acquisition computer is booted, and, if corrupted, may be downloaded explicitly with an XSYS command by the user. Interaction between the MBD-11 code and the XSYS applications tasks is controlled by a device driver conforming to VAX/VMS conventions.

The primary task of the MBD-11 code is to handle the eight independent DMA channels (numbered 0 to 7) between the CAMAC and the VAX. This is organized so that a specific event trigger originating in the data acquisition electronics results in one of eight LAMs (CAMAC look-at-me interrupt levels) being raised on the CAMAC branch, each LAM corresponding to one of the eight MBD-11 DMA channels. On being interrupted by the LAM, the MBD code executes a list of user-supplied commands which read out the event data, perform simple data manipulation, and transfer the results to an event buffer in the VAX memory.

The command lists executed by the MBD-11 code are supplied by the user in the form of a Data-Acquisition Program (DAP) file. The DAP statements which make up these lists are simple, self-explanatory declarations and operations which specify when the corresponding list is to be executed, the CAMAC commands to be issued when the event information is read, and any simple arithmetic operations to be performed on the data. The user supplies a list to be executed immediately after the DAP file lists are loaded (delimited by the INIT declaration), when the XSYS BEGIN (data taking) command is issued (delimited by the BEGIN declaration), when the XSYS HALT (data taking) command is issued (delimited by the HALT declaration), and a list to be executed when each of the possible event triggers in the current experiment occurs (delimited by EVENT declarations).

In the current coincidence and singles experiments the event channels 0 and 6 were used, for event data readout on receipt of the event trigger and scaler readout on receipt of a 10-second clock trigger respectively. Execution of the EVENT 0 list resulted in the readout of the required CAMAC modules (pattern register and ADC interface modules) and the transfer of the data to a buffer in the VAX memory. The EVENT 6 list resulted in the readout of the current integrator interface and the two scaler modules, and transfer of the data to memory. In each case the data transferred to the VAX buffer was preceded by two header words which contained information identifying the event and specifying its length.

XSYS allows for the experiment-specific sorting of event data by providing a compiler for the generalized event-analysis language, EVAL. EVAL was originally written by A. Holm at the Niels Bohr Institute [Hol79]. It has subsequently gone through several generations of revision, being integrated into XSYS at TUNL [Hol81]. The sorting of multi-parameter data consists of a sequence of numerical manipulation of input event data, testing of the results, and incrementing histograms (spectra) according to the results of these tests. EVAL is a language which is broad enough to allow these algorithms to be easily specified by the physicist with only a rudimentary exposure to computer programming, while retaining a simpilicity which allows the compiler to generate code which executes very quickly. Its integration into XSYS includes an efficient interface between the EVAL code and the XSYS data structures (such as the event, histogram and gate arrays). Provision is also made for the calling of FORTRAN subroutines from within the EVAL code — this is very convenient when more complicated numeric processing, such as relativistic kinematics calculations, is required as part of the event sorting procedure.

When the user initializes the sorting subprocess with the appropriate XSYS command (EVOP), the subprocess reads the specified DAP and EVAL files, constructs the lists to be executed by the MBD-11 code, compiles the EVAL program, and links the compiled code into the sorting program.

After data taking has begun, the sorting program dumps filled event buffers containing the raw data to tape (if required) and executes the compiled EVAL code to analyse the data. To reduce interrupt-fielding overheads in the VAX computer and the MBD-11, the buffers set up in the VAX memory to receive the incoming event stream consist of a circular linked list [Knu68] of buffers (usually three). Information describing these buffers is passed via the MBD-11 device driver to the MBD-11 code in the sorting program's input/output (i/o) call which begins data taking. The MBD-11 code has knowledge of the structure of these buffers, and when one is full it immediately starts filling the next buffer in the list if it is found to be empty (by examining a software status flag in the buffer header). When a buffer is filled the MBD-11 interrupts the VAX processor via a special real-time interrupt mechanism provided by the VMS operating system, which allows fast response and reduces overhead. This interrupt is vectored to a special entry point in the sorting program which initiates the output of the data to tape and calls the EVAL analysis code, and dismisses the interrupt. On completion of processing of the buffer's event data, the software status flag is set to indicate that the buffer is again free to be filled by the MBD-11 code with fresh event data. In this way the software overhead in i/o completion, and the re-issuing of another i/o call is avoided. Only if all the buffers are filled does the MBD-11 have to stop reading the incoming event stream, issue an i/o completion interrupt, and wait for the sorting program to re-issue a begin-data-taking i/o call.

In the coincident experiment a total of thirty-nine histograms were allocated to hold analysed data during on-line sorting. Histograms were allocated to hold the pattern register distribution, the pulse-height spectra of the raw coincident event data in each element of each telescope, the 2-dimensional particle identification ΔE versus E spectra of each two-element pair (one pair for telescope 1 and two pairs for the remaining telescopes), and the time distributions of events in telescope 1 in coincidence with one of the other three telescopes. 2-dimensional histograms were also allocated to hold the distribution of the energy of protons detected in telescope 1 versus the energy of coincident protons detected in another telescope — two spectra were defined for each telescope coincident pair, one to hold those events falling within a gate on the "true" peak in the corresponding time distribution, and the other those within a gate on a "random" peak. In addition, histograms were allocated to hold the pulse-height spectra of the raw singles data in each telescope element for the prescaled singles events.

A set of 2-dimensional gates was allocated for the particle identification ΔE versus E histograms (one gate associated with each of the histograms). These gates were defined when the beam was first obtained during the setting-up procedure, and determined whether or not the particle detected in the associated detector element pair was a proton. In addition two 1-dimensional gates were allocated for each of the coincidence time histograms, and were set on the "true" peak and a "random" peak during the setting-up procedure.

A simplified flow diagram of the EVAL program used for on-line sorting of the event data during acquisition of the coincident experiment data is shown in figure 2.7.

The coincident pattern register was first examined to determine whether a coincident or prescaled singles event had occurred. If the latter, then the appropriate elements' singles pulse-height histograms were incremented, depending on which telescope(s) had fired.

If it was a coincident event (that is, telescope 1 fired in coincidence with at least one of the other telescopes), telescope 1 elements ⟨B⟩ and ⟨C⟩ pulse-height histograms were incremented, and the corresponding ⟨B⟩ versus ⟨C⟩ particle identification histogram channel was calculated and the histogram incremented. If the event fell in the gate set on the proton locus of this histogram, the energy of the proton was calculated and a flag set to indicate the detection of a proton in telescope 1; otherwise the proton flag was cleared. Each telescope which was found to be in coincidence with telescope 1 (usually only one of the other three telescopes) was then processed in turn. The corresonding telescope ⟨A⟩ and ⟨B⟩ pulse-height histograms were incremented, and a test was made for a "low energy" event (that is, elements ⟨A⟩ and ⟨B⟩ had fired, while element ⟨C⟩ had not). If this test proved true, the corresponding ⟨A⟩ versus ⟨B⟩ particle identification histogram channel was calculated, the histogram incremented, and a test made as to whether the event fell in the gate set on the proton locus of this histogram. A flag to indicate the detection of a proton was set or cleared accordingly. If the event proved not to be a "low energy" one, then this particle identification procedure was performed on elements ⟨B⟩ and ⟨C⟩. The total energy of the particle was calculated, and the coincident time histogram was incremented. Finally, if the particle in this telescope was a proton as well as the coincident particle in telescope 1, a test was performed to determine whether the event fell in the "true" or "random"

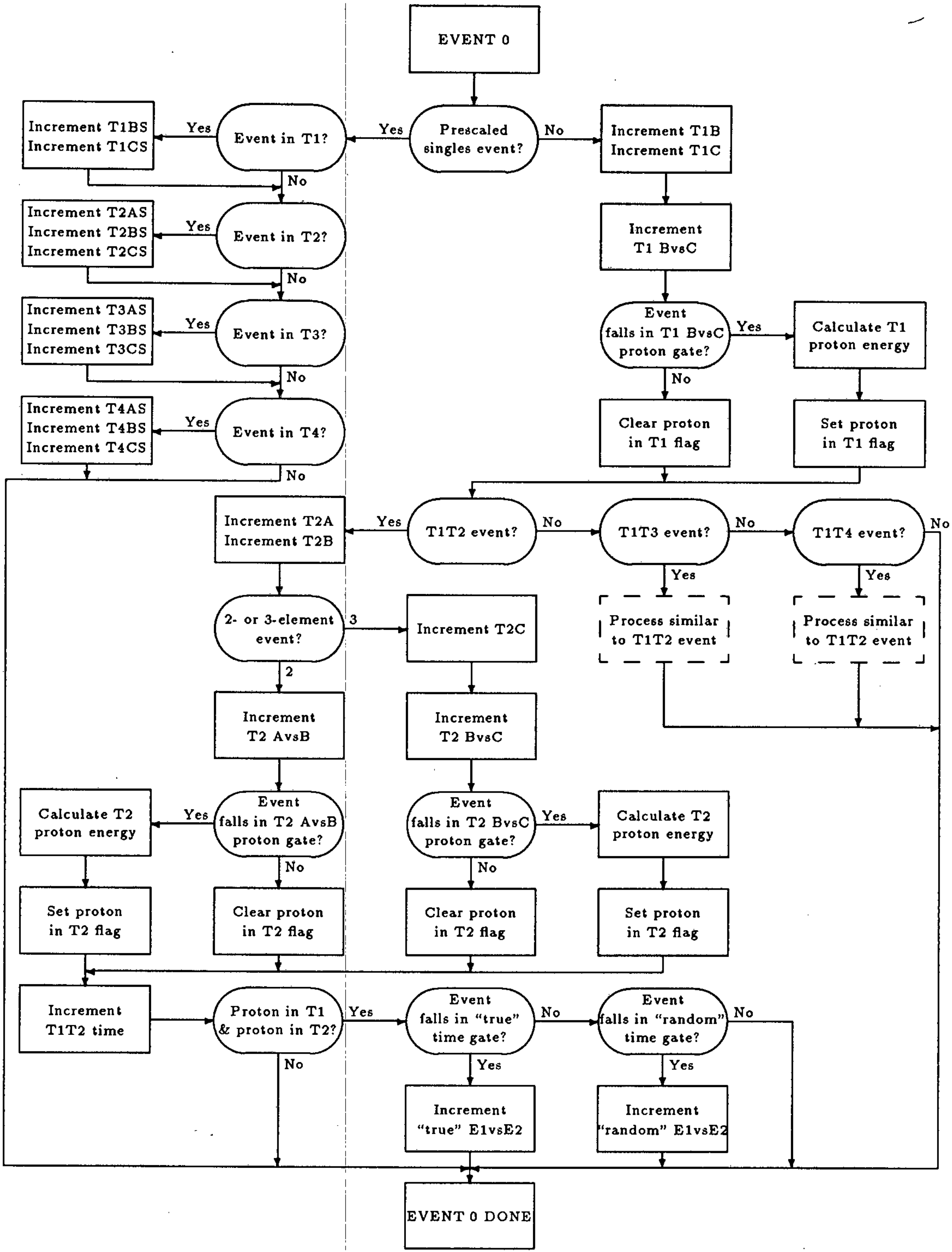

Figure 2.7: *Simplified flow diagram of the event analysis program.*

gate set on the coincident time histogram. If one of these tests was found to be true the corresponding "true" or "random" 2-dimensional coincident proton energy histogram was incremented.

For scaler events (event type 6), the current contents of the scalers were read and the values added to the corresponding cumulative scalers stored in the computer memory. The values read from the current integrator interface were also stored, and combining these with the value in the scaler counting the digital output from the current integrator, the accumulated charge was calculated and stored.

In the singles experiments two particle telescopes were mounted in the scattering chamber, and the requirement that a coincidence occur between the telescopes for event triggering and read out was, of course, removed. Each telescope was handled independently by the EVAL event sorting program, in a manner similar to the handling of the separate telescopes in the coincidence experiment. If a detected particle was found to be a proton (by falling in the appropriate particle identification gate locus), the total energy of the particle was calculated and the singles proton energy histogram for the appropriate telescope was incremented.

2.8 Experimental Procedure

2.8.1 Coincidence experiment

The components of the four particle telescopes (detectors, collimators, stands, etc.) and the targets were assembled and aligned in the scattering chamber as described in sections 2.3, 2.4 and 2.5. The electronics was set up as described in section 2.6, care being taken that no more earth loops than absolutely necessary were made.

The fourteen ADCs were "zeroed", that is, the zero intercept of the ADC conversion function was adjusted so that a dc level of 0 volt presented at the analogue input of the ADC would result in a digitized binary output value of 0. This procedure was carried out according to the manufacturer's instructions, using a calibrated precision pulser. As the adjustment is slightly sensitive to the conversion gain setting of the ADC, the gains were first set to the values to be used in the experiment, namely, 1024 for all the energy signals and 512 for the coincidence time signals.

After a test pump-down of the scattering chamber with all the equipment assembled in the chamber to ensure that an adequate vacuum could be reached, an initial calibration of the 1 mm Si detectors was performed. The vacuum in the chamber was broken by admitting dry nitrogen, the 30 μm Si detectors were removed, collimated ^{228}Th α-particle sources were placed in front of the 1 mm Si detectors, and the chamber was once again evacuated. The biases on the detectors was turned on, and the linear amplifiers on the energy signals were adjusted so that an energy of approximately 14 MeV corresponded to the maximum digitized value of 1023. The pulse-height distributions of the four detectors were acquired and recorded on magnetic storage. The chamber was opened, the ^{228}Th sources were removed and the 30 μm detectors replaced.

When the 200 MeV proton beam was introduced into the scattering chamber for the first time, the target frame containing the BeO scintillator was placed in the beam and viewed through a transparent port in the chamber by a cctv camera to allow the cyclotron operators to tune the beam spot striking the target. At this time, the high-voltage biases on the photomultiplier tubes were turned off to prevent any possible damage due to very high count rates. Once the beam was tuned to the satisfaction of the operators, the BeO target frame was replaced with the empty frame to allow further tuning to reduce the halo on the beam. The photomultiplier tube biases were turned on, and the count rates in the NaI detectors were monitored. Once the halo had been reduced to an acceptable level, which would not result in appreciable damage to the detectors, the CH_2 target was placed in the beam and the electronics was tuned (see section 2.6).

The threshold levels of the constant fraction discriminators (CFDs) on the timing signals were set as low as possible without allowing appreciable noise through. It was important that the small energy pulses in the ΔE Si detectors, caused by high energy protons passing through, were accepted as efficiently as possible. The ΔE versus E particle identification histograms were monitored to ensure that there was no cut off in the proton locus (at high proton energies) due to too high setting of the ΔE CFD threshold. The discriminator levels of the linear gate and stretcher (LGS) modules in the linear circuits were also set as low as possible to avoid any artificial cut-off.

The widths of the logic pulses derived from the various components of the fast electronics were adjusted so that the timing reference from each telescope was derived from the 1 mm Si detector, and the coincidence timing reference between telescope 1 and the other telescopes was determined by telescope 1 (as described in subsection 2.6.6). To enhance the number of coincidences between telescope 1 and each of the other three telescopes, thus making for easier tuning, each pair was placed in turn at a separation angle of approximately 90° so that the detectors viewed the (large cross section) H(p,p)H reaction — because of relativistic effects, at an incident energy of 200 MeV, the two protons are scattered at an angle a little less than 90° with respect to each another. This was possible for the T1-T2 and T1-T3 pair, but not for the T1-T4 pair because of geometrical constraints, and telescope 4 timing,therefore, had to be tuned with a very low coincidence count-rate.

The delays in the START and STOP signals to the three time to pulse height converters (TPHCs) were adjusted so that the "true" coincidence peak in each of the time distributions occurred near the middle of the 200 ns coincidence window, thus allowing two "random" coincidence peaks on either side of the "true" peak.

The pulsers were adjusted so that pulser coincidences appeared in the coincidence window, and the amplitudes of the pulser signals were set so that there was no interference with the particle event data — in practice this meant ensuring that the pulser peak in each of the ΔE versus E particle identification histograms was well clear of the proton locus.

The delays on the linear signals and the output of the TPHCs were adjusted together with those on the T1, T2, T3 and T4 gate signals derived from the timing electronics so that the LGS gates were opened at the correct time, allowing the linear signals to be passed on to the analogue to digital converters (ADCs).

The delay between the arrival of the event trigger at the input of the event trigger module and the raising of the CAMAC LAM by this module was set to 10 μs as described in subsection 2.6.7.

The widths and delays of the stretched logic inputs to the pattern register (see subsection 2.6.9) were adjusted and monitored on an oscilloscope to ensure that these inputs had settled before the strobe signal input was applied to latch the pattern.

The pulse heights of the amplified linear signals from the photomultiplier tubes mounted on the NaI crystals were adjusted so that a proton of approximately 200 MeV, stopping in a crystal, resulted in the corresponding ADC outputting a digitized value close to 1000.

The pulse heights of the amplified linear signals from the three 30 μm ΔE Si detectors were adjusted by monitoring the corresponding particle identification histograms until a suitable picture was obtained. (The amplifiers on the linear signals from the 1 mm Si detectors had been set up previously during their initial calibration — see above).

Software gates used for event sorting (see subsection 2.7.2) were set on the proton loci of the seven particle identification histograms, and on the "true" and one of the "random" peaks in each of the three time distribution histograms.

A set of runs to obtain energy calibrations of the NaI detectors was performed by setting the telescopes at various angles and acquiring singles (non-coincident) data from the CH_2 target. Again, for geometrical reasons, telescope 4 could not be moved more forward than 70° — the peak from the H(p,p)H scattering was however, still visible in the spectrum at this angle.

From the positions in the spectra of the elastic and a couple of inelastic peaks due to protons scattered from ^{12}C and H, and the kinematics of the reactions, the parameters of the NaI detector energy calibrations were calculated and set in the EVAL analysis program. The parameters for the 1 mm Si detectors, calculated from the initial calibration (see above) were also fed into the program. The calibration constants for the 30 μm detectors were set to zero (the contribution of these to the total energy is small, and was neglected during the on-line data acquisition).

The prescaling on the telescope singles events was set to a reasonable level so as not to swamp data taking — telescopes 1 and 2 prescaling was set to 4×10^2 (that is, 1 in 4×10^2 singles events was accepted), and 3 and 4 prescaling to 1×10^2.

The difference between the direction of the proton beam and the 0° alignment of the scattering chamber (and thus the telescopes) was determined by setting telescope 1 at the 20° position and acquiring singles data from the NaI detector for a fixed integrated beam current. The number of counts in the ^{12}C(p,p) elastic scattering peak in the spectrum was determined. The telescope was swung to the -20° position and a similar spectrum acquired for the same accumulated beam charge. The telescope was then moved by 0.1°, and the process repeated until the position where the integrated counts in the elastic peak equalled the number found at 20°. The beam direction offset was found to be 0.2°, and was taken into account when positioning the telescopes in subsequent data acquisition.

The empty frame was placed in the target position in the proton beam, and the cyclotron operators tuned the beam once more to reduce the halo to the minimum obtainable, in preparation for the acquisition of coincidence data. With a proton beam current of 5 nA the count rate (as measured on a ratemeter) in the NaI detector of telescope 1 was 5×10^1 compared to a count rate of 4×10^3 with the ^{12}C target — that is, a background due to halo striking the target of less than 2%.

Telescope 1 was placed at an angle of -20° relative to the proton beam and the arm on which the other three telescopes were mounted was placed at 70° — the telescope angles, therefore, were 20°, 70° and 120°. The ^{12}C target was placed in the proton beam, and rotated to an angle of 10° so that the target frame divided the angle between telescopes 3 and 4 in approximately equal portions.

Once all the setting-up procedures were completed, tape output was enabled, and subsequently acquired event data buffers were written to magnetic tape.

During the acquisition of coincidence data, a series of checks, described in the following paragraphs, was made to ensure the quality of the data being acquired.

The count rates in the NaI detectors of T1 and T2 were monitored as a rough check of beam quality. If they were observed to increase appreciably with no associated increase in beam current, the run was stopped, the blank frame inserted in the target position and the halo was checked. If required, the beam was retuned to acceptable levels. A halo check was also performed after the periodic accelerator problems (trips of the radio-frequency amplifiers, magnet coil power supplies, etc) which resulted in loss of the beam.

The coincidence time distribution histograms were monitored to ensure that the real to random ratios were kept within acceptable limits — the worst case was, of course, the approximate 2 to 1 ratio of the T1T2 time distribution, where both the telescopes were positioned at angles of 20° relative to the beam, and the individual count rates were very much higher than in the detectors positioned at wider angles. It was this real to random ratio that limited the current that could be tolerated on the target.

The histogram containing the accumulated pattern register contents was monitored to ensure that no (or very few) events with an invalid pattern were being accepted.

The inhibited and non-inhibited scaler pairs were monitored to ensure that the dead time introduced by the computer was not excessive. The electronic dead time was determined from time to time by comparing the scaled pulser inputs to the preamplifiers with the integrated pulser peaks in the various on-line histograms — in the worst case this dead time was approximately 5%.

From time to time the counts in various histograms were integrated and compared to the values in the corresponding scalers, to check consistency and ensure that data were not being lost somewhere.

The leakage current on the Si detectors was monitored at regular intervals, and if necessary, the biases were adjusted to ensure that the detectors remained fully depleted.

Coincidence data at three sets of angles were acquired. In addition to the first set given above, the second set at a primary (T1) angle of -20°, secondary angles of 45°, 95° and 145°, target at -15°, and the third at primary angle of -45°, secondary angles of 35°, 85° and 135°, target at -25°, were taken. The length of time given to the acquisition of each set was a compromise between the need for good data statistics, the number of shifts of 200 MeV proton beam available after cyclotron breakdowns, and the acceptable real to random ratio in the coincidence data. As the telescope angles increased, so the beam current which met the latter requirement also increased — for the second set a current of approximately 15 nA was found to be acceptable, while for the third set the current was increased to approximately 40 nA.

After the completion of the coincident data acquisition, the scattering chamber was opened, and the alignment of the detectors, etc. was rechecked, together with the geometrical measurements (target to detector distances, hard collimator thicknesses, etc.). Energy calibration measurements of the Si detectors were repeated as described above (this time calibrations of the 30 μm Si detectors as well as the 1 mm detectors were performed).

2.8.2 Singles experiments

Two separate sets of "singles" data (that is, inclusive ^{12}C(p,p$'$) measurements) were acquired on two different occasions, one at a proton energy of 90 MeV and the other at 120 MeV, to obtain the data required for the analysis of the continuum decay data of the coincident experiment.

On both occasions two independent particle telescopes were mounted on the two arms of the scattering chamber. Two sets of hard collimators, suitable for stopping 90 and 120 MeV protons respectively were used in these experiments. Active collimation was employed in the telescope which took the data at the most forward angles.

During the 120 MeV singles experiment, an LED-driving pulser, constructed by the laboratory's electronics staff, was available to drive the LEDs embedded in the crystals of the NaI detectors. These pulsers were then used to drive the LEDs for gain stabilization purposes, instead of the BNC tail pulse generators (see subsection 2.6.5) which had been used previously to drive the TEST inputs of the preamplifiers on the signals from the NaI detectors.

A similar experimental procedure as for the coincident experiment was employed, the most important differences being in the need to keep a more stringent check on the quality of the proton beam, particularly in the forward angle measurements, and the absence of telescope-telescope coincidences (and thus no real to random ratio limitation on the beam current).

Although event acquisition rates tended to be high during the singles experiments (of the order of a few kilohertz), the raw event buffers were capable of being written to tape without the introduction of further deadtime. This enabled the raw data to be replayed off-line during analysis, and thus allowed for tighter control of detector drifts, particle identification gates, etc.

The telescope angles were varied in steps of 5° from 10° to 100° with respect to the proton beam, and in steps of 10° from 100° to 160°.

The beam current was limited by the need to reduce gain drifts in the detectors, and to keep the electronic dead time negligible. The current was varied from about 1.5 nA at the most forward angles to approximately 8 nA at the backward angles.

At the most forward angles (10° to 20°), data were acquired with an empty frame before or after each run with the ^{12}C target to allow for subtraction of background due to halo-induced events in the target frame. Beyond 20° this background was negligible, and a simple check on the NaI detector count rate with the empty frame was made periodically to ensure that the proton beam had not drifted and required retuning. At the most forward angles each run was of the order of ten minutes duration, increasing to an hour at the more backward angles. At the extreme backward angles the measuring telescope was left at one angle for a number of runs while the other telescope measured a series of more forward angles.

Chapter 3

Data Analysis

3.1 Overview

The previous chapter described the gathering of the data in the coincidence and singles experiments. In the current chapter the methods employed in the subsequent replay and analysis of the event tapes are described. The results of the analysis, and their interpretation, are presented in detail in the following chapter.

The event data were successfully recovered from the magnetic tapes after problems were encountered in reading the data. XSYS event analysis (EVAL) routines were written to sort the data and generate the required energy spectra. Standard techniques were employed for charged-particle identification, the definition of sorting gates, detector calibrations and non-linear response corrections, and a number of data consistency checks were performed.

The data for determining the required cross sections were extracted from the sorted data histograms, and the necessary background subtractions, and corrections for reactions in the NaI(Tl) crystals, electronic dead time, effective target thickness, etc., were made in calculating the cross sections. The statistical errors were propagated throughout these calculations, and the systematic errors in the experiment and subsequent calculations of the cross sections were estimated.

Finally, the necessary DWIA calculations were performed for comparison with the measured (p,2p) cross sections, and for folding into the proposed model for predicting the observed continuum proton yield. A computer program was written to calculate the predicted continuum spectra according to this model, using as input the results of these DWIA calculations and the measured inclusive (p,p′) inelastic cross sections.

3.2 Replay

3.2.1 Data recovery

During the coincidence experiment, and after more than half the data had been acquired, an attempt was made to copy the filled event tapes for security purposes. Problems immediately arose due to hardware errors in reading the tapes (the drive on which the data had been written, and also similar and completely different drives from another manufacturer all exhibited similar read errors).

The magnetic tapes produced by the XSYS data acquisition system are the VAX/VMS version of "standard" ANSI-labelled format tapes. Most of the errors were found to occur in the (three) file header and (three) trailer records, which are written before and after a file's data records respectively. This indicated that the problem was probably caused by some timing error during the tape acceleration or deceleration phase, since these file-structuring records are written in quick succession. The data records, on the other hand, were written at much less frequent intervals due to the low data rate, the tape always coming to a rest between the writing of data records. This appeared to be confirmed by one of the files on the tape where some of the coincidence gating had been turned off — this was done between runs to check electronics and the experimenter had forgotton to restore the gating. This run which was acquired at a much higher data rate — with the tape probably not coming to rest between the writing of many of the data records — exhibited many errors in the data records. When the electronics staff examined the tape drive, however, no problem could be traced, the acceleration and deceleration timing, in particular, being found to be well within specifications. Subsequently, this drive has not exhibited a similar problem — during the remainder of the coincidence experiment, the data were written to tapes on a different drive. This experience has been added to the continuously-growing mythology that surrounds the recording and retrieving of precious data from magnetic tape at the lab.

The file-structuring records that were unreadable presented serious problems to the magnetic tape ACP (anciliary control process — that part of the VAX/VMS operating system that handles magnetic tape file structuring). In particular, if one of the header blocks was faulty, the data in the file could not be read with the normal XSYS file-oriented input/output calls.

In an attempt to recover these data in a form readable by XSYS, the current author wrote a computer program which reads a tape record by record and attempts to reconstruct the records which are found to be in error. It was written to operate in an interactive manner so that when an error is encountered the user is asked how to proceed. The program has knowledge of the format of a file-structured tape, and will present the user with a subset of options depending on where in the file a particular error is encountered — if necessary, the program will itself generate the expected header or trailer record from information it has extracted from previous header and trailer records. With the aid of this program, all the damaged files were recovered from the event tapes, and in all, approximately twenty data records had to be discarded from a total of more than seventy thousand records.

3.2.2 Software

The same XSYS software package was used for event data replay as that used during data gathering, and described in subsection 2.7.2. In the replay mode of operation, where input comes from tape and there is no data acquisition program (DAP) file, the sorting subprocess is controlled by the TPEVOP XSYS command (as opposed to the EVOP command described previously for use during data acquisition). As before, the event analysis language (EVAL) file is required to specify the required sorting to be performed.

The first EVAL file used during replay simply extracted the singles data from each of the detector telescopes and incremented the corresponding pulse-height histograms. This enabled the drifts in the NaI-phototube detector assemblies to be tracked during and between runs, and the necessary corrections to be applied to the succeeding analysis scans.

The second replay file sorted the data into a set of 2-dimensional histograms in which the one dimension corresponded to the total summed energy of the detected reaction products, and the second to the energy of the protons detected in telescope 1. To determine the total energy (assuming that all the data arose from 3-body events — 4- and more-body breakup events were not taken into account), the energy of the recoiling (undetected) nucleus was calculated from the measured energies of the two (detected) coincident protons, and the known parameters of the reaction (angles, masses and incident proton energy). The recoil energy was calculated in a FORTRAN relativistic three-body kinematics subroutine which was linked into the EVAL code as described previously.

The third replay EVAL file was very similar to the one used during data acquisition, and described in detail in subsection 2.7.2. The only addition was in allowing more than one gate on the "random" coincidence peaks in the time distribution histograms, in order to have a more accurate estimation of the average random coincidence background to be subtracted from the "true" coincident data. Additions were also made to correct for the non-linear responses and the gain drifts observed in the NaI detectors.

The singles experiments replay EVAL files were also very similar to those used during data acquisition, with suitable corrections being made to the energies detected in the NaI detectors to account for the non-linear responses and gain drifts.

3.3 Particle Identification

Conventional ΔE-E techniques were employed to separate the types of charged particles detected in the four particle telescopes. As described in section 2.5, the 2-element telescope 1 had a single ΔE-E pair, while the other three telescopes each had two ΔE-E pairs, the second being used for the identification of low energy charged particles. For each pair combination a 64×64 histogram was defined, and the EVAL sorting code incremented one of these histograms for each particle detected, depending on the event information stored in the pattern register (specifying which telescopes fired and whether it was a "low" energy event or not).

Two example ΔE-E histograms resulting from a set of coincidence experiment runs are shown in figure 3.1. One histogram is data taken from a telescope positioned at a forward primary angle where the yield of high energy protons and deuterons dominates, and the loci produced by these particles in the histogram are very pronounced. The second histogram is from the two Si detectors of a triple-element telescope at a much larger secondary angle where the energy and relative yield of protons and deuterons with respect to other particle types has dropped off dramatically, and the loci from the tritons, ^{3}He particles and alphas can be clearly seen.

The XSYS software allows the setting of 2-dimensional gates of arbitrary shape which are stored in one bit 2-dimensional arrays, the only restriction being that the gate array must be of the same x and y dimensions as the histogram on which it is to be placed. During replay such a gate was defined for each of the ΔE-E histograms, and after an initial scan of a set of data to

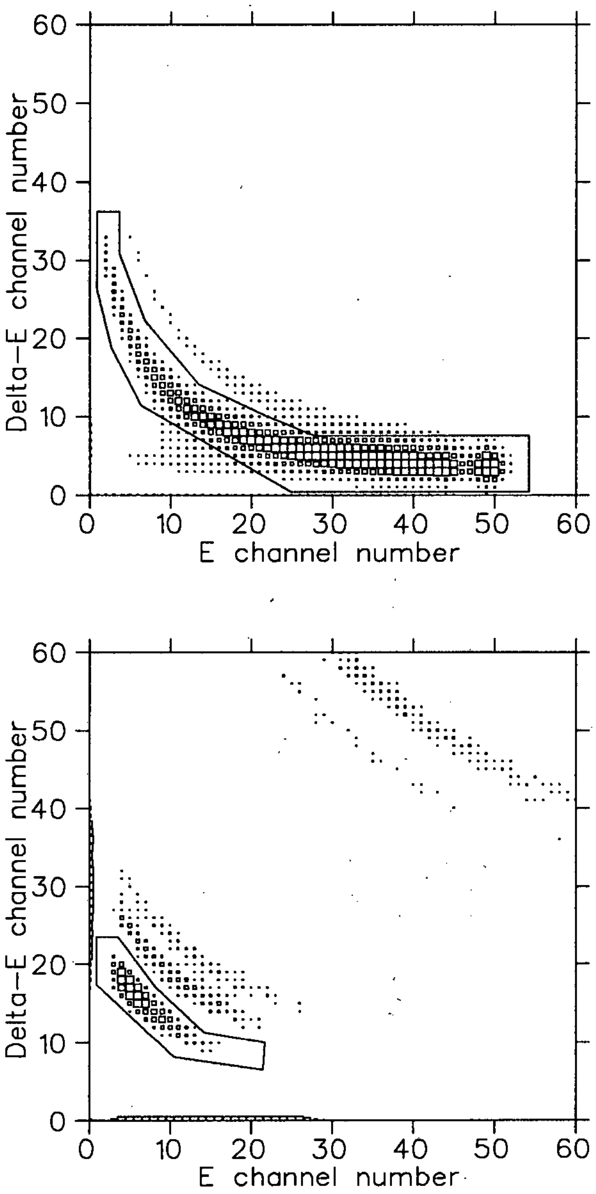

Figure 3.1: *Sample particle identification density plots (the size of the boxes being proportional to counts), from telescopes positioned at 20° (above) and 95° (below). Examples of 2-dimensional proton gates set on these data are also illustrated.*

allow sufficient counts to be accumulated in the histograms, each gate was set on the proton locus in the corresponding histogram. This was achieved with the aid of a subcommand of the XSYS DISPLAY command which allows a spectrum to be displayed, and a gate to be set on the displayed spectrum by defining the vertices of a closed polygon with the aid of the display terminal's hardware-generated cursor.

Such a gate set on the proton locus is also shown on each of the two particle-identification histograms illustrated in figure 3.1. These gates are accessible to the EVAL sorting code, and were used in subsequent replaying to identify protons.

3.4 Energy Calibrations

3.4.1 Si detectors

Energy calibrations of the Si detectors were made with the aid of collimated ^{228}Th α-particle sources as described in section 2.8.

^{228}Th sources emit α-particles at a number of discrete energies ranging from 5.34 to 8.78 MeV. These are all stopped within the volume of the 1 mm Si detectors, but those at the higher energies punch through the 30 μm detectors.

Figure 3.2 shows a ^{228}Th pulse-height spectrum obtained from one of the 1 mm Si detectors, together with a plot of the corresponding energy calibration curve derived from this spectrum. The calibration points shown at the lower energies on the curve were obtained from a pulse-height spectrum of α-particles which had punched through one of the 30 μm detectors placed between the ^{228}Th source and the 1 mm detector — the energies lost by the α-particles were calculated [Jip84] using the manufacturer-measured thickness of the 30 μm detector. The curve is a least-squares linear fit to

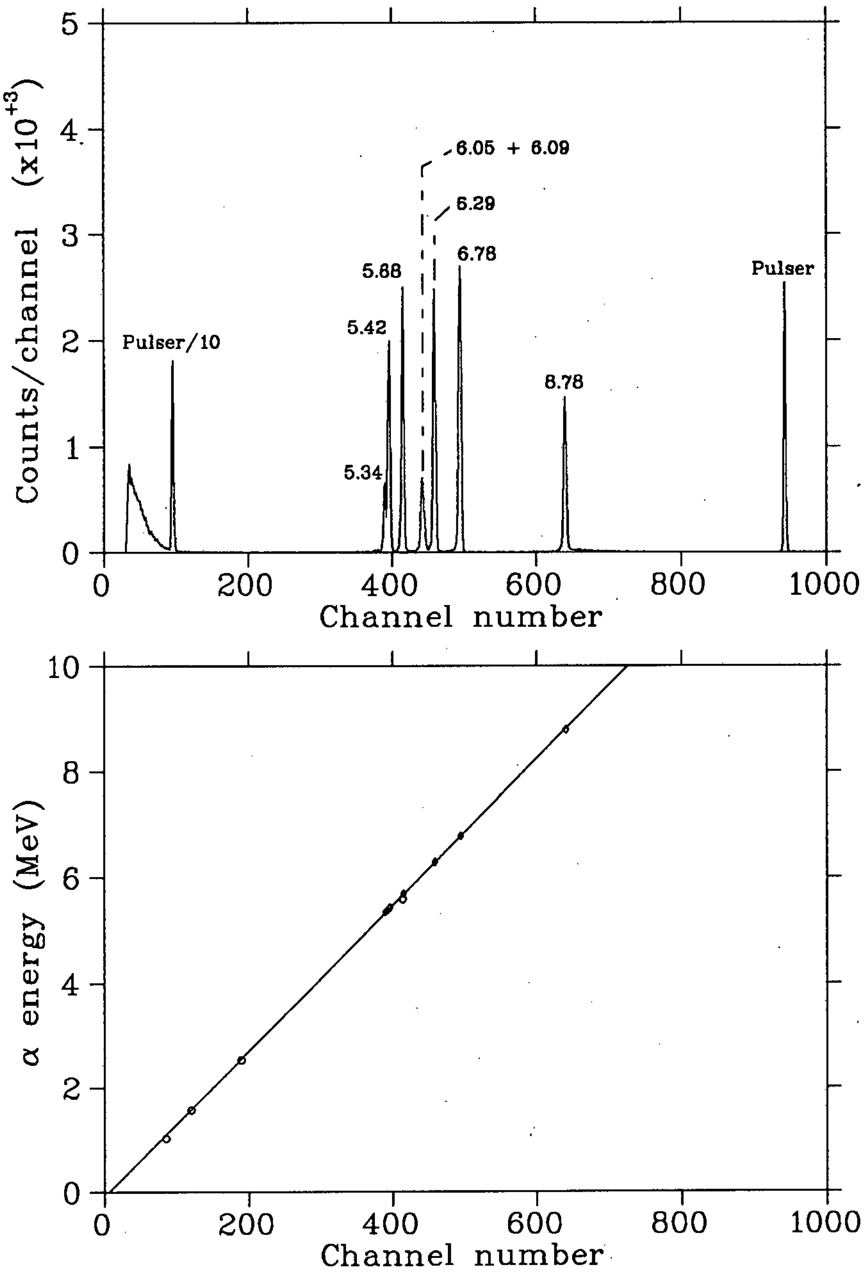

Figure 3.2: *Sample 1 mm Si detector calibration, showing the pulse-height spectrum from a* ^{228}Th α *source (above), and the energy calibration curve derived from this spectrum (below).*

the calibration points (without using the ADC zero intercept as one of the points — all the 1 mm detector calibration curves cross the energy axis within 100 keV of the zero intercept).

Figure 3.3 shows a ^{228}Th pulse-height spectrum obtained from one of the 30 μm Si detectors, together with the corresponding energy calibration curve derived from this spectrum. Each peak in the spectrum is labelled with the energy deposited in the detector volume by an α-particle emitted from ^{228}Th with energy specified in the parentheses. The calibration curve is a linear least-squares fit, similar to that for the 1 mm detector calibrations. The measured energy resolutions of the 30 μm detectors are degraded due to variations and uncertainties in the detector thicknesses, uncertainties in the energy-loss calculations, and the divergence of the α-particles from the collimated source.

The measured energy resolution and fitted linear calibration parameters for all the Si detectors used in the coincidence measurements are listed in table 3.1 — for the energy resolution of the 1 mm detectors, the FWHM (full width at half the maximum peak height) of the peak due to the 6.78 MeV α-particle is listed; for the 30 μm detectors, the FWHM of the peak due to the energy deposited by the 8.78 MeV α-particle (approximately 3.5 MeV, depending on actual thickness) is listed.

3.4.2 NaI(Tl) detectors

Sets of NaI detector calibration runs were acquired during the experiments, with a CH_2 target and the telescopes positioned at various angles, as described in section 2.8. Because of geometrical constraints on the positioning of the rotating arms on which the telescopes were mounted, the number of angles at which calibration points could be acquired was limited. In most cases, only a few points at the higher energies obtained from peaks due

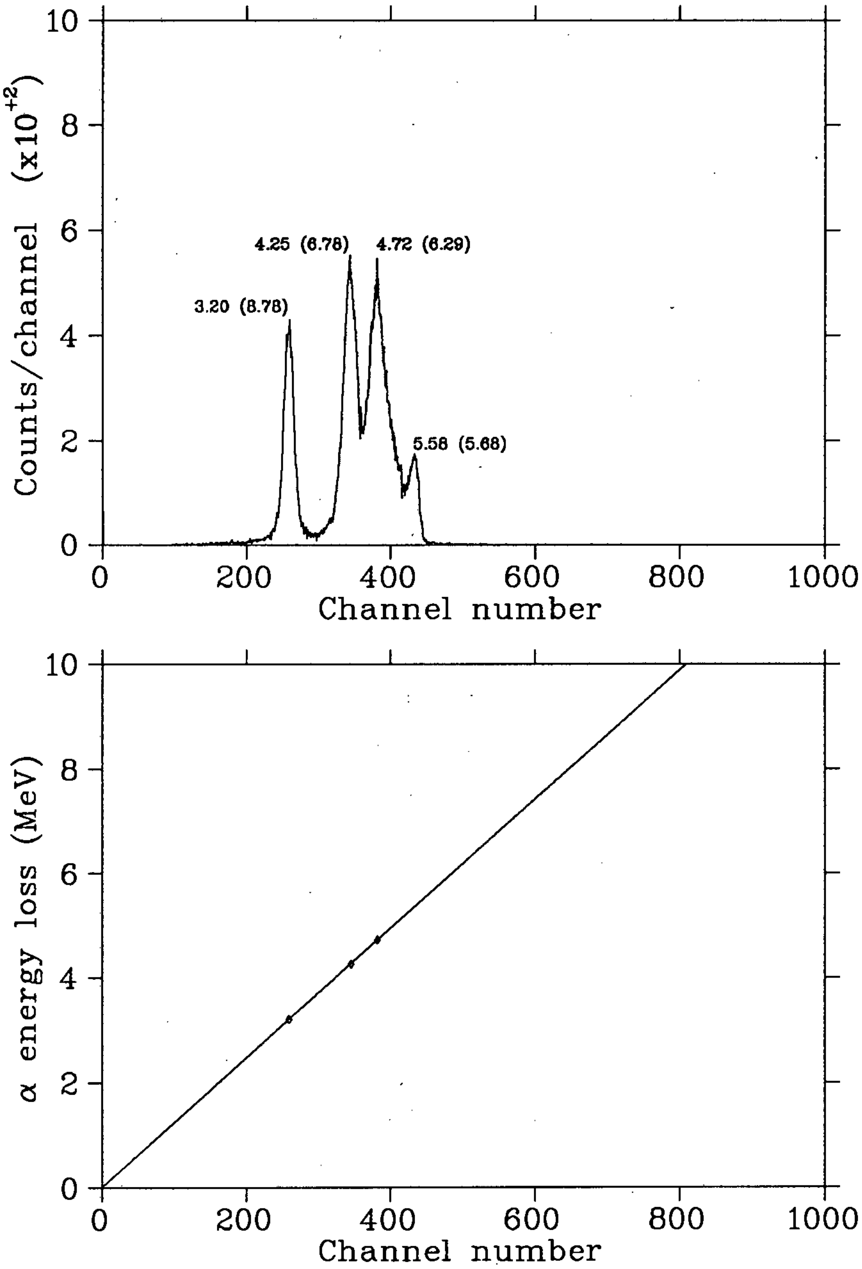

Figure 3.3: *Sample 30 μm Si detector calibration, showing the pulse-height spectrum from a* ^{228}*Th α source (above), and the energy calibration curve derived from this spectrum (below). Peaks are labelled with the energies (in MeV) deposited in the detector volume by α-particles emitted from the source with the energies in parentheses*

	6.78 MeV α	Linear Calibration (keV)	
Detector	FWHM (keV)	Slope (keV/bin)	Intercept (keV)
T1B	61.7	13.89	-23.0
T2B	59.3	13.89	-91.0
T3B	48.7	13.75	-105.0
T4B	50.2	13.25	109.0
	~3.5 MeV α		
T2A	230.8	3.80	4.0
T3A	276.4	3.73	-41.0
T4A	210.7	2.96	45.0

Table 3.1: *Si detector energy calibration parameters*

to elastic and inelastic scattering of the incident protons from ^{12}C and H were available for the calibrations. As the ADC zero intercept adjustment (see section 2.8) had been carefully performed as part of the set-up procedure, this point was also used in the calibration — the validity of including the zero point in the calibration set was confirmed when tracking drifts in the detectors (as explained below). Linear (quadratic in the case of the 120 MeV singles experiment) least-squares fits were made to the calibration points of each detector.

A NaI detector exhibits two major problems when used in a charged particle counter telescope. Firstly, the pulse-height response as a function of charged particle energy is non-linear (cf. [Dav87]), and secondly, the gain of the photomultiplier tube changes with time in an unpredictable manner (it may drift slowly in one direction, exhibit sudden relatively large changes, and change the direction of drift). This drift in gain is associated with detector count rate (in the current experiments it was observed in those detectors counting at a rate close to 10^4), and is presumably due to physical changes in the dynode surfaces caused by the relatively large currents passing down the phototube. The best solution to overcoming the problem of drift is to make use of a reference light source embedded in the NaI crystal. Although such a source in the form of a LED was provided in the detectors used in the experiments, the suitable hardware for driving these was not available for the coincidence and 90 MeV singles experiments, and was only used in the 120 MeV singles experiment after the hardware had become available. With such a reference source, the calibration may be performed, and any subsequent gain drifts (assumed to be linear) may be corrected by tracking the relative drift of the reference peak from its calibration position.

The non-linearity in the response of the detectors to charged particles requires a set of calibration points scanning the full energy region of interest. This was only possible in the singles experiments where each detector could be swung through a wide range of angles and reaction kinematics resulted in a suitable set of energies spanning the region of interest. However, since the detector count rates also change dramatically as a function of angle, the resulting gain shifts cannot be accounted for unless a reference peak is available in the pulse-height spectrum — attempting to keep the count rate constant by changing the beam current proves too tedious, and still does not eliminate drifts entirely. The non-linear response could therefore, not be accounted for in the 90 MeV singles experiment.

To correct for detector gain drifts in the coincidence and 90 Mev singles experiments, each individual run was sorted by an EVAL program which simply generated the pulse-height spectrum from all events in each of the NaI detectors. The centroids of peaks, resulting from proton elastic and inelastic scattering from H (the carbon targets are contaminated with a small amount of hydrogen) and ^{12}C, were determined for each run — at large angles (greater than approximately 70°) the yields in any of the peaks in a single run were too small to perform a centroid determination, but at these angles the count rates in the detectors were so low that gain drift was minimal. From these peaks the energy calibrations for each run were normalized to those of the calibration runs. Two linear least-squares fits to the peak centroid positions of each run were made, the first including, and the second excluding, the zero intercept point. It was found that only when the zero point was included did the parameters of the fitted calibration lines drift in a consistent manner. Without the zero point, the fit had to be performed on very few closely-grouped points at higher energies which resulted in the zero intercept varying from one run to the next in an unreasonable manner.

Figure 3.4 shows a pulse-height spectrum due to all the events occurring in a NaI detector during a coincidence experiment run, together with the linear least-squares fit to the indicated peak centroids and the zero intercept point.

For the 120 MeV singles experiment the centroid of the reference peak due to the pulsed LED light source was determined for each run, and the calibration parameters normalized to those obtained for a calibration run. The quadratic least-squares fitted curve to the calibration points for this experiment is shown in figure 3.5. Also illustrated in this figure is a linear fit to the upper calibration points and the zero intercept, demonstrating the effect of the non-linear NaI detector response to protons as a function of energy.

To make allowance for the non-linear detector response in the coincidence experiment, the event data were sorted with an EVAL program which calculated the "total" energy of the reaction products — that is, the sum of the two measured proton energies and the calculated recoil nucleus energy

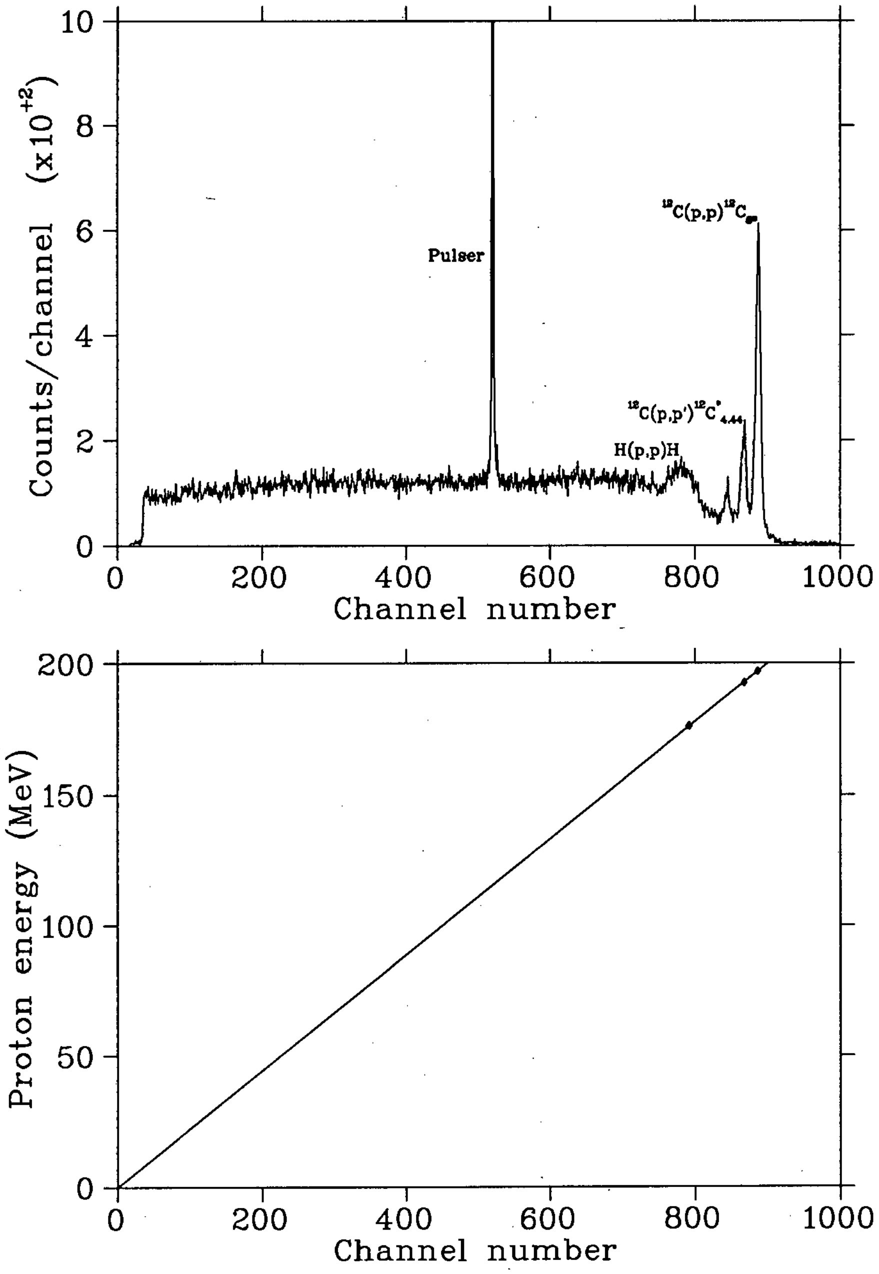

Figure 3.4: *Sample NaI(Tl) detector calibration, showing the pulse-height spectrum due to all detector events acquired during a single coincident experiment run (above), and the energy calibration curve derived from this spectrum (below).*

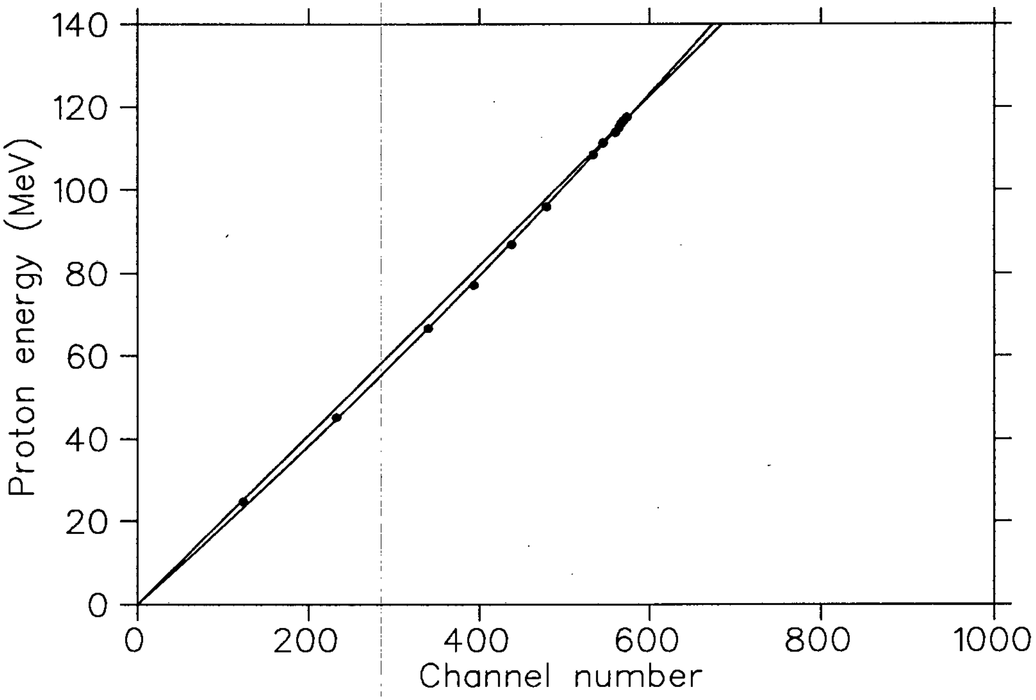

Figure 3.5: *Energy calibration of a NaI(Tl) detector used in the 120 MeV singles experiment. The curve is a quadratic least-squares fit to the measured calibration data points. Also shown is a linear least-squares fit to the data points at the higher energies and the zero point, illustrating the effect of the NaI(Tl) non-linear response.*

(see section 3.2). A density plot which shows this "total" energy as a function of the energy of one of the measured protons for one coincidence pair of angles is shown in the top illustration of figure 3.6. The pronounced locus at the top of this plot is due to the knockout of p-state protons from ^{12}C. This locus should be parallel to the x-axis and at a y-axis value of 200 Mev (the incident proton energy) less the binding energy of a p-state proton (approximately 16 MeV). The curved nature of this locus is due primarily to the non-linearities of the two NaI detector responses, which result in an over-estimation of the proton energies in each detector by about 4 MeV in the worst case (close to 100 MeV). In order to make an allowance for this it was assumed that the non-linearity was symmetric about the worst case point and equal contributions were made by the two detectors. A quadratic least-squares fit was made to the points lying along the centre of this locus for each set of coincidence angle pair data. From the parameters obtained, a suitable correction was made to the NaI detector energy calculations in the EVAL program, and the same data re-analysed. The results of this corrected sorting scan are illustrated in the lower plot of figure 3.6. A similar correction could not be made to the energy calibrations for the 90 MeV singles experiment, as the inclusive data do not have all the event information required to determine the total energy of the reaction products.

3.5 Energy Spectra

The energies deposited by particles in the telescopes were calculated in the EVAL code of the XSYS sorting subprocess. From the calibration and detector response parameters the program determined the particle energy by summing the energy deposited in each detector element of the particular telescope. A sample of a resulting proton energy spectrum from one of the

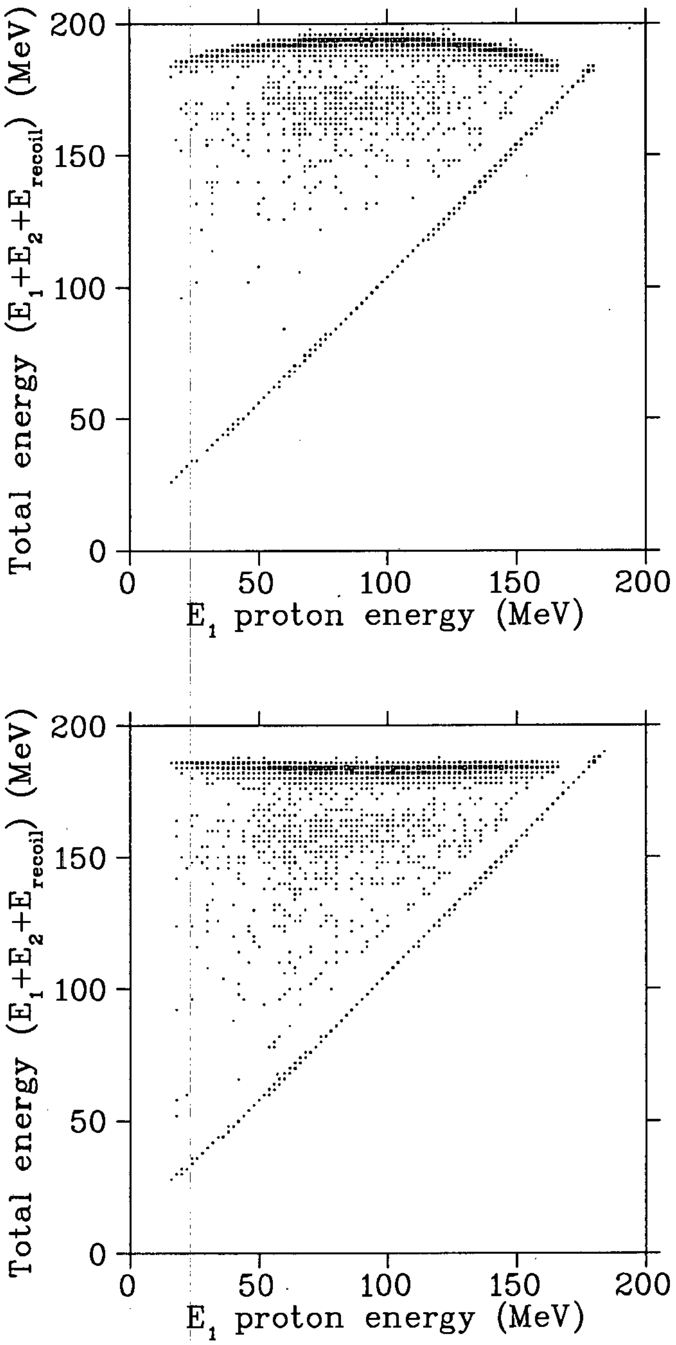

Figure 3.6: *Density plots of summed reaction product energy versus* E_1 *without corrections for NaI(Tl) non-linear response (above), and with corrections (below) — details in the text.*

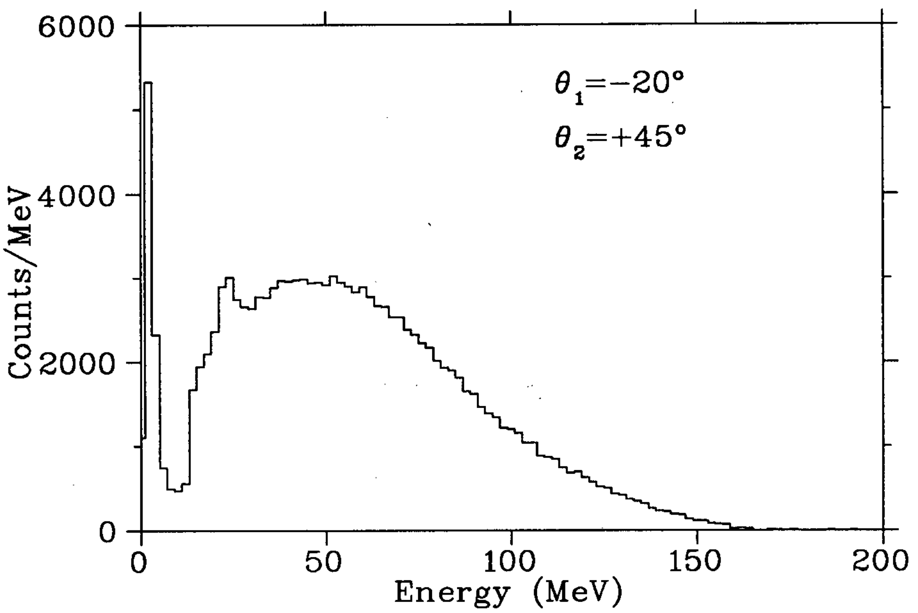

Figure 3.7: *Energy spectrum of protons detected in a 3-element particle telescope during the coincidence experiment.*

3-element telescopes positioned at one of the secondary angles during the coincidence experiment is shown in figure 3.7.

The very narrow peak at low energies (2–6 MeV) is the "evaporation peak" due to events in which the incident energy is dissipated amongst most of the nucleons in the target followed by statistical evaporation of protons from the excited nucleus. As expected for the lighter (that is, low A and Z) ^{12}C nucleus, this peak is less pronounced than in the case of the ^{58}Ni experiments [Cow80b] [Cia83].

The trough in the spectrum centred close to 10 MeV, between the evaporation peak and the low-energy region of the continuum, is accentuated in the current experiment due to electronic effects. This trough coincides with the energy at which protons began to punch through the second Si detector. However, the output pulse generated by these protons in the NaI was too small to cross the electronic thresholds in the discriminators. Events therefore which should have appeared in the region of the trough are thrown to slightly lower energies due to this undetected energy. No attempt was made to correct for this and calculate the true energies of these particles in the program, however, as the magnitude of the evaporation peak was similar to that expected, and as this region of the proton energy spectrum lies well outside the continuum region of interest. The evaporation region of the energy spectra was disregarded in the further analysis.

3.6 Coincidence Time Distributions

The time distribution information of coincidences between each of the three telescope pairs in the coincidence experiment was generated by the time-to-pulse height converter modules (see section 2.6), digitized and formed part of the data set recorded for each event. During analysis the EVAL sorting program incremented one of the three time distribution histograms depending on which of the coincidence telescope pairs had fired.

Two examples of the time distribution histograms are shown in figure 3.8. One is from a coincidence between the "primary" telescope, positioned at an angle of -20°, and a "secondary" telescope at 20°; the other is from a coincidence with the same primary angle and a secondary angle of 145°. The window on the coincidence time gating was set to approximately 200 ns (see subsection 2.6.6), thus allowing the acquisition of events resulting from a coincidence between a particle detected in the primary telescope and a particle in a secondary telescope originating from one of five successive beam packets. The timing electronics was tuned so that those events resulting from the coincidence between particles originating from the same beam packet fell close to the middle of the coincidence window.

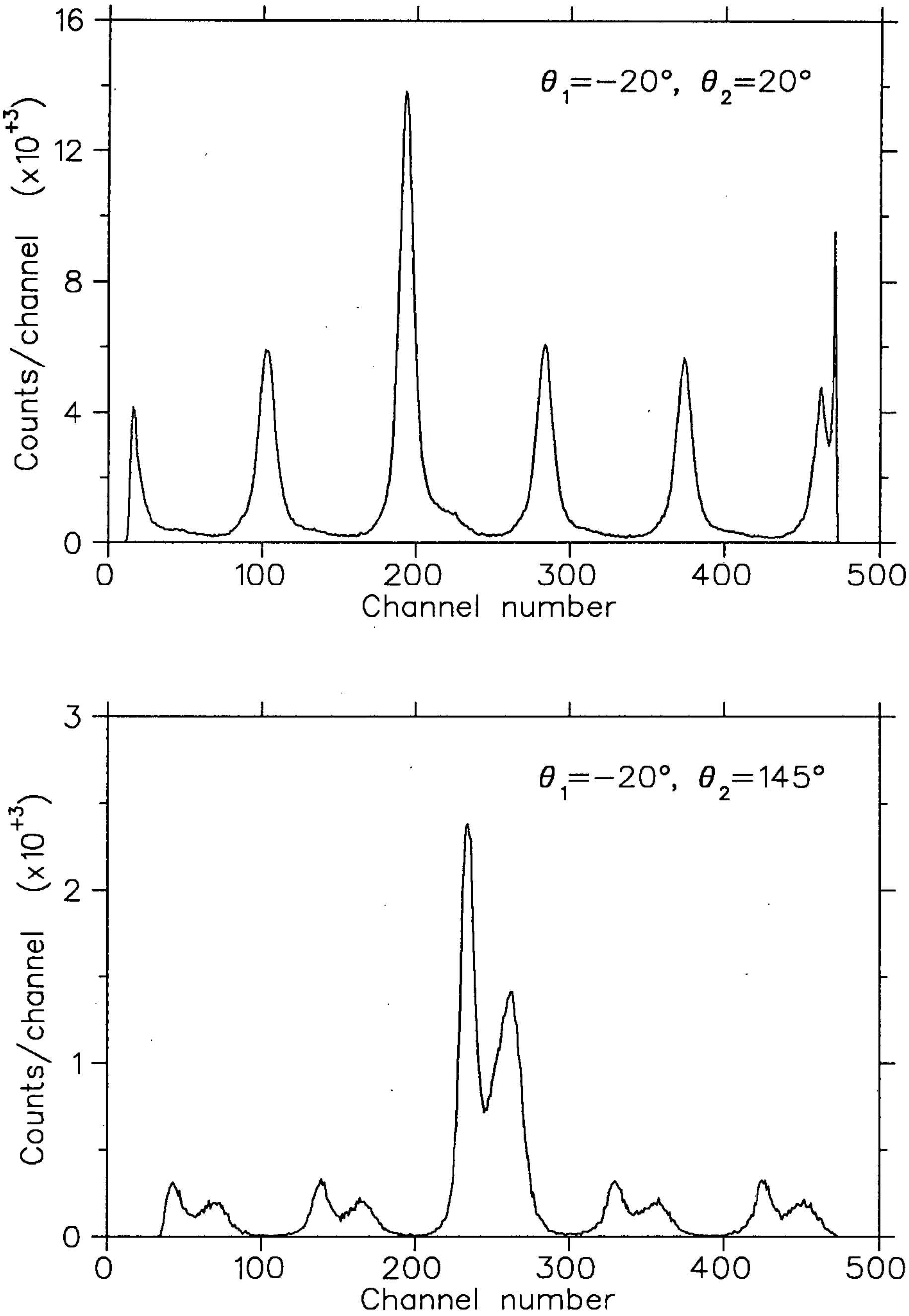

Figure 3.8: *Sample coincidence time distributions, from telescopes positioned at -20°,20° (above), and at -20°,145° (below).*

These events give rise to the larger peak in the histograms of figure 3.8. The smaller peaks are caused by "random" coincidences due to particles originating from events in different beam packets. The larger "true" coincidence peak, in addition to coincidences from particles originating in the same event in a beam packet ("true" events), also contains events due to coincidences from particles originating from different events in the same beam packet ("random events").

In the plot of the histogram from coincidences at a large secondary angle where the yield of protons and deuterons relative to the heavier particles has fallen dramatically, structure is seen in each of the peaks due to the average time-of-flight differences between the lighter and heavier mass particles.

An estimate of the random events falling within a true coincidence peak in the time distribution has to be made. This can only be done by measuring the number of events falling within neighbouring random peaks, and for this estimate to be accurate, there should be as little modulation of the number of protons in successive beam packets from the accelerator as possible. In the present experiment this microstructure in the accelerator beam was minimal, as can be seen from the similar sizes of the random peaks in the time distribution (integrated counts in the "random" peaks of the coincidence histograms in each of the nine sets of coincidence angle pairs were found to differ by less than 5% in all cases), and the necessary subtractions could be made with confidence.

For each time distribution, three 1-dimensional gates were defined, and before the full analysis sorting program was run, these gates were set on the histograms sorted by a set-up event scan — one on the "true peak", and the other two on the "random" peaks on either side of it. In all the runs, the peaks were well-separated (as illustrated in figure 3.8) and the gates could be easily set.

3.7 Pattern Register

During the scanning of the event data a histogram was defined for the pattern register, and for each event the contents of the pattern register were used to address this histogram, and the corresponding channel was incremented.

At the termination of the scan, this pattern register histogram was examined for consistency. In particular, the occurrence of event types which should not have been accepted (for example, $T1 \cap T2 \cap T3LO$) was checked. It was found that the only events of an unacceptable type that were acquired were cases similar to this example — where there appeared to be a coincidence between two of the high count rate telescopes, and a third telescope indicated a low energy event ($\langle A \rangle \cap \langle B \rangle \cap \langle \overline{C} \rangle$) without the associated event bit in this telescope being set ($(\langle A \rangle \cup \langle C \rangle) \cap \langle B \rangle$). However, as even in the worst case events of this type amounted to less than 0.04% of the number of corresponding acceptable events ($T1 \cap T2$ in the example quoted above), these were disregarded.

3.8 Event Tape Sorting

3.8.1 Coincidence experiment

Initial scans of samples of the event data were performed as described in the preceeding sections of this chapter to determine the 2-dimensional proton identification gates on the detectors' ΔE-E histograms, the 1-dimensional gates on the "true" and "random" peaks in the time distribution histograms, the detectors' energy calibration parameters for each run, and to check for abnormal event patterns in the data.

Once these gates and parameters had been determined a command procedure file was set up for each of the three sets of angle settings to automate the sorting of the data by the main EVAL analysis programs. The event data were scanned twice, the primary object of the first sorting program being to generate, for each pair of coincidence angles, the 2-dimensional spectra of "total" energy ($E_T \equiv$ sum of the energies of the two detected protons and the calculated recoil residual nucleus) versus the energy of the proton detected in the telescope at the primary angle (E_1 — the energies of the protons detected at the primary and secondary angles are referred to as E_1 and E_2 respectively). The object of the second sorting program was to generate the 2-dimensional coincidence proton energy spectra (E_1 versus E_2). In both cases, two spectra were defined for each angle pair, one to contain sorted event data which fell in the gate set on the "true" peak in the corresponding coincident time distribution spectrum, and the other that which fell in the gates set on the "random" peaks. These 2-dimensional spectra were defined as 128 × 128 channel arrays, the sorting programs analysing the event data so that the widths of the channels on both axes corresponded to 2 MeV.

3.8.2 Singles experiments

The sorting of the event data proceeded in a similar manner to that for the coincident experiment. After the initial scans of samples of the event data had been performed to determine the 2-dimensional proton identification gates on the detectors' ΔE-E histograms, and the detectors' energy calibration parameters for each run, command procedure files were set up to automate the final sorting of the data. The primary object of the sorting programs was to generate the proton singles (inclusive) energy spectra for each angle setting of the detectors. 1-dimensional histograms were defined to contain these spectra, the sorting programs analysing the event data so that the widths of the channels corresponded to 0.1 MeV.

3.9 Corrections

3.9.1 NaI(Tl) crystal reactions

The efficiency of NaI(Tl) detectors in charged-particle counter telescopes is degraded due to undetected energy losses which occur when an incoming charged particle undergoes nuclear reactions in the crystal. Contributions to this loss may result from a negative reaction Q-value, production of neutral particles (neutrons and photons) which escape from the crystal without undergoing further reactions, production of charged particles which have different energy-loss response functions in the crystal, and out-scattering of particles from the crystal before they are stopped in the crystal volume. Out-scattering is an effect which only contributes to a decrease in detector efficiency close to the edges of the crystal. In the current experiments, where collimation resulted in charged particles from the target entering a small cross-sectional area (3.4% of the total cross-sectional area) at the centre of the NaI crystals, this effect is very small [Cam77].

When a monoenergetic beam of protons (in the energy range from a few tens to a few hundreds MeV) is stopped in a NaI detector the resulting spectrum has a full-energy peak with a FWHM resolution which is typically 2% or less. Due to energy losses described above, the number of counts in this peak is not equal to the number of incident protons entering the front face of the crystal, the fraction lost from the peak being distributed over the lower energy bins of the spectrum. The ratio of the number of protons found in this low energy tail to the number in the full-energy peak has been calculated and measured by a number of workers (for example, [Mea69b] [Pal69] [Cam77] [Gou78]), and varies from 1.4% at 30 MeV incident proton energy to 34.0% at 200 MeV [Mea69a].

When the beam of protons stopped in the detector is not monoenergetic, the picture becomes more complicated. In this case, the energy spectrum may be considered to consist of a series of full-energy peaks (the width being determined by the binning width), each of which has an associated tail. It is usual to make a correction (increase) to the bin of highest energy due to losses to its associated tail. The bins at a lower energy are then corrected (reduced) for this tail. The process is repeated for each preceeding bin (adjacent bin at a lower energy) until the whole spectrum has been corrected.

A program was written by the author to perform the calculations for these corrections on the proton energy spectra extracted from the analysed data in the current experiments. The energy spectra were binned with a channel width of 1 or 2 MeV (that is, of the order of the detector resolution). Because of the form of the gates set on the proton loci in the ΔE-E particle identification histograms, the tail associated with each full-energy bin does not extend all the way down to zero energy, but is truncated by this particle identification gate, the energy width of which varies for each particular energy (typically it is narrow at lower energies and increases in width towards the higher energies — for the coincidence experiment, this gate width varied from approximately 10 MeV to 100 MeV). This varying width was accounted for in the program.

Following Green *et al.* [Gre83], who fitted previously measured and calculated tail-to-peak ratios as a function of incident proton energy (for protons stopped in NaI in the energy range of interest in the present study), the ratios were calculated according to the formula

$$f(E) = \left(\frac{E}{354}\right)^{1.8}$$

where E is the full kinetic energy of the proton in MeV. Green *et al.* assumed two different shapes for the reaction tail. Initially, the tail contribution was assumed to be constant from zero proton energy up to the energy of the lower edge of the peak. They later found a better fit assuming that the tail contribution increased linearly from zero at zero proton energy to a maximum at the lower edge of the peak. This latter assumption was used in the present calculations.

From the calculated ratio appropriate to the bin energy, the program determines the number of counts to be added to the maximum energy bin in a spectrum due to losses to the tail. The number of counts in the tail which contributes to the total in the next lower energy bin is then calculated and subtracted from this bin's total. This process of subtracting tail contributions due to the maximum energy bin is repeated until the lower edge of the gate region appropriate to this energy (or the zero energy bin) is reached. The whole procedure is then carried out for the bin below the maximum, and so on until the zero energy bin is reached.

Energy losses due to the few reactions in the thin Si semiconductor detectors were neglected.

3.9.2 Electronic dead time

Corrections for electronic dead time were made by considering the pulser events which occurred in the data. During acquisition the pulser triggers were scaled in one of the inhibited scalers (see subsection 2.6.10). For each run (or set of runs) at a particular angular setting of the detector telescopes, the number of counts occuring in the pulser peak appearing in each of the ΔE versus E histograms was determined — the electronics had been tuned so that this peak appeared well away from the charged-particle loci in these histograms. These measured integrated counts were compared with the scaler value to determine the electronic dead time in each of the telescopes.

In the coincidence experiment, where the count rates in the telescopes at the most forward angles determined the maximum beam current that could be tolerated while still achieving an acceptable real-to-random event ratio, the electronic dead time was approximately 4%. The dead time dropped off to approximately 0.4% in the telescope positioned 100° further away from the beam direction.

In the singles experiments the count rates in the individual telescopes determined the acceptable beam current on target. In order to reduce the gain drifts in the NaI detectors, a beam current was employed which limited the count rates to a conservative maximum of 2×10^3, which resulted in an electronic dead time which never exceeded 0.4%.

3.9.3 Computer dead time

The data acquisition system was dead from the time that an event trigger pulse arrived at the CAMAC event trigger module until this module was cleared at the end of the associated event read-out cycle by the program running in the microprogrammed branch driver (described in subsection 2.6.8). During this time the event trigger module provided a "busy" output, and this signal was used to veto the acceptance of further events and inhibit the scalers, preventing them from updating. Thus, computer dead time was corrected for automatically by this hardware.

3.9.4 Target thickness

The target was rotated about the vertical axis through its centre during the course of both the singles and coincidence experiments, to prevent the target ladder from shielding one or more of the detector telescopes when these were positioned at particular angles. The effective target thickness as seen by the incident proton beam, therefore, changed as a function of this angle (θ_T), given by

$$t_{eff} = \frac{t_T}{\cos\theta_T}$$

where t_T is the measured target thickness. This effective target thickness was used in the calculations of the required cross sections.

3.10 Error Analysis

3.10.1 Statistical errors

It was assumed that the statistical error associated with each bin in the sorted 1- and 2-dimensional sorted energy histograms was of the normal $\sqrt{n_i}$ form where n_i is the number of counts in the histogram bin i. During data acquisition, events were gathered until an acceptable level of statistical error on the bins in the energy region of interest had been achieved, given the limitation on the beam time available for the experiments.

In all subsequent calculations (random background subtractions, geometrical corrections, etc.) performed on these histogram data, the statistical errors were propogated in the orthodox manner. In the singles experiments these errors were of the order of 2–4% for all angles of the detector telescopes. In the coincidence experiment the errors were dependent on the count rate of the detector telescope positioned at the secondary angle. Since the data from three secondary angles were acquired simultaneously, and the outer telescopes mounted on the secondary arm of the scattering chamber were separated by an angle of 100°, the count rates in these three detector telescopes varied dramatically. A compromise, therefore, had to be made between statistical accuracy at the most backward angle and the accelerator beam time allocated to the measurement.

The resulting statistical errors are shown on the extracted cross section data points which are presented in the plots in the following chapter.

3.10.2 Systematic errors

The largest single contribution to the experimental systematic error is that due to uncertainties in the thicknesses of the ^{12}C targets, approximately 8% (see section 2.4).

The solid angles subtended by the detectors were calculated from the geometrical parameters listed in table 2.1. The uncertainties in the distances from the position in the target where a detected event occurred, to the defining exit holes in the collimators directly in front of the telescopes, are dominated by the size of the beam spot on the target ($\sim$ 2 mm). Combining this with the uncertainties in the measured radii of the exit holes in the collimators for each of the telescopes according to the formula

$$\delta\Omega = \sqrt{(2 \cdot \delta r)^2 + (2 \cdot \delta d)^2}$$

where $\delta\Omega$, δr and δd are the percentage errors on the solid angle, radius and target-collimator distance respectively, gives a maximum uncertainty in the solid angles of approximately 1%.

Further uncertainties are introduced by the setting of the gates on the particle identification and time distribution histograms (this latter applying to the coincidence experiment). For each telescope there is some leakage of deuteron events into the gate on the proton locus, particularly in the region corresponding to higher particle energy, and conversely, some proton events may fall outside the gate. The latter condition is very small as the gates were always set to clearly encompass events lying on the higher ΔE side of the proton locus. Deuteron event leakage into the gate is however, enhanced by the reaction of deuterons in the NaI crystal which results in some energy not being detected, and the consequent "tailing" of the deuteron locus into the region of the gate. The picture is further complicated by the effects of the proton gate on the crystal-reaction corrections applied to the energy spectra (see subsection 3.9.1). Cameron *et al.* quote uncertainties much less than 1% in their tail-to-peak efficiency ratios [Cam77], and it is estimated that the total contribution of the effects of the proton gate is less than 5%.

The "true" and "random" peaks in the time distribution were found to be clearly separated (see figure 3.8), and no additional uncertainty was introduced in the setting of the gates on these peaks in the coincidence experiment. There is an uncertainty introduced, however, in the determination of the number of "random" events to be subtracted from the energy spectra gated on this "true" peak (due to coincidences from particles originating from different events in the same beam packet). This uncertainty results from the time structure superimposed on the accelerated beam, which in the case of the present coincident experiment was found to be negligible, and the uncertainty introduced by this procedure is estimated therefore, to be less than 2%.

The uncertainties introduced into the cross section determinations by the correction for electronic dead time were estimated to be less than 2%, and other uncertainties from the angle calibrations, beam current integration, slit scattering into the detectors from the collimators, etc. were also estimated to contribute less than 2%.

Although the maximum possible systematic error from the combination (sum) of the contributions from these sources is 20%, it is believed that the realistic overall systematic error is closer to 10%.

3.11 Experimental Cross Sections

3.11.1 Inclusive ^{12}C(p,p$'$) cross sections

Once the command procedure files had been set up, incorporating the detector energy and drift calibration data, and the definitions of the proton gates set on the ΔE-E particle identification histograms (described above), the event data for each telescope angle setting of the singles experiments were sorted by the EVAL routine into proton energy spectra with bin widths of 1 MeV.

The absolute differential cross section (in b·sr^{-1}·MeV^{-1}) may be written

$$\frac{\partial^2\sigma}{\partial\Omega\partial E} = \frac{1}{\Delta\Omega\,\Delta E}\cdot\frac{N}{N_0\,n_a}$$

where

$\Delta\Omega$ is the collimated solid angle (in steradians) subtended by the detector telescope,

ΔE is the width of the energy bins (in MeV),

N is the (corrected) number of protons observed in a bin,

N_0 is the number of protons incident on the target, and

n_a is the number of atomic nuclei per unit area of the target (in b^{-1}).

Setting

$$N_0 = \frac{C}{e}$$

where

C is the measured total integrated charge falling on the beam stop, and

e is the proton charge,

and

$$n_a = \frac{t_T\, N_A}{\cos\theta_T\, A}$$

where

t_T is the measured thickness of the target expressed in mass per unit area,

θ_T is the target angle (that is, the angle between the normal to the target and the beam direction),

N_A is Avagadro's number, and

A is the atomic mass of the target,

the differential cross section may be written

$$\frac{\partial^2\sigma}{\partial\Omega\partial E} = \frac{1}{\Delta\Omega\,\Delta E} \cdot \frac{N\,e\,\cos\theta_T\,A}{C\,t_T\,N_A}$$

In the cases where an empty frame background measurement had proved necessary during data acquisition (at telescope angle settings of 20° and less), the empty frame proton spectra were normalised to the corresponding ^{12}C proton spectra by multiplying the background spectra with the ratio of the integrated beam current of the two runs. The normalised background spectra were then subtracted from the ^{12}C spectra.

The proton spectrum at each angle setting was corrected, as described above, for NaI crystal reactions and electronic dead time. The cross sections were calculated using the above formula and the experimental variables (namely, collimated detector solid angle, energy bin width, integrated beam charge, and target thickness and angle).

3.11.2 ^{12}C(p,2p) knockout cross sections

One of the command procedures set up to sort the coincidence experiment data, once the necessary energy calibration parameters had been determined, invoked an event analysis routine which sorted the data into a set of 2-dimensional energy spectra of total summed energy of the reaction products versus the energy of the coincident protons detected in the primary telescope (see section 3.2). For each angle pair two spectra were generated, one gated on the "true" coincidence peak and the other on the "random" peaks in the corresponding time distribution. The "random" spectra were normalised by dividing each bin by the number of time peaks falling in the "random" gates, and the resulting spectra were subtracted from the respective "true" spectra.

An example of one of these random-background-subtracted spectra was shown in figure 3.6. Gates centred on the prominent p-state proton knockout loci in these spectra were defined — these gates were rectangular in shape, parallel to, and extending over all energies along, the E_1 axis, and centred at an energy of approximately 184 MeV on the E_{TOT} axis (corresponding to the incident kinetic energy less the binding energy of a p-state proton) with a width of approximately 10 MeV along this axis.

The data within each of these gates were projected onto the E_1 axis to produce the so-called "energy sharing spectra". In this case, the absolute differential cross section (in b·sr^{-2}·MeV^{-1}) may be written

$$\frac{\partial^3\sigma}{\partial\Omega_1\partial\Omega_2\partial E_1} = \frac{1}{\Delta\Omega_1\,\Delta\Omega_2\,\Delta E_1}\cdot\frac{N\,e\,\cos\theta_t\,A}{C\,t\,N_A}$$

where the symbols are the same as in the expressions for the inclusive cross sections, and the subscripts 1 and 2 refer to detection in the primary and secondary telescopes respectively.

The energy sharing proton spectrum for each angle pair was corrected for NaI crystal reactions and electronic dead time as described earlier. In this case each data bin in the spectrum was corrected for the loss in counts due to a proportion of the protons of the corresponding E_1 and E_2 energies undergoing NaI crystal reactions in the two detectors — as this knockout locus is at the kinematic limit for three-body breakup, there is no contribution to counts in the bins in the locus from protons of higher energy. The cross sections were calculated using the above formula and the experimental variables (namely, collimated detector solid angles, energy bin width, integrated beam charge, and target thickness and angle).

3.11.3 Continuum cross sections

The final command procedure set up to sort the coincidence experiment data, once the necessary energy calibration parameters had been determined, invoked the event analysis routine which sorted the data into a set of 2-dimensional spectra of the energy of the proton detected in the telescope at the primary angle versus the energy of the coincident proton detected in the telescope at the secondary angle. As in the case of the (p,2p) knockout analysis, two spectra were generated for each angle pair, one gated on the "true" coincidence peak and the other on the "random" peaks in the corresponding time distribution. The "random" spectra were normalised by dividing each bin by the number of time peaks falling in the "random" gates, and the resulting spectra were subtracted from the respective "true" spectra.

Figure 3.9 shows a set of coincidence energy spectra generated for the angle pair (-20°,45°), illustrating the results of sorting the data gated on the "true" and "random" peaks, and the resulting subtracted spectrum.

To generate the continuum decay spectra for comparison with model calculations, energy spectra of protons detected at the secondary angles in coincidence with protons of three different energies detected at the primary angle were extracted. Three rectangular gates were defined, spanning the entire energy region along the E_2 axis and centred at the required energies (namely, 70, 100 and 130 MeV) along the E_1 axis (with widths of 10 MeV

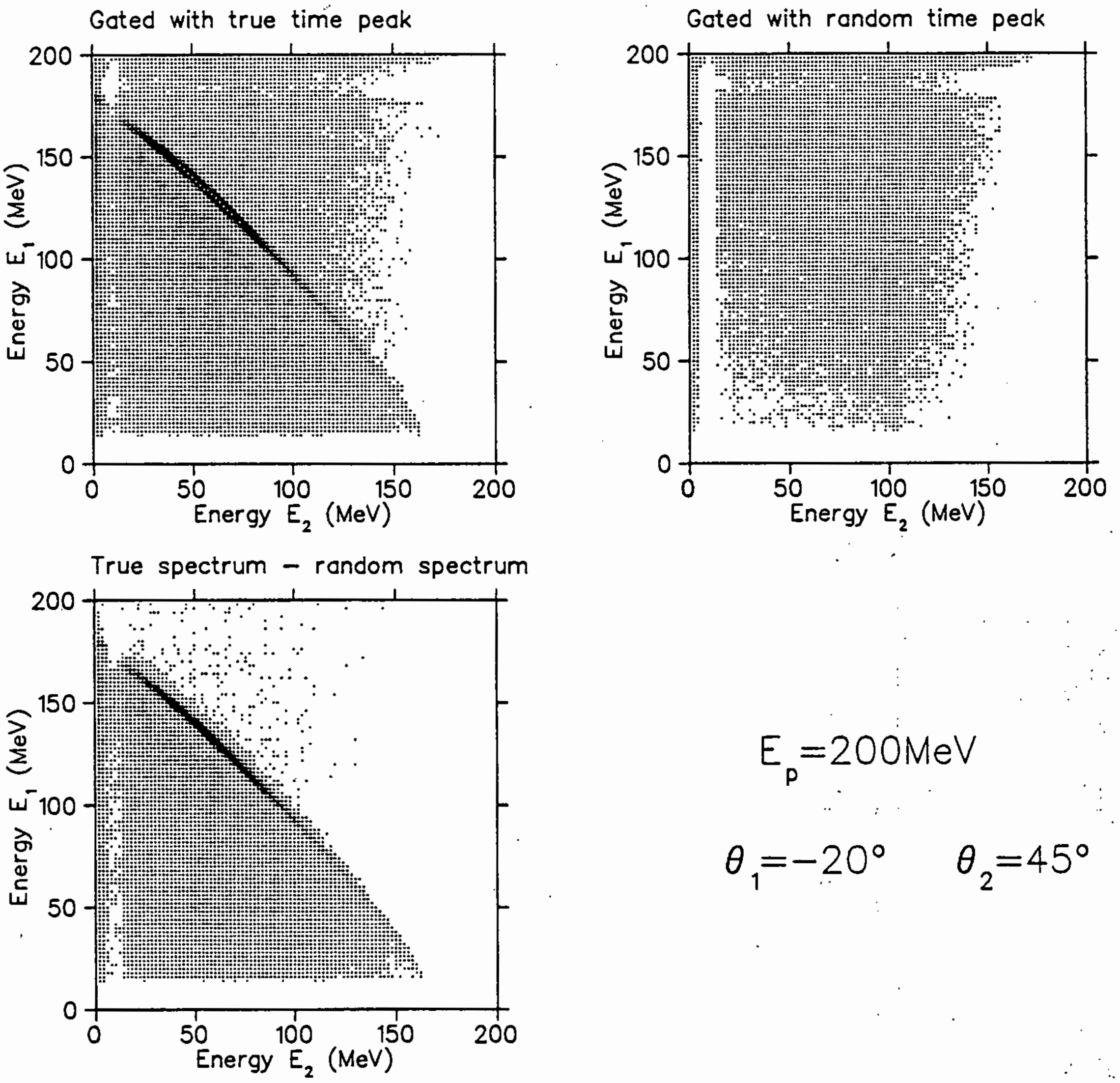

Figure 3.9: *Coincidence proton energy distributions from sort of (-20°,45°) data with gates set on "true" and "random" peaks in corresponding time distribution. The resulting subtracted (true - random) spectrum is shown below.*

along the E_1 axis to ensure reasonable statistical accuracy). Such a gate, centred at E_1=100 MeV, is illustrated for the (-20°,20°) data in figure 3.10. The events falling within each of these gates were projected onto the E_2 axis for each of the coincidence proton spectra of each telescope angle pair.

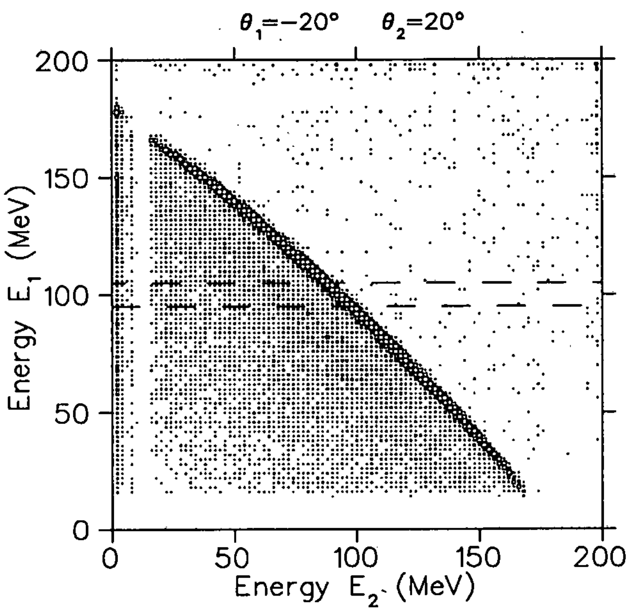

Figure 3.10: *Coincidence proton energy distributions from sort of (-20°,20°) data, after subtraction of "random" background. The 10 MeV wide gate centered at 100 MeV along the E_1 axis to obtain the projected continuum energy spectra is illustrated.*

For a primary angle of -20° six such projected spectra were extracted, and for a primary angle of -45° three spectra were extracted. In addition, a fourth spectrum at a primary angle of -45° was obtained by renaming the primary and secondary angles of the (-20°,45°) measurement. By defining rectangular gates parallel to the E_1 axis at the three required energies along the E_2 axis, and projecting the data in the gates onto the E_1 axis, continuum spectra at a primary angle of -45° and secondary angle of 20° were obtained.

The absolute differential cross section (in b·sr^{-2}·MeV^{-2}) may be written

$$\frac{\partial^4\sigma}{\partial\Omega_1\partial E_1\partial\Omega_2\partial E_2} = \frac{1}{\Delta\Omega_1\,\Delta E_1\,\Delta\Omega_2\,\Delta E_2}\cdot\frac{N\,e\,\cos\theta_t\,A}{C\,t\,N_A}$$

where the symbols are the same as before.

The continuum proton energy spectrum for each angle pair was corrected for NaI crystal reactions and electronic dead time as described above. The cross sections were calculated using the above formula and the experimental variables (namely, collimated detector solid angles, E_1 energy gate width, E_2 energy bin width, integrated beam charge, and target thickness and angle).

3.12 DWIA Calculations

A number of sets of DWIA calculations were performed with the computer program *THREEDEE* [Cha82] for comparison with, and interpretation of, the cross sections determined from the experimental data.

The program uses Woods-Saxon optical potentials for the scattering states, which, if the spin-orbit terms are neglected, take the form

$$-U(r) = \frac{V}{1+e^x} + \frac{iW}{1+e^{x'}} + \frac{4iW_De^{x'}}{(1+e^{x'})^2} - U_{COUL}(R_{COUL})$$

where $x = \frac{r-R_0A^{1/3}}{a}$, $x' = \frac{r-R_0'A^{1/3}}{a'}$ and $U_{COUL}(R_{COUL})$ is the coulomb potential due to a sphere of radius $R_{COUL}A^{1/3}$.

A set of energy-dependent optical potential parameters, taken from [Wes83], and listed in table 3.2, was used for the scattering states in the calculations. For the bound state, the program adjusts the potential V to generate a wave function with the specific binding energy. In the present

V	$84.88 - 13.59\ln(E)$	
W	$9.004\ln(E) - 36.81$	$E \geq 150$MeV
	$4.801\ln(E) - 15.84$	25MeV$\leq E < 150$MeV
	0	$E < 25$MeV
W_D	0	$E > 75$MeV
	$11.8 - 2.733\ln(E)$	33MeV$\leq E \leq 75$MeV
	$2.592 - 0.004795(E-25)^2$	17MeV$\leq E < 33$MeV
	$2.127\ln(E) - 3.742$	$E < 17$MeV
R_0	1.16	
R_0'	1.37	
R_{COUL}	1.25	
a	0.75	
a'	0.63	

Table 3.2: *Energy-dependent set of optical potential parameters used in the DWIA calculations. The variables are defined in the text.*

study, for the (p,2p) knockout calculations, the binding energies were set to 15.9 MeV for the $p_{3/2}$ state in ^{12}C and 36.9 MeV for the $s_{1/2}$ state, taken from the data summarized by Frullani and Mougey [Fru84]. For the (p,pn) calculations, the binding energies of the neutron were set to 18.7 MeV for the $p_{3/2}$ state, taken from the evaluation of Wapstra and Audi [Wap85], and 39.7 MeV for the $s_{1/2}$ state, being the same separation from the p state as for the protons. Other bound state parameters were taken from [Bho76] ($R_0 = 1.64$ and $a = 0.65$), and masses from the 1983 atomic mass evaluation of Wapstra and Audi [Wap85] were used.

To ensure reasonable convergence of the three dimensional numerical integration performed by the program *THREEDEE*, the numbers of Gaussian points for the r, θ and ϕ integrals were set to 16 in each case, and the number of steps (with a length of 0.1 fm) used in generating the wave functions was set to 121.

For comparison purposes, cross sections were also calculated using a set of average energy optical potentials (at 200 MeV for the incoming scattering state, and 100 MeV for the outgoing states) in the analysis of the "clean" quasifree ^{12}C(p,2p) knockout data. At 200 MeV, the optical potential parameters were taken from [Mey81], and at 100 MeV, from [Li68]. These parameters are listed in table 3.3.

	100MeV	200MeV
V	21.59	9.0
W	0	13.5
W_D	5.39	0
R_0	1.296	1.39
R'_0	1.396	1.12
R_{COUL}	1.33	1.3
a	0.508	0.55
a'	0.52	0.68

Table 3.3: *Average energy sets of optical potential parameters used in the DWIA calculations for the 100 MeV [Li68] and 200 MeV [Mey81] scattering states. The variables are defined in the text.*

The first set of calculations was performed to determine cross sections for the ^{12}C(p,2p) quasifree knockout reaction at an incident energy of 200 MeV, in which protons are knocked out of the outer ($1p_{3/2}$) shell in ^{12}C, and the outgoing protons are observed at the nine coincidence angle pairs of the experiment. In this case distorted waves were employed for both outgoing protons, and calculations were performed for in-plane geometry in energy increments of 5 MeV for the second outgoing proton. Calculations were performed using both the energy-dependent and average energy optical potential parameters listed above, and both the initial- (IEP) and final-energy prescriptions (FEP) for the two-body scattering approximation.

The second set of calculations was performed to determine the angular distributions of nucleons resulting from a quasifree ^{12}C(p,pN) reaction at an incident energy of 200 MeV, for the cases in which the proton emerges at the primary angles of -20° and -45° with energies of 70, 100 and 130 MeV. These calculations were required for describing the first step in the proposed reaction mechanism for the generation of the continuum yields. In this case the protons observed at the primary angle were represented by distorted waves, while the secondary protons (or neutrons) were represented by plane waves. Plane waves are appropriate in the latter case since the multiple scattering of these knocked out particles, which is normally accounted for in the DWIA treatment by distortion, is explicitly described in the reaction model by the use of suitable experimental cross sections for the interaction of these particles with the residual nucleus. Calculations were performed using the energy-dependent optical potential parameters listed above, for the knockout of either a proton or neutron from the outer $1p_{3/2}$ and inner $1s_{1/2}$ shells of ^{12}C, using both the IEP and FEP for the two-body scattering approximation, and covering both in- and out-of-plane angles in steps of 5° in the region where the yield was found to be significant.

The *THREEDEE* program exhibits numerical problems at a secondary scattering angle of 0°. To overcome this, calculations were performed at 1° and $-1°$, and the average of the resulting two cross section values taken as the 0° value.

Another problem occurs when calculating the (p,2p) cross section if the kinematics is such that the p+p centre-of-mass scattering angle approaches

0° or 180°. Due to the coulomb interaction the p+p cross section is very sharply peaked at these angles. In the calculations performed in the current work, this only occurred at a primary proton energy and angle of 70 MeV and $-20°$ respectively, and close to a secondary angle of $-10°$. The unphysically large (p,2p) cross section which resulted was discarded by interpolating the cross section values on either side of the large peak.

3.13 Continuum Decay Model Calculations

Two sets of calculations were performed to model the coincident proton decay of the continuum according to the proposed reaction mechanism. Following the treatment introduced by Ciangaru [Cia84a], and described in subsection 1.2.2, an equation was derived which expresses the continuum cross section in terms of a convolution integral over a three-body quasifree knockout doorway cross section and an empirical inelastic scattering probability describing the multiple scattering probability of one of the quasifree particles.

In the first set of calculations, the contribution to the continuum proton yield was restricted (as Ciangaru had done) to the case in which the initial quasifree knockout process results in in-plane knocked out nucleons. Ciangaru also only considered the contribution from proton knockout, but in the present work it was thought that a significant portion of the observed proton yield could result from the initial knockout of other particles (in particular, neutrons), followed by the appropriate interaction of these with the residual nucleus ((n,p) in the case of neutrons) giving rise to protons in the exit channel. Calculations were, therefore, performed for the two cases of proton and neutron knockout in the initial interaction. The cross section for the continuum (equation 1.22) may be rewritten

$$\begin{aligned}\frac{d^4\sigma(\theta_1 E_1 \theta_2 E_2)}{d\Omega_1 dE_1 d\Omega_2 dE_2} &= \sum_N \Bigg[\int d\theta_2' \sin\theta_2' \sum_\lambda \frac{d^3\sigma_{\lambda\alpha}^{QF}(\theta_1 E_1 \theta_2' E_2')}{d\Omega_1 dE_1 d\Omega_2'} \times \\ &\qquad \frac{1}{2\pi\sigma_{tot}^{inel}(E_2')} \; \frac{d^2\sigma^{inel}(\theta_2'' E_2 E_2')}{d(\Omega_2 - \Omega_2')dE_2} \Bigg]_N\end{aligned}$$

where the N indicates the summation index of separate evaluations for the initial knockout of protons and neutrons.

The cross sections for the initial quasifree interaction, $\frac{d^3\sigma_{\lambda\alpha}^{QF}(\theta_1 E_1 \theta_2' E_2')}{d\Omega_1 dE_1 d\Omega_2'}$, were calculated by the program *THREEDEE*, as described in the previous section, for the two cases of (p,2p) and (p,pn) knockout, using both the IEP and FEP for the two-body scattering approximation.

The interaction of the knocked out nucleon with the residual nucleus, $\frac{d^2\sigma^{inel}(\theta_2'' E_2 E_2')}{d(\Omega_2 - \Omega_2')dE_2}$, was described, in the case of protons, by the experimental ^{12}C(p,p′) differential cross sections. There is some uncertainty as to the appropriate energy at which to take these experimental data. In the present work, cuts were made in the coincident data corresponding to the detection of protons at the primary angles with energies of 70, 100 and 130 MeV, implying the transfer of energies of 130, 100 and 70 MeV to the target nucleus respectively. This energy is distributed between the separation of the bound nucleon from one of the target nucleus orbits, the kinetic energies of this knocked out nucleon and the residual nucleus, and the excitation of the residual nucleus. Although nucleons from the $1p_{3/2}$ state in ^{12}C (binding energy ~15 MeV) have a relatively sharply peaked distribution, those from the $1s_{1/2}$ state (binding energy ~35 MeV) have a much broader distribution of energies, centered at ~60 MeV in the case of the 100 MeV cut, with the residual part of the target nucleus excited to roughly 20 MeV. For such a cut, this implies a system approximated by a projectile with an incident energy equal to 80 MeV interacting with a target in its ground state. It was concluded therefore that the available ^{12}C(p,p′) experimental data at energies of 120, 90 and 62 MeV were appropriately close to the actual energies required for both shells of ^{12}C for the three cuts employed.

For (p,pn) knockout, the appropriate experimental data required are for the (n,p) reaction on a mass-11 or mass-12 system at similar energies. Apart for some ^{12}C(n,p) measurements at 60 Mev [Sub83], the required data were not available. However, it was expected that the shapes of the differential cross sections in the continuum region for (p,p′) and (n,p) reactions on the same target should be similar, and this expected similarity is confirmed by the 60 MeV (n,p) data of Subramanian *et al.* who compared these to the appropriate (p,p′) data. In addition, the measured differential (n,p) cross sections were found to have absolute values approximately half those of the corresponding (p,p′) cross sections measured at an incident proton energy of 62 MeV by Bertrand and Peelle [Ber73].

A computer program was written to perform these calculations, using Simpson's method for the required numerical integration. A file of the experimental inelastic cross section data was constructed for each of the three energies to be read by the program for scattering angles ranging from 5° to 165° in steps of 5°, the data being interpolated from adjacent sets where a suitable angle set was not available. In addition, for those sets of data where the peak due to H(p,p) elastic scattering from the hydrogen contamination in the carbon targets was apparent (that is, where it was built on the continuum region of the spectrum), this peak was removed from the data by interpolating a smooth curve through the data on either side of the peak. Files of the DWIA cross section calculations were also constructed in steps of 5°. For each energy increment the program steps through the angular region where the DWIA cross section is significant, and folds this cross section with the appropriate (p,p′) scattering data for a scattering angle determined by the initial quasifree knockout angle and the secondary angle at which the proton is observed. At each energy increment the set of folded values is then integrated over the in-plane quasifree knockout angle. The program assumes a relative spectroscopic factor of unity for the first (p) state, and a spectroscopic factor for the second (s) state relative to the p state is entered as a variable into the program (in this work a value of 0.4, deduced from electron scattering results [Fru84] was used).

The values for the integrated inelastic proton and neutron cross section were obtained from calculations performed by the nuclear reaction computer code *ALICE* [Bla84] for incident protons and neutrons with energies of 90 MeV on ^{12}C, and the detection of a proton in the exit channel. These calculations give values of 226.2 mb and 345.2 mb for the total reaction cross sections for incident protons and neutrons respectively. In the energy region of interest (namely, 70 MeV to 130 MeV) the proton reaction cross section is reasonably constant, while the neutron reaction cross section is also constant to a first approximation within the limits of the simple model proposed here.

In the second set of calculations, the treatment was improved by explicitly including the contribution of nucleons which are scattered out of plane in the initial quasifree process, and their subsequent interaction with the residual nucleus results in protons which are detected in-plane. The continuum cross section then becomes

$$\frac{d^4\sigma(\theta_1 E_1 \theta_2 E_2)}{d\Omega_1 dE_1 d\Omega_2 dE_2} = \sum_N \left[\int d\Omega_2' \sum_\lambda \frac{d^3\sigma_{\lambda\alpha}^{QF}(\theta_1 E_1 \theta_2' E_2' \beta)}{d\Omega_1 dE_1 d\Omega_2'} \times \right.$$
$$\left. \frac{1}{2\pi\sigma_{tot}^{inel}(E_2')} \quad \frac{d^2\sigma^{inel}(\gamma E_2 E_2')}{d(\Omega_2 - \Omega_2')dE_2} \right]_N$$

where β is the out-of-plane angle of the knocked out nucleon, and γ is the angle between this nucleon and the in-plane proton resulting from the interaction of this nucleon with the residual nucleus, and observed in the detector positioned at the secondary angle θ_2. $d\Omega_2'$ is the solid angle element of integration, and may be written

$$d\Omega_2' = \sin\theta_2' d\theta_2' d\beta \ .$$

The angle γ may be derived from the "cosine law" of solid analytical geometry (cf. [Kin50]), resulting in the expression

$$\cos\gamma = \cos\beta\cos(\theta_2' - \theta_2) \ .$$

A computer program was written to perform these calculations, being very similar to the original program except for the extension to a second integration loop for the out-of-plane angle, β, which was performed in 5° steps. The calculations were performed for the positive hemisphere only, since the DWIA cross sections should be symmetrical about the in-plane angle, and the resulting continuum cross sections were doubled to account for the negative out-of-plane contribution.

Chapter 4

Results and Discussion

4.1 Overview

The results of the data analysis and model calculations described in the previous chapter are now presented in three sections together with the interpretation and discussion of these results.

First the measured inclusive ^{12}C(p,p$'$) cross sections are summarized, and this section is followed by a discussion of the results of the analysis of the ^{12}C(p,2p) discrete state knockout data. Finally, the analyses of the ^{12}C(p,2p) continuum decay data are presented, and these are interpreted in terms of the model of the proposed reaction mechanism in which an initial quasifree nucleon-nucleon knockout process is succeeded by the interaction of the knocked out nucleon with the residual nucleus.

4.2 Inclusive ^{12}C(p,p$'$) Cross Sections

The inclusive ^{12}C(p,p$'$) cross sections, at incident proton energies of 90 and 120 MeV, were measured in steps of 5° from 10° to 90°, and thereafter in steps of 10° to 160°.

These two measurements form part of the on-going study, at the National Accelerator Centre, of continuum yields produced in inclusive (p,p$'$) reactions in the incident proton energy range from approximately 100 to 200 MeV on a variety of targets. A detailed analysis of the present inclusive 90 MeV measurements with the ^{12}C target, together with other measurements at an incident energy of 200 MeV, have been published in the literature [För88], while the 120 MeV measurements are currently undergoing detailed analysis.

In the present investigation of the coincident proton decay of the continuum, these two inclusive measurements were used solely in the interpretation of the coincidence continuum data, and thus a detailed analysis of the inclusive spectra does not form part of this thesis, and merely a summary of the published results of these inclusive measurements will be given here.

The continuum spectra confirm the presence of a pronounced broad peak at the forward angles (less than 30°). The measured experimental cross sections have been compared with calculations based on a DWIA model similar to the work of Wesick *et al.* [Wes85] using the program THREEDEE [Cha82]. Reasonable agreement with the data was found (using realistic normalization factors and the initial energy prescription for the two-body scattering amplitudes), at both the forward (<30°) and more backward (>30°) angles, lending support to the importance of a quasifree N-N interaction as a major component in determining the shapes of the spectra.

Figure 4.1 shows a sample of the measured differential cross sections for the ^{12}C(p,p′) reaction at an incident proton energy of 90 MeV at six angles of the detector telescope, namely, 15°, 20°, 30°, 45°, 60° and 90°. The data are presented in 1 MeV steps, the data points being connected by line segments to illustrate the trend of the data with more clarity. The statistical errors are not indicated on these plots. Figure 4.2 shows a similar sample of the cross sections measured at the same angles at an incident proton energy of 120 MeV.

In both sets of plots, a prominent peak is observed in the cross section data at the angles 30°, 45° and 60°, showing a marked kinematic shift with scattering angle. This peak is due to the elastic scattering of protons from the hydrogen which contaminates the carbon targets. Although the contamination is relatively small, this is compensated for by the H(p,p) cross section which is extremely large. When subsequently using these cross section data as input to the calculations for determining the continuum yields, the peaks due to proton elastic scattering from hydrogen were removed by interpolating a smooth curve through the data on either side of the peaks.

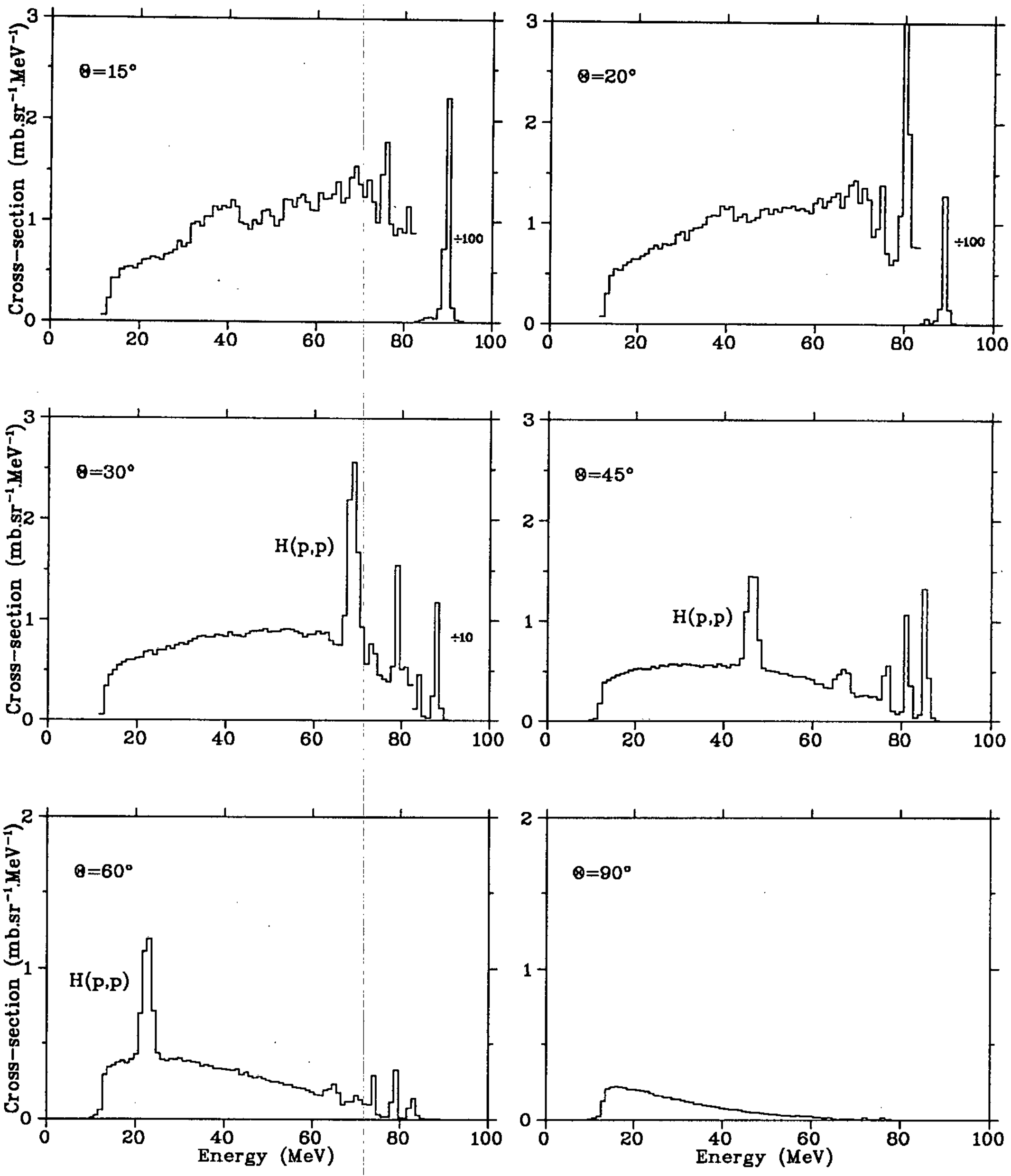

Figure 4.1: *A sample of six measured differential* $^{12}C(p,p')$ *cross sections at an incident proton energy of 90 MeV. The corresponding scattering angle, θ, is indicated on each plot. The statistical errors are not indicated, and the data points, plotted in 1 MeV steps, are connected by line segments to illustrate the trend of the data with more clarity. The prominent peak due to H(p,p) elastic scattering is indicated on three of the plots.*

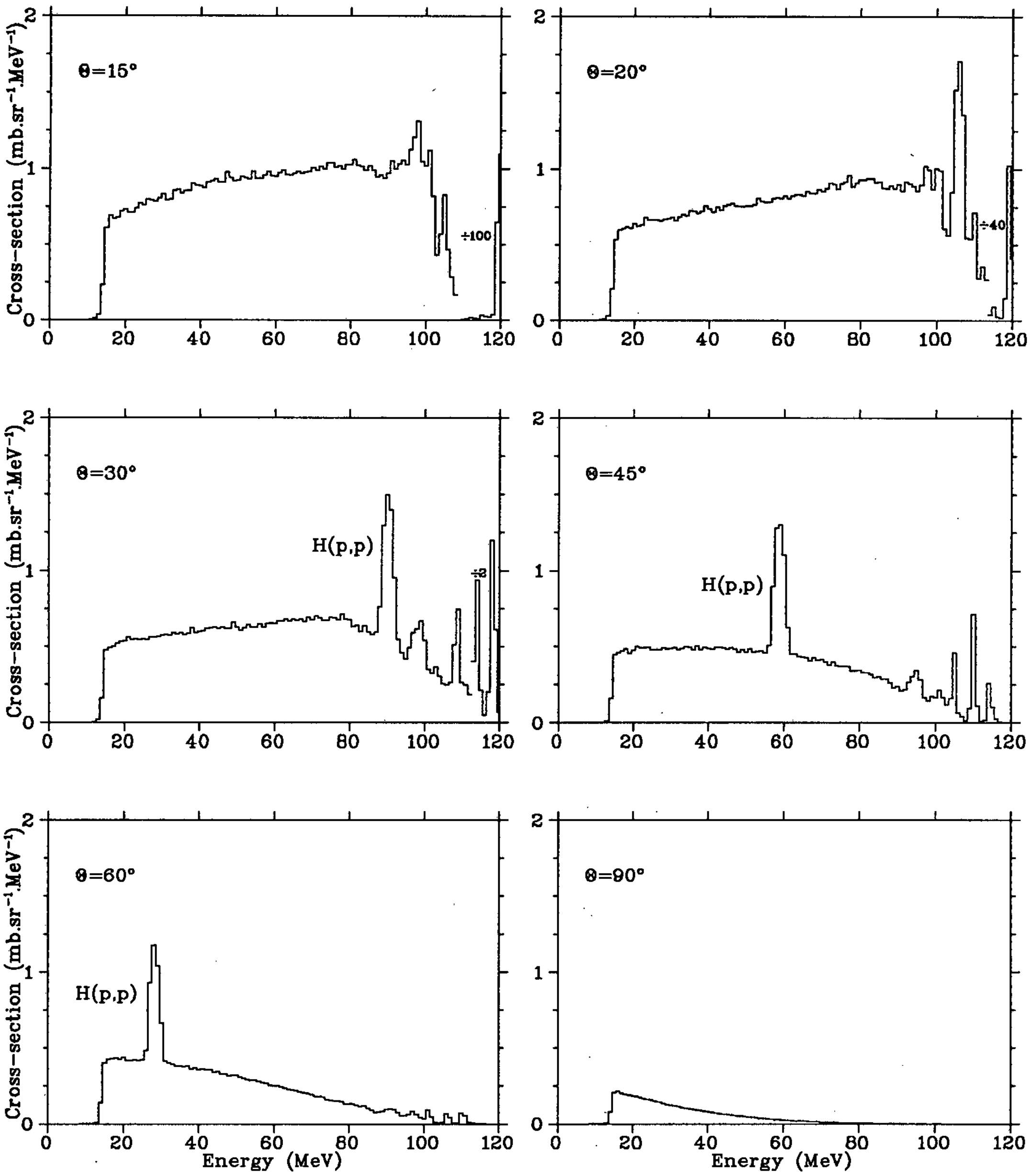

Figure 4.2: *A sample of six measured differential* $^{12}C(p,p')$ *cross sections at an incident proton energy of 120 MeV. The corresponding scattering angle,* θ*, is indicated on each plot. The prominent peak due to H(p,p) elastic scattering is indicated on three of the plots.*

4.3 ^{12}C(p,2p) Discrete-State Knockout

The measured cross sections for the knockout of p-state protons from ^{12}C by 200 MeV incident protons are plotted in the energy-sharing distributions of figures 4.3 to 4.5. These show the cross sections extracted from the data in the p-state knockout locus in the coincident proton summed energy spectra (see figure 3.6) at the nine pairs of coincident proton angles — six secondary angles (θ_2) at the primary angle (θ_1) of -20° and three secondary angles at the primary angle of -45°. The extracted cross sections are plotted as dots, together with the associated statistical error bars, as a function of the energy (E_1) of the proton observed in the detector at the primary angle. For the θ_1=-20°,θ_2=70° plot, the prominent peak due to H(p,p) elastic scattering from the hydrogen contamination in the ^{12}C target, centered at an E_1 energy close to 159 MeV, is not shown.

On each plot two curves are drawn, the results of the DWIA calculations performed with the aid of the computer program *THREEDEE*. The continuous curves are the results from calculations in which the final-energy prescription was employed in the approximation for the two-body scattering amplitudes, while the dashed curves are the results obtained using the initial-energy prescription. Two graphs are plotted for each angle pair, one for the DWIA calculations performed with the average energy optical potentials and the second using the more realistic energy-dependent set of potentials (detailed in section 3.12).

The spectroscopic factors used to normalize the data are also shown on each of the graphs. These spectroscopic factors correspond to the C^2S_{LJ} factor in equation 1.20 for the differential cross section.

The shapes of the DWIA curves give a reasonable fit to the measured cross sections. For the primary angle of $-20°$ and at large secondary angles

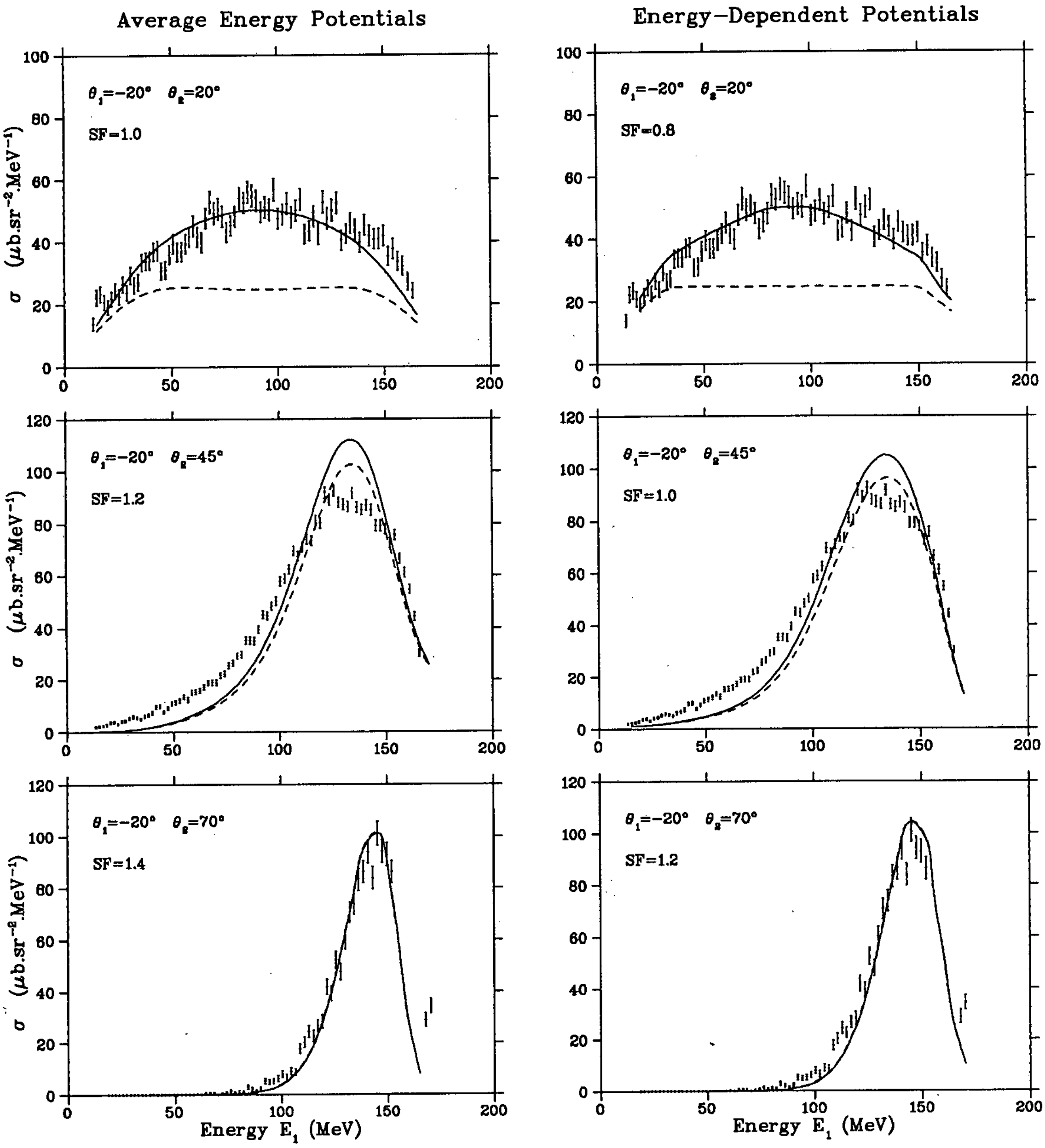

Figure 4.3: *Cross sections for the (p,2p) knockout of p-state protons from* ^{12}C *by incident protons of 200 MeV for the coincident angle pairs shown. Measured cross sections are shown as dots with the associated statistical error bars. DWIA calculations are drawn as continuous curves (calculated using the final-energy prescription) or dashed curves (calculated using the initial-energy prescription). The spectroscopic factors employed to normalize the curves to the data are shown on each graph. On the left are the results of calculations performed using average energy potentials, and on the right those using an energy-dependent set of potentials.*

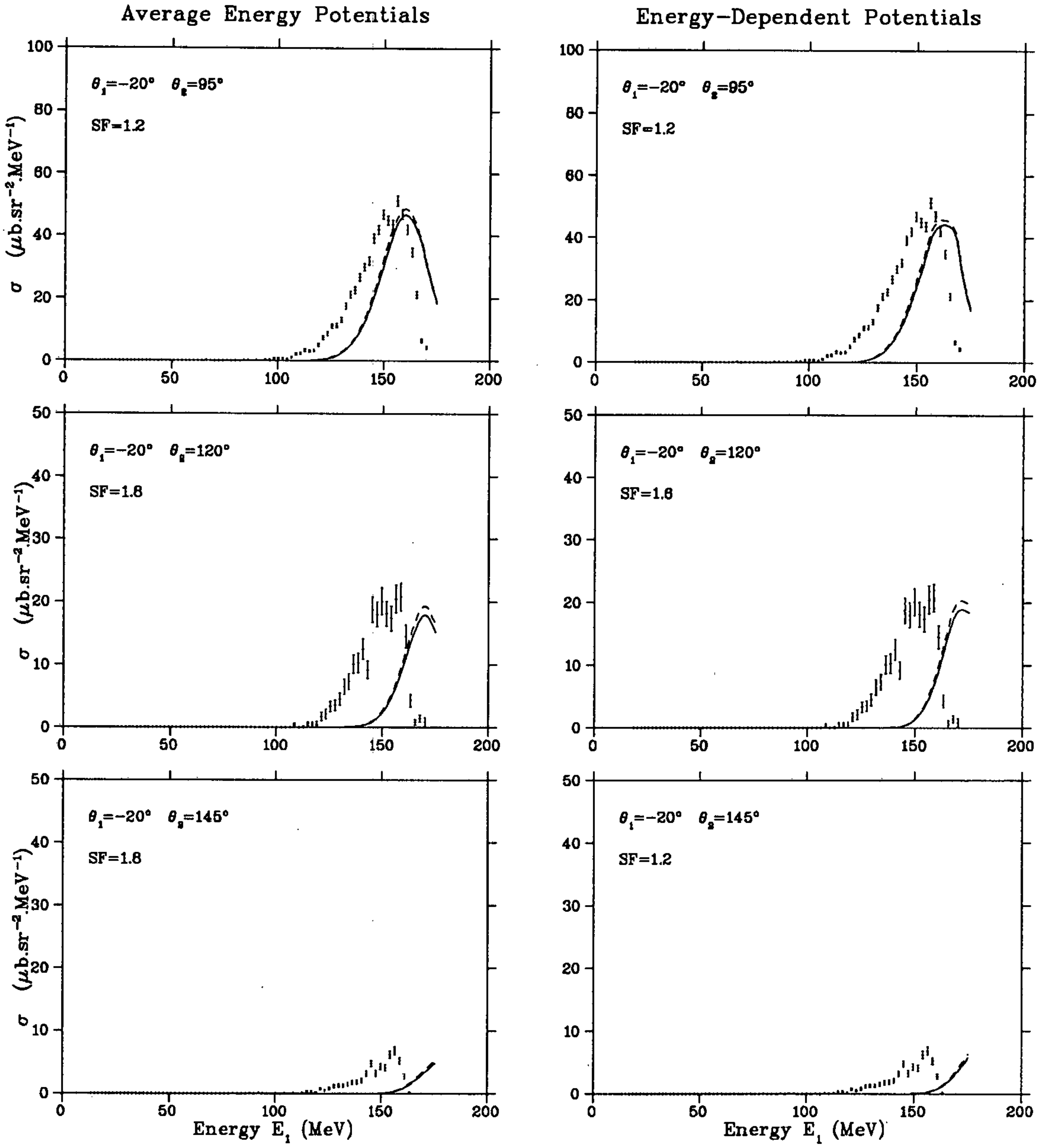

Figure 4.4: *Cross sections for the (p,2p) knockout of p-state protons from* ^{12}C *by incident protons of 200 MeV for the coincident angle pairs shown. Measured and calculated data are shown as in figure 4.3.*

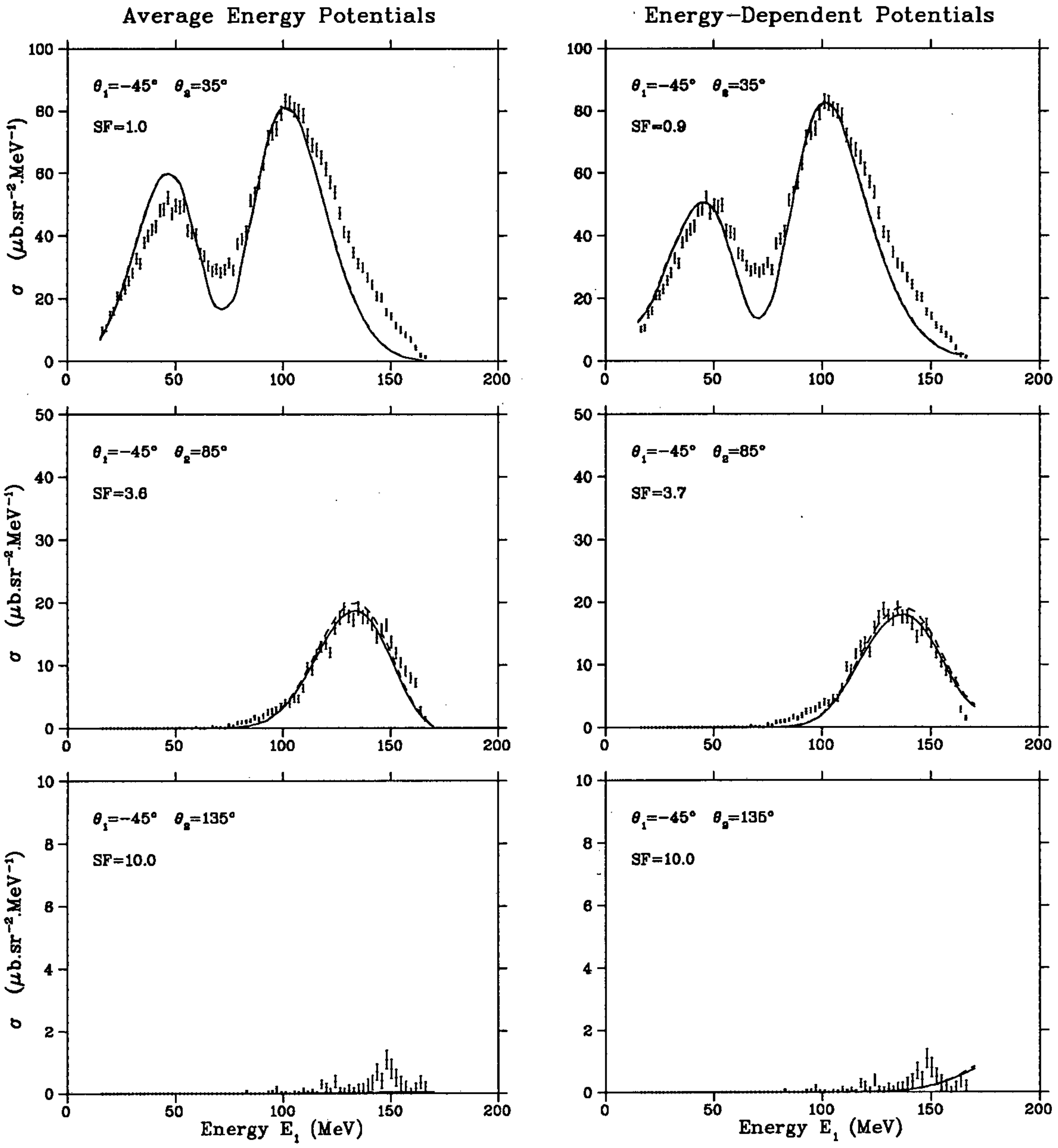

Figure 4.5: *Cross sections for the (p,2p) knockout of p-state protons from* ^{12}C *by incident protons of 200 MeV for the coincident angle pairs shown. Measured and calculated data are shown as in figure 4.3.*

($\Delta\theta = |\theta_1 - \theta2| > 110°$), the peak of the calculated yield shifts to an energy higher than that of the measured yield, and this difference increases with secondary angle (ΔE =~6 MeV at $\Delta\theta = 115°$ and ΔE =~19 MeV at $\Delta\theta = 140°$). A similar shift in the peak of the calculated yield with respect to the measured yield is absent in the −45° secondary angle data at $\Delta\theta = 130°$.

DWIA calculations performed with the average energy and energy-dependent potential parameter sets result in very similar curve shapes, with relatively minor changes in magnitude (the greatest difference being approximately 20% in the −20°, 20° case).This apparent insensitivity to reasonable changes in the optical model parameters has been found by other workers for the same reaction at a lower incident energy. For example, in their DWIA treatment of the ^{12}C(p,2p) reaction at an incident proton energy of 100 MeV Bhowmik *et al.* [Bho76] studied the sensitivity of their calculations to the optical potential parameters and the bound state wave function. They reported that the distorted momentum distributions were independent of the optical potentials used for the incoming channel, and, that while the choice of potential for the outgoing channels affected the absolute magnitude, the qualitative shapes did not alter. In addition, they tested whether the use of ^{12}C parameters for the residual ^{11}B nucleus was reasonable by allowing parameters of the potential well for the outgoing channel to vary. It was found that variations up to 25% in these parameters did not change the momentum distribution by more than 10%. Devins *et al.* [Dev79], in an experiment also at 100 MeV incident energy, confirm this lack of sensitivity of the DWIA calculations to the incoming and outgoing channel parameters.

In the present study, differences between calculations performed using the IEP and FEP approximations for the two-body amplitudes are negligible, except in the $-20°, 20°$ case where the spectroscopic factors using the two prescriptions differ by a factor close to 2. Here the FEP approximation produces a shape giving a better fit to the measured data. This large difference in the predicted magnitudes at $-20°, 20°$ could be an indication of the importance of off-shell effects and the inadequacies of the on-shell approximations for the two-body scattering in the DWIA treatment, particularly as the binding energy of the outer shell $1p_{3/2}$ proton in ^{12}C is relatively large (~16 MeV). The IEP and FEP approximations represent the extreme cases, while a more accurate half off-shell prescription is expected to lie between the two limits.

The extracted spectroscopic factors used to normalize the calculated cross sections to the data indicate a tendency to increase with the angle of the secondary proton. DWIA analyses of continuum yields from the inclusive ^{12}C(p,p$'$) reaction at incident energies of 150 Mev [Wes83] and 90 and 200 Mev [För88], in which the calculated DWIA cross sections were integrated over the solid angle of the unobserved particle, found an increasing trend in the value of the spectroscopic factors with scattering angle between 20° and 75°.

Disregarding the data at larger secondary angles ($\Delta\theta > 120°$), where the DWIA predictions appear to be less convincing, average values for the spectroscopic factors of 1.15 and 1.00 are obtained from calculations using the average energy and energy-dependent potential sets respectively (and the FEP approximation), compared to the value of 2.85 from a shell model calculation of Cohen and Kurath [Coh67].

In a high resolution (overall summed proton energy resolution of 330 keV) measurement of the ^{12}C(p,2p) reaction at an incident proton energy of 100 MeV, Devins *et al.* [Dev79] extracted spectroscopic factors from DWIA calculations for all states in the residual ^{11}B nucleus below 7 MeV excitation. They divided their data into two sets of five angle pairs each, the first set being for symmetric geometry ($\theta_1 = -\theta_2$, $E_1 = 41.35$MeV) and the second for asymmetric geometry ($\theta_1 = -25°$, $\theta_1 \neq |\theta_2|$, $E_1 = 59.5$MeV). It was found that for the symmmetric geometry data, the summed spectroscopic factor for the $l = 1$ states was equal to 2.66, while for the asymmetric data the factor was equal to 1.33. Most of the strength was due to the ground state ($3/2^-$) contribution (2.0 and 1.0 respectively), and the majority of the remainder to $l = 1$ knockout to the 2.125 MeV($1/2^-$) and 5.020 MeV($3/2^-$) excited states. Devins *et al.* concluded that their results did not indicate large admixtures of $1f$ components in the ground state wave function of ^{12}C, as had been previously postulated [Bou67]. The difference in spectroscopic factors extracted from the symmetric and asymmetric sets was interpreted as a failure of the DWIA treatment to adequately predict the rapid fall-off of the transition amplitude for single-step knockout. In the present study, where the summed proton energy resolution was of the order of 6 MeV, knockout to the individual states in the residual nucleus could not be distinguished. The spectroscopic factors are reasonably close to the asymmetric values found by Devins *et al.*, and in the only symmetric angle pair measurement (at -20°,20°), a value of 2.15 is obtained at the equal-energy point using the IEP approximation (compared to the value of 1.0 using the FEP).

In an earlier measurement of the ^{12}C(e,e′p) reaction, Mougey *et al.* [Mou76], using a DWIA treatment, extracted spectroscopic factors of 2.5 and 1.0 for the knockout of a proton from the $1p_{3/2}$ and $1s_{1/2}$ orbitals respectively. A similar study of the same reaction by Ulmer *et al.* [Ulm87] found average occupation numbers of 4.05 and 1.29 for the p and s shells respectively, although some doubt has been expressed concerning the general applicability of these values [Van88c] due to the limited momentum region sampled in this experiment. In recent high resolution ^{12}C(e,e′p) knockout measurements [Van88a] [Van88b], it was found that spectroscopic strengths were reduced by more than 40% compared with those predicted by the independent-particle shell model. In the latter, coupled channel effects were included in the analysis of the experimental data, which resulted in a summed spectroscopic factor for the three $l = 1$ states of 2.18 (1.72 for the $3/2^-$ ^{11}B ground state). Several weak transitions to excited states consistent with direct knockout from orbitals above the $1p$ shell of ^{12}C were observed, but the extracted strengths are such that these are unimportant in the present study. Fits to the data using DWIA calculations for $1f_{7/2}$ and $2s_{1/2}$ direct knockout gave spectroscopic factors of 3.8×10^{-3} and 8.1×10^{-3} respectively, while a coupled channel calculation resulted in a value of 6.1×10^{-4} for the $1f_{7/2}$ state (this discrepency in the derived spectroscopic factors was attributed to interference between direct and two-step channels).

In experimental studies of quasifree knockout in the ^{16}O(p,2p) reaction, the extracted spectroscopic factor from the work performed at an incident energy of 100 MeV [Sam81][Sam86] was found to be a factor of 2 larger than that from the work performed at 200 MeV [Kit76][Kit80]. This discrepancy could not be fully explained with certainty. In the latter (200 MeV) work too, the factor was found to be 0.7 times that of the shell model expectation. In an attempt to resolve the problem of the DWIA-predicted cross sections being too large, Kitching *et al.* considered the intrinsic nonlocality of the nucleon-nucleon potential by including a nonlocal component in the optical model potential. This was parametrised by a range parameter in their DWIA code, and resulted in a reduction of the predicted (p,2p) cross sections by between 20% and 50%. In the present work, the DWIA calculations, using the energy-dependent set of optical potentials, were repeated

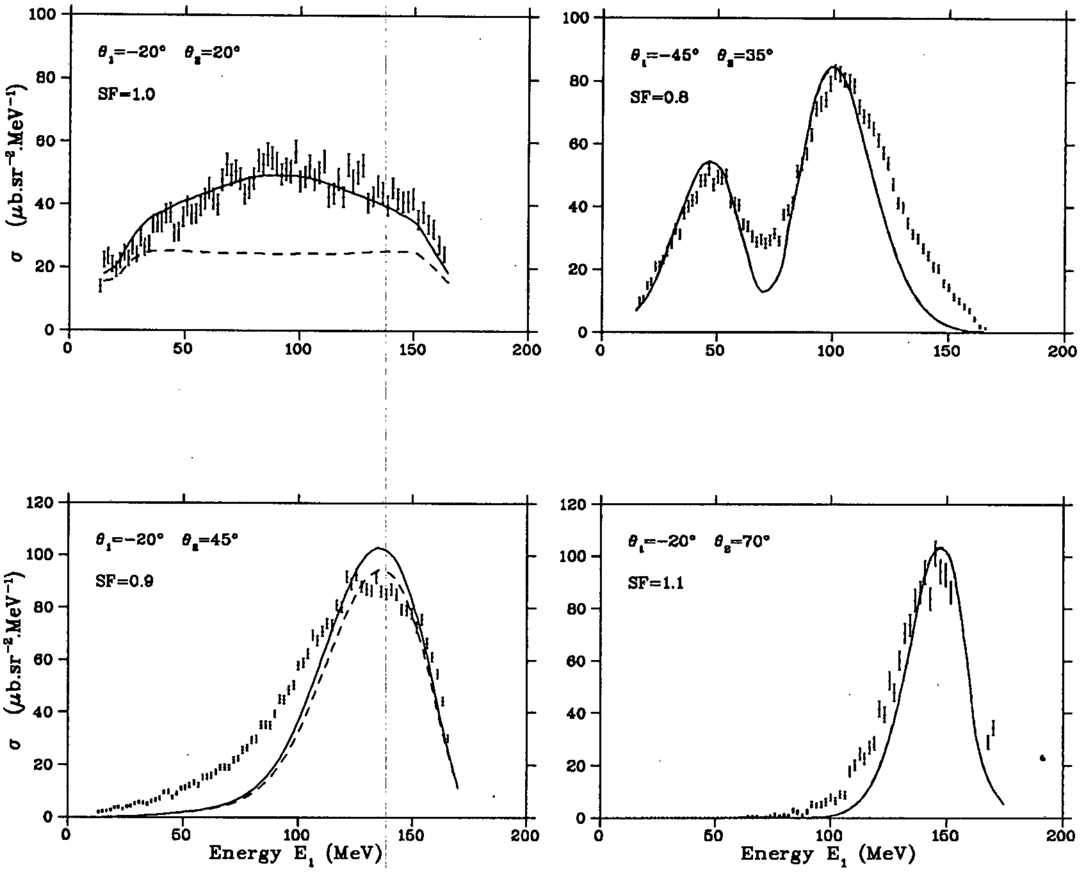

Figure 4.6: *Cross sections for the (p,2p) knockout of p-state protons from* ^{12}C *by incident protons of 200 MeV for the coincident angle pairs shown. Measured cross sections are shown as dots with the associated statistical error bars. DWIA calculations, using the same energy-dependent set of potentials as previously, in which nonlocal components in the optical model potentials (with a range parameter of 1.15 fm.) were used, are drawn as continuous curves (calculated using the final-energy prescription) or dashed curves (calculated using the initial-energy prescription). The spectroscopic factors employed to normalize the curves to the data are shown on each graph.*

with the inclusion of a nonlocal component (which had been neglected in the previous calculations). The results of some of these calculations, using a non-local range parameter of 1.15 fm., are shown in figure 4.6, fitted to the experimental data. This value of the range parameter is somewhat larger than that normally employed (typically 0.85 fm.), but was used in the present study as it had been found to give a better fit to the 200 MeV ^{16}O(p,2p) data [Ant81]. In the kinematic region of concern in the present continuum decay study, spectroscopic factors were found to vary by less than 20% for all the coincident angle pairs, compared with the calculations where the nonlocal component was neglected. Changes in the shape of the cross section distributions were negligible.

The primary interest in the ^{12}C(p,2p) quasifree knockout reaction in the present study is its role as the initial step in the proposed reaction mechanism for the production of the observed continuum yield. For the necessary calculations to be performed (described in the following section), DWIA cross sections for (p,2p) knockout were required, for energies of the proton detected at the primary angle (E_1), of 70, 100 and 130 MeV. From the fits to the data in figures 4.3 to 4.5 it can be seen that, at these energies, the DWIA calculations give good agreement with the shape and magnitude of the measured data using a consistent value, close to the average, for the spectroscopic factor. The fact that the absolute value of the spectroscopic factor is lower than that which might be expected as a result of ^{12}C(p,2p) experiments performed at other energies, has no detrimental impact on the application of this DWIA treatment in an understanding of the coincident continuum yield in the present work. In those regions in the present study where the DWIA calculations and spectroscopic factors are less satisfactory, the contribution to the quasifree knockout yield at the three energies of interest is negligible.

4.4 Continuum Decay

The method employed in the extraction of the continuum decay cross sections from the coincident proton data was described in detail in subsection 3.11.3. To summarize, cross sections were determined at three energies of the proton detected at the primary angle, namely, 70±5 MeV, 100±5 MeV and 130±5 MeV. At the primary angle of -20°, six sets of cross sections were obtained as a function of the secondary coincident proton energy at the secondary angles 20°, 45°, 70°, 95°, 120° and 145°, while at the primary angle of -45°, four sets were obtained at the secondary angles 20°, 35°, 85° and 135°. The regions of the coincident proton spectra which are labelled the "continuum" also contain data from the "clean" knockout of protons from the inner $1s_{1/2}$ orbital of ^{12}C. However, the $1s$ state has a relatively large width (of the order of 30 MeV), and, in addition, the cuts on the coincident proton energy spectra intercept a limited region of the kinematic locus of the $1s$ state knockout. It is concluded, therefore, that the contributions of the "clean" $1s_{1/2}$ knockout to the extracted continuum cross sections are small, and may be neglected in the subsequent analysis.

As a first test of the validity of the proposed reaction mechanism, a procedure similar to that employed by Cowley *et al.* [Cow80b] and Ciangaru *et al.* [Cia83] was performed. If one considers this mechanism, in which the incident 200 MeV proton initially interacts with a single target nucleon, is scattered through a relatively small angle (-20° or -45°) in this quasifree process, and is emitted from the nucleus without suffering any further interactions, then the struck nucleon may be thought of as an intranuclear projectile which interacts with the residual nucleus very much like an external projectile striking the nucleus with an energy equal to that which is transferred to the knocked out nucleon by the 200 MeV incident proton. If such a mechanism has indeed some validity, and provided that the yield of quasifree knockout particles is peaked in a particular direction in such a way that a "beam" of intranuclear projectiles may be defined, then the spectrum of protons measured in coincidence with the scattered incident proton should be related to the (p,p′) spectrum measured at the appropriate energy and angle.

In the present work cuts were made corresponding to the detection of protons at the primary angles with energies averaging 70, 100 and 130 MeV, and making some allowance for the knockout of a bound nucleon in the target, it was thus assumed that it was appropriate to compare these data with the ^{12}C(p,p′) singles data measured at the incident proton energies of 120, 90 and 62 MeV respectively. (Strictly, of course, inelastic scattering from a mass-11 system should be used, but as discussed in section 1.3, the expected slight differences between the inelastic data for mass-11 and mass-12 systems over the energy range of interest should not be significant).

The comparison between the measured ^{12}C(p,2p) continuum decay cross sections and the measured ^{12}C(p,p′) inelastic cross sections at the three energies, E_1, are shown in figures 4.7 and 4.8, where the peak in some of the inelastic data sets, due to H(p,p) elastic scattering from the hydrogen contamination in the carbon targets, has been removed where necessary, leading to the gaps in the data shown in the plots. At each primary proton energy, the (p,p′) inelastic data set (the continuous curve) chosen for comparison with the coincidence data (points) at a particular pair of angles (θ_1 and θ_2) was arbitrarily selected from the available data sets to give the best agreement in shape. The inelastic data set was then normalized to fit the absolute magnitude of the coincidence data. The normalization factors used in obtaining the plots in figures 4.7 and 4.8 are listed in table 4.1.

The impressive agreement in the shape of the compared coincident and singles data in the figures provides strong evidence in support of the pro-

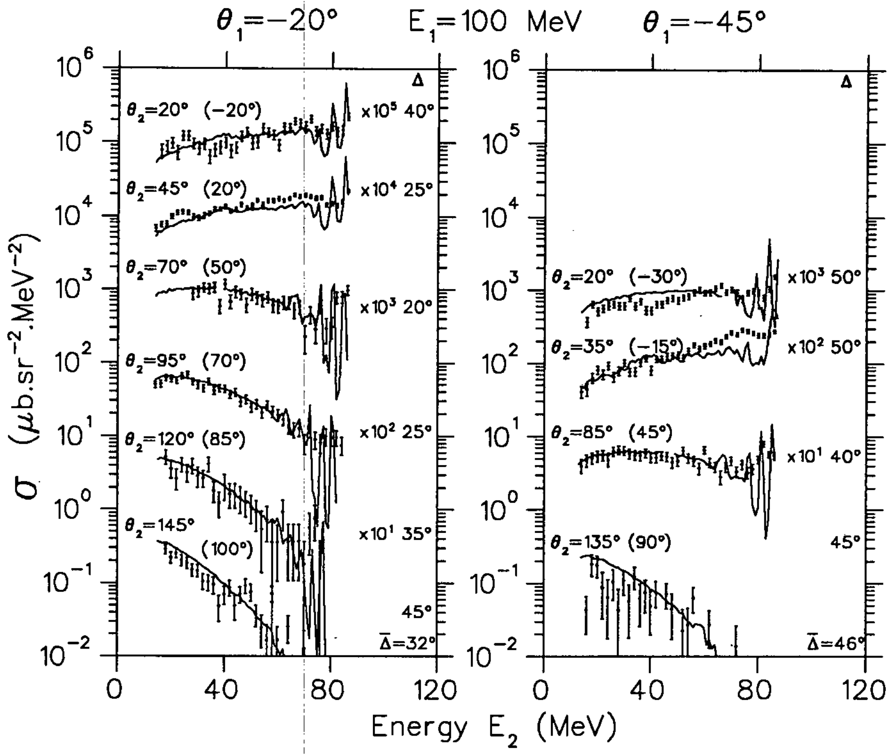

Figure 4.7: *^{12}C(p,2p) continuum decay cross sections as a function of the energy, E_2, of the proton observed at the secondary angle, θ_2. The data are for the primary proton energy of 100±5 MeV. Data for the primary angle (θ_1) of -20° are shown on the left, and those for -45° on the right. The secondary angle is indicated with each data set. Statistical error bars are shown with the data points. The continuous curves are arbitrarily normalized cross section data for ^{12}C(p,p′) inelastic scattering at an incident energy of 90 MeV (shown without error bars for clarity). The peak appearing in some of the ^{12}C(p,p′) data sets due to H(p,p) elastic scattering from the hydrogen contamination of the carbon targets has been removed. The inelastic scattering angles are indicated in parentheses. The value listed in the column, labelled Δ, to the right of each data curve, is the difference between the angle of observation of the secondary coincident proton, θ_2, and the scattering angle of the inelastic data to which the coincident data is compared. The plots are displaced by increasing factors of 10 (as indicated) for clarity.*

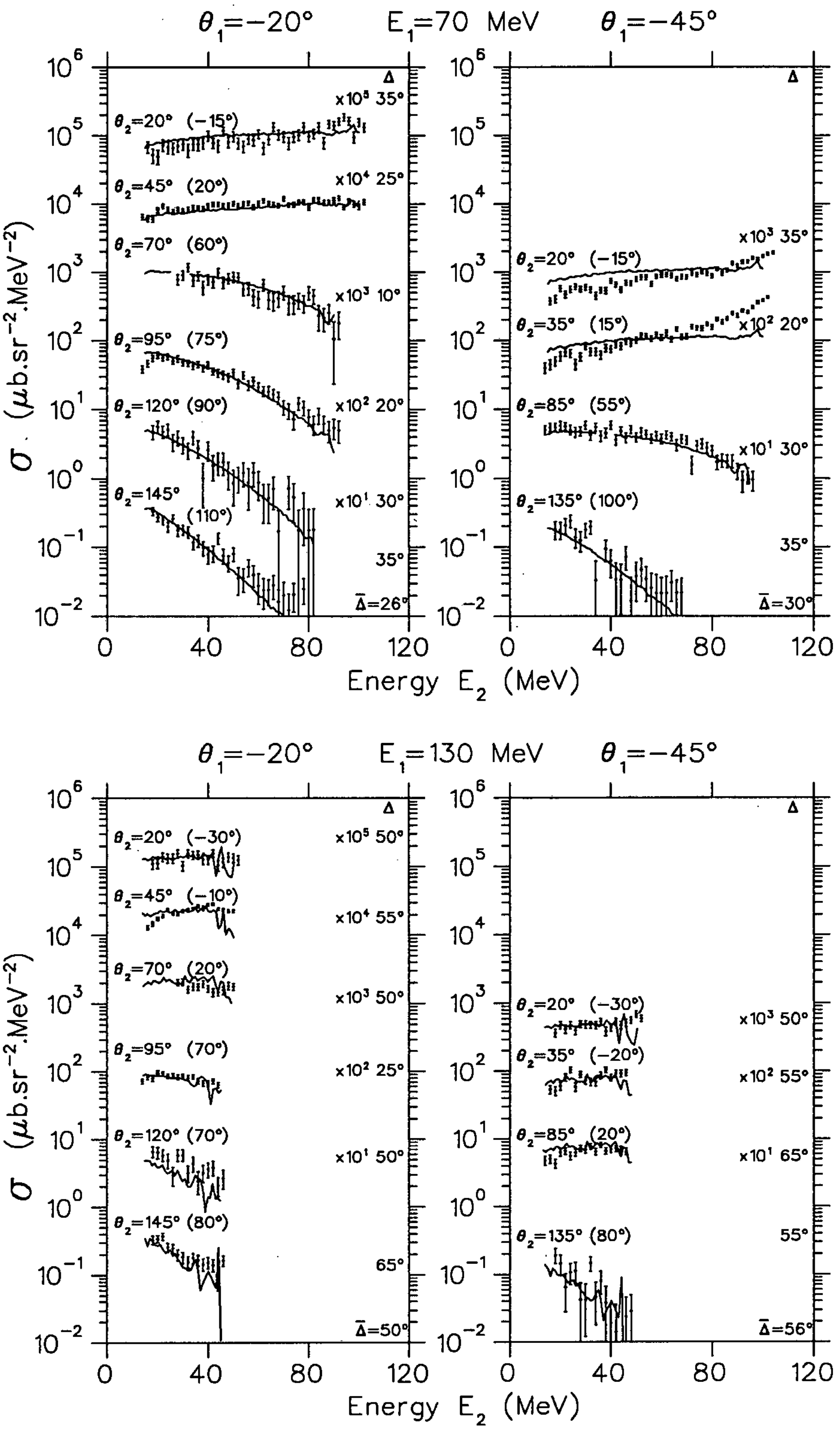

Figure 4.8: *Continuum decay cross sections for E_1=70±5 MeV (above) and E_1=130±5 MeV (below) compared with inelastic (p,p′) measurements at 120 MeV and 62 MeV. Details are similar to those given in figure 4.7.*

E_1	θ_1	θ_2	Normalization
70 MeV	-20°	20°, 45°	1.1×10^{-3}
		70°, 95° 120°,145°	2.4×10^{-3}
	-45°	20°, 35° 85°,135°	1.1×10^{-3}
100 MeV	-20°	20°, 45°	1.1×10^{-3}
		70°, 95° 120°,145°	2.0×10^{-3}
	-45°	20°, 35° 85°,135°	1.1×10^{-3}
130 MeV	-20°	20°, 45°	1.0×10^{-3}
		70°, 95° 120°,145°	1.0×10^{-3}
	-45°	20°, 35° 85°,135°	3.5×10^{-3}

Table 4.1: *Factors used for normalizing the* ^{12}*C(p,p′) inelastic data to the coincident data in figures 4.7 and 4.8.*

posed mechanism in which the nucleons knocked out in the initial quasifree process act as an intranuclear "beam" of particles which interact with the residual nucleus. It is probable that too much emphasis should not be placed on the factors used to normalize the singles data to the continuum spectra, except to say in passing that in their similar analysis of the ^{58}Ni(p,2p) data, also measured at an incident proton energy of 200 MeV, Ciangaru *et al.* [Cia83] obtained relative normalization factors ranging in value between 0.5 and 2.1 (that is, varying by a factor of 4).

Of great interest too, are the angles listed in the column labelled Δ, to the right of each data set. For each set, this is the difference between the angle of observation of the secondary coincident proton, θ_2, and the scattering angle of the inelastic data to which the coincident data are compared — this is the angle θ_2'' shown in figure 1.1 which illustrates the proposed reaction mechanism. If the initial quasifree interaction results in a "beam" of intranuclear projectiles with a reasonably well-defined direction, then each Δ angle should correspond to the average direction in which the knocked out particles are emitted in the initial quasifree process.

As described in section 3.12, in-plane DWIA calculations were performed to model the initial quasifree interaction for both (p,2p) and (p,pn) knockout at the primary energies and angles used in the present experimental study. The results of these calculations, in which both the initial energy (IEP) and final energy (FEP) prescriptions were used for the two-body scattering approximation, are shown in figures 4.9 to 4.14.

The figures show the contribution from the knockout of nucleons from both the *p* state (relative spectroscopic factor = 2.5 as plotted) and the *s* state (relative spectroscopic factor = 1.0), and the summed contribution from these two states. From the figures it can be seen that at a primary angle of -20° the DWIA yield of secondary particles (both protons and neutrons) is relatively sharply peaked at the primary proton energies of 100 and 70 MeV. At 130 MeV the yield exhibits a rather broader distribution with a double-humped character. At a primary angle of -45° the yield is also relatively sharply peaked at primary energies of 100 and 130 MeV, while at 70 MeV the yield has a distribution with two closely-spaced sharp peaks. Table 4.2 lists the average angle of the summed contribution for each set of calculations, together with the appropriate $\bar{\Delta}$ angle taken from the corresponding fits of the (p,p′) singles data to the continuum spectra.

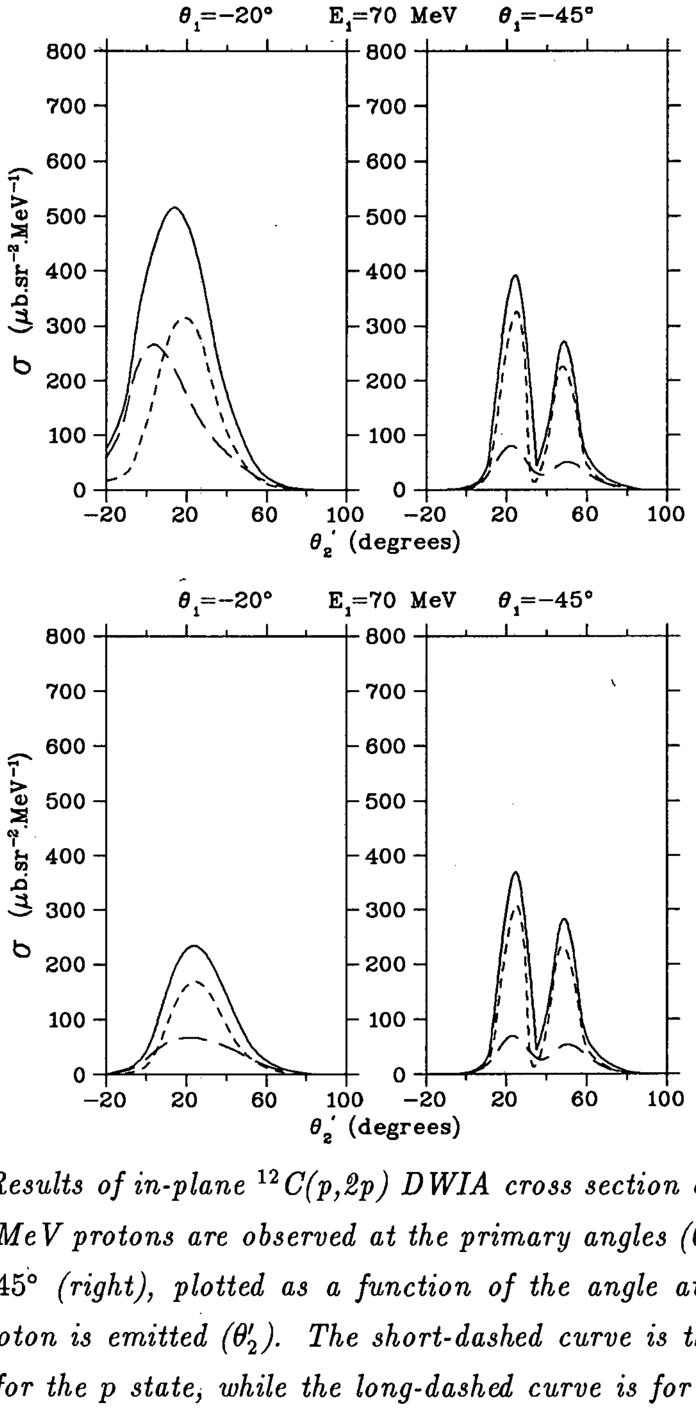

Figure 4.9: *Results of in-plane* ^{12}*C(p,2p) DWIA cross section calculations in which 70 MeV protons are observed at the primary angles* (θ_1) *of* $-20°$ *(left) and* $-45°$ *(right), plotted as a function of the angle at which the secondary proton is emitted* (θ'_2)*. The short-dashed curve is the result of calculations for the p state, while the long-dashed curve is for the s state (spectroscopic factors of 2.5 and 1.0 were used for the two states respectively). The summed cross section for the two states is shown as the continuous curve. Calculations using the final energy prescription (FEP) for the two-body scattering approximation are shown above, while those using the initial energy prescription (IEP) are shown below.*

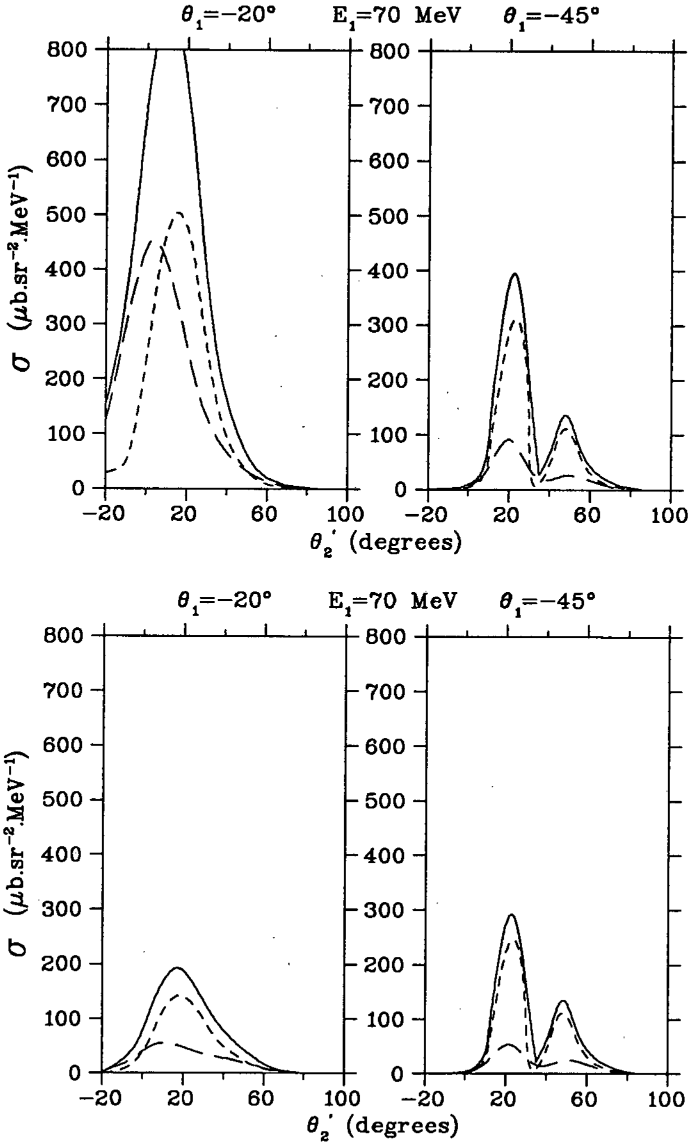

Figure 4.10: *Results of in-plane* $^{12}C(p,pn)$ *DWIA cross section calculations in which 70 MeV protons are observed at the primary angles* (θ_1) *of* $-20°$ *(left) and* $-45°$ *(right), plotted as a function of the angle at which the secondary neutron is emitted* (θ_2')*. FEP calculations are shown above, and IEP calculations below. Other details are similar to figure 4.9.*

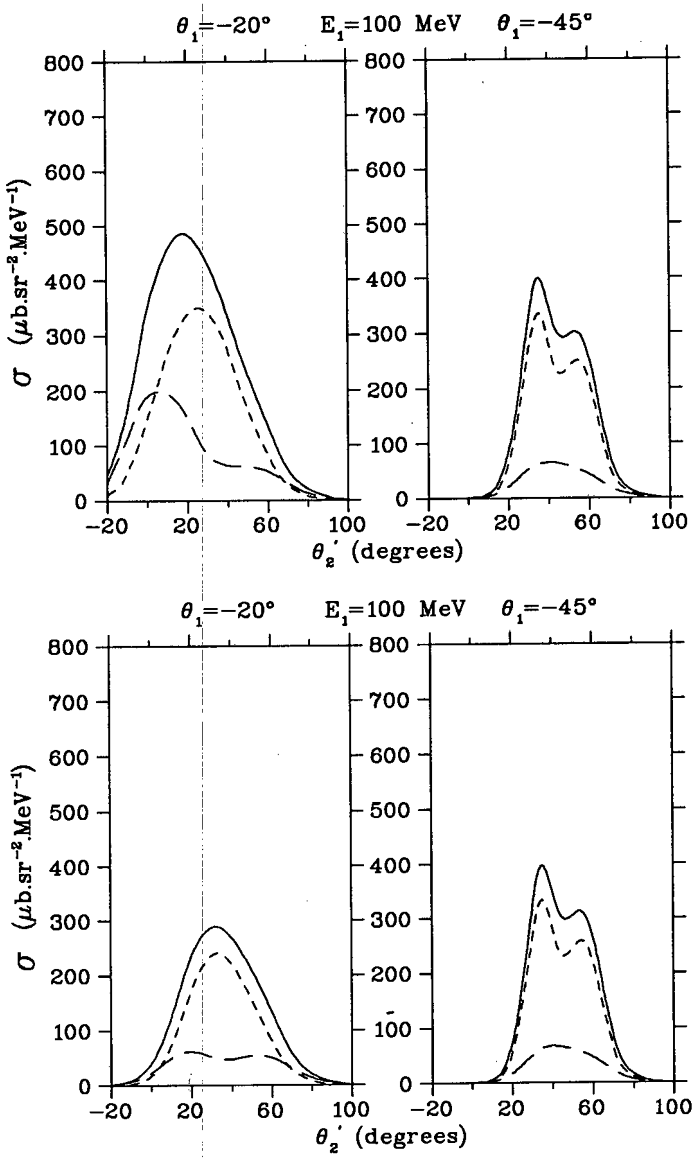

Figure 4.11: *Results of in-plane $^{12}C(p,2p)$ DWIA cross section calculations in which 100 MeV protons are observed at the primary angles (θ_1) of* $-20°$ *(left) and* $-45°$ *(right), plotted as a function of the angle at which the secondary proton is emitted (θ_2'). FEP calculations are shown above, and IEP calculations below. Other details are similar to figure 4.9.*

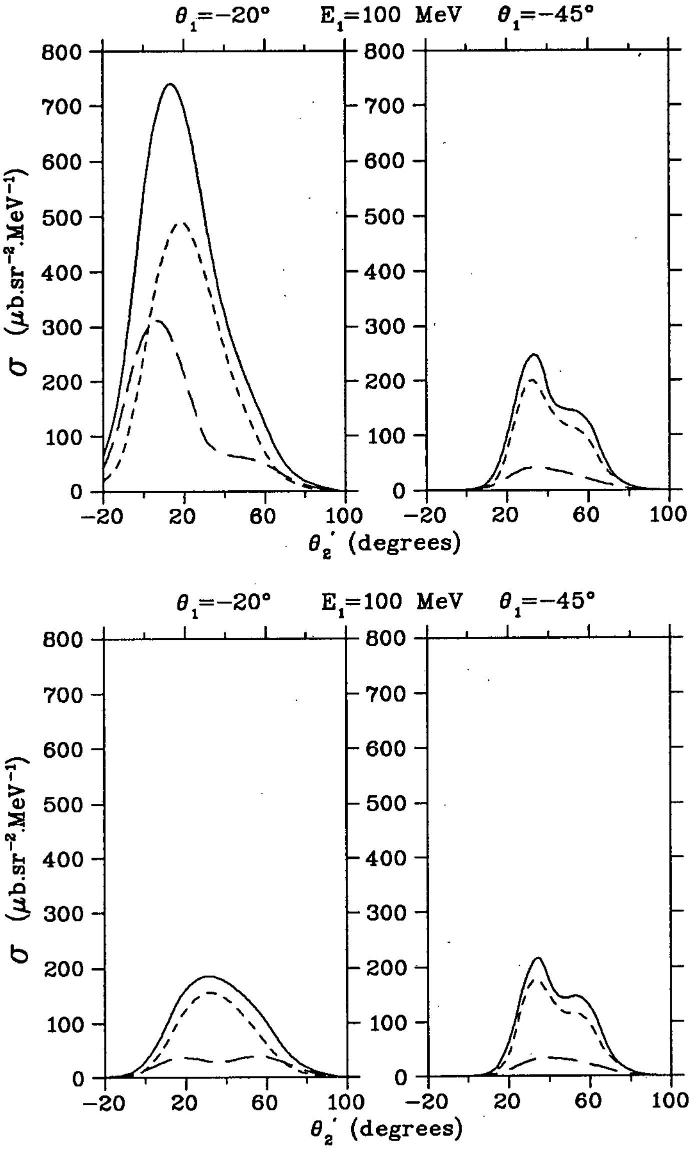

Figure 4.12: *Results of in-plane* ^{12}*C(p,pn) DWIA cross section calculations in which 100 MeV protons are observed at the primary angles* (θ_1) *of* −20° *(left) and* −45° *(right), plotted as a function of the angle at which the secondary neutron is emitted* (θ_2')*. FEP calculations are shown above, and IEP calculations below. Other details are similar to figure 4.9.*

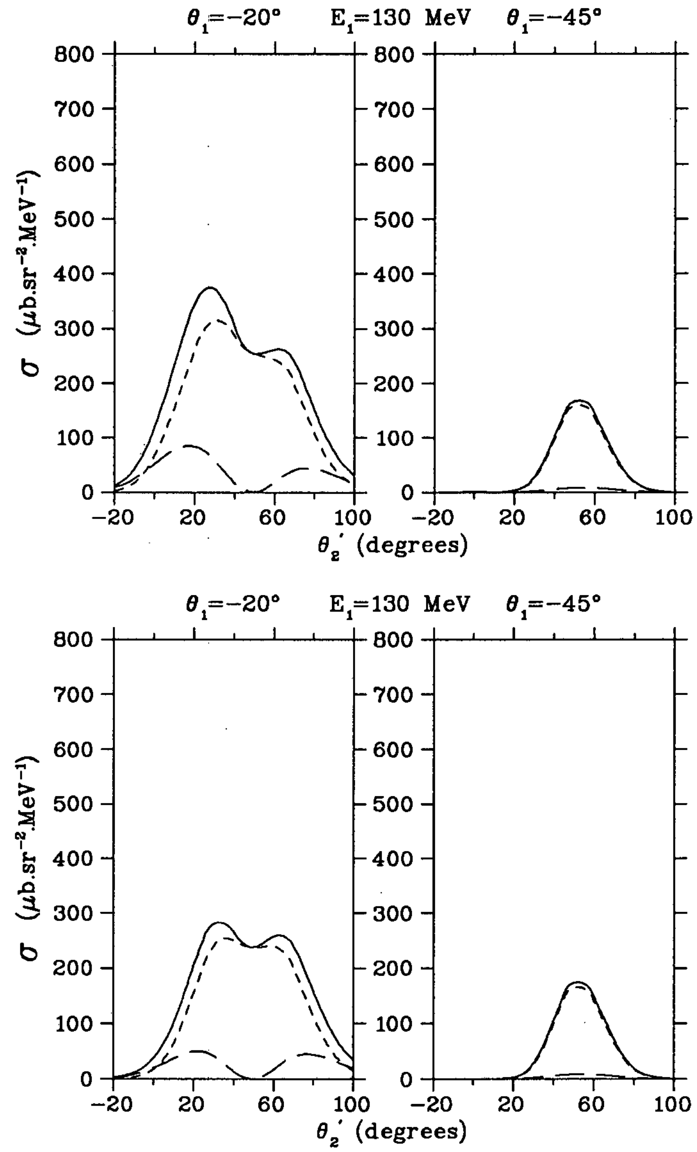

Figure 4.13: *Results of in-plane* $^{12}C(p,2p)$ *DWIA cross section calculations in which 130 MeV protons are observed at the primary angles* (θ_1) *of* −20° *(left) and* −45° *(right), plotted as a function of the angle at which the secondary proton is emitted* (θ_2')*. FEP calculations are shown above, and IEP calculations below. Other details are similar to figure 4.9.*

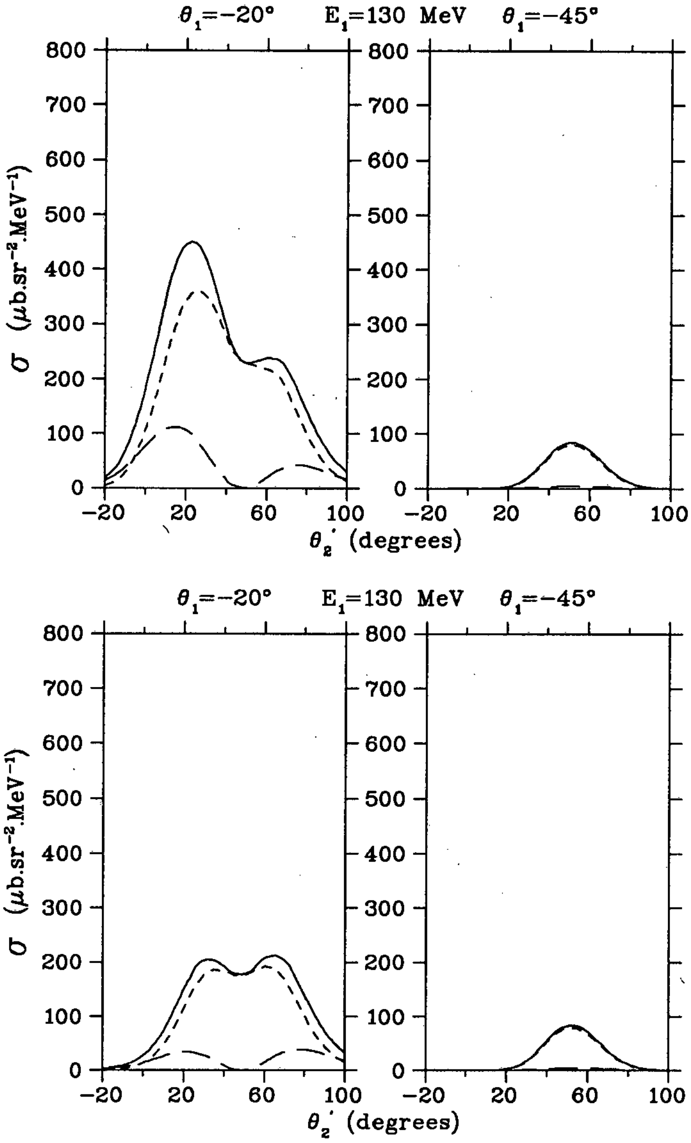

Figure 4.14: *Results of in-plane* $^{12}C(p,pn)$ *DWIA cross section calculations in which 130 MeV protons are observed at the primary angles* (θ_1) *of* −20° *(left) and* −45° *(right), plotted as a function of the angle at which the secondary neutron is emitted* (θ_2')*. FEP calculations are shown above, and IEP calculations below. Other details are similar to figure 4.9.*

E_1	θ_1	IEP		FEP		$\bar{\Delta}$
		(p,2p)	(p,pn)	(p,2p)	(p,pn)	
70 MeV	−20°	24°	18°	14°	11°	26°
	−45°	34°	32°	34°	32°	30°
100 MeV	−20°	35°	31°	19°	16°	32°
	−45°	46°	42°	46°	42°	46°
130 MeV	−20°	50°	50°	40°	42°	50°
	−45°	53°	52°	53°	52°	56°

Table 4.2: *Average direction of the intranuclear "beam" of knocked out nucleons following an initial quasifree interaction between incident protons of 200 MeV and* ^{12}C *target nucleons, as predicted by DWIA calculations in which the knocked out nucleons are described by plane waves. Angles are listed for the three outgoing energies (*E_1 *= 70, 100 and 130 MeV) of the scattered proton observed at the primary angles of observation (*$\theta_1 = -20°$ *and −45°). The angles are the average angles of the knocked out proton or neutron yield, calculated using either the initial energy (IEP) or final energy (FEP) prescription for the two-body scattering approximation. The final column, labelled* $\bar{\Delta}$*, lists the angles obtained when fitting the (p,p′) data to the coincidence cross sections as described in the text.*

It can be seen from this table that the average angles of the DWIA yields for both (p,2p) and (p,pn) knockout are reasonably close to the $\bar{\Delta}$ angles derived from the experimental data fits. At the primary angle of −45° both the IEP and FEP two-body scattering approximation calculations show good agreement with the corresponding $\bar{\Delta}$ angles. At −20°, the IEP calculations predict peak yields at angles very close to the $\bar{\Delta}$ angles, while the FEP calculations are peaked at a somewhat more forward primary angle. All the calculations follow the experimental trend of increasing $\bar{\Delta}$

with increasing primary energy.

Despite the crudeness of this initial test of the proposed reaction mechanism, these results lend clear and encouraging support to the mechanism's validity in describing the observed continuum yields.

The next stage in the interpretation of the extracted experimental continuum cross sections in terms of the proposed reaction mechanism was the calculations of the convolution integrals over in-plane three-body quasifree knockout doorway cross sections and the empirical inelastic scattering probabilities which are assumed to describe the multiple scattering probabilities of the knocked out quasifree particles. The details of this procedure have been described in section 3.13.

The results of the in-plane DWIA calculations, required for input to the convolution procedure, have been shown in figures 4.9 to 4.14 for both (p,2p) and (p,pn) knockout, using plane waves (for reasons described in section 3.12) to describe the knocked out nucleons, which are the only particles in the model which are assumed to interact explicitly with the residual nucleus. Also shown in these figures are the results using the IEP and FEP for the two-body scattering approximations. It can be seen from the figures that at the primary proton angle, θ_1, of $-45°$ these two extreme approximations result in DWIA cross sections which are virtually identical, both in magnitude and in θ_2' angular distribution. At $\theta_1 = -20°$ however, the two prescriptions give markedly differing magnitudes for the resulting cross sections (the FEP cross sections being consistently larger than corresponding IEP values). The angular distributions of the FEP cross sections are also shifted to lower θ_2' angles relative to the corresponding IEP distributions. In addition, it can be seen that these differences become more marked as the energy of the proton detected at the primary angle decreases. It is suspected that this points primarily to the inadequacy of the on-shell approximations in the DWIA treatment of the off-shell nuceon-nucleon scattering. It should be noted that the ^{12}C nucleus has states which are relatively tightly bound (~16 MeV and ~36 MeV), and this will enhance any off-shell effects in the interaction.

Comparison of the differences in the DWIA cross sections for the proton and neutron knockout yields in the figures indicates the importance of taking the contribution of the latter as well as the former into account when determining the continuum decay yield. Although it is clear from the figures that the angular distribution of the knocked out nucleons are very similar, the magnitude of the yields can be very different. For $\theta_1 = -45°$, the neutron yield is less than the proton yield at all three E_1 energies, but shows a relative increase with decreasing E_1. At $E_1 = 130$ MeV the ratio of the neutron to proton yield is approximately 0.4, at $E_1 = 100$ MeV it is approximately 0.6, and at $E_1 = 70$ MeV it is approximately 0.8. However, for $\theta_1 = -20°$, although the trend is similar with an increasing yield ratio with decreasing E_1 energy, here the relative neutron yield is significantly greater. For the FEP calculations the ratios at the three energies are approximately 1.1, 1.4 and 1.9 respectively, and for the IEP calculations they are 0.8, 0.7 and 0.8. Taking into account the ratio of the (p,n) to (p,p′) differential cross sections (approximately 0.5) and the total reaction cross sections for protons and neutrons (226.2 mb and 345.2 mb respectively), as discussed in section 3.13, this implies that the relative contribution of an initial (p,pn) knockout process to the measured coincident proton continuum yields varies between approximately 0.13 and 0.62 that of the contribution of the (p,2p) knockout process. It is therefore important that such a source of the observed continuum yield which may be significant at certain geometries, should be included in the calculations.

The in-plane convolution procedure was performed at the required primary and secondary proton energies and angles. Contributions from both proton and neutron knockout were taken into account using spectroscopic values of 2.5 and 1.0 for the p and s states in ^{12}C respectively, and the total reaction cross section values, for the interaction of the knocked out protons and neutrons with the residual nucleus, used in the calculations are those specified in section 3.13 (226.2 mb and 345.2 mb respectively).

The results of this convolution procedure are compared with the measured ^{12}C(p,2p) continuum decay cross sections at the three E_1 energies in figures 4.15 to 4.18. In figures 4.15 and 4.16 the DWIA calculations describing the initial quasifree process were performed using the FEP approximation for the two-body scattering approximation, while in the calculations shown in figures 4.17 and 4.18 the IEP approximation was used. Some of the initial results obtained with essentially the same treatment have been published in the literature [Cow88].

No attempt was made to optimize the fit of the calculated continuum decay cross sections to the data by varying the spectroscopic factors from the values quoted above, which are taken from electron scattering results. From the figures it can be seen that good agreement with the data is achieved without the necessity for renormalization. In the $\theta_1 = -45°$ case, where the DWIA cross sections are insensitive to the two-body nucleon-nucleon scattering approximation, the calculated continuum spectra fit the data almost identically. For $\theta_1 = -20°$, the IEP approximation was shown to predict lower knockout nucleon yields than the FEP approximation (figures 4.9 to 4.14), and this is reflected in the corresponding calculated continuum spectra.

At the primary proton energy of 70±5 MeV, the calculated spectra tend to underpredict the measured cross sections, particularly at $\theta_1 = -20°$. This can be explained in terms of the assumption made in the proposed

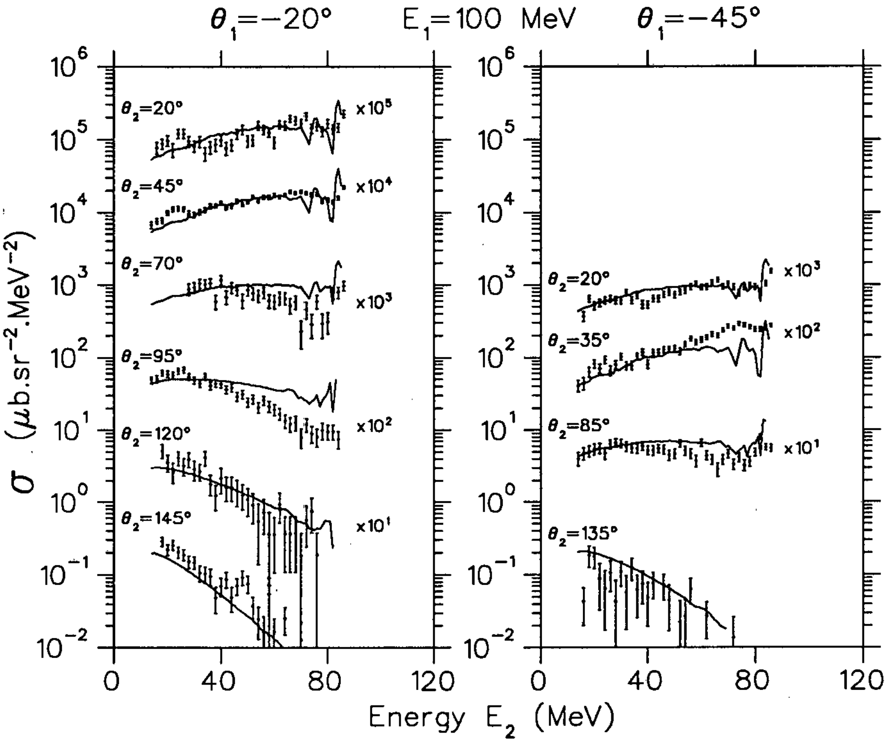

Figure 4.15: *$^{12}C(p,2p)$ continuum decay cross sections as a function of the energy, E_2, of the proton observed at the secondary angle, θ_2. The data are for the primary proton energy of 100±5 MeV. Data for the primary angle (θ_1) of -20° are shown on the left, and those for -45° on the right. The secondary angle is indicated with each data set. Statistical error bars are shown with the data points. The continuous curves are the results of calculations performed by the continuum decay model program in which the contributions from the initial knockout of only in-plane nucleons have been included. The DWIA calculations describing the initial knockout process were performed using the final energy prescription (FEP) for the two-body scattering approximation. The plots are displaced by increasing factors of 10 (as indicated) for clarity.*

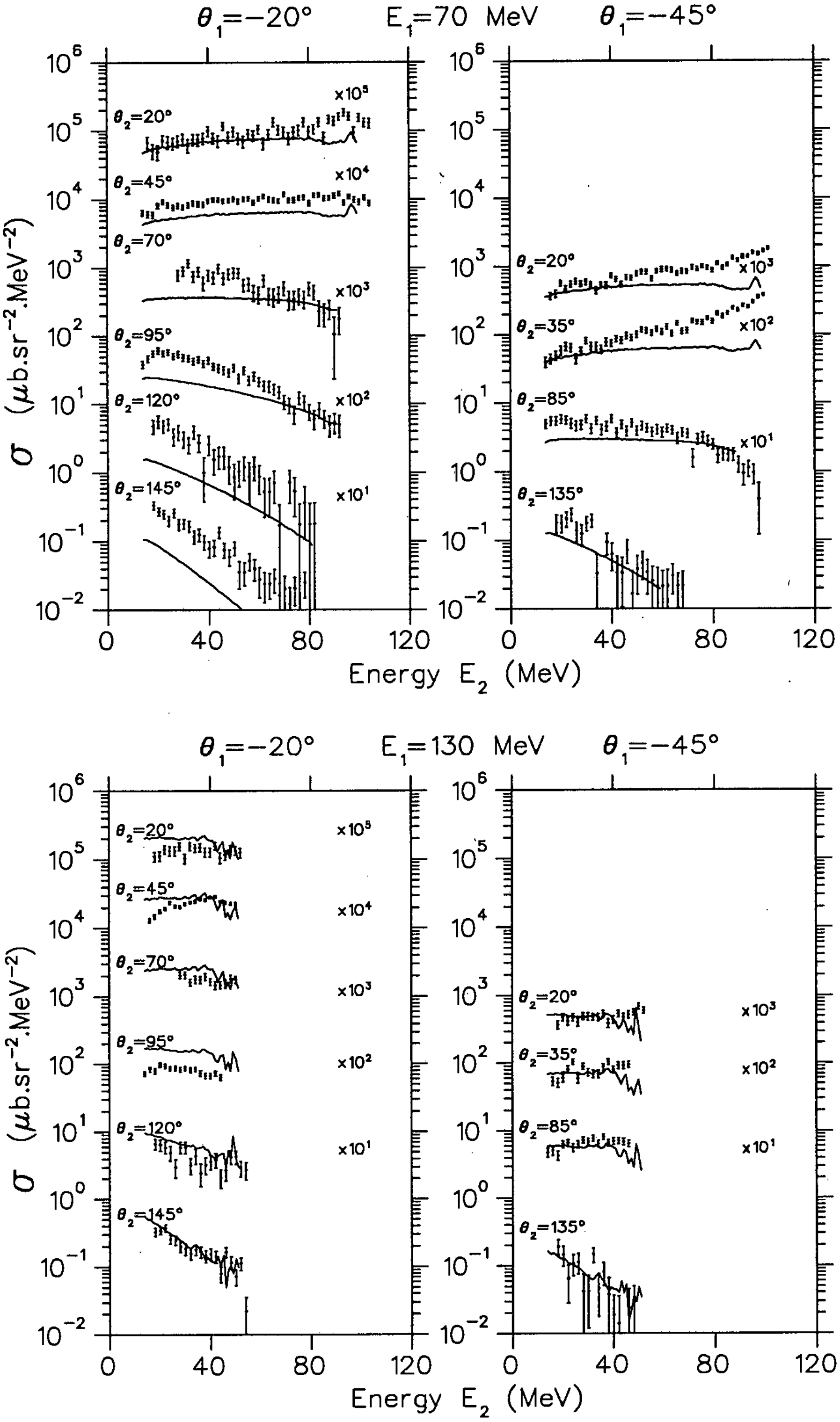

Figure 4.16: *^{12}C(p,2p) continuum decay cross sections for E_1=70±5 MeV (above) and E_1=130±5 MeV (below) compared with in-plane continuum decay model calculations. The DWIA calculations describing the initial knockout process were performed using the final energy prescription (FEP) for the two-body scattering approximation. Details are similar to those given in figure 4.15.*

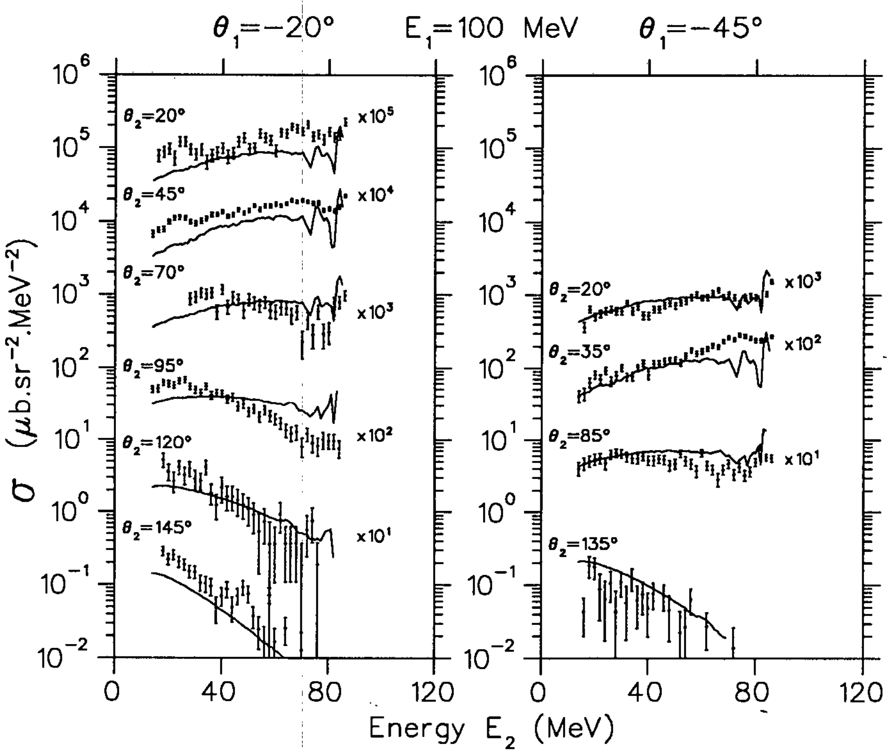

Figure 4.17: *^{12}C(p,2p) continuum decay cross sections as a function of the energy, E_2, of the proton observed at the secondary angle, θ_2. The data are for the primary proton energy of 100±5 MeV. Data for the primary angle (θ_1) of -20° are shown on the left, and those for -45° on the right. The secondary angle is indicated with each data set. Statistical error bars are shown with the data points. The continuous curves are the results of calculations performed by the continuum decay model program in which the contributions from the initial knockout of only in-plane nucleons have been included. The DWIA calculations describing the initial knockout process were performed using the initial energy prescription (IEP) for the two-body scattering approximation. The plots are displaced by increasing factors of 10 (as indicated) for clarity.*

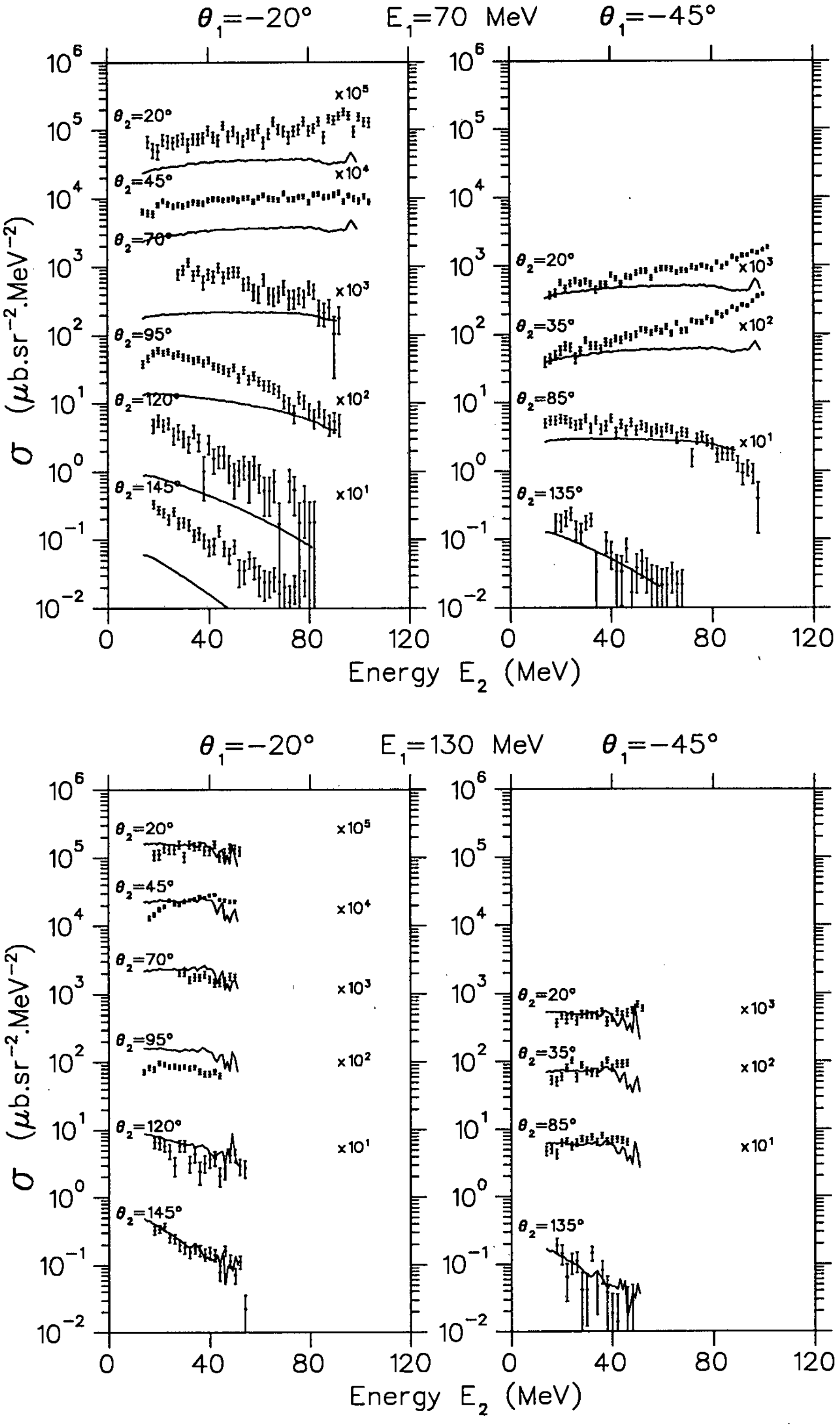

Figure 4.18: $^{12}C(p,2p)$ *continuum decay cross sections for* $E_1=70\pm5$ *MeV (above) and* $E_1=130\pm5$ *MeV (below) compared with in-plane continuum decay model calculations. The DWIA calculations describing the initial knockout process were performed using the initial energy prescription (IEP) for the two-body scattering approximation. Details are similar to those given in figure 4.17.*

model that the proton detected at the primary angle is the scattered incident proton, which emerges from the nucleus after the initial quasifree knockout process without undergoing any further interactions. This assumption is expected to be reasonably valid only when the energy of this proton is relatively large. As this energy decreases it is expected that more and more of the protons detected at this angle have resulted from the further interaction of the incident and knocked out nucleons with the residual nucleus following the initial quasifree process. The fact that there are more protons than predicted by the model at this energy supports this expectation.

At the secondary angles, θ_2, close to 90°, there is a tendency (particularly at the primary energies of 70 and 100 MeV) for the calculated cross sections not to decrease as rapidly as a function of energy E_2 as the measured cross sections. It has been seen in the fit of the inelastic (p,p′) data to the measured spectra (figures 4.7 and 4.8) that a fit with a suitable slope may be achieved by selecting an appropriate inelastic data set. This suggests that, in the θ_2 region close to 90°, the DWIA treatment predicts angular distributions of knocked out nucleons peaked at angles which result in average θ_2'' scattering angles (the angle between the knocked out nucleon before interaction with the residual nucleus and the secondary angle at which the proton is detected after this interaction) which are somewhat too small.

By considering only the in-plane nucleon knockout contribution to the continuum yields, this treatment in effect assumes an out-of-plane integration step of unity. That is, the out-of-plane value for the DWIA cross section is assumed to be constant, equal to the calculated in-plane (0°) DWIA cross section, in the out-of-plane range of 0.0 ± 0.5 radians ($0.0\pm28.6°$). A more rigorous treatment, which includes the out-of-plane knockout contributions explicitly, was developed in the present study and has been described in section 3.13.

The results of the DWIA calculations which were performed to model the initial quasifree interaction for both ^{12}C(p,2p) and ^{12}C(p,pn) knockout, in which the knocked out nucleons are emitted both in- and out-of-plane (angle β), are shown in figures 4.19 to 4.30.

In these figures surface curves are drawn depicting the DWIA cross sections as a function of the in-plane angle at which the knocked out nucleon is emitted, θ_2', and the out-of-plane angle, β. The rectangular surface grid is drawn in 5° increments along both the θ_2' and β axes. The cross section value axes (z-axes) of all the plots are normalized to the same value so that intelligent comparisons can be made — the absolute values may be inferred by referring to the in-plane plots of figures 4.9 to 4.14. Cross sections are shown for p and s state knockout at the three energies of interest of the primary proton using both the IEP and FEP approximations at the θ_1 primary angles of $-20°$ and $-45°$.

It is apparent from these figures that, except in the case of both proton and neutron knockout at $E_1 = 130$ MeV and $\theta_1 = -20°$, the cross sections fall off very rapidly with increasing out-of-plane angle. In the $E_1 = 130$ MeV, $\theta_1 = -20°$ case the distributions are somewhat broader with the rapid fall-off in cross section starting closer to 15° out-of-plane.

The convolution procedure taking into account the out-of-plane contributions was performed at the required primary and secondary proton energies and angles, using the same total neutron and proton reaction cross section values as were used in the in-plane procedure described above, and relative spectroscopic factor values of 1.0 for the p state and 0.4 for the s state (the ratio of the p to s state spectroscopic factors was obtained from electron scattering results). The resulting cross sections were then normal-

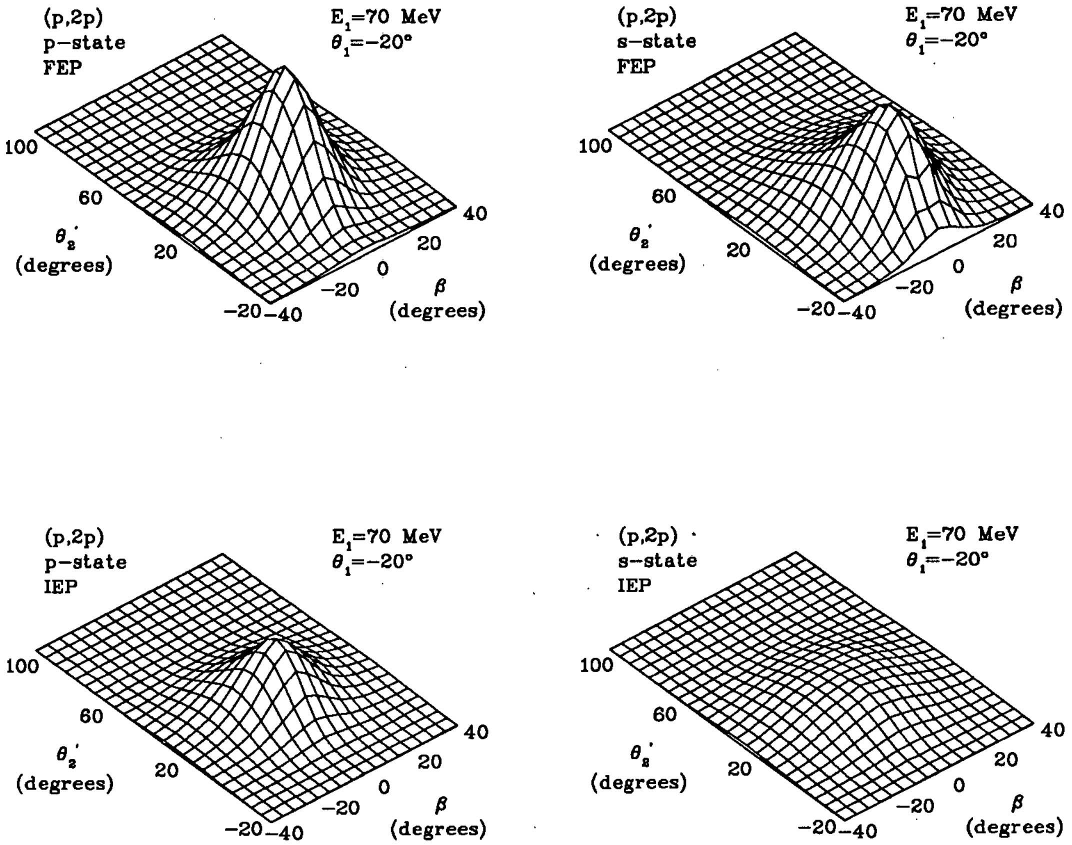

Figure 4.19: *Results of in- and out-of-plane* ^{12}*C(p,2p) DWIA cross section calculations in which 70 MeV protons are observed at the primary angle* (θ_1) *of* $-20°$, *plotted as a function of the in-plane angle at which the secondary proton is emitted* (θ_2') *and the out-of-plane angle* (β). *The plotted surface grid is in* $5°$ *increments along the* θ_2' *and* β *axes. The two surface curves at the top are from calculations using the FEP approximation, and the two at the bottom from IEP approximation calculations. The two curves on the left are for p state knockout, and the two on the right for s state. The cross section value axes (z-axes) are all normalized to the same value for comparison purposes (the absolute values may be inferred by comparing with the in-plane plots of figures 4.9 to 4.14.*

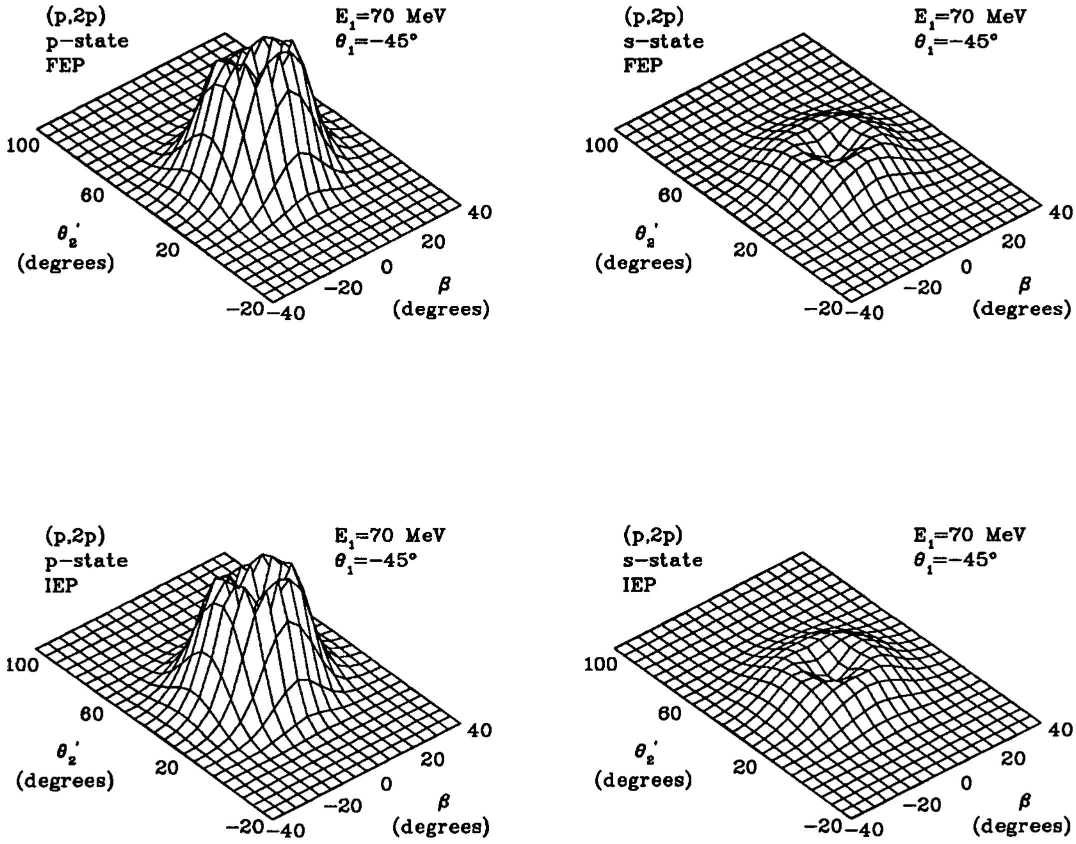

Figure 4.20: *Results of in- and out-of-plane* ^{12}*C(p,2p) DWIA cross section calculations in which 70 MeV protons are observed at the primary angle* (θ_1) *of* −45°. *Other details are similar to those given in figure 4.19.*

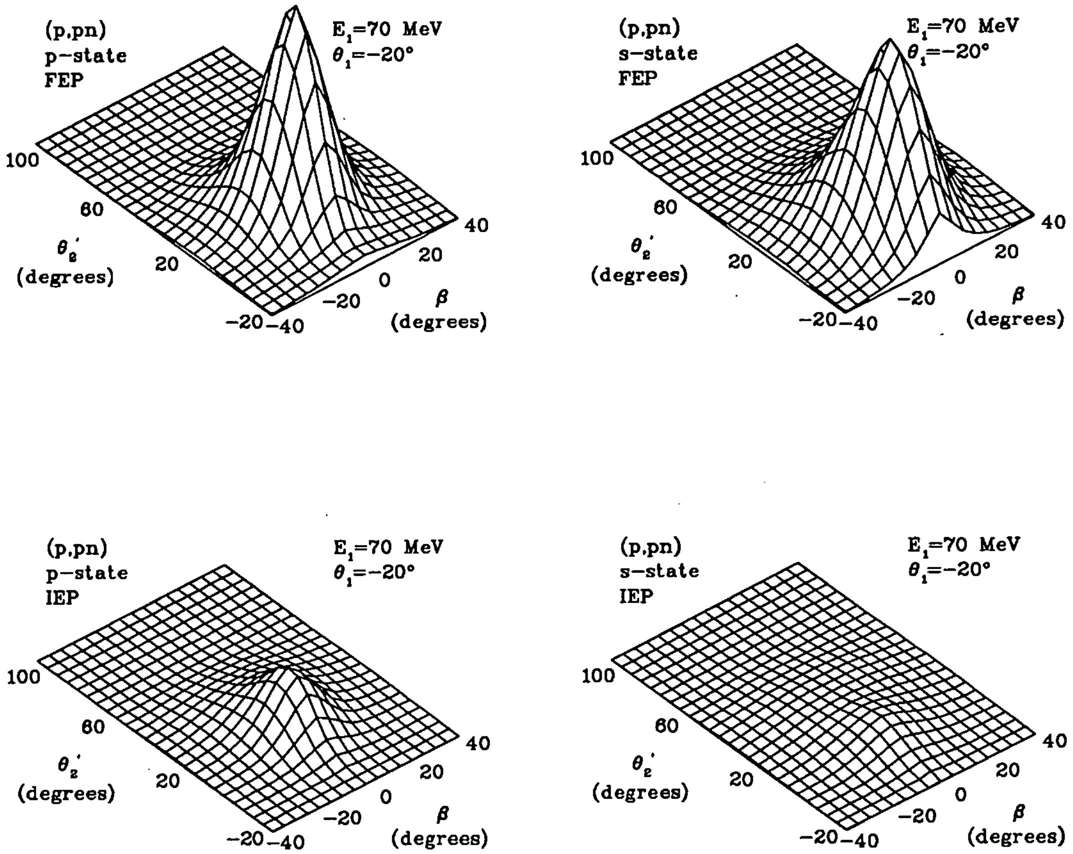

Figure 4.21: *Results of in- and out-of-plane* ^{12}*C(p,pn) DWIA cross section calculations in which 70 MeV protons are observed at the primary angle (θ_1) of −20°. Other details are similar to those given in figure 4.19.*

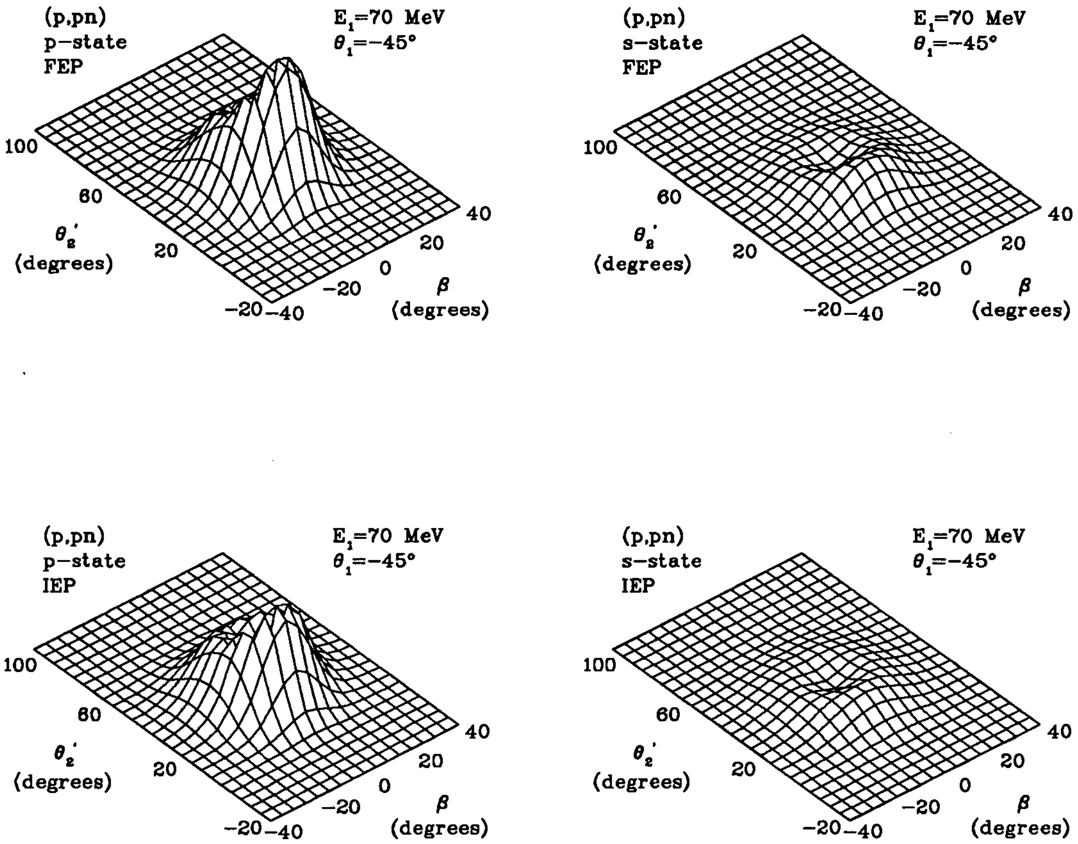

Figure 4.22: *Results of in- and out-of-plane* ^{12}*C(p,pn) DWIA cross section calculations in which 70 MeV protons are observed at the primary angle* *(θ_1) of* $-45°$. *Other details are similar to those given in figure 4.19.*

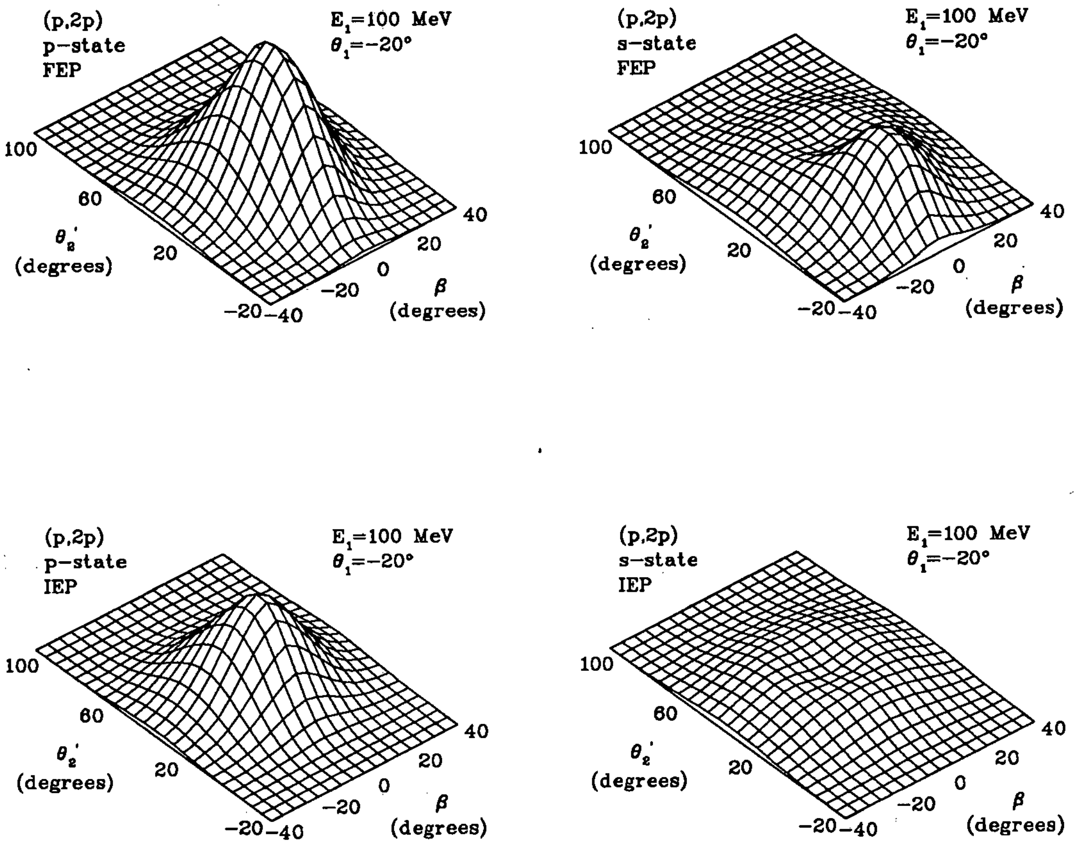

Figure 4.23: *Results of in- and out-of-plane* ^{12}*C(p,2p) DWIA cross section calculations in which 100 MeV protons are observed at the primary angle* (θ_1) *of* −20°. *Other details are similar to those given in figure 4.19.*

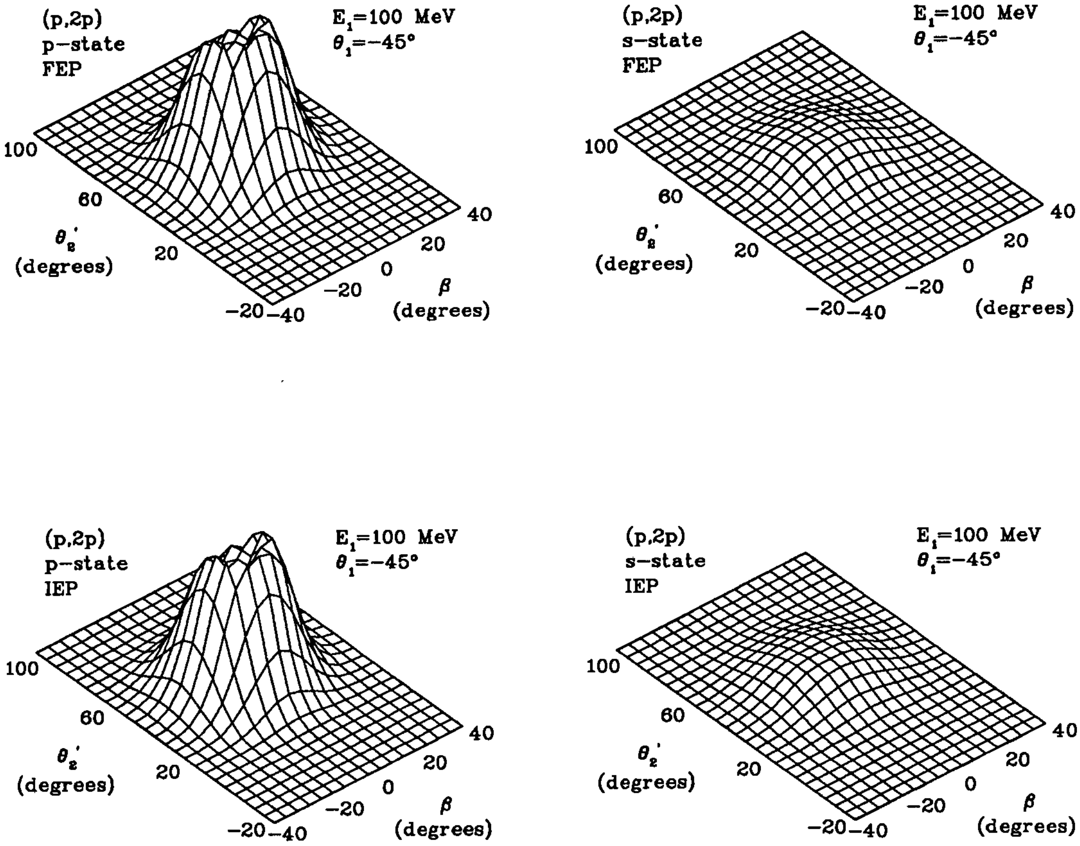

Figure 4.24: *Results of in- and out-of-plane* ^{12}*C(p,2p) DWIA cross section calculations in which 100 MeV protons are observed at the primary angle* (θ_1) *of* $-45°$. *Other details are similar to those given in figure 4.19.*

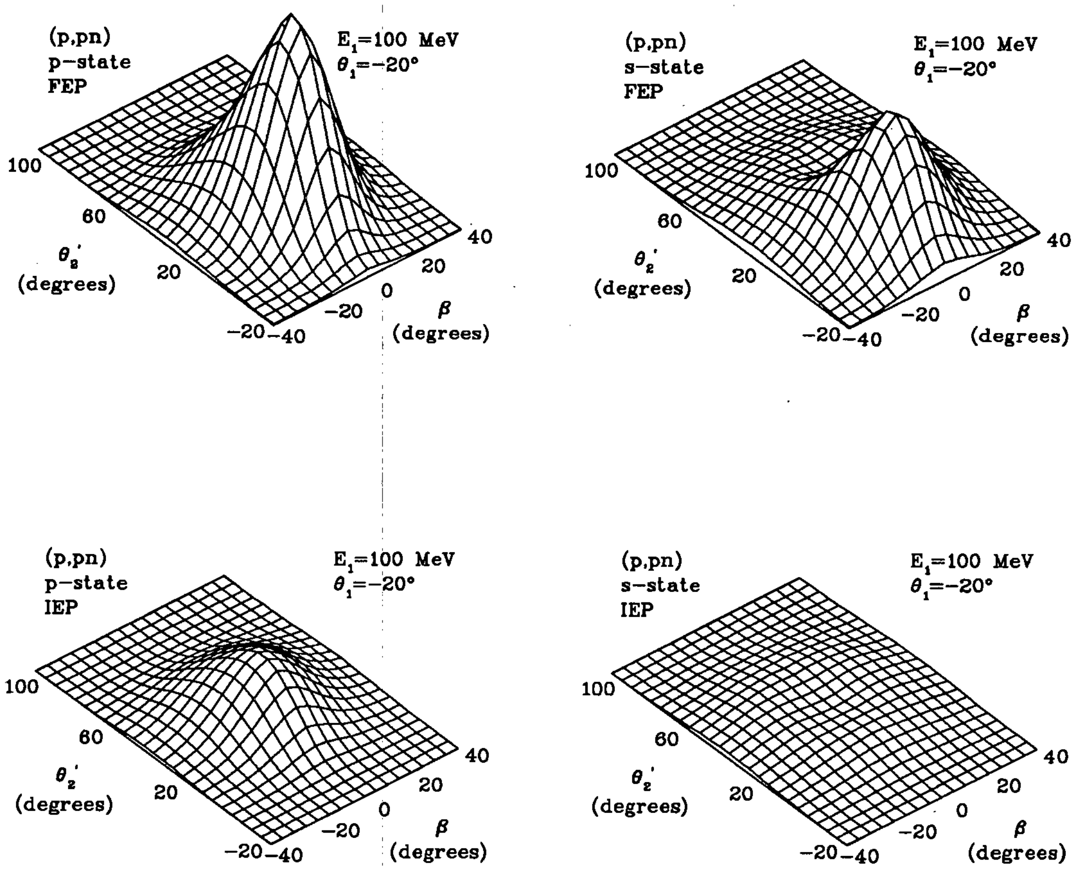

Figure 4.25: *Results of in- and out-of-plane* ^{12}*C(p,pn) DWIA cross section calculations in which 100 MeV protons are observed at the primary angle* (θ_1) *of* −20°. *Other details are similar to those given in figure 4.19.*

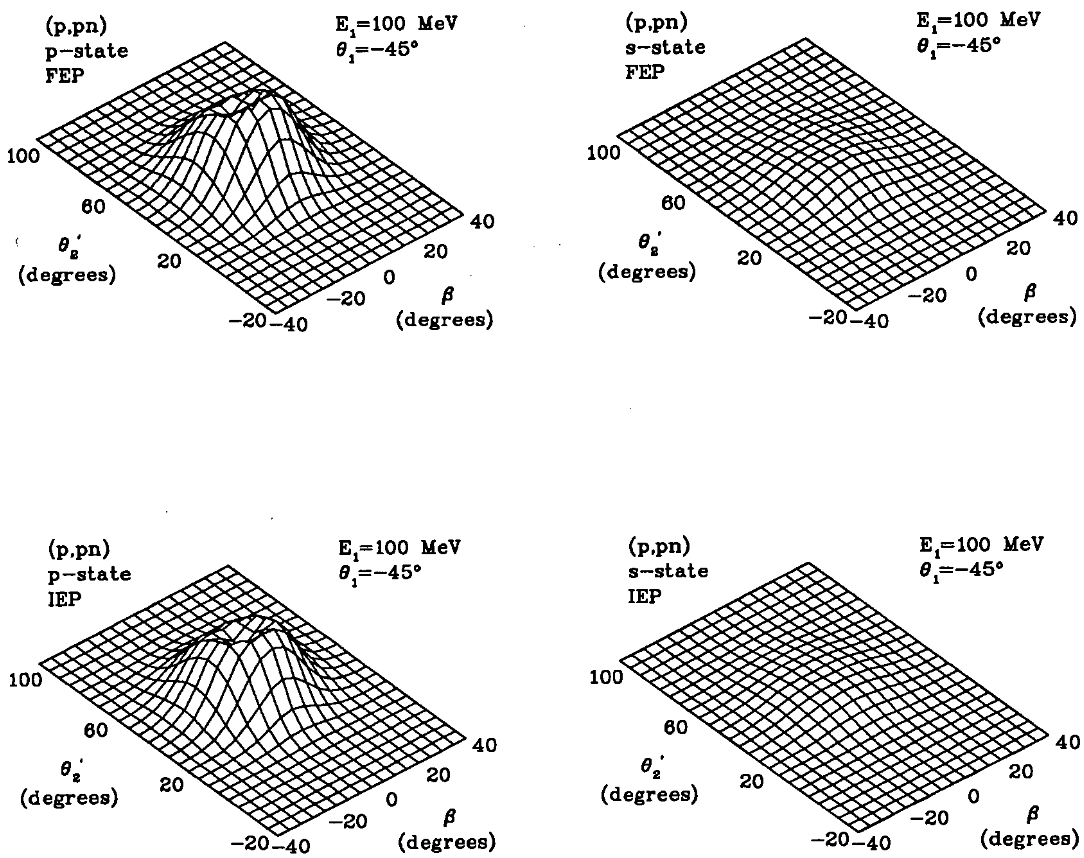

Figure 4.26: *Results of in- and out-of-plane* ^{12}*C(p,pn) DWIA cross section calculations in which 100 MeV protons are observed at the primary angle* (θ_1) *of* –45°. *Other details are similar to those given in figure 4.19.*

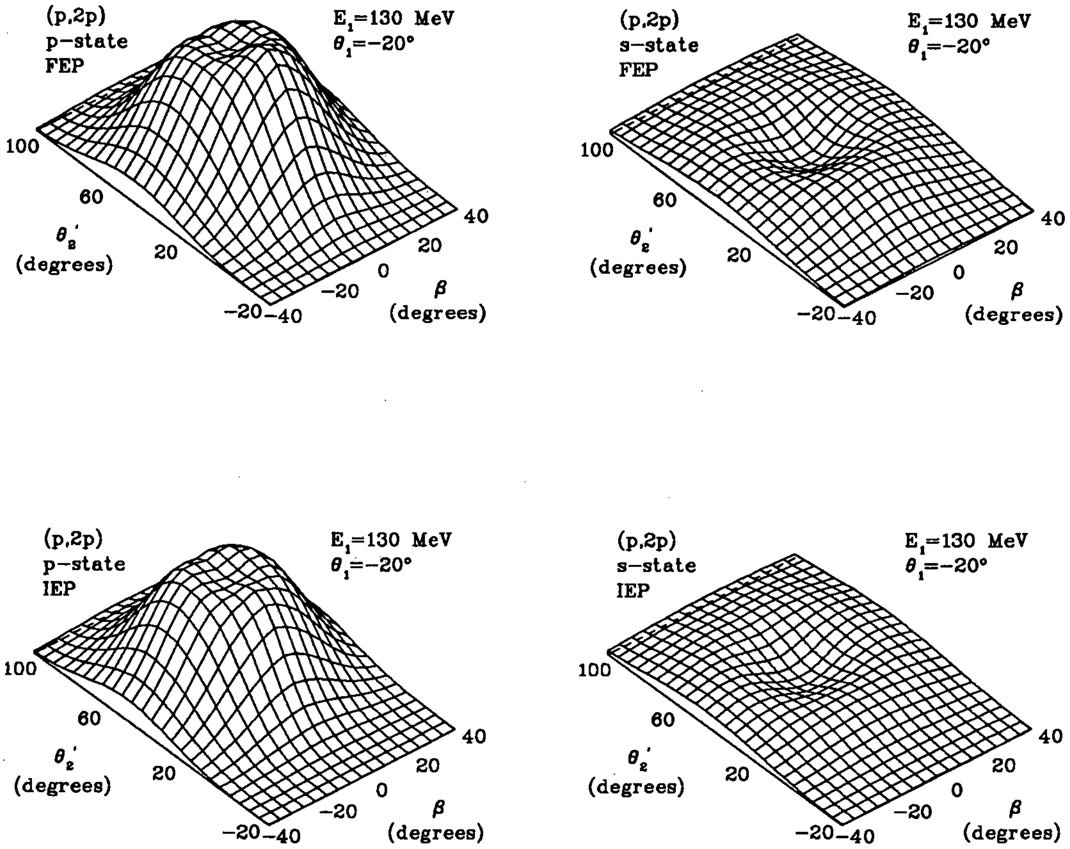

Figure 4.27: *Results of in- and out-of-plane $^{12}C(p,2p)$ DWIA cross section calculations in which 130 MeV protons are observed at the primary angle (θ_1) of $-20°$. Other details are similar to those given in figure 4.19.*

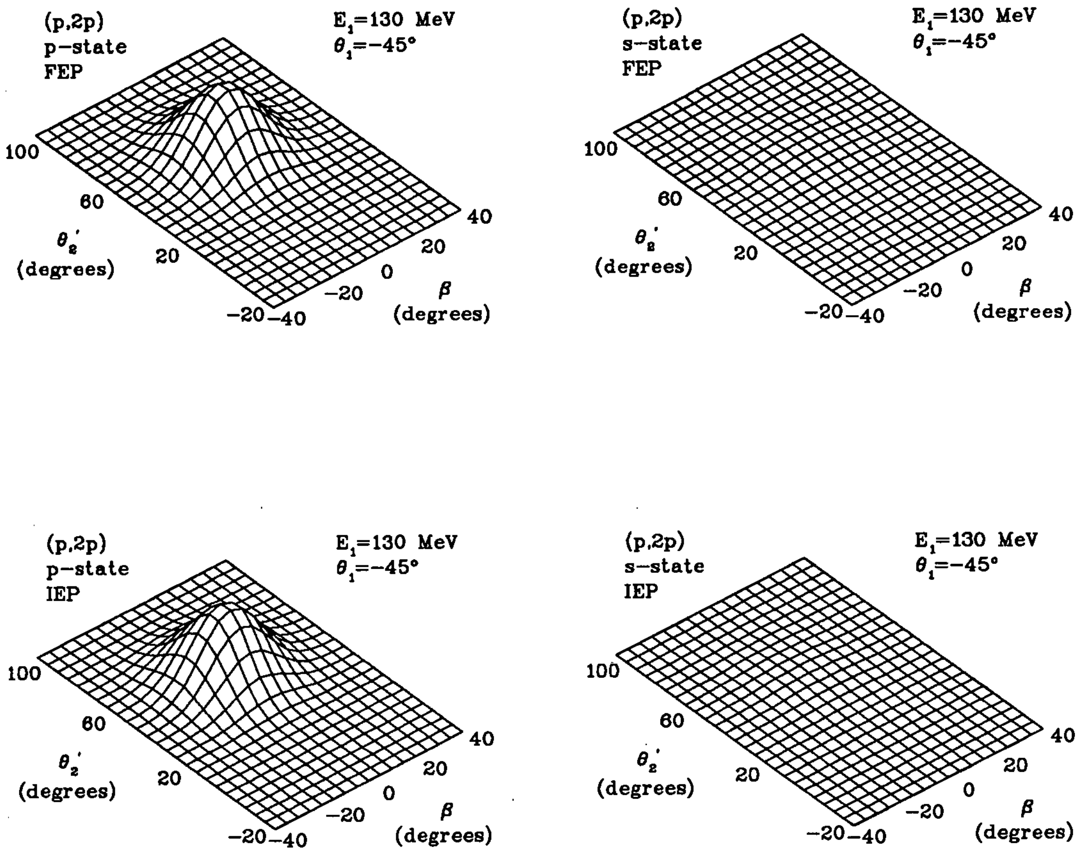

Figure 4.28: *Results of in- and out-of-plane* ^{12}*C(p,2p) DWIA cross section calculations in which 130 MeV protons are observed at the primary angle* (θ_1) *of* −45°. *Other details are similar to those given in figure 4.19.*

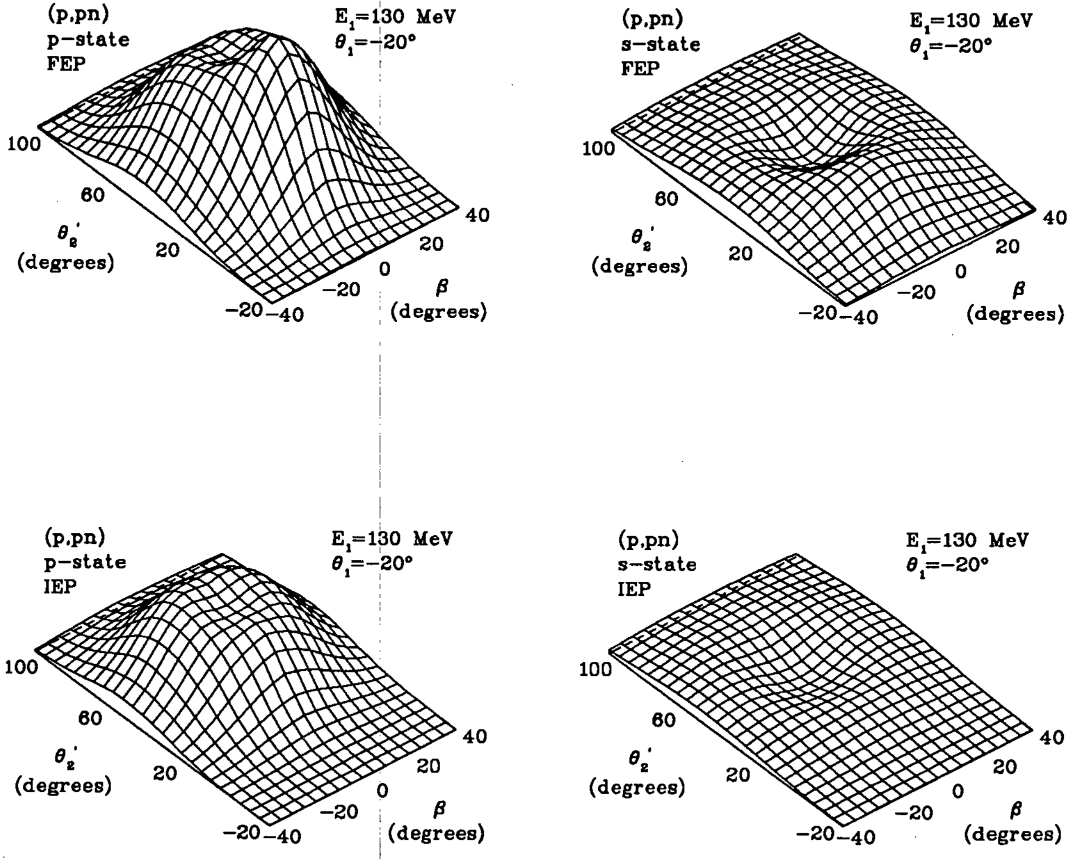

Figure 4.29: *Results of in- and out-of-plane* ^{12}*C(p,pn) DWIA cross section calculations in which 130 MeV protons are observed at the primary angle* (θ_1) *of* −20°. *Other details are similar to those given in figure 4.19.*

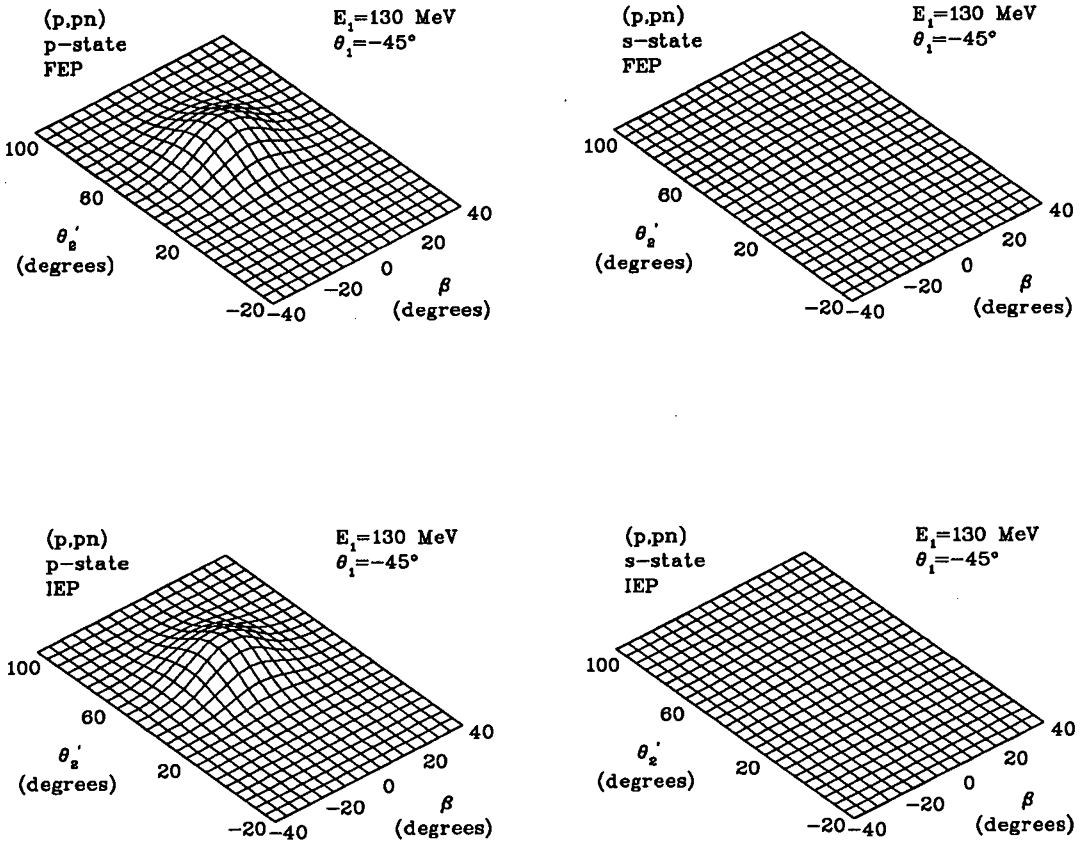

Figure 4.30: *Results of in- and out-of-plane* ^{12}*C(p,pn) DWIA cross section calculations in which 130 MeV protons are observed at the primary angle* (θ_1) *of -45°. Other details are similar to those given in figure 4.19.*

ized to the experimental cross section data to give an effective spectroscopic factor for each data set.

The normalized results of the convolution procedure are compared with the measured ^{12}C(p,2p) continuum decay cross sections in figures 4.31 to 4.34, and the effective spectroscopic factors are listed in table 4.3.

Once again, as expected from the results of the calculations shown in figures 4.19 to 4.30, there is good agreement between the calculated and measured cross sections, with the shapes of the calculated spectra being very similar to those resulting from the calculations limited to in-plane calculations.

As before, there is a tendency for the calculated cross sections not to decrease as rapidly as a function of energy E_2 as the measured cross sections, for the data close to the secondary angle, θ_2, of 90°. It has been suggested above that this could be due to the DWIA treatment predicting angular distributions of knocked out nucleons which are peaked at angles which result in average θ_2'' scattering angles which are too small. This in turn implies that the DWIA-predicted angles (θ_2') are too large. It was seen in the analysis of the ^{12}C(p,2p) discrete-state knockout data that, in some cases, the DWIA treatment appears to offset the energy distribution of the coincident proton yield compared to the measured data. If this is interpreted in terms of the kinematics of the reaction, this may suggest an angular distribution which has some angular offset compared to the experimental data. However, the observed differences in the knockout energy distributions only occur in kinematic regions where the assumed contribution to the continuum decay yield (at E_1 values of 70, 100 and 130 MeV) is negligible. This could then be a valid argument only if the assumption that the primary proton does not undergo further interactions with the residual nucleus after the initial quasifree scattering is untrue. As has been indi-

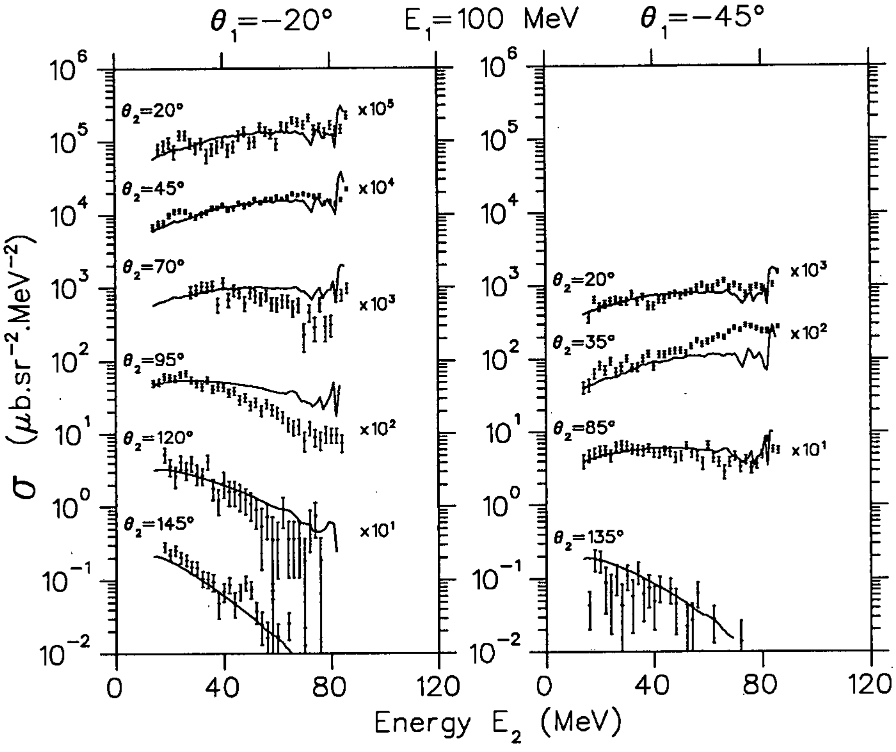

Figure 4.31: *$^{12}C(p,2p)$ continuum decay cross sections as a function of the energy, E_2, of the proton observed at the secondary angle, θ_2. The data are for the primary proton energy of 100±5 MeV. Data for the primary angle (θ_1) of -20° are shown on the left, and those for -45° on the right. The secondary angle is indicated with each data set. Statistical error bars are shown with the data points. The continuous curves are the results of calculations performed by the continuum decay model program in which the contributions from the initial knockout of both in-plane and out-of-plane nucleons have been included. The DWIA calculations describing the initial knockout process were performed using the final energy prescription (FEP) for the two-body scattering approximation. The plots are displaced by increasing factors of 10 (as indicated) for clarity.*

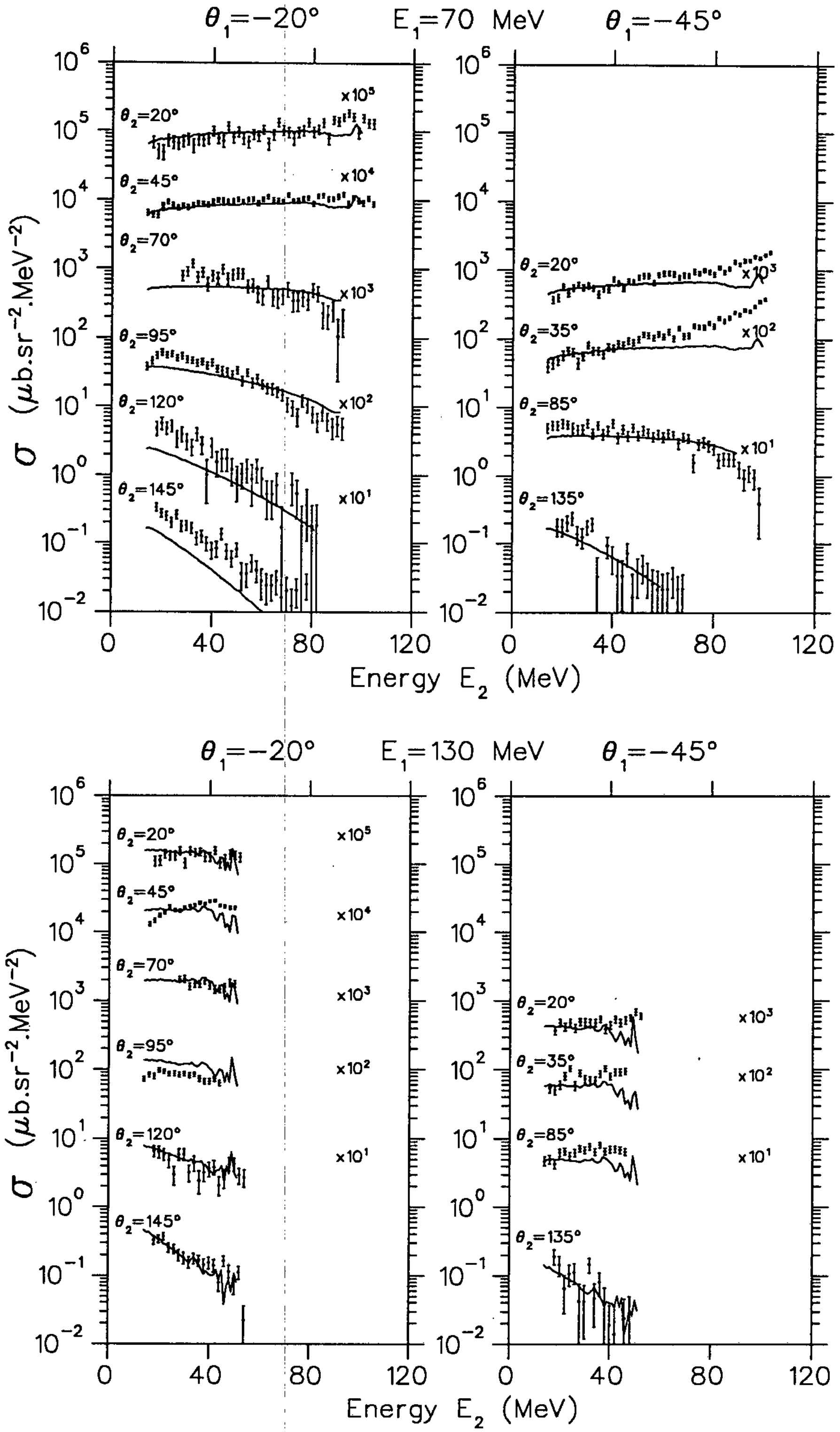

Figure 4.32: $^{12}C(p,2p)$ *continuum decay cross sections for* E_1*=70±5 MeV (above) and* E_1*=130±5 MeV (below) compared with continuum decay model calculations including both in- and out-of-plane knockout contributions. The DWIA calculations describing the initial knockout process were performed using the final energy prescription (FEP) for the two-body scattering approximation. Details are similar to those given in figure 4.31.*

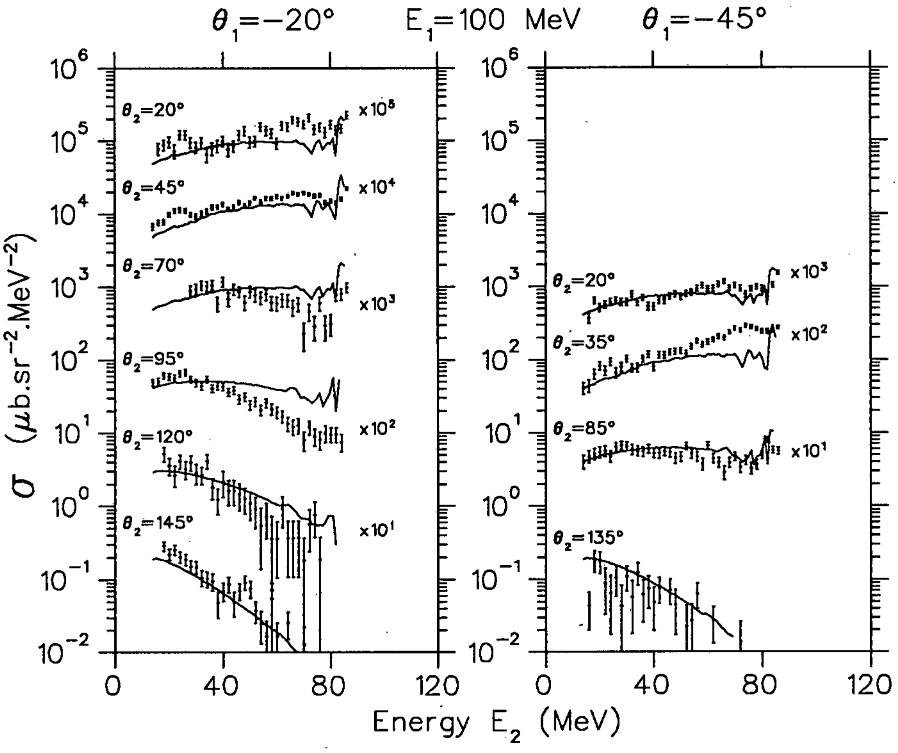

Figure 4.33: ^{12}*C(p,2p) continuum decay cross sections as a function of the energy,* E_2*, of the proton observed at the secondary angle,* θ_2*. The data are for the primary proton energy of 100±5 MeV. Data for the primary angle* (θ_1) *of -20° are shown on the left, and those for -45° on the right. The secondary angle is indicated with each data set. Statistical error bars are shown with the data points. The continuous curves are the results of calculations performed by the continuum decay model program in which the contributions from the initial knockout of both in-plane and out-of-plane nucleons have been included. The DWIA calculations describing the initial knockout process were performed using the initial energy prescription (IEP) for the two-body scattering approximation. The plots are displaced by increasing factors of 10 (as indicated) for clarity.*

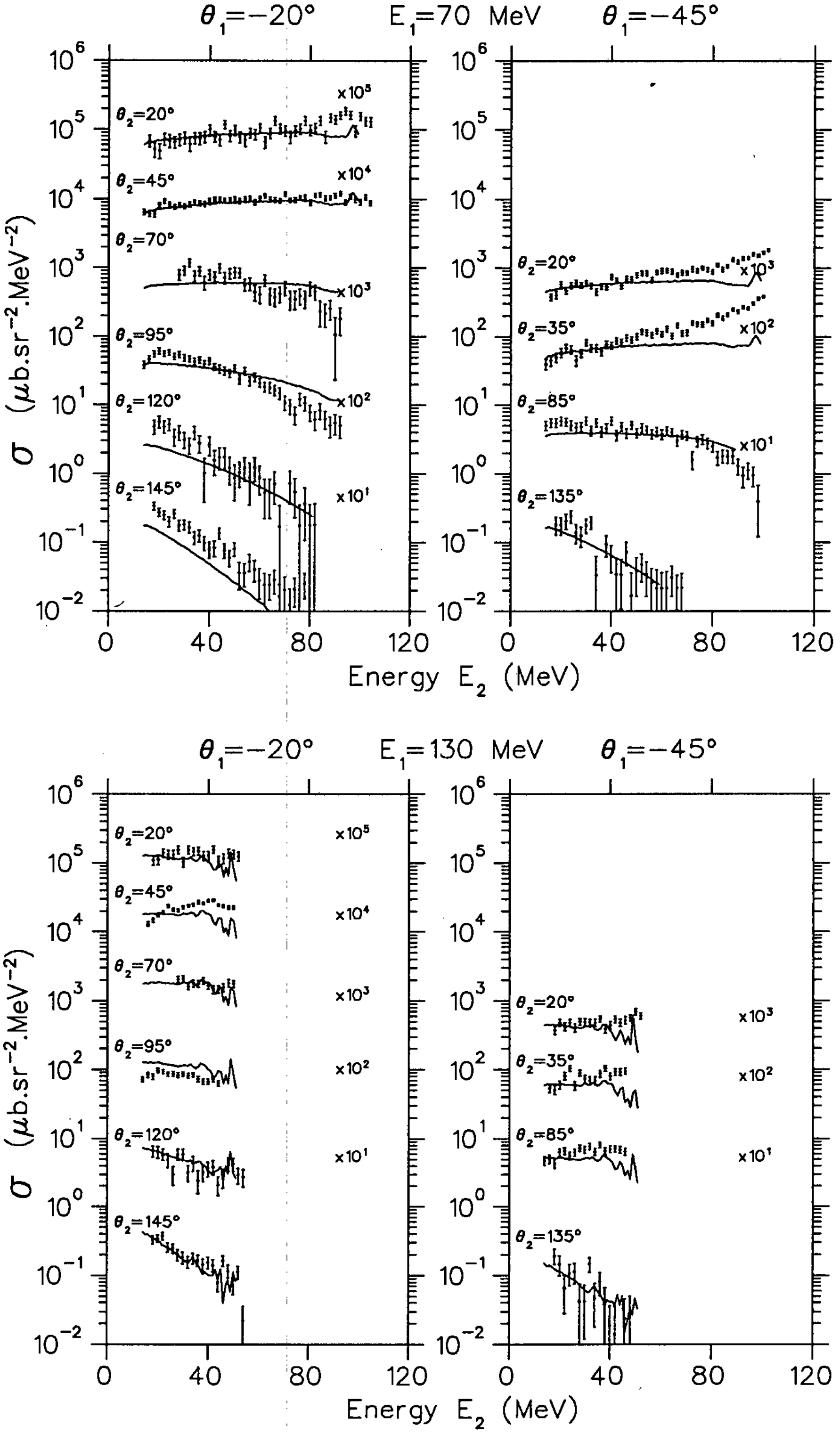

Figure 4.34: $^{12}C(p,2p)$ *continuum decay cross sections for* E_1*=70±5 MeV (above) and* E_1*=130±5 MeV (below) compared with continuum decay model calculations including both in- and out-of-plane knockout contributions. The DWIA calculations describing the initial knockout process were performed using the initial energy prescription (IEP) for the two-body scattering approximation. Details are similar to those given in figure 4.33.*

E_1	θ_1	OSA	SF(p state)	SF(s state)
70 MeV	-20°	FEP	5.7	2.3
		IEP	10.0	4.0
	-45°	FEP	4.0	1.6
		IEP	4.0	1.6
100 MeV	-20°	FEP	3.3	1.3
		IEP	4.0	1.6
	-45°	FEP	3.3	1.3
		IEP	3.3	1.3
130 MeV	-20°	FEP	2.0	0.8
		IEP	2.0	0.8
	-45°	FEP	4.0	1.6
		IEP	4.0	1.6

Table 4.3: *Spectroscopic factors (SF) used in normalizing the calculated continuum decay cross sections (the results of the convolution of the in- and out-of-plane DWIA knockout cross sections with the* $^{12}C(p,p')$ *inelastic data) to the coincident data in figures 4.31 to 4.32. The column labelled OSA indicates the two-body scattering approximation (FEP or IEP) used in the DWIA calculations.*

cated, this assumption appears to be reasonable except for the expected E_1 = 70 MeV case. It may be concluded, therefore, that this tendency of the calculated cross sections not to decrease as rapidly as the measured cross sections is unlikely to be due to any inadequacy in the DWIA angular distribution predictions.

The spectroscopic factors, listed in table 4.3, used to normalize the calculated continuum decay cross sections to the data also exhibit an interesting feature. From the table it can be seen that a single factor for each $< E_1, \theta_1 >$ set is capable of achieving the good fits illustrated in figures 4.31 to 4.34. Since a single distribution of DWIA cross sections was used for each set, this implies that the replacement of the multiple scattering probabilities for the knocked out nucleon by the inelastic scattering probability is a good approximation, and that the observed differences between the various sets originate in the DWIA treatment of the initial quasifree knockout process.

It has been seen that differences in the predicted DWIA cross sections for the initial knockout process, using the FEP and IEP approximations for the half off-shell nucleon-nucleon scattering, are negligible at the primary angle of −45°. This is reflected in the similar values obtained for all the data sets when fitting the calculated cross sections to the data at this angle. However, at the primary angle of −20°, where off-shell effects should be more pronounced, there is a large spread in the spectroscopic factors between the data sets at different E_1 energies, and also between sets at different θ_1 angles with the same E_1 energy. In addition, there are large differences between the values obtained using the FEP and IEP at the lowest primary proton energy of 70 MeV where off-shell effects are expected to be enhanced.

Redish *et al.* [Red70], for example, have reported that in (p,2p) knockout reactions below an incident proton energy of 200 MeV, on-shell approximations for the two-body scattering result in cross sections which can differ significantly from calculations in which off-shell amplitudes are employed, and that such effects increase with the binding energy of the struck nucleon. All this suggests that off-shell effects should be considered in a fuller DWIA treatment of the initial quasifree interaction than the one employed here, if the small, but persistent, discrepencies observed in the present analysis are to be eliminated.

Finally, the fact that the spectroscopic factors, listed in table 4.3, tend to be significantly greater than those obtained in the discrete state knockout studies (both (p,2p) and (e,e′p)) should be addressed. In the reaction model proposed in the present study, the outgoing primary proton, which is assumed to undergo no further interaction before detection, is described by a distorted wave function to account for the attenuation of flux. The knocked out nucleon, on the other hand, is described by a plane wave in the DWIA treatment, since it is assumed that the convolution with the inelastic scattering probabilities fully accounts for the further interaction of these particles with the residual nucleus. From the spectroscopic factors required to normalize these calculations to the measured coincident continuum cross sections, it appears that this procedure underpredicts the yield of knockout particles by a factor in the region of 2 relative to discrete state knockout. It should be noted, however, that in a study of the continuum yields from the inclusive ^{12}C(p,p′) reaction at an incident energy of 200 MeV, which was described in terms of a simple quasifree knockout model, Förtsch et al.[För88] found $1p_{3/2}$ state spectroscopic factors which ranged in value from approximately 2.4 to 3.4, which are consistent with those of the present work.

Although there is some uncertainty in the present study in the treatment of the knockout of neutrons in the initial interaction, primarily due to the lack of suitable experimental (n,p) data, it is believed that this treatment is reasonably accurate and the uncertainty could not account for a large discrepency in the spectroscopic factors. There will also be contributions to the coincident continuum proton yield from other possible reaction channels (for example, cluster knockout such as (p,pd) followed by the breakup of the deuteron with the resulting proton being detected in the exit channel). However, due to the much lower cross sections involved (cf.,for example, ^{16}O(p,2p) and ^{16}O(p,pd) cross sections in [Sam81]), contributions from these other possible channels are not expected to account fully for the large spectroscopic factors found in the present study, and it is concluded that further theoretical refinement of the DWIA treatment of the initial quasifree interaction is probably required to resolve the discrepency.

Chapter 5

Summary and Conclusion

In the present study the cross sections for coincident proton decay of the continuum induced by 200 MeV incident protons on ^{12}C were measured, and interpreted in terms of a relatively simple reaction model in which the incident proton interacts initially with a single target nucleon while the remaining portion of the nucleus acts as a spectator in this quasifree process. It is assumed in the model that this initial interaction can be described in a distorted wave impulse approximation (DWIA) treatment, and that following this interaction the scattered incident proton emerges from the nucleus to be detected without undergoing any further interactions. The knocked out nucleon, on the other hand, is subject to multiple scattering in the nuclear medium, leading to the emergence of a proton which is detected in coincidence with the original proton. It is further assumed that the multiple scattering chain, which describes this interaction of the knocked out nucleon, may be replaced in the model by the experimentally-determined inelastic scattering probability.

Coincident proton energy spectra were measured at a wide range of coincident angle pairs, covering a larger region of phase space than that usually selected in knockout studies, with an energy resolution of approximately 4 MeV and subtended solid angles of approximately 2 msr. The primary protons (that is, the protons assumed in the model to be scattered without further secondary interactions) were observed at angles (θ_1) of −20° and −45°. The corresponding angles (θ_2) at which the coincident secondary protons were observed were 20°, 45°, 70°, 95°, 120° and 145° (for $\theta_1 = -20°$), and 20°, 35°, 85° and 135° (for $\theta_1 = -45°$).

As a first test of the applicability of the DWIA treatment used in this study, the kinematic regions of the coincident proton spectra corresponding to the knockout of protons from the outer $1p_{3/2}$ orbital of ^{12}C, which do not undergo further interactions with the residual nucleus, were analysed. The extracted (p,2p) knockout cross sections were compared with the predictions of the DWIA theory in which both detected protons were described by distorted wave functions.

The DWIA cross section distributions, calculated by the computer program *THREEDEE*, were found to well reproduce the shapes of the experimental cross sections as a function of the energy of one of the quasifree protons, except that energy shifts between the two distributions were apparent at extreme geometries. This disagreement was found in an energy region whose contribution to the coincident continuum decay in the kinematic region of interest in the present study was negligible.

Normalization of the absolute magnitudes of the calculated distributions to the experimental energy-sharing distributions (disregarding the extreme geometry measurements) gave an average spectroscopic factor of 1.1 ± 0.3. This tends to be lower than the values of 1.33 and 2.66 obtained in a high-resolution ^{12}C(p,2p) measurement at 100 MeV incident energy by Devins *et al.* [Dev79] for "asymmetric" and "symmetric" geometries respectively, the 2.5 [Mou76] and 2.18 [Van88a][Van88b] values obtained in ^{12}C(e,e′p) knockout experiments, and the value of 2.85 from a shell model calculation [Coh67]. A similar factor of 2 difference in the spectroscopic factors extracted from ^{16}O(p,2p) experiments at 100 [Sam81] [Sam86] and 200 Mev [Kit76] [Kit80] incident proton energy may indicate a common source of discrepency.

The present study found no significant differences (a maximum of approximately 20% for the -20°,20° geometry case) in the predicted cross sections when using two different realistic (average energy and energy-dependent) optical potential parameter sets. In addition, except in the -20°,20° case where a difference in spectroscopic factors close to 2 was required to fit the data, the DWIA treatment was found to be insensitive to the choice of the initial (IEP) or final (FEP) energy prescriptions for the two-body scattering approximation.

The DWIA calculations were repeated with the inclusion of a nonlocal component (with a range parameter of 1.15 fm.[Ant81]) in the optical model potentials, to test the sensitivity to nonlocality. Changes in the shapes of the cross section distributions were found to be negligible compared to those predicted by the calculations in which nonlocal components were neglected, and absolute magnitudes were found to vary by less than 20% in the kinematic region of interest to the continuum decay study.

From this initial investigation it was concluded that the DWIA treatment is indeed appropriate for modelling the initial quasifree nucleon knockout process in the proposed reaction mechanism.

Three sets of continuum decay cross sections were extracted from the measured coincident proton energy spectra, corresponding to protons detected at the primary energies of 70±5 MeV, 100±5 MeV and 130±5 MeV.

As a first crude test of the reaction mechanism these cross sections were compared with arbitrarily normalized ^{12}C(p,p$'$) cross sections, the inelastic data set being chosen to give the best fit to the coincident data. Good agreement in the shape of the compared spectra was obtained. The difference, θ_2'', between the secondary proton angle of observation, θ_2, of the coincident data and the scattering angle of the inelastic data to which it was compared, θ_2', was determined for each angle set. DWIA calculations for ^{12}C(p,2p) and ^{12}C(p,pn) knockout, in which the primary and secondary outgoing nucleons were described by distorted and plane wave functions respectively, were performed by the computer program *THREEDEE*. The average angles of the distribution of the predicted DWIA yields were compared with the θ_2'' angles extracted from the data. Reasonable agreement between these angles was found for all the data sets, with DWIA calculations in which the IEP approximation for the two-body scattering was used, giving somewhat better agreement for the $\theta_1 = -20°$ cases than those in which the FEP approximation was used. It was concluded that this agreement demonstrates firm support for the correctness of the proposed reaction mechanism, and this motivated the further theoretical analysis.

The proposed reaction mechanism was modelled in terms of a convolution integral over the DWIA cross sections describing the initial quasifree knockout process and the inelastic scattering probabilities describing the multiple scattering undergone by further interactions of the secondary nucleons — these probabilities are replaced by experimental inelastic scattering cross sections and calculated total reaction cross sections. In the more complete version of the model, the contributions were determined for nucleons which are knocked out both in- and out-of-plane in the initial quasifree process, with the subsequent interaction with the residual nucleus resulting in the detection of secondary in-plane protons. Contributions from both ^{12}C(p,2p) and ^{12}C(p,pn) knockout were included, and in the latter case, due to the lack of suitable experimental data, the (n,p) cross sections required to describe the interaction of the knocked out neutrons with the residual nucleus were replaced with the corresponding (p,p′) cross sections, normalized by a factor of 0.5, based on a comparison of data measured at 60 MeV incident nucleon energy — it is believed that the uncertainties introduced by this approximation for the (n,p) cross sections are too small to account for the discrepencies found in the normalized spectroscopic factors described below. DWIA calculations were performed for nucleon knockout from both the *p* and *s* states of ^{12}C, using both the IEP and FEP for the two-body scattering approximations. The value of the ratio of *s* state to *p* state spectroscopic factors used in the determination of the continuum decay cross sections was 0.4, obtained from the results of (e,e′p) experiments.

Good agreement was found between the normalized calculated continuum decay cross sections and the measured cross sections. A tendency for the calculated cross sections not to decrease as rapidly (as a function of energy E_2) as the measured cross sections was observed for the data close to $\theta_2 = 90°$. It was suggested that this could be due to the DWIA treatment of the initial quasifree process predicting knockout nucleon angular distributions with a mean angle which is too large. However, based on the results of the "clean" (that is, discrete state) (p,2p) knockout analysis, it was concluded, assuming that the primary protons have not undergone further interactions, that this suggestion was unlikely to be valid,.

The present study has shown that the contribution of neutron, as well as proton, knockout to the observed coincident proton decay of the continuum is significant, particularly at the smaller primary angle of −20° — this contribution was found to range from 0.13 to 0.62 that of the proton contribution, depending on the selected coincident geometry.

At $\theta_1 = -45°$ consistent spectroscopic factors, with an average value of 3.7 ± 0.3, were obtained for the three data sets ($E_1 = 70 \pm 5$, 100 ± 5 and 130 ± 5 MeV) using both the IEP and FEP approximations. However, at $\theta_1 = -20°$, spectroscopic factors were found to decrease with increasing E_1 energy — using the IEP approximation these factors were 10.0, 4.0 and 2.0 for $E_1 = 70$, 100 and 130 MeV respectively, and using the FEP approximation 5.7, 3.3 and 2.0. The assumption that the proton detected at the primary angle has not undergone any further interactions after the initial knockout process, is expected to becomes less accurate as the E_1 energy becomes smaller, and this should account, in part, for some of the increase in the spectroscopic factor at $E_1 = 70$ MeV. However, large differences are also observed between the corresponding spectroscopic factors determined using the IEP and FEP for the two-body scattering approximations. It is concluded that off-shell effects account for a great deal of this uncertainty, particularly as ^{12}C is a nucleus in which the nucleons in both the outer as well as the inner orbitals are relatively tightly bound. In addition, these spectroscopic factors are much greater than those obtained from the analysis of the "clean" (p,2p) knockout region of the coincident proton energy spectra, implying some inadequacy in the DWIA treatment employed. Compared to theory, the "clean" (p,2p) knockout spectroscopic factors extracted from the experimental data appear too low, while for the continuum decay data the factors appear too high. Despite the reasons for these differences not being immediately manifest, the range of extracted spectroscopic factor values is still reasonable, and those for the continuum data are consistent with the values obtained in an inclusive ^{12}C(p,p′) reaction study of the continuum at 200 MeV [För88].

Finally, it is concluded that the present study has successfully confirmed the general validity of the proposed relatively simple reaction model in describing the observed coincident proton decay of the continuum, induced by 200 MeV protons on ^{12}C. The results of the study motivate an improved theoretical description of the model's initial nucleon-nucleon quasifree interaction, in which, for example, an adequate treatment of the off-shell contribution is incorporated. In addition, the rescattering portion of the interaction should also be founded on a theoretical treatment, particularly as the present results encourage the performance of similar measurements on the currently untried heavy nuclei, for which the reaction mechanism is expected to be more complicated.

Appendix A

Cross Section Tables

E_2	σ (μb.sr^{-2}.MeV^{-2})		
(MeV)	$\theta_2 = 20°$	$\theta_2 = 45°$	$\theta_2 = 70°$
17.0	0.685±0.130	0.610±0.062	
19.0	0.521±0.125	0.601±0.060	
21.0	0.495±0.120	0.820±0.069	
23.0	0.731±0.140	0.932±0.071	
25.0	0.688±0.143	0.837±0.069	
27.0	0.665±0.130	0.766±0.064	
29.0	0.712±0.137	0.808±0.066	0.789±0.139
31.0	0.761±0.140	0.781±0.067	0.911±0.145
33.0	0.616±0.139	0.836±0.068	1.190±0.161
35.0	0.753±0.138	0.886±0.071	0.757±0.131
37.0	0.749±0.147	0.869±0.067	0.898±0.139
39.0	0.781±0.143	0.844±0.069	0.602±0.134
41.0	1.007±0.162	0.948±0.072	0.796±0.136
43.0	0.793±0.140	0.988±0.072	0.727±0.136
45.0	0.719±0.137	0.984±0.072	0.992±0.151
47.0	1.177±0.159	0.948±0.071	0.713±0.136
49.0	0.820±0.149	0.972±0.075	0.821±0.143
51.0	0.979±0.156	1.006±0.073	0.859±0.148
53.0	0.780±0.142	0.933±0.073	0.845±0.139
55.0	0.706±0.136	1.012±0.075	0.564±0.112
57.0	0.901±0.150	1.030±0.075	0.584±0.126
59.0	0.864±0.149	0.904±0.073	0.443±0.116
61.0	1.062±0.156	1.033±0.076	0.409±0.110
63.0	0.663±0.132	1.115±0.079	0.662±0.130
65.0	0.897±0.157	0.997±0.076	0.395±0.104

Table A.1: *Measured* ^{12}*C(p,2p) continuum cross sections at an incident proton energy of 200 MeV for* E_1*=70±5 MeV and* θ_1*=-20°.*

E_2	σ (μb.sr^{-2}.MeV^{-2})		
(MeV)	$\theta_2 = 20°$	$\theta_2 = 45°$	$\theta_2 = 70°$
67.0	1.352±0.183	0.983±0.076	0.379±0.109
69.0	1.043±0.165	0.948±0.073	0.416±0.107
71.0	0.971±0.162	1.185±0.081	0.509±0.120
73.0	0.788±0.157	0.967±0.076	0.348±0.107
75.0	0.971±0.164	0.983±0.076	0.350±0.105
77.0	1.028±0.178	1.050±0.078	0.388±0.103
79.0	1.343±0.189	1.075±0.079	0.354±0.100
81.0	0.994±0.166	0.889±0.074	0.503±0.111
83.0	1.071±0.168	1.140±0.081	0.451±0.110
85.0	1.353±0.184	1.167±0.083	0.232±0.093
87.0	0.796±0.154	1.035±0.080	0.215±0.080
89.0	1.492±0.199	1.045±0.078	0.253±0.081
91.0	1.404±0.198	1.128±0.081	0.106±0.083
93.0	1.618±0.204	1.204±0.084	0.181±0.077
95.0	1.873±0.218	0.898±0.075	0.070±0.074
97.0	1.635±0.214	1.096±0.083	0.146±0.068
99.0	0.956±0.176	0.989±0.085	0.052±0.046
101.0	1.592±0.212	0.920±0.085	
103.0	1.332±0.197	1.059±0.089	
105.0	1.301±0.202	0.884±0.081	
107.0	1.502±0.204	0.939±0.080	
109.0	1.608±0.210	0.763±0.071	
111.0	1.327±0.200	0.885±0.077	
113.0	1.707±0.215	0.757±0.072	
115.0	1.699±0.220	0.794±0.072	

Table A.2: *Measured* $^{12}C(p,2p)$ *continuum cross sections at an incident proton energy of 200 MeV for* E_1*=70±5 MeV and* θ_1*=-20°.*

E_2 (MeV)	σ (μb.sr^{-2}.MeV^{-2})		
	$\theta_2 = 95°$	$\theta_2 = 120°$	$\theta_2 = 145°$
17.0	0.465±0.053		
19.0	0.551±0.056	0.478±0.108	0.334±0.042
21.0	0.611±0.057	0.564±0.110	0.275±0.037
23.0	0.556±0.053	0.479±0.094	0.251±0.036
25.0	0.580±0.054	0.514±0.100	0.200±0.033
27.0	0.505±0.053	0.342±0.094	0.260±0.036
29.0	0.538±0.053	0.394±0.095	0.177±0.031
31.0	0.483±0.051	0.308±0.080	0.181±0.029
33.0	0.468±0.050	0.257±0.066	0.165±0.029
35.0	0.429±0.047	0.397±0.083	0.118±0.025
37.0	0.450±0.047	0.275±0.077	0.126±0.026
39.0	0.395±0.046	0.101±0.063	0.098±0.023
41.0	0.436±0.046	0.259±0.079	0.079±0.021
43.0	0.357±0.043	0.155±0.062	0.083±0.022
45.0	0.334±0.043	0.173±0.060	0.136±0.025
47.0	0.314±0.040	0.173±0.060	0.075±0.018
49.0	0.291±0.039	0.121±0.052	0.060±0.015
51.0	0.341±0.043	0.086±0.045	0.080±0.018
53.0	0.236±0.036	0.104±0.042	0.036±0.015
55.0	0.311±0.038	0.122±0.046	0.036±0.013
57.0	0.222±0.035	0.087±0.052	0.052±0.014
59.0	0.256±0.037	0.123±0.047	0.040±0.014
61.0	0.212±0.032	0.088±0.039	0.028±0.013
63.0	0.184±0.029	0.052±0.030	0.024±0.011
65.0	0.181±0.031	0.053±0.030	0.024±0.010

Table A.3: *Measured $^{12}C(p,2p)$ continuum cross sections at an incident proton energy of 200 MeV for E_1=70±5 MeV and θ_1=-20°.*

E_2	σ (μb.sr^{-2}.MeV^{-2})		
(MeV)	$\theta_2 = 95°$	$\theta_2 = 120°$	$\theta_2 = 145°$
67.0	0.165±0.030	0.071±0.035	0.028±0.011
69.0	0.149±0.029	0.017±0.017	0.016±0.008
71.0	0.109±0.024	0.000±0.000	0.020±0.011
73.0	0.097±0.024	0.072±0.036	0.012±0.009
75.0	0.072±0.021	0.054±0.031	0.021±0.009
77.0	0.123±0.025	0.018±0.018	0.000±0.006
79.0	0.107±0.025	0.036±0.026	0.025±0.010
81.0	0.078±0.020	0.018±0.018	0.004±0.004
83.0	0.061±0.019	0.018±0.018	
85.0	0.083±0.022		
87.0	0.062±0.018		
89.0	0.050±0.017		
91.0	0.054±0.017		
93.0	0.051±0.018		
95.0	0.021±0.012		
97.0	0.034±0.015		
99.0	0.025±0.015		
101.0	0.026±0.015		
103.0	0.026±0.011		
105.0	0.017±0.009		
107.0	0.026±0.012		
109.0	0.009±0.006		

Table A.4: *Measured $^{12}C(p,2p)$ continuum cross sections at an incident proton energy of 200 MeV for E_1=70±5 MeV and θ_1=-20°.*

E_2	σ (μb.sr^{-2}.MeV^{-2})			
(MeV)	$\theta_2 = 20°$	$\theta_2 = 35°$	$\theta_2 = 85°$	$\theta_2 = 135°$
17.0	0.376±0.045	0.445±0.074	0.548±0.081	0.066±0.023
19.0	0.403±0.048	0.496±0.077	0.548±0.079	0.181±0.052
21.0	0.576±0.054	0.584±0.085	0.582±0.080	0.176±0.049
23.0	0.468±0.051	0.677±0.090	0.565±0.078	0.206±0.051
25.0	0.554±0.055	0.644±0.088	0.505±0.079	0.241±0.051
27.0	0.607±0.056	0.449±0.076	0.467±0.074	0.139±0.042
29.0	0.561±0.054	0.571±0.079	0.479±0.073	0.126±0.041
31.0	0.603±0.055	0.815±0.088	0.587±0.076	0.178±0.041
33.0	0.553±0.051	0.679±0.084	0.425±0.069	0.196±0.041
35.0	0.450±0.048	0.676±0.086	0.554±0.072	0.033±0.029
37.0	0.541±0.052	0.612±0.082	0.408±0.070	0.007±0.026
39.0	0.535±0.053	0.765±0.089	0.456±0.072	0.093±0.032
41.0	0.740±0.060	0.741±0.087	0.591±0.076	0.064±0.028
43.0	0.654±0.057	0.865±0.090	0.363±0.064	0.034±0.026
45.0	0.552±0.051	0.825±0.087	0.485±0.067	0.034±0.023
47.0	0.693±0.059	0.959±0.094	0.391±0.063	0.073±0.027
49.0	0.681±0.059	0.897±0.091	0.513±0.069	0.017±0.019
51.0	0.787±0.063	1.001±0.096	0.393±0.061	0.038±0.022
53.0	0.840±0.063	1.173±0.102	0.464±0.063	0.047±0.021
55.0	0.837±0.063	1.139±0.100	0.426±0.061	0.034±0.018
57.0	0.668±0.057	1.060±0.099	0.379±0.058	0.026±0.016
59.0	0.863±0.066	1.203±0.103	0.407±0.059	0.021±0.019
61.0	0.910±0.067	1.089±0.102	0.374±0.059	0.022±0.014
63.0	0.925±0.068	1.287±0.108	0.424±0.058	0.022±0.016
65.0	0.889±0.067	1.036±0.100	0.399±0.055	0.031±0.014

Table A.5: *Measured* $^{12}C(p,2p)$ *continuum cross sections at an incident proton energy of 200 MeV for* E_1=70±5 *MeV and* θ_1=-45°.

E_2 (MeV)	σ (μb.sr^{-2}.MeV^{-2})			
	$\theta_2 = 20°$	$\theta_2 = 35°$	$\theta_2 = 85°$	$\theta_2 = 135°$
67.0	0.796±0.063	1.457±0.112	0.303±0.054	0.022±0.012
69.0	0.856±0.066	1.126±0.103	0.372±0.053	0.022±0.013
71.0	0.846±0.064	1.147±0.104	0.356±0.052	0.004±0.013
73.0	0.967±0.071	1.591±0.116	0.160±0.045	0.009±0.011
75.0	0.911±0.066	1.517±0.116	0.296±0.050	0.018±0.009
77.0	1.008±0.069	1.505±0.114	0.316±0.049	
79.0	0.965±0.070	1.733±0.118	0.277±0.046	
81.0	0.884±0.066	1.568±0.118	0.251±0.044	
83.0	1.119±0.074	2.038±0.127	0.171±0.039	
85.0	0.957±0.070	1.852±0.126	0.181±0.039	
87.0	1.070±0.073	2.092±0.132	0.178±0.037	
89.0	1.338±0.082	2.473±0.138	0.179±0.038	
91.0	1.247±0.078	2.307±0.136	0.129±0.034	
93.0	1.406±0.083	2.693±0.144	0.093±0.031	
95.0	1.411±0.084	2.591±0.145	0.112±0.029	
97.0	1.595±0.089	3.053±0.153	0.095±0.030	
99.0	1.528±0.088	3.578±0.162	0.039±0.027	
101.0	1.697±0.092	3.845±0.170	0.091±0.029	
103.0	1.846±0.095	4.268±0.175	0.031±0.022	
105.0	1.923±0.098	4.170±0.176	0.083±0.024	
107.0	1.663±0.093	4.623±0.182	0.088±0.024	
109.0	1.815±0.097	4.382±0.179	0.079±0.028	
111.0	1.633±0.092	3.650±0.172	0.113±0.026	
113.0	1.652±0.094	3.010±0.164	0.028±0.018	
115.0	2.297±0.108	2.778±0.158	0.009±0.016	

Table A.6: *Measured* $^{12}C(p,2p)$ *continuum cross sections at an incident proton energy of 200 MeV for* E_1=70±5 *MeV and* θ_1=-45°.

E_2 (MeV)	σ (μb.sr^{-2}.MeV^{-2})		
	$\theta_2 = 20°$	$\theta_2 = 45°$	$\theta_2 = 70°$
17.0	0.778±0.144	0.759±0.065	
19.0	0.882±0.148	0.775±0.066	
21.0	0.969±0.157	0.991±0.073	
23.0	0.727±0.151	1.121±0.081	
25.0	1.215±0.175	1.138±0.081	
27.0	1.212±0.175	1.110±0.076	
29.0	0.953±0.154	0.981±0.073	0.876±0.159
31.0	0.821±0.143	0.940±0.074	0.931±0.150
33.0	0.946±0.157	1.013±0.075	1.059±0.156
35.0	0.649±0.137	1.086±0.078	1.025±0.156
37.0	0.793±0.154	1.227±0.082	1.063±0.156
39.0	0.863±0.164	1.243±0.083	0.590±0.134
41.0	0.990±0.157	1.357±0.084	1.177±0.173
43.0	0.765±0.151	1.170±0.081	0.684±0.144
45.0	0.855±0.150	1.233±0.082	0.925±0.151
47.0	1.206±0.184	1.442±0.088	0.854±0.138
49.0	1.373±0.185	1.298±0.083	0.616±0.137
51.0	0.963±0.162	1.410±0.087	0.858±0.154
53.0	1.000±0.163	1.635±0.093	0.768±0.146

Table A.7: *Measured* $^{12}C(p,2p)$ *continuum cross sections at an incident proton energy of 200 MeV for* E_1*=100±5 MeV and* θ_1*=-20°.*

E_2 (MeV)	σ (μb.sr^{-2}.MeV^{-2}) $\theta_2 = 20°$	$\theta_2 = 45°$	$\theta_2 = 70°$
55.0	1.562±0.199	1.453±0.090	0.715±0.136
57.0	1.377±0.188	1.619±0.093	0.792±0.135
59.0	1.265±0.184	1.632±0.093	0.609±0.132
61.0	0.927±0.163	1.727±0.096	0.592±0.123
63.0	1.627±0.199	1.641±0.093	0.670±0.134
65.0	1.574±0.207	1.742±0.096	0.654±0.128
67.0	1.939±0.209	1.922±0.103	0.525±0.124
69.0	1.831±0.219	1.851±0.099	0.584±0.121
71.0	1.684±0.215	1.937±0.102	0.227±0.094
73.0	2.093±0.226	1.849±0.100	0.456±0.117
75.0	1.448±0.207	1.765±0.097	0.287±0.104
77.0	1.531±0.201	1.790±0.099	0.594±0.123
79.0	1.304±0.194	1.444±0.092	0.290±0.109
81.0	1.658±0.218	1.504±0.093	0.311±0.102
83.0	1.413±0.203	1.400±0.090	0.776±0.140
85.0	1.477±0.207	1.586±0.095	0.800±0.143
87.0	2.247±0.247	2.242±0.110	0.980±0.150
89.0	3.655±0.301	3.865±0.140	0.578±0.116

Table A.8: *Measured* $^{12}C(p,2p)$ *continuum cross sections at an incident proton energy of 200 MeV for* E_1=*100±5 MeV and* θ_1=*-20°.*

E_2 (MeV)	σ (μb.sr^{-2}.MeV^{-2})		
	$\theta_2 = 95°$	$\theta_2 = 120°$	$\theta_2 = 145°$
17.0	0.511±0.056		
19.0	0.614±0.058	0.519±0.115	0.287±0.042
21.0	0.598±0.058	0.357±0.094	0.222±0.038
23.0	0.569±0.056	0.267±0.085	0.255±0.039
25.0	0.653±0.059	0.412±0.089	0.205±0.035
27.0	0.679±0.061	0.322±0.088	0.189±0.032
29.0	0.547±0.053	0.395±0.092	0.152±0.029
31.0	0.494±0.053	0.287±0.088	0.148±0.029
33.0	0.445±0.051	0.269±0.069	0.107±0.026
35.0	0.550±0.055	0.416±0.090	0.103±0.024
37.0	0.413±0.049	0.179±0.057	0.095±0.025
39.0	0.444±0.051	0.125±0.047	0.049±0.019
41.0	0.432±0.049	0.217±0.085	0.070±0.020
43.0	0.366±0.046	0.162±0.060	0.087±0.022
45.0	0.389±0.047	0.163±0.060	0.049±0.018
47.0	0.293±0.041	0.145±0.057	0.071±0.018
49.0	0.315±0.043	0.127±0.048	0.092±0.021
51.0	0.244±0.036	0.109±0.045	0.076±0.020
53.0	0.270±0.039	0.091±0.041	0.038±0.013

Table A.9: *Measured* $^{12}C(p,2p)$ *continuum cross sections at an incident proton energy of 200 MeV for* E_1*=100±5 MeV and* θ_1*=-20°.*

E_2 (MeV)	σ (μb.sr^{-2}.MeV^{-2}) $\theta_2 = 95°$	$\theta_2 = 120°$	$\theta_2 = 145°$
55.0	0.207±0.034	0.054±0.040	0.025±0.012
57.0	0.260±0.036	0.073±0.037	0.017±0.010
59.0	0.214±0.035	0.036±0.036	
61.0	0.193±0.033	0.036±0.026	
63.0	0.168±0.030	0.093±0.041	
65.0	0.135±0.029	0.037±0.026	
67.0	0.122±0.028	0.037±0.026	
69.0	0.127±0.029	0.037±0.026	
71.0	0.080±0.024	0.018±0.018	
73.0	0.120±0.025		
75.0	0.090±0.023		
77.0	0.082±0.023		
79.0	0.100±0.026		
81.0	0.096±0.023		
83.0	0.096±0.022		
85.0	0.075±0.020		
87.0	0.031±0.018		

Table A.10: *Measured* ^{12}*C(p,2p) continuum cross sections at an incident proton energy of 200 MeV for* E_1*=100±5 MeV and* θ_1*=-20°.*

E_2 (MeV)	σ (μb.sr^{-2}.MeV^{-2})			
	$\theta_2 = 20°$	$\theta_2 = 35°$	$\theta_2 = 85°$	$\theta_2 = 135°$
17.0	0.365±0.055	0.439±0.082	0.469±0.090	
19.0	0.640±0.064	0.631±0.094	0.508±0.088	0.185±0.059
21.0	0.515±0.062	0.811±0.100	0.543±0.090	0.176±0.058
23.0	0.562±0.064	0.705±0.102	0.560±0.089	0.088±0.055
25.0	0.609±0.065	0.931±0.107	0.480±0.089	0.066±0.048
27.0	0.636±0.065	0.655±0.099	0.636±0.090	0.106±0.047
29.0	0.608±0.065	0.791±0.100	0.667±0.089	0.043±0.040
31.0	0.610±0.065	1.014±0.108	0.650±0.087	0.111±0.041
33.0	0.777±0.071	0.764±0.100	0.592±0.090	0.057±0.039
35.0	0.606±0.067	0.771±0.101	0.561±0.086	0.124±0.041
37.0	0.702±0.069	1.022±0.108	0.553±0.084	0.062±0.036
39.0	0.535±0.063	1.171±0.114	0.599±0.080	0.076±0.036
41.0	0.529±0.063	0.803±0.103	0.523±0.077	0.049±0.029
43.0	0.642±0.069	1.153±0.114	0.520±0.078	0.076±0.029
45.0	0.645±0.067	1.149±0.116	0.548±0.074	0.000±0.023
47.0	0.730±0.071	1.255±0.117	0.536±0.074	0.072±0.027
49.0	0.776±0.070	1.279±0.117	0.451±0.074	0.045±0.028
51.0	0.729±0.073	1.309±0.122	0.470±0.070	0.004±0.022
53.0	0.798±0.072	1.187±0.119	0.645±0.073	0.022±0.021

Table A.11: *Measured* $^{12}C(p,2p)$ *continuum cross sections at an incident proton energy of 200 MeV for* E_1*=100±5 MeV and* θ_1*=-45°.*

E_2	σ (μb.sr^{-2}.MeV^{-2})		
(MeV)	$\theta_2 = 20°$	$\theta_2 = 35°$	$\theta_2 = 85°$
55.0	0.833±0.076	1.489±0.126	0.514±0.072
57.0	0.933±0.078	1.779±0.134	0.470±0.069
59.0	1.017±0.083	1.600±0.129	0.371±0.068
61.0	0.928±0.082	1.725±0.132	0.658±0.073
63.0	0.934±0.083	1.866±0.139	0.444±0.065
65.0	1.063±0.086	2.051±0.140	0.390±0.060
67.0	1.175±0.089	1.970±0.140	0.284±0.059
69.0	0.943±0.081	2.340±0.146	0.388±0.058
71.0	1.029±0.085	2.643±0.154	0.469±0.063
73.0	0.931±0.082	2.511±0.154	0.336±0.053
75.0	0.776±0.077	2.883±0.161	0.422±0.060
77.0	0.924±0.081	2.744±0.156	0.326±0.055
79.0	0.986±0.084	2.617±0.158	0.370±0.057
81.0	0.928±0.084	2.414±0.157	0.491±0.060
83.0	0.793±0.077	2.415±0.155	0.803±0.069
85.0	1.048±0.086	2.498±0.156	0.579±0.059
87.0	1.534±0.099	2.737±0.161	0.559±0.061
89.0	2.669±0.124	3.571±0.178	0.323±0.052

Table A.12: *Measured* $^{12}C(p,2p)$ *continuum cross sections at an incident proton energy of 200 MeV for* E_1=*100±5 MeV and* θ_1=*-45°.*

E_2	σ (μb.sr^{-2}.MeV^{-2})		
(MeV)	$\theta_2 = 20°$	$\theta_2 = 45°$	$\theta_2 = 70°$
17.0	0.665±0.145	1.302±0.086	
19.0	1.103±0.180	1.476±0.093	
21.0	1.119±0.179	1.752±0.098	
23.0	1.405±0.194	1.920±0.103	
25.0	1.327±0.195	2.358±0.113	
27.0	1.326±0.200	2.099±0.106	
29.0	1.556±0.206	2.039±0.105	2.061±0.213
31.0	1.034±0.177	2.272±0.109	2.082±0.223
33.0	1.576±0.211	2.392±0.112	1.624±0.192
35.0	1.479±0.204	2.459±0.114	1.779±0.205
37.0	1.499±0.205	2.674±0.119	1.762±0.202
39.0	1.286±0.198	2.574±0.116	1.958±0.218
41.0	1.287±0.195	2.787±0.120	1.653±0.194
43.0	1.580±0.203	2.867±0.122	1.462±0.191
45.0	1.054±0.185	2.441±0.114	1.484±0.187
47.0	1.173±0.192	2.364±0.113	1.565±0.199
49.0	1.390±0.209	2.260±0.111	1.823±0.220
51.0	1.353±0.197	2.269±0.113	1.770±0.205
53.0	1.257±0.199	2.641±0.120	2.501±0.242

Table A.13: *Measured* $^{12}C(p,2p)$ *continuum cross sections at an incident proton energy of 200 MeV for* E_1*=130±5 MeV and* θ_1*=-20°.*

E_2	σ (μb.sr^{-2}.MeV^{-2})		
(MeV)	$\theta_2 = 95°$	$\theta_2 = 120°$	$\theta_2 = 145°$
17.0	0.847±0.070		
19.0	0.799±0.068	0.660±0.126	0.329±0.045
21.0	0.974±0.073	0.641±0.125	0.342±0.043
23.0	0.939±0.074	0.585±0.112	0.373±0.046
25.0	0.866±0.070	0.489±0.116	0.256±0.038
27.0	0.880±0.071	0.299±0.091	0.247±0.038
29.0	0.833±0.067	0.586±0.112	0.199±0.036
31.0	0.865±0.069	0.588±0.115	0.182±0.036
33.0	0.818±0.067	0.320±0.086	0.156±0.029
35.0	0.850±0.066	0.436±0.109	0.179±0.031
37.0	0.737±0.064	0.245±0.090	0.166±0.030
39.0	0.681±0.061	0.322±0.091	0.144±0.029
41.0	0.674±0.061	0.362±0.087	0.154±0.030
43.0	0.734±0.061	0.383±0.094	0.141±0.028
45.0	0.638±0.057	0.209±0.063	0.079±0.021
47.0	0.649±0.057	0.268±0.081	0.164±0.029
49.0	0.745±0.062	0.425±0.099	0.115±0.024
51.0	0.864±0.066	0.427±0.095	0.071±0.019
53.0	1.048±0.073	0.292±0.075	0.112±0.023

Table A.14: *Measured* ^{12}*C(p,2p) continuum cross sections at an incident proton energy of 200 MeV for* E_1*=130±5 MeV and* θ_1*=-20°.*

E_2 (MeV)	σ (μb.sr^{-2}.MeV^{-2})			
	$\theta_2 = 20°$	$\theta_2 = 35°$	$\theta_2 = 85°$	$\theta_2 = 135°$
17.0	0.317±0.045	0.539±0.075	0.502±0.075	
19.0	0.373±0.049	0.512±0.074	0.430±0.069	0.191±0.047
21.0	0.482±0.055	0.603±0.082	0.631±0.076	0.144±0.048
23.0	0.419±0.055	0.808±0.093	0.659±0.079	0.065±0.037
25.0	0.480±0.056	1.048±0.097	0.559±0.072	0.107±0.037
27.0	0.405±0.054	0.587±0.084	0.625±0.077	0.112±0.037
29.0	0.497±0.057	0.888±0.092	0.719±0.076	0.042±0.033
31.0	0.489±0.058	0.734±0.091	0.682±0.077	0.042±0.030
33.0	0.484±0.055	0.695±0.088	0.767±0.078	0.146±0.036
35.0	0.480±0.056	0.693±0.087	0.645±0.073	0.047±0.029
37.0	0.543±0.057	0.873±0.094	0.807±0.080	0.080±0.029
39.0	0.391±0.053	1.040±0.099	0.661±0.076	0.038±0.028
41.0	0.441±0.054	0.806±0.091	0.700±0.072	0.019±0.018
43.0	0.540±0.059	0.921±0.099	0.711±0.074	0.014±0.021
45.0	0.478±0.057	0.925±0.099	0.684±0.073	0.009±0.017
47.0	0.520±0.060	0.955±0.100	0.642±0.070	
49.0	0.566±0.061	1.072±0.102	0.966±0.079	
51.0	0.694±0.068	1.199±0.109	1.504±0.093	
53.0	0.601±0.063	1.372±0.111	1.897±0.102	

Table A.15: *Measured* ^{12}*C(p,2p) continuum cross sections at an incident proton energy of 200 MeV for* E_1=*130±5 MeV and* θ_1=*-45°.*

E_1 (MeV)	σ (μb.sr^{-2}.MeV^{-1})	E_1 (MeV)	σ (μb.sr^{-2}.MeV^{-1})	E_1 (MeV)	σ (μb.sr^{-2}.MeV^{-1})
12.7	4.744±1.185	61.5	45.223±3.288	115.8	43.606±3.219
14.4	13.975±1.993	63.4	41.691±3.192	117.9	48.180±3.358
16.2	22.324±2.466	65.3	39.913±3.160	120.0	42.571±3.194
17.9	23.475±2.508	67.3	47.821±3.314	122.2	52.865±3.532
19.6	20.958±2.416	69.2	52.821±3.520	124.3	47.647±3.444
21.3	19.270±2.268	71.1	49.311±3.410	126.5	50.304±3.468
23.1	22.043±2.332	73.1	50.642±3.468	128.6	52.582±3.458
24.8	24.599±2.470	75.0	48.304±3.369	130.8	40.610±3.188
26.6	22.721±2.388	77.0	43.269±3.139	133.0	42.687±3.183
28.4	26.669±2.528	79.0	45.385±3.226	135.1	45.970±3.288
30.1	23.999±2.482	81.0	48.278±3.345	137.3	43.888±3.254
31.9	29.525±2.721	82.9	54.071±3.497	139.5	39.799±3.156
33.7	26.269±2.640	84.9	52.724±3.417	141.7	45.518±3.252
35.5	27.200±2.581	87.0	56.018±3.530	143.9	42.023±3.211
37.3	33.677±2.816	89.0	54.874±3.478	146.2	40.932±3.117
39.1	34.000±2.796	91.0	53.348±3.414	148.4	41.052±3.204
41.0	34.128±2.946	93.0	49.698±3.355	150.6	41.987±3.201
42.8	37.015±2.934	95.0	51.273±3.423	152.8	35.404±2.990
44.6	37.340±3.032	97.1	50.532±3.458	155.1	37.764±3.260
46.5	30.800±2.654	99.1	56.963±3.552	157.4	33.794±2.947
48.3	31.140±2.818	101.2	47.508±3.296	159.6	32.266±2.999
50.2	35.980±3.042	103.3	48.911±3.317	161.9	27.224±2.782
52.0	39.442±3.100	105.3	52.457±3.443	164.2	24.426±2.432
53.9	36.852±3.002	107.4	48.042±3.329	166.5	8.935±1.623
55.8	36.999±3.004	109.5	50.241±3.395	168.7	1.043±0.752
57.7	39.484±3.069	111.6	53.816±3.455	171.0	1.675±0.889
59.6	41.771±3.198	113.7	42.566±3.136	173.4	2.523±1.363

Table A.16: *Measured $^{12}C(p,2p)$ p state knockout cross sections at an incident proton energy of 200 MeV and θ_1=-20°,θ_2=20°.*

E_1 (MeV)	σ (μb.sr^{-2}.MeV^{-1})	E_1 (MeV)	σ (μb.sr^{-2}.MeV^{-1})	E_1 (MeV)	σ (μb.sr^{-2}.MeV^{-1})
12.7	0.852±0.212	61.5	15.539±0.922	115.8	73.386±1.884
14.4	1.980±0.340	63.4	15.969±0.951	117.9	81.094±1.976
16.2	2.255±0.399	65.3	17.289±0.958	120.0	80.284±1.962
17.9	2.482±0.400	67.3	18.920±0.999	122.2	91.831±2.120
19.6	2.754±0.420	69.2	19.130±1.007	124.3	89.156±2.102
21.3	3.769±0.444	71.1	18.986±1.015	126.5	92.588±2.128
23.1	3.897±0.469	73.1	21.904±1.068	128.6	88.107±2.072
24.8	3.099±0.416	75.0	22.516±1.091	130.8	87.205±2.059
26.6	4.197±0.477	77.0	25.700±1.162	133.0	86.489±2.058
28.4	4.462±0.489	79.0	26.537±1.186	135.1	91.713±2.125
30.1	5.322±0.551	81.0	29.326±1.245	137.3	86.261±2.070
31.9	5.812±0.570	82.9	29.857±1.287	139.5	85.332±2.058
33.7	5.569±0.548	84.9	35.265±1.360	141.7	87.075±2.081
35.5	5.101±0.543	87.0	35.271±1.348	143.9	85.144±2.054
37.3	6.226±0.584	89.0	35.104±1.339	146.2	79.233±1.996
39.1	6.666±0.607	91.0	39.551±1.408	148.4	79.187±1.999
41.0	7.376±0.651	93.0	45.069±1.490	150.6	77.891±1.992
42.8	9.711±0.732	95.0	44.784±1.481	152.8	72.674±1.918
44.6	9.918±0.741	97.1	48.454±1.531	155.1	75.718±1.984
46.5	7.785±0.641	99.1	50.357±1.575	157.4	66.480±1.861
48.3	9.210±0.723	101.2	57.871±1.674	159.6	61.193±1.799
50.2	10.990±0.783	103.3	58.993±1.701	161.9	54.834±1.723
52.0	11.511±0.810	105.3	62.485±1.740	164.2	44.303±1.570
53.9	12.166±0.810	107.4	69.559±1.825	166.5	30.267±1.323
55.8	13.491±0.869	109.5	67.542±1.802	168.7	9.570±0.777
57.7	12.493±0.854	111.6	70.940±1.849	171.0	2.786±0.513
59.6	15.287±0.917	113.7	73.994±1.887	173.4	3.473±0.558

Table A.17: *Measured* $^{12}C(p,2p)$ *p state knockout cross sections at an incident proton energy of 200 MeV and* θ_1*=-20°,*θ_2*=45°.*

E_1 (MeV)	σ (μb.sr^{-2}.MeV^{-1})	E_1 (MeV)	σ (μb.sr^{-2}.MeV^{-1})
71.1	0.000±0.271	120.0	28.386±2.490
73.1	0.383±0.383	122.2	41.680±3.005
75.0	0.766±0.469	124.3	39.416±2.868
77.0	1.340±0.506	126.5	52.397±3.318
79.0	0.574±0.574	128.6	47.802±3.207
81.0	0.957±0.574	130.8	60.077±3.556
82.9	0.957±0.428	133.0	70.640±3.831
84.9	2.871±0.834	135.1	73.763±3.994
87.0	2.106±0.690	137.3	83.235±4.245
89.0	1.149±0.606	139.5	86.221±4.283
91.0	2.299±0.766	141.7	93.999±4.448
93.0	5.175±1.067	143.9	83.893±4.213
95.0	4.794±0.996	146.2	101.116±4.652
97.1	5.181±1.102	148.4	94.197±4.473
99.1	6.145±1.152	150.6	92.874±4.459
101.2	7.879±1.289	152.8	86.308±4.278
103.3	6.540±1.247	155.1	251.872±7.224
105.3	9.050±1.402	157.4	1001.918±14.316
107.4	8.674±1.322	159.6	1092.543±14.962
109.5	17.756±1.930	161.9	957.632±14.047
111.6	20.291±2.054	164.2	507.341±10.264
113.7	24.382±2.257	166.5	136.323±5.386
115.8	22.674±2.149	168.7	28.942±2.565
117.9	26.786±2.377	171.0	34.454±2.738

Table A.18: *Measured* ^{12}*C(p,2p) p state knockout cross sections at an incident proton energy of 200 MeV and* θ_1*=-20°,*θ_2*=70°. The peak in the cross section values close to* E_1*=159 MeV is due to H(p,p) elastic scattering from the hydrogen contamination in the* ^{12}*C target.*

E_1 (MeV)	σ (μb.sr^{-2}.MeV^{-1})	E_1 (MeV)	σ (μb.sr^{-2}.MeV^{-1})
87.0	0.176±0.108	128.6	11.277±0.737
89.0	0.132±0.098	130.8	13.192±0.791
91.0	0.308±0.132	133.0	17.508±0.920
93.0	0.132±0.098	135.1	21.303±1.018
95.0	0.484±0.146	137.3	22.670±1.052
97.1	0.396±0.159	139.5	26.772±1.138
99.1	0.837±0.192	141.7	30.033±1.205
101.2	0.793±0.197	143.9	32.034±1.241
103.3	0.838±0.212	146.2	39.228±1.375
105.3	0.574±0.159	148.4	42.008±1.427
107.4	1.105±0.238	150.6	46.884±1.516
109.5	2.124±0.337	152.8	45.042±1.474
111.6	2.304±0.343	155.1	43.703±1.470
113.7	3.417±0.409	157.4	51.343±1.592
115.8	3.155±0.405	159.6	47.083±1.538
117.9	3.338±0.410	161.9	42.047±1.455
120.0	5.217±0.498	164.2	34.861±1.333
122.2	7.459±0.604	166.5	21.251±1.052
124.3	8.860±0.655	168.7	6.637±0.603
126.5	11.119±0.728	171.0	4.379±0.530

Table A.19: *Measured* ^{12}*C(p,2p) p state knockout cross sections at an incident proton energy of 200 MeV and* θ_1=-20°,θ_2=95°.

$\theta_2 = 120°$		$\theta_2 = 145°$	
E_1 (MeV)	σ (μb.sr^{-2}.MeV^{-1})	E_1 (MeV)	σ (μb.sr^{-2}.MeV^{-1})
117.9	0.583±0.336	117.9	0.312±0.134
120.0	0.583±0.337	120.0	0.178±0.126
122.2	1.754±0.646	122.2	0.760±0.184
124.3	2.147±0.756	124.3	0.492±0.148
126.5	3.325±0.853	126.5	0.807±0.201
128.6	3.528±0.831	128.6	1.214±0.234
130.8	4.517±0.982	130.8	1.261±0.255
133.0	6.496±1.165	133.0	1.264±0.263
135.1	7.300±1.232	135.1	1.539±0.300
137.3	10.087±1.440	137.3	1.769±0.311
139.5	10.310±1.510	139.5	1.865±0.325
141.7	12.524±1.603	141.7	2.098±0.347
143.9	9.170±1.410	143.9	3.201±0.419
146.2	18.791±2.019	146.2	4.814±0.504
148.4	18.044±1.985	148.4	3.265±0.448
150.6	20.110±2.090	150.6	4.290±0.490
152.8	18.155±1.976	152.8	4.118±0.487
155.1	17.404±1.962	155.1	6.220±0.580
157.4	20.508±2.177	157.4	6.846±0.627
159.6	20.783±2.194	159.6	5.234±0.549
161.9	14.518±1.840	161.9	2.767±0.390
164.2	4.310±1.026	164.2	0.141±0.141
166.5	0.824±0.412	166.5	0.331±0.142
168.7	1.448±0.620	168.7	0.332±0.237
171.0	0.831±0.719	171.0	0.476±0.269

Table A.20: *Measured ^{12}C(p,2p) p state knockout cross sections at an incident proton energy of 200 MeV, and the angle pairs* θ_1*=-20°,*θ_2*=120° and* θ_1*=-20°,*θ_2*=145°.*

E_1 (MeV)	σ (μb.sr^{-2}.MeV^{-1})	E_1 (MeV)	σ (μb.sr^{-2}.MeV^{-1})	E_1 (MeV)	σ (μb.sr^{-2}.MeV^{-1})
12.7	2.279±0.467	59.6	34.449±1.643	111.6	69.002±2.120
14.4	10.145±0.924	61.5	33.651±1.611	113.7	67.467±2.081
16.2	10.663±1.023	63.4	30.477±1.559	115.8	64.974±2.048
17.9	14.839±1.158	65.3	28.739±1.530	117.9	61.372±2.046
19.6	16.090±1.180	67.3	29.526±1.540	120.0	57.187±1.983
21.3	20.921±1.340	69.2	28.272±1.511	122.2	53.957±1.912
23.1	21.057±1.367	71.1	29.301±1.548	124.3	47.288±1.830
24.8	23.026±1.331	73.1	31.376±1.568	126.5	41.276±1.695
26.6	25.825±1.452	75.0	29.040±1.527	128.6	39.759±1.698
28.4	28.217±1.501	77.0	37.428±1.654	130.8	34.784±1.623
30.1	32.858±1.594	79.0	38.986±1.658	133.0	31.303±1.540
31.9	31.207±1.492	81.0	41.354±1.710	135.1	29.910±1.460
33.7	37.827±1.663	82.9	51.360±1.830	137.3	26.798±1.416
35.5	40.079±1.724	84.9	53.689±1.870	139.5	24.410±1.357
37.3	42.033±1.773	87.0	56.925±1.923	141.7	20.830±1.283
39.1	43.060±1.739	89.0	63.062±2.025	143.9	20.393±1.223
41.0	48.204±1.878	91.0	71.344±2.218	146.2	15.747±1.118
42.8	48.545±1.893	93.0	72.944±2.265	148.4	14.303±1.046
44.6	52.172±1.979	95.0	74.220±2.256	150.6	11.457±0.961
46.5	47.069±1.888	97.1	79.212±2.276	152.8	10.044±0.928
48.3	49.637±1.953	99.1	83.029±2.313	155.1	8.422±0.830
50.2	49.222±1.982	101.2	82.384±2.268	157.4	7.042±0.753
52.0	49.821±2.016	103.3	80.410±2.236	159.6	4.441±0.658
53.9	41.708±1.815	105.3	79.871±2.236	161.9	1.975±0.538
55.8	41.128±1.791	107.4	78.479±2.174	164.2	1.423±0.407
57.7	40.457±1.748	109.5	72.021±2.162	166.5	0.561±0.357

Table A.21: *Measured* $^{12}C(p,2p)$ *p state knockout cross sections at an incident proton energy of 200 MeV and* θ_1=-45°,θ_2=35°.

E_1 (MeV)	σ (μb.sr^{-2}.MeV^{-1})	E_1 (MeV)	σ (μb.sr^{-2}.MeV^{-1})
73.1	0.472±0.164	120.0	12.034±0.812
75.0	0.331±0.157	122.2	15.945±0.941
77.0	0.803±0.226	124.3	17.563±0.980
79.0	0.897±0.226	126.5	18.899±1.034
81.0	1.038±0.241	128.6	17.778±0.964
82.9	1.180±0.254	130.8	17.235±0.975
84.9	1.699±0.320	133.0	19.069±1.049
87.0	1.416±0.299	135.1	17.654±1.019
89.0	1.936±0.344	137.3	17.697±1.017
91.0	2.551±0.390	139.5	16.569±1.003
93.0	2.694±0.409	141.7	14.456±0.931
95.0	2.932±0.428	143.9	15.577±0.939
97.1	3.501±0.454	146.2	16.360±0.990
99.1	4.072±0.483	148.4	13.690±0.934
101.2	3.886±0.488	150.6	11.897±0.870
103.3	4.648±0.506	152.8	10.393±0.806
105.3	4.653±0.502	155.1	9.029±0.765
107.4	6.322±0.576	157.4	8.008±0.746
109.5	9.708±0.719	159.6	7.232±0.685
111.6	9.197±0.730	161.9	2.923±0.473
113.7	11.739±0.790	164.2	1.467±0.332
115.8	12.951±0.826	166.5	0.711±0.337
117.9	13.498±0.877	168.7	1.580±0.398

Table A.22: *Measured $^{12}C(p,2p)$ p state knockout cross sections at an incident proton energy of 200 MeV and θ_1=-45°,θ_2=85°.*

References

[Aga75] D. Agassi, H. A. Weidenmüller and G. Mantzouranis, Phys. Rep. **22** (1975) 145.

[And77] H. H. Andersen and J. F. Ziegler, *The Stopping and Ranges of Ions in Matter*, Volumes **3**, **4** and **5**, Pergamon Press (New York, 1977).

[And81] B. D. Anderson, A. R. Baldwin, A. M. Kalend, R. Madey, J. W. Watson, C. C. Chang, H. D. Holmgren, R. W. Koontz and J. R. Wu, Phys. Rev. Lett. **46** (1981) 226.

[Ant81] L. Antonuk, P. Kitching, C. A. Miller, D. A. Hutcheon, W. J. McDonald, G. C. Neilson, W. C. Olsen and A. W. Stetz, Nucl. Phys. **A370** (1981) 389.

[Ber62] T. Berggren and G. Jacob, Phys. Lett. **1** (1962) 258.

[Ber73] F. E. Bertrand and R. W. Peelle, Oak Ridge National Laboratory Report No. **ORNL-4799** (1973).

[Bho76] R. K. Bhowmik, C. C. Chang, J. -P. Didelez and H. D. Holmgren, Phys. Rev. C **13** (1976) 2105.

[Bla71] M. Blann, Phys. Rev. Lett. **27** (1971) 337.

[Bla84] M. Blann, Lawrence Livermore National Laboratory Report No. **UCID-20169** (1984).

[Boa85] D. H. Boal, *Advances in Nuclear Physics, Volume* **15**, eds J. W. Negele and E. Vogt, Plenum Press (New York,1985) 85.

[Bon78] B. E. Bonner, J. E. Simmons, C. R. Newsom, P. J. Riley, G. Glass, J. C. Hiebert, M. Jain and L. C. Northcliffe, Phys. Rev. C **18** (1978) 1418.

[Bot84] A. H. Botha and H. N. Jungwirth, Proc. Tenth Intern. Conf. on Cyclotrons and their Applications (Michigan, 1984) 263.

[Bou67] M. Bouten, P. Van Leuven and H. Depuydt, Nucl. Phys. **A94** (1967) 687.

[Cam77] J. M. Cameron, P. Kitching, R. H. McCamis, C. A. Miller, G. A. Moss, J. G. Rogers, G. Roy, A. W. Stetz, C. A. Goulding and W. T. H. Van Oers, Nucl. Instrum. Methods **143** (1977) 399.

[Cha77] N. S. Chant and P. G. Roos, Phys. Rev. C **15** (1977) 57.

[Cha82] N. S. Chant, *Code THREEDEE*, University of Maryland, unpublished.

[Cha83] N. S. Chant and P. G. Roos, Phys. Rev. C **27** (1983) 1060.

[Che50] G. F. Chew, Phys. Rev. **80** (1950) 196.

[Che52a] G. F. Chew and G. C. Wick, Phys. Rev. **85** (1952) 636.

[Che52b] G. F. Chew and M. L. Goldberger, Phys. Rev. **87** (1952) 778.

[Che81] T. Chen, R. E. Segel, P. T. Debevec, J. Wiggins, P. P. Singh and J. V. Maher, Phys. Lett. **103B** (1981) 192.

[Chr80] R. Chrien, T. J. Krieger, R. J. Sutter, M. May, H. Palevsky, R. L. Stearns, T. Kozlowski and T. Bauer, Phys. Rev. **C21** (1980) 1014.

[Cia83] G. Ciangaru, C. C. Chang, H. D. Holmgren, A. Nadasen, P. G. Roos, A. A. Cowley, S. Mills, P. P. Singh, M. K. Saber and J. R. Hall, Phys. Rev. C **27** (1983) 1360.

[Cia84a] G. Ciangaru, C. C. Chang, H. D. Holmgren, A. Nadasen and P. G. Roos, Phys. Rev. C **29** (1984) 1289.

[Cia84b] G. Ciangaru, Phys. Rev. C **30** (1984) 479.

[Coh65] S. Cohen and D. Kurath, Nucl. Phys. **73** (1965) 1.

[Coh67] S. Cohen and D. Kurath, Nucl. Phys. **A101** (1967) 1.

[Cow80a] A. A. Cowley, C. C. Chang and H. D. Holmgren, Phys. Rev. C **22** (1980) 2633.

[Cow80b] A. A. Cowley, C. C. Chang, H. D. Holmgren, J. D. Silk, D. L. Hendrie, R. W. Koontz, P. G. Roos, C. Samanta and J. R. Wu, Phys. Rev. Lett. **45** (1980) 1930.

[Cow87] A. A. Cowley, private communication.

[Cow88] A. A. Cowley, J. V. Pilcher, J. J. Lawrie and D. M. Whittal, Phys. Lett. B **201** (1988) 196.

[Dav87] C. Davids, D. Kovar, C. Beck, M. Vineyard, A. Konstantaras, C. Maguire, F. Prosser, V. Reinert, K. Kwiatkowsky and J. Kolata, Physics Division Annual Review, Argonne National Laboratory, **ANL-87-13** (1987) 157.

[Dev79] D. W. Devins, D. L. Friesel, W. P. Jones, A. C. Attard, I. D. Svalbe, V. C. Officer, R. S. Henderson, B. M. Spicer and G. G. Shute, Aust. J. Phys. **32** (1979) 323.

[Ern87] J. Ernst, W. Friedland and H. Stockhorst, Z. Phys. A **328** (1987) 333.

[Fes80] H. Feshbach, A. Kerman and S. Koonin, Ann. of Phys. **125** (1980) 429.

[För88] S. V. Förtsch, A. A. Cowley, J. V. Pilcher, D. M. Whittal, J. J. Lawrie, J. C. van Staden and E. Friedland, Nucl. Phys. **A485** (1988) 258.

[Fra81] S. Frankel, W. Frati, C. F. Perdrisat and O. B. Van Dyck, Phys. Rev. C **24** (1981) 2684.

[Fru84] S. Frullani and J. Mougey, *Advances in Nuclear Physics, Volume* **14**, eds J. W. Negele and E. Vogt, Plenum Press (New York,1984) 1.

[Gou78] C. A. Goulding and J. G. Rogers, Nucl. Instrum. Methods **153** (1978) 511.

[Gou81] C. R. Gould, L. G. Holzsweig, S. E. King, Y. C. Lau, R. V. Poore, N. R. Roberson and S. A. Wender, IEEE Trans. Nucl. Sci. **NS-28** No. 5 (1981) 3708.

[Gou83] C. R. Gould and N. R. Roberson, IEEE Trans. Nucl. Sci. **NS-30** No. 5 (1983) 3758.

[Gre83] R. E. L. Green, D. H. Boal, R. L. Helmer, K. P. Jackson and R. G. Korteling, Nucl. Phys. **A405** (1983) 463.

[Gri66] J. J. Griffin, Phys. Rev. Lett. **17** (1966) 478.

[Hol79] A. Holm, IEEE Trans. Nucl. Sci. **NS-26** No. 4 (1979) 4569.

[Hol81] L. G. Holzsweig and R. V. Poore, IEEE Trans. Nucl. Sci. **NS-28** No. 5 (1981) 3815.

[Hol82] H. D. Holmgren, C. C. Chang, G. Ciangaru and A. A. Cowley, Proc. Third Intern. Conf. on Nuclear Reaction Mechanisms (Varenna, Italy, 1982) 221.

[Hou71] E. Hourany, T. Yuasa, J. P. Didelez, M. Hage Ali, F. Reide and F. Takeuchi, Nucl. Phys. **A162** (1971) 624.

[Hry67] A. Z. Hrynkiewicz, S. Kopta, S. Szymczyk and T. Walczak, Nucl. Instrum. Methods **49** (1967) 229.

[IUC83] Indiana University Cyclotron Facility Scientific and Technical Report (1983) 214.

[IUC84] Indiana University Cyclotron Facility Scientific and Technical Report (1984) 165.

[Jac65] D. F. Jackson and T. Berggren, Nucl. Phys. **62** (1965) 353.

[Jac71] D. F. Jackson, Nucl. Phys. **A173** (1971) 225.

[Jac76] D. F. Jackson, Nucl. Phys. **A257** (1976) 221.

[Jai67] A. K. Jain and D. F. Jackson, Nucl. Phys. **A99** (1967) 113.

[Jai70] A. K. Jain, N. Sarma and B. Banerjee, Nucl. Phys. **A142** (1970) 330.

[Jai73] A. K. Jain, J. Y. Grossiord, M. Chevallier, P. Gaillard, A. Guichard, M. Gusakow and J. R. Pizzi, Nucl. Phys. **A216** (1973) 519.

[Jam69] A. N. James, P. T. Andrews, P. Butler, N. Cohen and B. G. Lowe, Nucl. Phys. **A133** (1969) 89.

[Jip84] P. Jipsen, *ELOSS, A program for calculating the ranges of ions in matter*, National Accelerator Centre (1984), unpublished.

[Kal83] A. M. Kalend, B. D. Anderson, A. R. Baldwin, R. Madey, J. W. Watson, C. C. Chang, H. D. Holmgren, R. W. Koontz, J. R. Wu and H. Machner, Phys. Rev. C **28** (1983) 105.

[Kin50] J. H. Kindle, *Theory and Problems of Plane and Solid Analytic Geometry*, Schaum Publishing Company (New York, 1950).

[Kin81] S. E. King, Y. C. Lau and C. R. Gould, IEEE Trans. Nucl. Sci. **NS-28** No. 5 (1981) 3822.

[Kit76] P. Kitching, C. A. Miller, D. A. Hutcheon, A. N. James, W. J. McDonald, J. M. Cameron, W. C. Olsen and G. Roy, Phys. Rev. Lett. **37** (1976) 1600.

[Kit80] P. Kitching, C. A. Miller, W. C. Olsen, D. A. Hutcheon, W. J. McDonald and A. W. Stetz, Nucl. Phys. **A340** (1980) 423.

[Kit85] P. Kitching, W. J. McDonald, Th. A. J. Maris and C. A. Z. Vasconcellos, *Advances in Nuclear Physics, Volume* **15**, eds J. W. Negele and E. Vogt, Plenum Press (New York,1985) 43.

[Knu68] D. E. Knuth, *The Art of Computer Programming*, Vol. 1, Addison-Wesley Publishing Company (Reading, Massachusetts, 1968) 278.

[Kro70] F. R. Kroll and N. S. Wall, Phys. Rev. C **1** (1970) 138.

[Law87] J. J. Lawrie, private communication.

[Li68] T. Y. Li and S. K. Mark, Can. J. Phys. **46** (1968) 2645.

[Lim64] K. L. Lim and I. E. McCarthy, Phys. Rev. **133** (1964) B1006; Phys. Rev. Lett. **13** (1964) 446.

[Lim66] K. L. Lim and I. E. McCarthy, Nucl. Phys. **88** (1966) 433.

[Lis84] J. Lisantti, J. R. Tinsley, D. M. Drake, I. Bergqvist, L. W. Swenson, D. K. McDaniels, F. E. Bertrand, E. E. Gross, D. J. Horen and T. P. Sjoreen, Phys. Lett. **147B** (1984) 23.

[Mac79] H. Machner, Phys. Lett. **86B** (1979) 129.

[Mac84] H. Machner, D. Protić, G. Riepe, J. P. Didelez, N. Frascaria, E. Gerlic, E. Hourani and M. Morlet, Phys. Lett. **138B** (1984) 39.

[Mac87] H. Machner, Z. Phys. A **327** (1987) 175.

[Mar58] Th. A. J. Maris, P. Hillman and H. Tyrén, Nucl. Phys. **7** (1958) 1.

[Mar59] Th. A. J. Maris, Nucl. Phys. **9** (1959) 577.

[Mea69a] D. F. Measday and C. Richard-Serre, CERN Report **69-17** (1969).

[Mea69b] D. F. Measday and C. Richard-Serre, Nucl. Instrum. Methods **76** (1969) 45.

[Mey81] H. O. Meyer, P. Schwandt, G. L. Moake and P. P. Singh, Phys. Rev. C **23** (1981) 616.

[Mou76] J. Mougey, M. Bernheim, A. Bussière, A. Gillebert, Phan Xuan Hô, M. Priou, D. Royer, I. Sick and G. J. Wagner, Nucl. Phys. **A262** (1976) 461.

[Nak76] K. Nakamura, S. Hiramatsu, T. Kamae, H. Muramatsu, N. Izutsu and Y. Watase, Nucl. Phys. **A268** (1976) 381.

[Pal69] J. N. Palmieri and J. Wolfe, Nucl. Instrum. Methods **76** (1969) 55.

[Pee68] R. W. Peelle, T. A. Love, N. W. Hill and R. T. Santoro, Phys. Rev. **167** (1968) 981.

[Rav87] D. A. Raavé, *The Control and Auxiliary Equipment of the National Accelerator Centre Precision 1.5m Scattering Chamber*, Master Diploma in Electrical Engineering dissertation, Cape Technikon (1987), unpublished.

[Red70] E. F. Redish, G. J. Stephenson Jr., and G. M. Lerner, Phys. Rev. C **2** (1970) 1665.

[Roo65] P. G. Roos and N. S. Wall, Phys. Rev. **140** (1965) B1237.

[Sam81] C. Samanta, Ph. D. thesis, University of Maryland (1981) unpublished.

[Sam86] C. Samanta, N. S. Chant, P. G. Roos, A. Nadasen, J. Wesick and A. A. Cowley, Phys. Rev. **C34** (1986) 1610.

[Seg82] R. E. Segel, T. Chen, L. L. Rutledge, J. V. Maher, J. Wiggins, P. P. Singh and P. T. Debevec, Phys. Rev. **C26** (1982) 2424.

[Seg85] R. E. Segel, S. M. Levenson, P. Zupranski, A. A. Hassan, S. Mukhopadhyay and J. V. Maher, Phys. Rev. **C32** (1985) 721.

[Smi83] C. A. Smith and J. R. Anderson, IEEE Trans. Nucl. Sci. **NS-30** No. 5 (1983) 3756.

[Sub83] T. S. Subramanian, J. L. Romero, F. P. Brady, J. W. Watson, D. H. Fitzgerald, R. Garrett, G. A. Needham, J. L. Ullmann, C. I. Zanelli, D. J. Brenner, and R. E. Prael, Phys. Rev. C **28** (1983) 521.

[Tam77] T. Tamura, T. Udagawa, D. H. Feng and K. -K. Kan, Phys. Lett. **66B** (1977) 109.

[Tan81] I. Tanihata, S. Nagamiya, S. Schnetzer and H. Steiner, Phys. Lett. **100B** (1981) 121.

[Ulm87] P. E. Ulmer, H. Baghaei, W. Bertozzi, K. I. Blomqvist, J. M. Finn, C. E. Hyde-Wright, N. Kalantar-Nayestanaki, S. Kowalski, R. W. Lourie, J. Nelson, W. W. Sapp, C. P. Sargent, L. Weinstein, B. H. Cottman, P. K. Teng, E. J. Winhold, M. Yamazaki, J. R. Calarco, F. W. Hersman, J. J. Kelly, M. E. Schulze and G. Audit, Phys. Rev. Lett. **59** (1987) 2259.

[Van88a] G. van der Steenhoven, H. P. Blok, E. Jans, M. de Jong, L. Lapikás, E. N. M. Quint and P. K. A. de Witt Huberts, Nucl. Phys. **A480** (1988) 547.

[Van88b] G. van der Steenhoven, H. P. Blok, E. Jans, L. Lapikás, E. N. M. Quint and P. K. A. de Witt Huberts, Nucl. Phys. **A484** (1988) 445.

[Van88c] G. van der Steenhoven, H. P. Blok, E. Jans, L. Lapikás and P. K. A. de Witt Huberts, Phys. Rev. Lett. **61** (1988) 2000.

[Wac72] J. W. Wachter, W. A. Gibson and W. R. Barrus, Phys. Rev. **C6** (1972) 1496.

[Wal66] N. S. Wall and P. G. Roos, Phys. Rev. **150** (1966) 811.

[Wap85] A. H. Wapstra and G. Audi, Nucl. Phys. **A432** (1985) 1.

[Wes83] J. S. Wesick, Ph. D. thesis, University of Maryland (1983) unpublished.

[Wes85] J. S. Wesick, P. G. Roos, N. S. Chant, C. C. Chang, A. Nadasen, L. Rees, N. R. Yoder, A. A. Cowley, S. J. Mills and W. W. Jacobs, Phys. Rev. **C32** (1985) 1474.

[Wol52] P. A. Wolff, Phys. Rev. **87** (1952) 434.

[Wu79] J. R. Wu, C. C. Chang and H. D. Holmgren, Phys. Rev. **C19** (1979) 698.

[Wu80] J. R. Wu, Phys. Lett. **91B** (1980) 169.